Energy Island North Sea

Metocean Assessment

Part B: Data Analyses – Energy Island

Metocean site conditions for detailed design of the energy island

Report
IO number: 4500087261

Prepared for Energinet Eltransmission A/S

2023-08-09

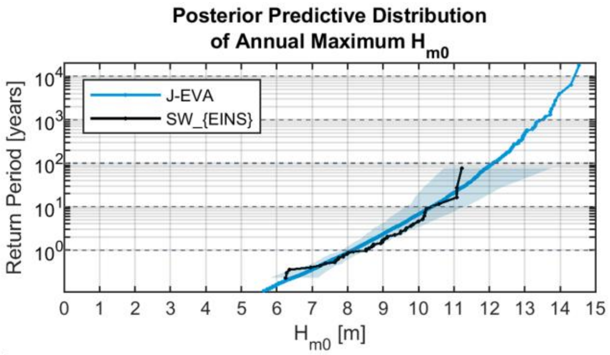

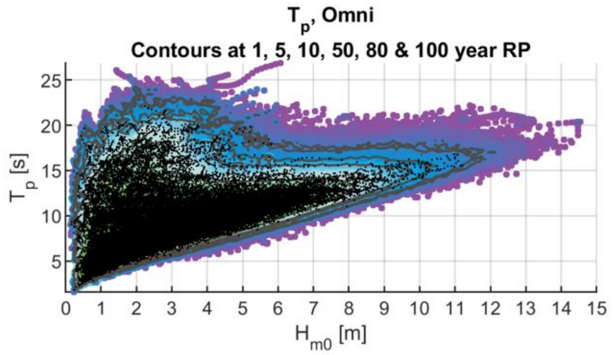

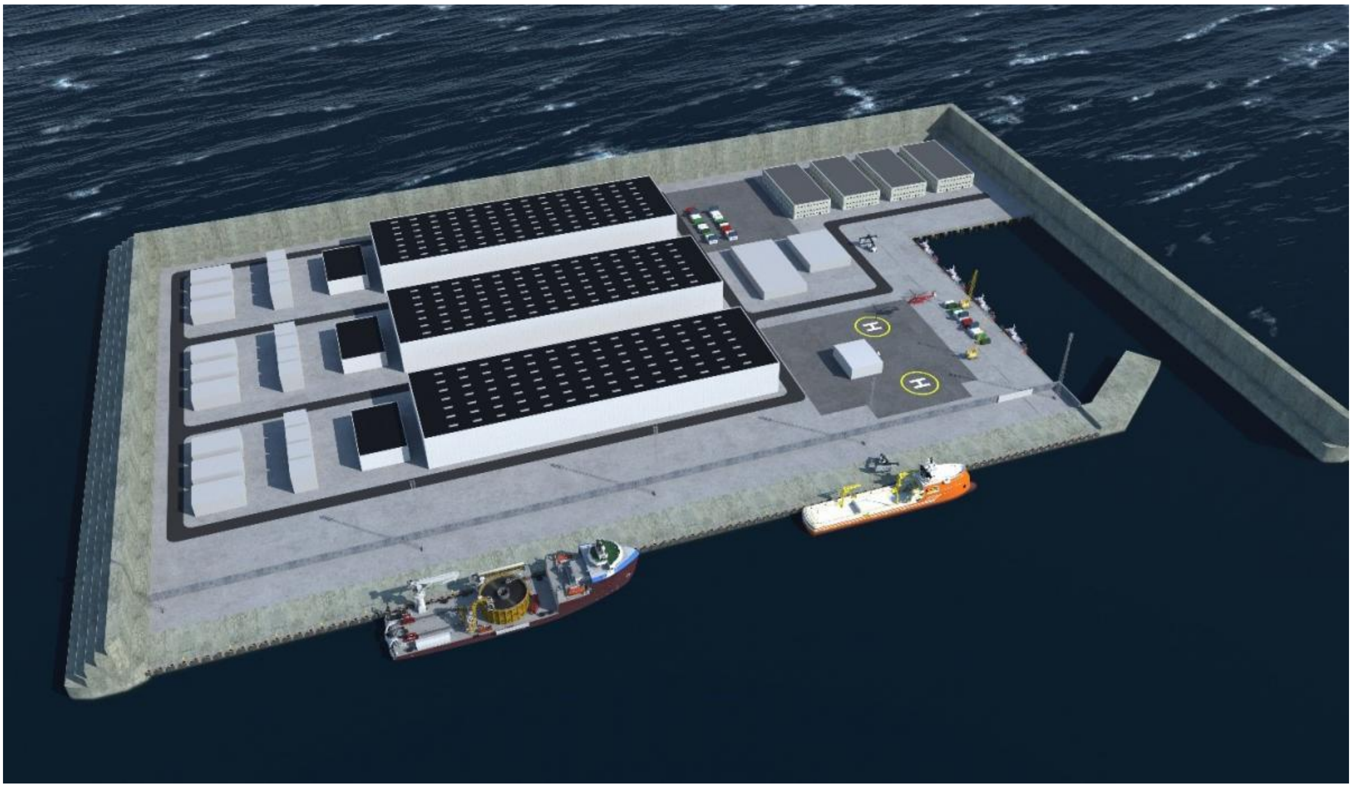

Energy Island North Sea

Metocean Assessment

Part B: Data Analyses – Energy Island

Metocean site conditions for detailed design of the energy island

Report
IO number: 4500087261

Prepared for: Energinet Eltransmission A/S
Represented by Mr Kim Parsberg Jakobsen

Contact person:	Patrick Dich Grode, pdg@dhihroup.com, +45 4516 9070
Project Manager:	Patrick Dich Grode
Quality Supervisor:	Patrick Dich Grode, Jacob Berg, Ameya Sathe
Author:	Ameya Sathe, Eduardo Gonzalez - Gorbena Eisenmann, Patrick Dich Grode
Project No.:	11828428
Approved by:	Jesper Ulrik Fuchs

Revision:	**Date:**	**Description:**
1.2	2023-08-09	Final report including final comments from client and certifier. Appendix A attachments removed and provided as separate files.
1.1	2023-07-17	Final report including final comments from client and certifier.
1.0	2023-06-30	Final report including final comments from client and certifier.
0.2	2023-06-16	Revised draft report including comments from client and certifier.
0.1	2023-04-21	Draft report issued for comments by client and certifier.
Classification:	Confidential	
File name:	11828428_DHI_EINS_Metocean_Part_B_Analyses_Island	

DHI A/S • Agern Allé 5 • • DK-2970 Hørsholm • Denmark
Telephone: +45 4516 9200 • dhi@dhigroup.com • www.dhigroup.com • Company Reg. No.: 36466871

Contents

Executive Summary **7**

1 Introduction **11**

2 Analysis Points **12**

3 Wind **13**

3.1 Normal wind conditions 14
3.1.1 Normal wind profile 14
3.1.2 Time series 14
3.1.3 Wind rose 14
3.1.4 Histogram (Weibull parameters) 15
3.1.5 Monthly statistics 16
3.1.6 Directional statistics 16
3.2 Extreme wind conditions 17
3.2.1 Extreme wind profile (height conversion) 17
3.2.2 Wind averaging (temporal conversion) 17
3.2.3 Extreme wind speed 17

4 Water Level **20**

4.1 Normal water level conditions 21
4.1.1 Time series 21
4.1.2 Tidal levels 21
4.1.3 Histogram 22
4.1.4 Monthly statistics 23
4.2 Extreme water level conditions 24
4.2.1 Extreme high water levels 25
4.2.2 Extreme low water levels 27

5 Current **29**

5.1 Normal current conditions 30
5.1.1 Normal current profile 30
5.1.2 Time series 30
5.1.3 Current roses 31
5.1.4 Histogram 33
5.1.5 Monthly statistics 34
5.1.6 Directional statistics 34
5.1.7 Maps of normal current speed 35
5.2 Extreme current conditions 36
5.2.1 Extreme current profile 37
5.2.2 Extreme current speed 37
5.2.3 Extreme current rose 39
5.2.4 Maps of extreme current speed 43

6 Waves **46**

6.1 Normal wave conditions 47
6.1.1 Time series 47
6.1.2 Wave roses 48
6.1.3 Histogram 49
6.1.4 Monthly statistics 50
6.1.5 Directional statistics 50
6.1.6 Scatter diagrams (H_{m0}) 51
6.1.7 Wind-wave misalignment 57
6.1.8 Swell waves 58

6.1.9 Assessment of wave spectra ... 59
6.1.10 Maps of mean H_{m0} ... 60
6.2 Extreme wave conditions ... 62
6.2.1 Extreme significant wave height, H_{m0} ... 63
6.2.2 Maps of extreme H_{m0} ... 67
6.2.3 Variables conditioned on H_{m0} ... 70
6.2.4 Extreme maximum wave height, H_{max} ... 76
6.2.5 Extreme maximum wave crest, C_{max} ... 78
6.2.6 Wave breaking and limitations ... 80

7 Other Atmospheric Conditions ... 89

7.1 Rainfall ... 89
7.1.1 Data ... 89
7.1.2 Methodology ... 89
7.1.3 Results ... 91
7.2 Air temperature, humidity, and solar radiation ... 96
7.3 Lightning ... 98
7.4 Visibility ... 100

8 Other Oceanographic Conditions ... 102

8.1 Water temperature, salinity, and density ... 102

9 Marine growth ... 109

10 References ... 111

11 Appendix A: List of Data Reports ... 116

12 Appendix B: Comparison of J-EVA and T-EVA ... 117

13 Appendix C: T-EVA – Traditional EVA ... 127

13.1 Summary of approach ... 127
13.2 Long-term distributions ... 128
13.3 Individual wave and crest height ... 129
13.3.1 Individual waves (modes) ... 129
13.3.2 Convolution of short-term variability with long-term storm density ... 130
13.4 Subset extremes ... 131
13.4.1 Optimised directional extremes ... 131
13.5 Uncertainty assessment ... 132
13.6 Confidence limits ... 133
13.7 Joint probability analyses (JPA) ... 133

14 Appendix D: J-EVA Summary ... 136

14.1 Joint Extreme Values Analysis (J-EVA) ... 136
14.2 J-EVA storm model ... 137
14.2.1 Directional and seasonal variability ... 137
14.3 J-EVA statistical model ... 138
14.3.1 Estimation of the model parameters ... 138
14.3.2 Conditional extreme model ... 139
14.4 J-EVA simulation ... 140
14.4.1 Directional Scaling ... 140
14.4.2 Simulation Optimization ... 141
14.5 Convolution of short-term distributions ... 141
14.6 Sampling of tidal signal ... 141
14.7 Limitations on wave height ... 142

15 Appendix E: J-EVA – Storm Model ... 143

15.1 Characterisation of Historical Storms 143
15.2 Wave Height and Storm Duration 143
15.3 Associated Environmental Variables 145
15.4 Simulation of Intra-Storm Variation 147
15.4.1 Similarity and Storm Resampling 147
15.4.2 Historical Storm Scaling 148
15.5 Heights and Periods of Individual Waves 149
15.5.1 Associated Wave Periods 150

16 Appendix F: J-EVA – Statistical Model 151

16.1 Model components 151
16.2 Marginal models 152
16.3 Rate of occurrence 153
16.4 Conditional extremes 153
16.5 Covariates 155
16.6 Parameter estimation 158
16.7 Simulation and return value estimation 162

Nomenclature

Variable	Abbrev.	Unit
Atmosphere		
Wind speed @ 10 m height	WS_{10}	m/s
Wind direction @ 10 m height	WD_{10}	°N (clockwise from)
Air pressure @ mean sea level	P_{MSL}	hPa
Air temperature @ 2 m height	$T_{air,2m}$	°C
Relative humidity @ 2 m height	RH_{2m}	-
Downward solar radiation flux	SR	W/m^2
Visibility	VIZ	km
Ocean		
Water level	WL	mMSL
Current speed	CS	m/s
Current direction	CD	°N (clockwise to)
Water temperature	T_{water}	°C
Water Salinity	Salinity	-
Water density	ρ_{water}	Kg/m^3
Waves		
Significant wave height	H_{m0}	m
Peak wave period	T_p	s
Mean wave period	T_{01}	s
Zero-crossing wave period	T_{02}	s
Peak wave direction	PWD	°N (clockwise from)
Mean wave direction	MWD	°N (clockwise from)
Direction standard deviation	DSD	°

Executive Summary

Energinet Eltransmission A/S (Energinet) requested a metocean site conditions assessment to form part of the site conditions and to serve as the basis for the design of the Energy Island North Sea (EINS).

This study provides detailed metocean conditions for EINS and establishes a metocean database for the energy island and the related offshore wind farm (OWF) area development area around the island as shown in Figure 0.1.

Table 0.1 provides a summary of metocean guidelines, EVA methodology, and analyses of **Part B** (**island area, this report**), and Part C (OWF area).

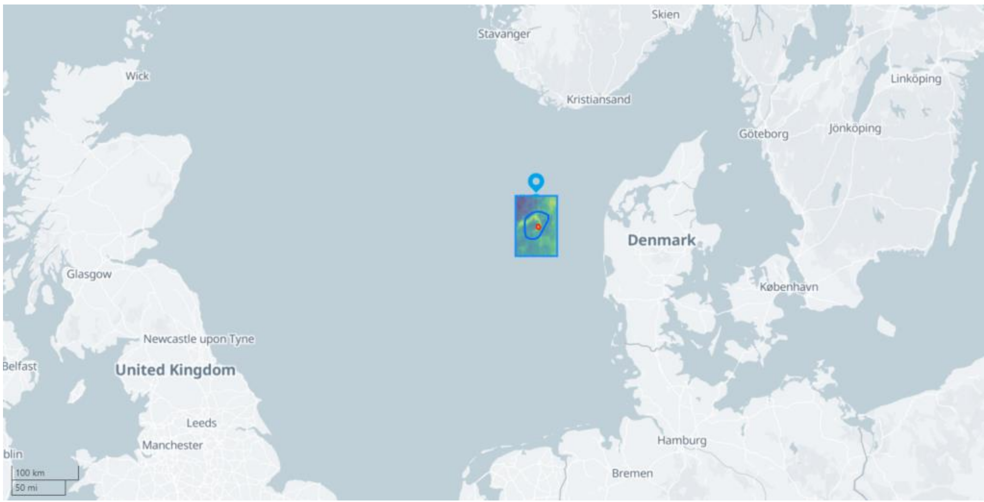

Figure 0.1 Location of the Energy Island North Sea, the related offshore wind farm development area, and measurement stations
The hindcast database (light blue polygon) entails: Waves: EINS-SW-CFSR, Ocean: EINS-SW-CFSR, Atmosphere: Global-AT-CFSR.

Table 0.1 Summary of metocean guidelines, EVA methodology, and analyses
Analyses concern normal and extreme conditions included at each analysis point. The Part A report, [1], forms the data basis for Part B (Island) and Part C (OWF) analysis reports.

Subject	**Part B (Island)** Points: EINS-1-5	**Part C (OWF)** Points: OWF-1-8
Extremes - methodology	J-EVA (directional)	T-EVA (omni only)
Analyses - Wind	✓	÷
Analyses - Water Level	✓	✓
Analyses - Current	✓	✓
Analyses - Waves	✓	✓
Wind-Wave misalignment	✓	✓
Other Metocean Conditions	✓	✓

Summary of data basis, Part A, [1]

All metocean hindcast model data covered the period 1979-01-01 to 2022-10-01 (43+ years) at 30-min interval. Wind and other atmospheric data were adopted from CFSR (rainfall data from ERA5), while a local hindcast 2D hydrodynamic model, HD_{EINS}, was set up to simulate water levels and currents, and a dedicated spectral wave model SW_{EINS}, was set up to simulate waves. 3D currents, water temperature and salinity were adopted from the DHI United Kingdom and North Sea 3-dimensional (HD_{UKNS3D}) hydrodynamic model.

The hindcast data was compared to a comprehensive set of local wind, water level, current, wave and CTD (sea temperature and salinity) measurements (2021-11-15 to 2022-11-15.) supplemented by long-term measurements from other stations in the North Sea and found to be accurate and applicable for assessments of normal and extreme metocean conditions at EINS.

Recommendations for wind profiles/averaging, current profiles, and short-term wave distributions were established based on the local measurements.

Sea level rise (SLR) was estimated at +0.8 m by the year 2113 (end of lifetime). It is recommended that designers consult Energinet for any given design requirements, to decide on the safety policy and procedure with respect to relevant climate change effects. A (potentially conservative) guideline on climate change effects on wind and waves is suggested in NORSOK, [2].

The metocean hindcast data developed for EINS covers the entire light blue polygon in Figure 0.1. It entails all hindcast wave, ocean, and atmospheric variables and was provided to Energinet on a hard disk in MIKE dfs file formats. The dfs files can be read using either the Python MikeIO[1] or the DHI-MATLAB-Toolbox[2] open source libraries available at GitHub.

Normal conditions

At EINS the mean wind speed is 8.8 m/ s and mean significant wave height is 1.9 m (see Figure 0.3) with peak wave periods most frequently between 4 – 8 s. The wave conditions are characterized by a mix of swell from the North Atlantic and local wind-sea predominantly from the west, with a dominance of extremes from the northwest, see Figure 0.2.

The tides are weak with HAT = +0.38 mMSL and LAT = -0.33 mMSL, giving a total tidal envelope of 0.71 m. The highest and lowest total water levels in the hindcast period is +1.7 mMSL and -1.2 mMSL and occur during winter (Nov. – Feb.). The mean total current speed is 0.17±0.03 m/s dominated by residual (especially during extreme events).

[1] https://github.com/DHI/mikeio
[2] https://github.com/DHI/DHI-MATLAB-Toolbox

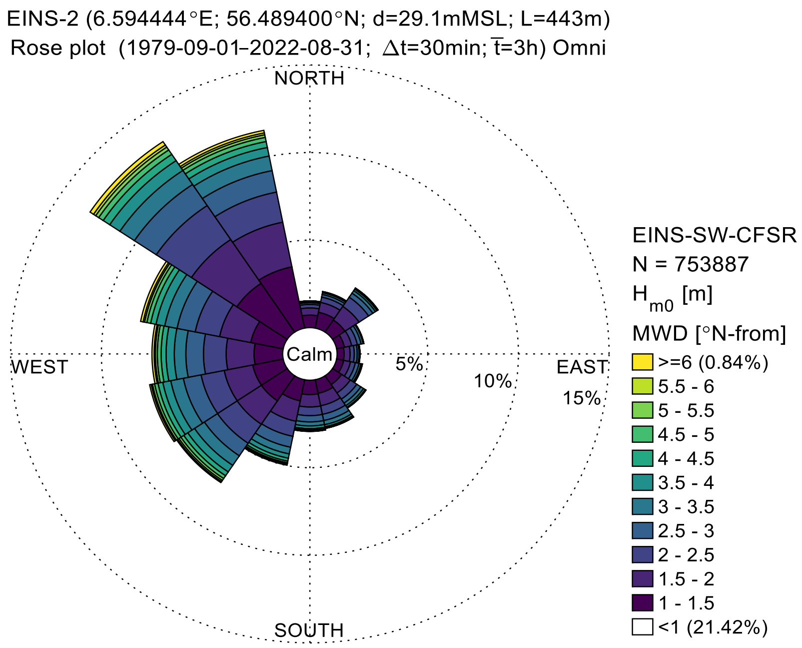

Figure 0.2 Wave rose at EINS-2

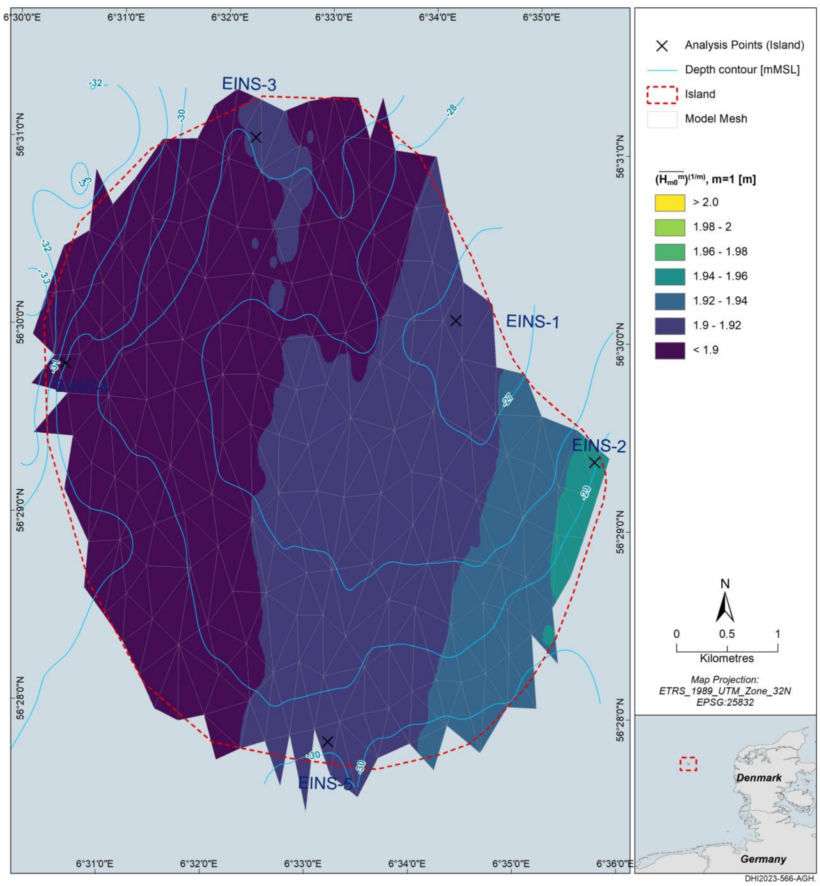

Figure 0.3 Spatial variation of $\overline{H_{m0}}$ across EINS

Extreme conditions

Extreme metocean conditions were established using DHI's state-of-the-art Joint Extreme Value Analysis (J-EVA) analysis toolbox. Extreme values were established for return periods up to 10,000 years for wind, waves (significant wave height, maximum individual wave height based on Glukhovskiy, and maximum crest height based on Forristall), water levels, and currents. Joint probability of metocean conditions is also provided.

The annual, omni-directional extreme value estimates at the analysis point EINS-2 are presented in Table 0.2. Variation of extreme CS_{tot} and H_{m0} is also calculated across the EINS site. The maximum variation of CS_{tot} is about 0.3 m/s for a 100-year return period (see Figure 5.15), and that of H_{m0} is about 2 m for a 50- and 100-year return period (see Figure 6.23 and Figure 6.24). The directional extreme values are scaled according to DNV-RP-C205, [3].

Comparisons between measured and modelled relation between H_{max} and T_{Hmax} demonstrated a very good agreement, and assessment of several common wave limitation approaches suggests that the extreme sea states are prone to steepness- or depth-induced wave breaking at EINS. In conclusion, we used the DNV steepness criteria with an upper bound of T_{Hmax} to limit H_{max}, and a ratio of 0.85 between the C_{max} and H_{max} to limit C_{max} accordingly.

Table 0.2 Summary of omni marginal extreme values at EINS-2 (d = 29.1 mMSL)
Conditioned (joint) variables are given in Section 6.2.3.

Variable	Extreme value (omni) - Return Period [Year]							
	1	5	10	50	80	100	10^3	10^4
Extreme Wind Speed, WS [m/s], 10m, 10 min	26.8	30.1	31.4	34.3	35.1	35.5	39.7	44.7
High Water level, Total, HWL_{tot} [mMSL]	1.2	1.4	1.5	1.7	1.7	1.8	2.1	2.4
Low Water level, Total, LWL_{tot} [mMSL]	-0.8	-1.0	-1.0	-1.1	-1.2	-1.2	-1.4	-1.6
High Water level, Residual, HWL_{res} [m]	1.0	1.3	1.4	1.6	1.7	1.7	2.0	2.3
Low Water level, Residual, LWL_{res} [m]	-0.7	-0.9	-0.9	-1.1	-1.1	-1.1	-1.3	-1.6
Current Speed, Total, Surface, $CS_{surface}$ m/s]	1.0	1.2	1.3	1.5	1.5	1.5	1.8	2.1
Current Speed, Total, Depth-averaged, CS_{tot} [m/s]	0.7	0.8	0.9	1.0	1.1	1.1	1.3	1.5
Current Speed, Total, Near-seabed, $CS_{near\text{-}seabed}$ [m/s]	0.5	0.7	0.7	0.8	0.8	0.8	1.0	1.1
Significant wave height, 3hr, H_{m0} [m]	8.1	9.7	10.3	11.6	12.0	12.1	13.5	14.6
Peak wave period, assoc. with H_{m0}, $T_p\|H_{m0}$ [s]	13.2	14.7	15.3	16.4	16.7	16.8	17.9	18.7
Mean zero-crossing period, assoc. with H_{m0}, $T_{02}\|H_{m0}$ [s]	8.9	9.8	10.1	10.7	10.9	10.9	11.6	12.0
Maximum wave height, H_{max} [m]	14.7	17.2	18.2	20.3	20.8	21.1	23.3	23.4
Wave period assoc. with H_{max}, T_{Hmax} [s]	11.4	12.5	13.0	13.8	14.1	14.2	15.1	15.1
Maximum crest level with respect to SWL, $C_{max,SWL}$	9.7	12.1	13.1	15.3	16.0	16.3	19.2	19.9
Maximum crest level with respect to MSL, $C_{max,MSL}$	10.3	12.9	13.9	16.3	17.0	17.3	20.3	20.4

1 Introduction

This study provides detailed metocean conditions for the Energy Island North Sea (EINS) and establishes a metocean database for the island and the adjacent offshore wind farm (OWF) development area (see Figure 1.1).

Energinet Eltransmission A/S (Energinet) was instructed by the Danish Energy Agency (DEA) to initiate site investigations, including a metocean conditions assessment, to form part of the site conditions assessment and to serve as the basis for the design and construction of EINS and related OWF's. The study includes an assessment of climate change considering an 80-year lifetime.

Energinet commissioned DHI A/S (DHI) to provide this study with Scope of Work (SoW) defined in [4]. Later, the work was extended to cover also FEED level metocean conditions for the offshore wind farm area cf. scope in [5]. The study refers to the following common practices and guidelines:

- DNV-RP-C205, [3]
- IEC 61400-3-1, [6]

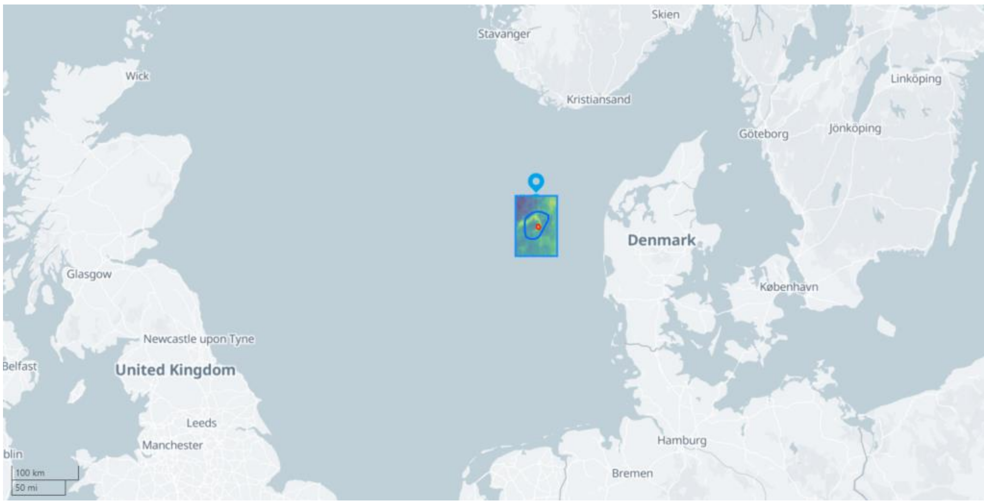

Figure 1.1 The location of the Energy Island North Sea (red dot), and related offshore wind farm development area (dark blue)
The hindcast database (light blue polygon) entails: Waves: *EINS-SW-CFSR*, Ocean: *EINS-SW-CFSR*, Atmosphere: *Global-AT-CFSR*.

The deliverables included time series data of hindcast metocean parameters, normal, extreme, and joint analyses at five (5) and eight (8) locations within the EINS and OWF areas respectively, a metocean database (see Figure 1.1), and four (4) separate reports:

- **Part A: Data Basis – Measurements and Models, [1]**
  Establishment of bathymetry, measurements and hindcast metocean data.
- **Part B: Data Analyses – Energy Island, [7] (this report)**
  Metocean site conditions for detailed design of the energy island.
- **Part C: Data Analyses – Wind Farm Area, [8]**
  FEED level metocean site conditions for the offshore wind farm area.
- **Part D: Data Basis – Hindcast Revalidation Note**, [9]
  Revalidation of the hindcast metocean data vs. extended measurements.

2 Analysis Points

This section presents the EINS points selected for analysis.

Figure 2.1 shows a map of the five (5) analysis points within the EINS area, and Table 2.1 presents the coordinates and water depths of the points. The EINS-1, EINS-2, and EINS-3 analysis points are the locations of lowest water depth, maximum H_{m0} and maximum total current speed, respectively. EINS-4 and EINS-5 represent the western and southern regions of EINS. Results at **EINS-2** are presented in the body of this report, while results at all locations are given in the data reports (listed in Table 11.1) which are attached to this report.

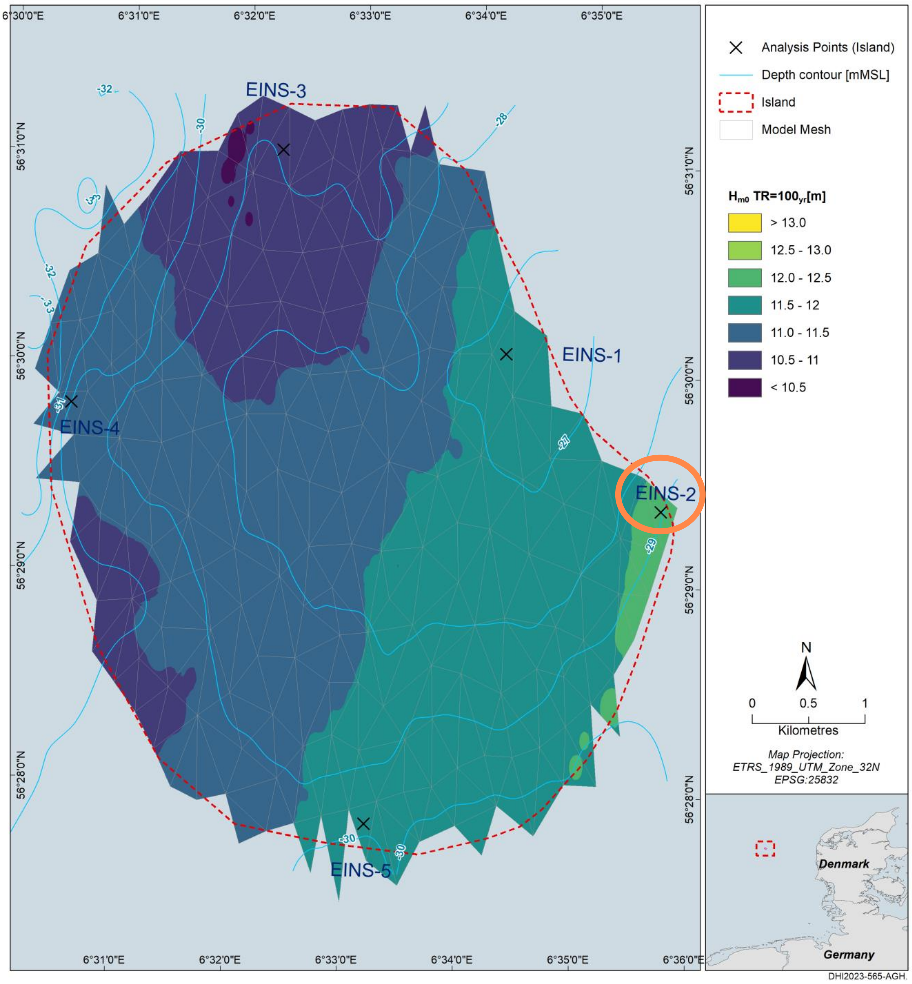

Figure 2.1 Map of the Energy Island North Sea (EINS) analysis points

Table 2.1 Coordinates and water depths of the EINS analysis points

#	Point Name (A-z)	Description	Longitude WGS84 [°E]	Latitude WGS84 [°N]	Depth, Survey [mMSL]	Depth, HD_{EINS} [mMSL]	Depth, SW_{EINS} [mMSL]
1	EINS-1	Shallowest	6.5714	56.5016	26.3	27.0	26.6
2	EINS-2	Max H_{m0}	6.5944	56.4894	28.9	29.1	29.1
3	EINS-3	Max CS_{tot}	6.5383	56.5172	28.8	28.9	28.9
4	EINS-4	West	6.5094	56.4962	30.1	30.2	30.1
5	EINS-5	South	6.5533	56.4638	29.8	29.8	29.8

3 Wind

This section presents a summary of the wind data basis established in [1], followed by a presentation of normal and extreme wind conditions.

The wind data was adopted from [2] and consisted of CFSR data during the period 1979 – 2022 (43.75 years). For convenience, we interpolated the CFSR data from its native resolution (~23 km and 1 hour) to the mesh and output time step of the wave model of this study (~400 m and 1800 s). The wind dataset is denoted EINS-AT-CFSR. Table 3.1 summarises the metadata of the EINS-AT-CFSR dataset.

Table 3.1 Metadata of the EINS-AT-CFSR dataset
Time series data was provided to Energinet (.csv, .mat, .nc, .dfs0).

Name	Value
Dataset ID:	EINS-AT-CFSR
Start Date [UTC]:	1979-01-01 01:00:00
End Date [UTC]:	2022-09-30 23:30:00
Time Step [s]:	1800 (interpolated from 3600 s)
Cell Size [m]:	~400 (interpolated from ~23 km)

The CFRS wind is considered representative of a 2-hour averaging period, see [2], at 10 m height. Methods of converting to other temporal averages and heights are assessed for normal and extreme conditions respectively.

The wind analyses are presented in speed bins of 1.0 m/s and directional bins of 22.5° at 10 (and 30) m height. The direction is from where the wind is coming from. Table 3.2 presents the variables of the EINS-AT-CFSR dataset, including the bin sizes applied in figures and tables.

Table 3.2 Wind variables of the EINS-AT-CFSR dataset
The wind direction is from where the wind is blowing.

Variable name	Abbrev.	Unit	Bin size
Wind speed at 10 m height	WS_{10}	m/s	1.0
Wind direction at 10 m height	WD_{10}	°N-from	22.5

The wind analyses cover the data period 1979-09-01 – 2022-08-31 (43 years), a round number of years, which is preferrable for extreme value analyses. The normal conditions apply a 30-min interval (as the hindcast models), while the extreme conditions (J-EVA) apply a 1-hour interval (as native in CFSR).

The main body of this report presents results at EINS-2 (the location of max H_{m0}), while results at all analysis points are given in the data reports (listed in Table 11.1) which are attached to this report. The data reports contain all (scatter) tables and figures presented below.

3.1 Normal wind conditions

The normal wind conditions are presented in terms of:

- Normal wind profile
- Time series
- Wind rose
- Histogram (Weibull parameters)
- Monthly statistics
- Directional statistics

3.1.1 Normal wind profile

Wind profiles are assessed in Section 3.2.1 in Part A, [1]. It is recommended to apply a power profile with α = 0.08 to convert normal (average) wind speeds from 10 to 30 m height (this corresponds to a factor of 1.09).

3.1.2 Time series

Figure 3.1 shows a time series of wind speed at EINS-2 during the considered 43-year period. The mean is 8.8 m/s, and the maximum is 32.3 m/s (6th Nov. 1985).

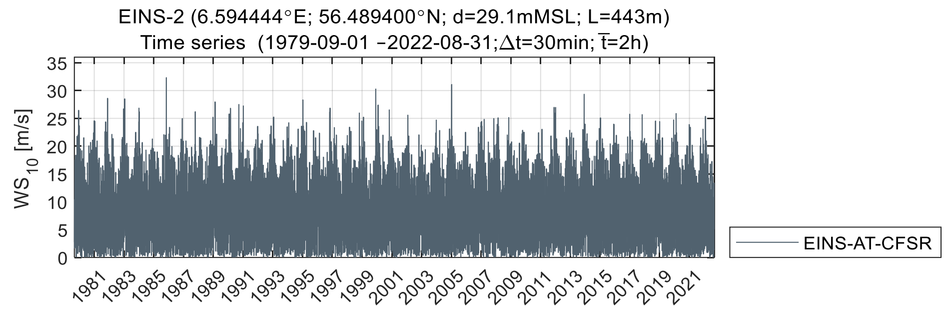

Figure 3.1 Time series of wind speed at EINS-2

3.1.3 Wind rose

Figure 3.2 shows a wind rose at EINS-2. As typical for the North Sea, wind occurs from all directions, but with a predominance from west, and least frequently from northeast.

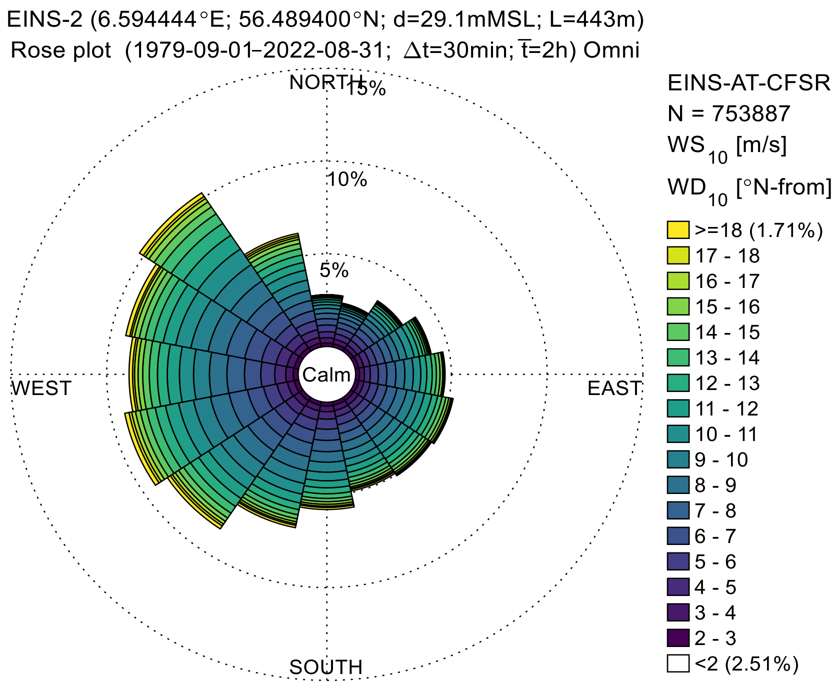

Figure 3.2 Wind rose at EINS-2; WS_{10} vs WD_{10}

3.1.4 Histogram (Weibull parameters)

Figure 3.3 shows a histogram of wind speed at EINS-2. The figure shows a mean value (m) of 8.79 m/s and omni Weibull parameters of A = 9.91 and k = 2.35. Weibull parameters for all directions are given in the data reports.

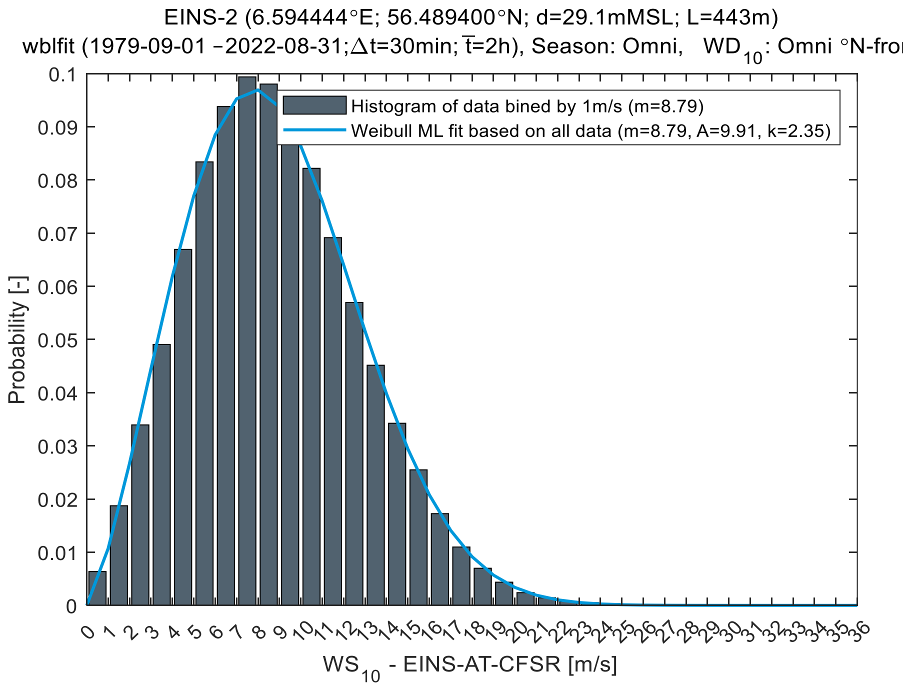

Figure 3.3 Histogram of wind speed (w. Weibull parameters) at EINS-2

3.1.5 Monthly statistics

Figure 3.4 shows monthly statistics of wind speed at EINS-2. The mean varies from 7 m/s during summer to 11 m/s during winter. The strongest wind speeds occurred during the months of Nov., Dec., and Jan.

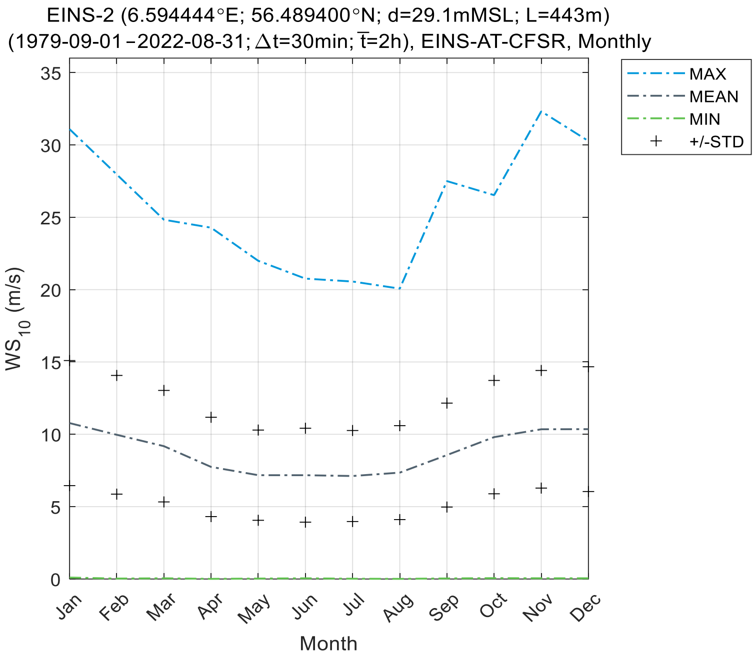

Figure 3.4 Monthly statistics of wind speed at EINS-2

3.1.6 Directional statistics

Figure 3.5 shows directional statistics of wind speed at EINS-2. The mean is strongest from the northwest at almost 10 m/s, and weakest from northeast at about 7 m/s. The strongest winds occur from the (north-)western sector.

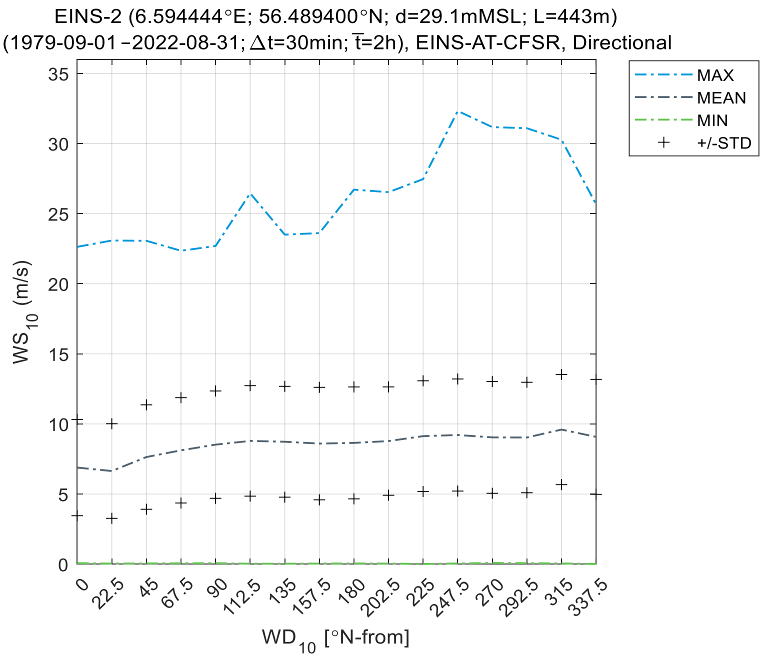

Figure 3.5 Directional statistics of wind speed at EINS-2

3.2 Extreme wind conditions

The extreme wind conditions are estimated following the steps outlined in Appendix D: J-EVA Summary. The storm events selected for the J-EVA analyses are described in Section 6.2 and shown in Figure 6.19. A J-EVA statistical model (see Section 14.3) has been set up, followed by simulation including directional scaling (see Section 14.4 in Appendix D: J-EVA Summary) to estimate the extremes of the 10 m wind speed.

3.2.1 Extreme wind profile (height conversion)

Wind profiles are assessed in Section 3.2.1 in Part A, [1]. It is recommended to apply a power profile with $\alpha = 0.10$ to convert extreme wind speeds from 10 to 30 m height (this corresponds to a factor of 1.12).

3.2.2 Wind averaging (temporal conversion)

Wind averaging was assessed in Section 3.2.2 in Part A, [1]. It is recommended to adopt the IEC factors for converting between averaging times of extreme wind speeds within the range of 2 hours (CFSR) and 10-min, i.e., a factor of 1.08 to convert from 2-h to 10-min average duration of extreme wind speeds. A more cautious/conservative approach may be to adopt the Frøya profile for temporal conversion of extreme wind speeds.

3.2.3 Extreme wind speed

Figure 3.6 shows directional annual number of exceedances of the 10 m wind speed from the 80,000-year simulation, which is used to calculate the best estimate for 1-, 5-, 10-, 50-, 80-, and 100-year return period extremes. Best estimates for larger return periods are calculated based on simulating up to 4 x 10^6 years of events, where the minimum number of exceedances $N_e = 50$ is chosen for the 80,000-year return period.

80.000 years is not provided as return period values, but the J-EVA simulations are run up to 80.000 years to support the directional scaling that needs directional values of 8 times the considered return periods (see Section 14.4.1 and 14.4.2). The extreme values are presented (Table 3.3 and Table 3.4) for a maximum return period of 10,000 years.

The model fits the omni-directional data very well. There is hardly any variation in the quality of the fit to the directional values, which is very good for all directions. From a J-EVA point of view, it is also important that all data points representing storm events are within the light blue shaded area since this means that they have been resampled in the simulation.

Table 3.3 and Table 3.4 provide the values of the directional extreme wind speeds at 10 m and 30 m height. The values are representative of 10-min average wind speed. Extreme wind speeds of a 2-hour averaging period are presented in the Excel tables (listed in Table 11.1) which are attached to this report. The directional extreme values are scaled according to DNV-RP-C205, [3].

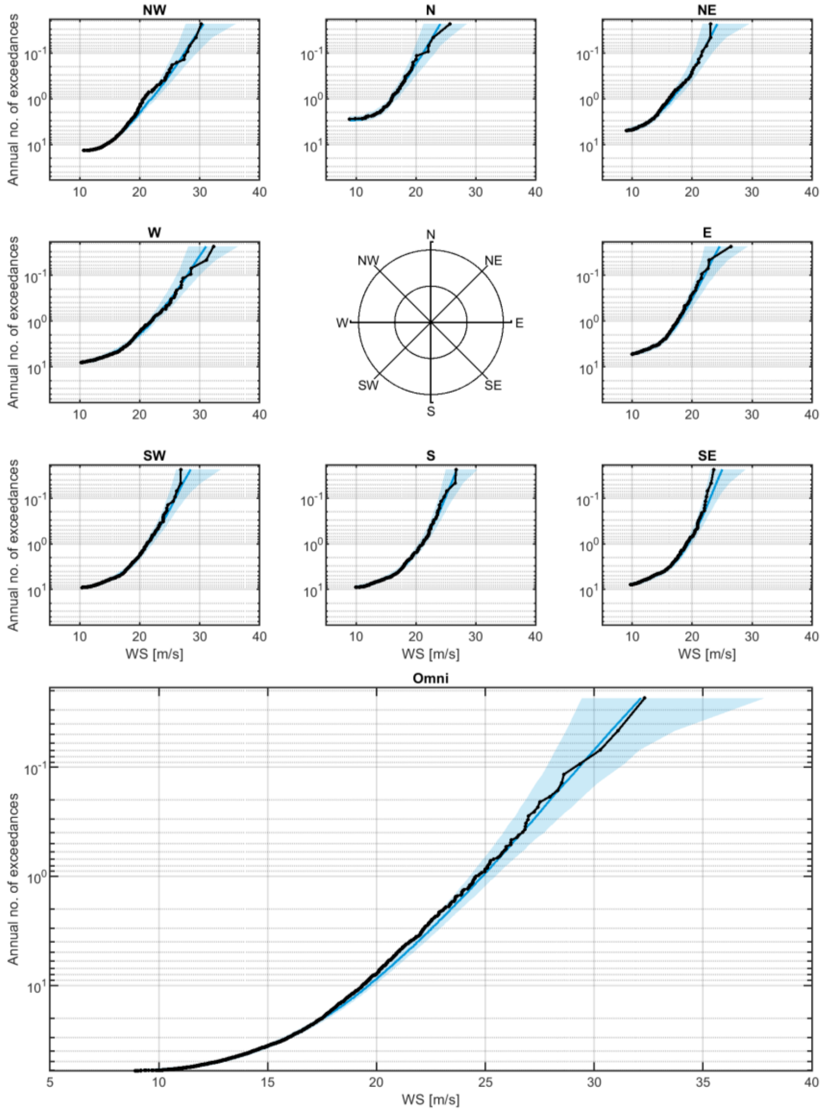

Figure 3.6 Directional exceedance probability of 10 m height wind speed at EINS-2

Hindcast data is shown in black. The blue line is the best estimate using the integrated posterior distribution parameters. The shaded area is the 2.5-97.5% credible interval.

Table 3.3 Directional 10-min extreme wind speed, 10 m height, at EINS-2

22.5° Directional Extreme Wind Speed , WS [m/s], 10m, 10 min								
Direction (WD [°N-from])	Return Period [years]							
	1	5	10	50	80	100	1000	10000
Omni	26.8	30.1	31.4	34.3	35.1	35.5	39.7	44.7
0	19.1	22.4	23.7	26.4	27.0	27.3	30.9	34.9
22.5	17.9	22.5	23.7	26.2	27.0	27.2	30.9	34.9
45	21.9	24.7	25.8	28.3	28.9	29.4	33.5	38.6
67.5	21.7	24.5	25.6	28.1	28.7	29.1	33.0	36.9
90	21.9	24.7	25.9	28.3	28.9	29.3	32.9	37.3
112.5	22.6	25.2	26.1	28.4	28.9	29.3	32.4	36.0
135	23.4	25.6	26.5	28.4	29.1	29.3	32.5	36.1
157.5	24.1	26.2	27.0	28.8	29.3	29.6	32.2	35.3
180	25.5	27.8	28.5	30.1	30.7	30.9	33.6	36.6
202.5	25.7	28.2	29.2	31.2	32.0	32.2	36.1	40.4
225	26.1	28.8	29.9	32.4	33.2	33.5	37.8	42.7
247.5	26.8	30.1	31.4	34.3	35.1	35.5	39.7	44.7
270	26.8	30.1	31.4	34.3	35.1	35.5	39.7	44.7
292.5	26.8	30.1	31.4	34.3	35.1	35.5	39.7	44.7
315	26.8	30.1	31.4	34.3	35.1	35.5	39.7	44.7
337.5	24.9	28.0	29.2	32.0	32.7	33.2	37.4	42.3

Table 3.4 Directional 10-min extreme wind speed, 30 m height, at EINS-2

22.5° Directional Extreme Wind Speed , WS [m/s], 30m, 10 min								
Direction (WD [°N-from])	Return Period [years]							
	1	5	10	50	80	100	1000	10000
Omni	29.9	33.6	35.1	38.3	39.2	39.7	44.4	49.9
0	21.3	25.0	26.4	29.4	30.1	30.5	34.5	38.9
22.5	20.0	25.1	26.4	29.3	30.1	30.4	34.5	38.9
45	24.5	27.6	28.8	31.6	32.3	32.8	37.4	43.0
67.5	24.2	27.4	28.6	31.3	32.1	32.4	36.9	41.2
90	24.5	27.6	28.9	31.6	32.3	32.7	36.8	41.6
112.5	25.2	28.1	29.2	31.7	32.3	32.7	36.2	40.1
135	26.2	28.6	29.5	31.7	32.4	32.7	36.3	40.3
157.5	26.9	29.3	30.1	32.2	32.7	33.0	35.9	39.4
180	28.4	31.0	31.8	33.6	34.2	34.5	37.5	40.9
202.5	28.7	31.5	32.5	34.8	35.7	35.9	40.3	45.1
225	29.2	32.2	33.4	36.2	37.0	37.4	42.2	47.6
247.5	29.9	33.6	35.1	38.3	39.2	39.7	44.4	49.9
270	29.9	33.6	35.1	38.3	39.2	39.7	44.4	49.9
292.5	29.9	33.6	35.1	38.3	39.2	39.7	44.4	49.9
315	29.9	33.6	35.1	38.3	39.2	39.7	44.4	49.9
337.5	27.8	31.2	32.5	35.7	36.5	37.0	41.7	47.3

4 Water Level

This section presents a summary of the water level data basis established in [1], followed by a presentation of normal and extreme water level conditions.

The water level data was adopted from the hydrodynamic model forced by CFSR established for EINS (HD_{EINS}) in [2]. The water level consists of a tidal and a non-tidal (residual) component. The two components were separated by harmonic analysis (see Section 4.1.2). The water level dataset is denoted EINS-HD-CFSR. Table 4.1 summarises the metadata of the EINS-HD-CFSR dataset.

Table 4.1 Metadata of the EINS-HD-CFSR dataset
Time series data is provided to Energinet (.csv, .mat, .nc, and .dfs0).

Name	Value
Dataset ID:	EINS-HD-CFSR
Start Date [UTC]:	1979-01-01 01:00:00
End Date [UTC]:	2022-09-30 23:30:00
Time Step [s]:	1800
Cell Size [m]:	~400 (Island area)

The water level data is relative to mean sea level (MSL).

The water level analyses are presented in bins of 0.1 m. Table 4.2 presents the water level variables of the EINS-HD-CFSR dataset, including the bin sizes applied in figures and tables throughout this report.

Table 4.2 Water level variables of the EINS-AT-CFSR dataset

Variable name	Abbrev.	Unit	Bin size
Water Level – Total	WL_{total}	mMSL	0.1
Water Level – Tide	WL_{tide}	mMSL	0.1
Water Level - Residual	$WL_{residual}$	m	0.1

The water level analyses cover the data period 1979-09-01 – 2022-08-31 (43 years), a round number of years, which is preferrable for extreme value analyses. The normal conditions apply a 30-min interval (as the hindcast models), while the extreme conditions (J-EVA) apply a 1-hour interval (as native in CFSR).

The main body of this report presents results at EINS-2 (the location of max H_{m0}), while results at all analysis points are given in the data reports (listed in Table 11.1) which are attached to this report. The data reports contain all (scatter) tables and figures presented below.

4.1 Normal water level conditions

The normal water level conditions are presented in terms of:

- Time series
- Tidal levels
- Histogram
- Monthly statistics

4.1.1 Time series

Figure 4.1 shows a time series of water level at EINS-2 during the 43-year period, for total, tidal, and residual components. The 'de-tiding' of water level is explained in Section 4.1.2. The highest total and residual water levels are 1.67 mMSL and 1.59 m (6th Nov. 1987). The tidal levels are given in Section 4.1.2.

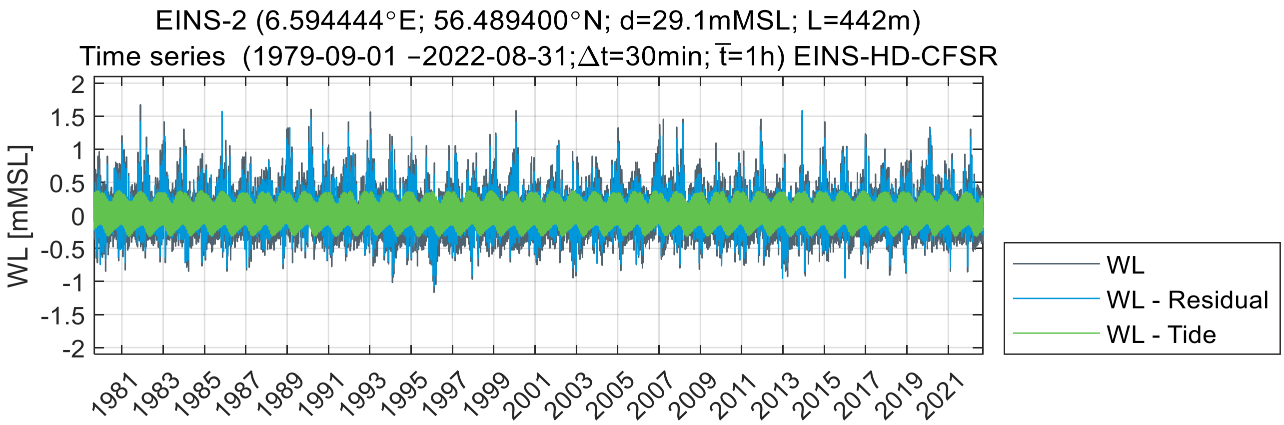

Figure 4.1 Time series of water level at EINS-2

4.1.2 Tidal levels

The tides are weak at EINS, but to quantify this, astronomical water levels (tidal levels) are provided below. The levels were calculated using harmonic analysis to separate the tidal and non-tidal (residual) components of the total water level time series from the hydrodynamic model (after subtracting the mean of the data).

Figure 4.1 shows the time series of the total, astronomical tidal and residual water level at EINS-2, while Table 4.3 summarises the astronomical water levels. The tide can be characterised as semi-diurnal (i.e., two high tides per day). The HAT is +0.38 mMSL and LAT -0.33 mMSL, giving a total tidal envelope of 0.71 m.

The harmonic analysis was conducted using the U-tide toolbox, [10], which is based on the IOS tidal analysis method by the Institute of Oceanographic Sciences as described in [11], and integrates the approaches defined in [12] and [13]. The residual water level was derived by subtracting the predicted tidal level from the total water level. The astronomical water levels are defined as (https://ntslf.org/tgi/definitions):

- HAT: Maximum predicted WL
- MHWS: Average of the two successive high waters reached during the 24 hours when the tidal range is at its greatest (spring tide)
- MHWN: Average of the two successive high waters reached during the 24 hours when the tidal range is at its lowest (neap tide)
- MLWN: Average of the two successive low waters reached during the 24 hours when the tidal range is at its lowest (neap tide)
- MLWS: Average of the two successive low waters reached during the 24 hours when the tidal range is at its greatest (spring tide)
- LAT: Minimum predicted WL

Table 4.3 Tidal levels at EINS-2

Tidal level	Abbreviation	Value	Unit
Highest astronomical tide	HAT	0.38	mMSL
Mean high water springs	MHWS	0.25	mMSL
Mean high water neaps	MHWN	0.13	mMSL
Mean sea level	MSL (z0)	0.00	mMSL
Mean low water neaps	MLWN	-0.13	mMSL
Mean low water springs	MLWS	-0.19	mMSL
Lowest astronomical tide	LAT	-0.33	mMSL

4.1.3 Histogram

Figure 4.2 shows a histogram of total water level at EINS-2.

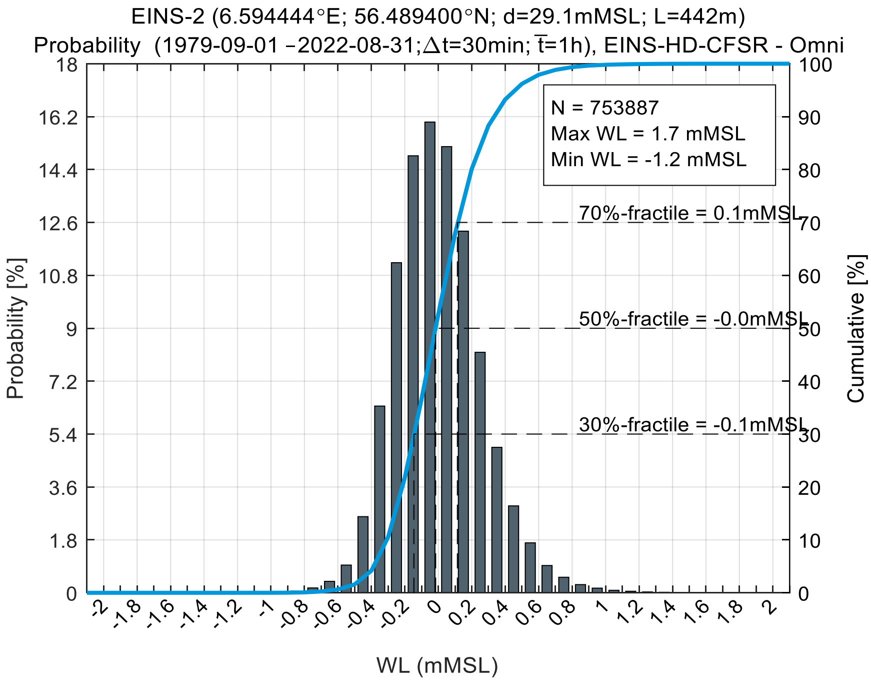

Figure 4.2 Histogram of total water level at EINS-2

4.1.4 Monthly statistics

Figure 4.3 shows monthly statistics of total water level at EINS-2. The monthly mean water level varies within ± 0.1 m during the year, being lowest in spring/summer and highest in winter. The highest (+1.7 mMSL), as well as the lowest (-1.2m MSL) water level, occurs during winter (Nov. – Feb.).

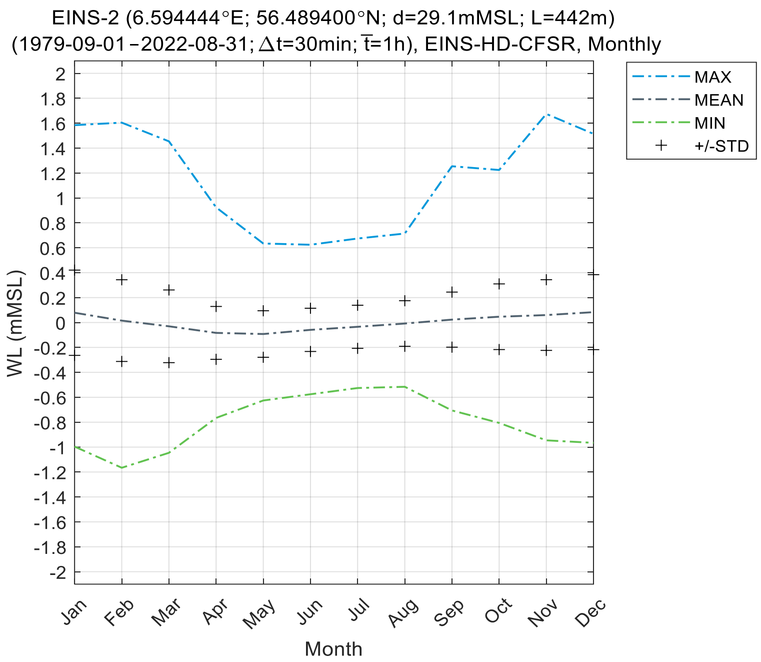

Figure 4.3 Monthly statistics of total water level at EINS-2.

4.2 Extreme water level conditions

The extreme water level conditions are estimated following the steps outlined in Appendix D: J-EVA Summary. The input water level time series was from the HD_{EINS} model. The storm events selected for the J-EVA analyses are separately chosen for the high and low water levels. Only seasonal variability is considered as explained in Section 14.2.1, as there is no directionality associated to water level. Filtering of the storm events is carried out using a criteria of regression quantile > 0.7 on the storm events. The resulting 'retained' and 'removed' events are shown as an example for the HWL_{res} in Figure 4.4. Similar selection is made for LWL_{res}, HWL_{tot}, and LWL_{tot}.

A J-EVA statistical model (see Section 14.3) has been set up, followed by simulation (see Section 14.4) to estimate the extremes of the high and low water levels. The extreme water levels are presented separately for the expected construction completion in 2033 and for the expected lifetime of the island, which is (until) 2113.

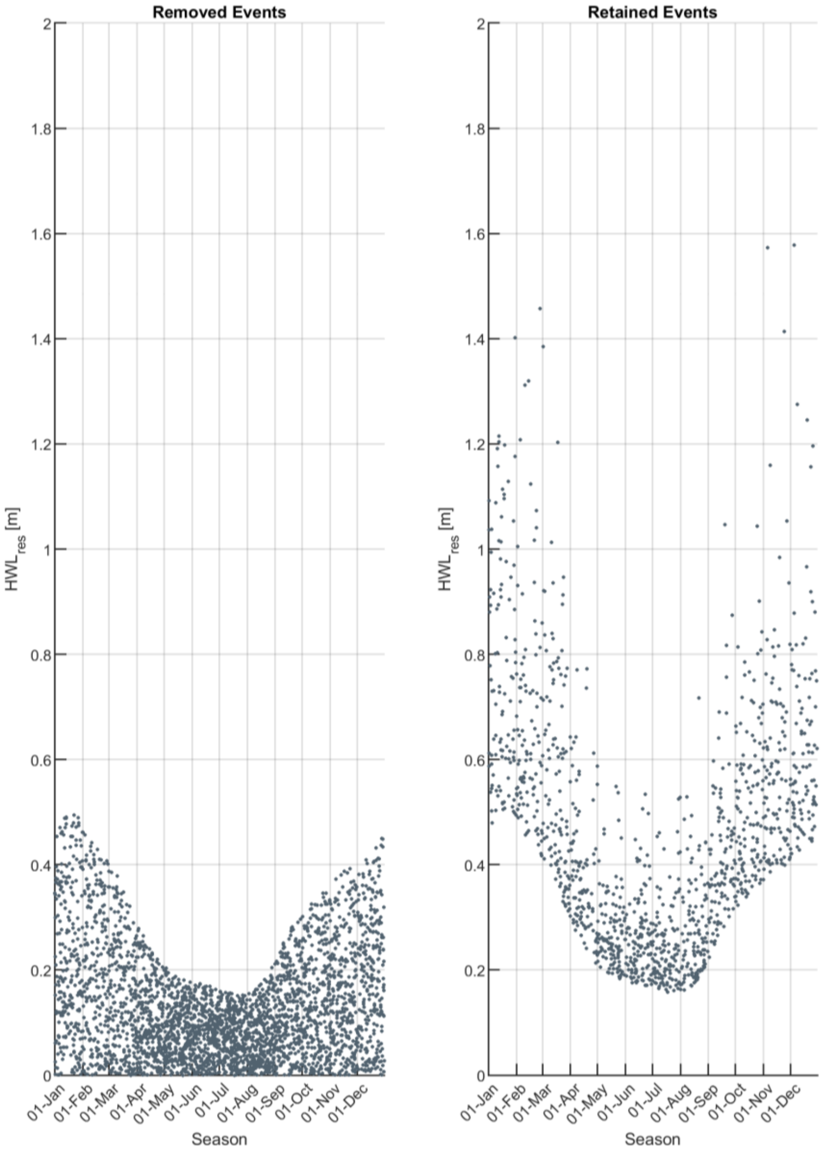

Figure 4.4 Selected events for residual high water level, HWL_{res} at EINS-2. Events above the 0.7 quantiles are retained for the J-EVA analysis.

4.2.1 Extreme high water levels

Figure 4.5 and Figure 4.6 show the best estimate of the residual and total high water level, respectively, from an 80,000-year simulation, which is used to calculate the best estimate for 1-, 5-, 10-, 50-, 80-, and 100-year return periods. Best estimates for larger return periods are calculated based on simulating up to 8 x 10^6 years of events, where the minimum number of exceedances N_e = 100 is chosen for the 80,000-year return period. The extreme values are presented (Table 4.4 - Table 4.7) for a maximum return period of 10,000-year.

The model fits the data, which is indicated by the dashed black line, quite well for larger return periods. For smaller periods (<10 years), there is a slight overestimation because the presented (example) fit to the spline model is made based on data that is representative of return periods that are larger than 10 years.

Extreme High Water Levels for year 2033

Table 4.4 provides the extreme residual and total high water levels for the expected construction completion in year 2033.

Table 4.4 Extreme High Water Levels for year 2033 at EINS-2

Variable	Return Period [years]							
	1	5	10	50	80	100	1000	10000
HWL_{tot} [mMSL]	1.2	1.4	1.5	1.7	1.7	1.8	2.1	2.4
HWL_{res} [mMSL]	1.0	1.3	1.4	1.6	1.7	1.7	2.0	2.3

Extreme High Water Levels for year 2113

Table 4.5 provides the extreme residual and total high water for the expected lifetime of the Island year 2113. Following Part A, [1], a sea level rise (SLR) of 0.8 m was added to the HWL relative to the vertical reference of today.

Table 4.5 Extreme High Water Levels for year 2113 at EINS-2
The levels are relative to the vertical reference (MSL) of today.

Variable	Return Period [years]							
	1	5	10	50	80	100	1000	10000
HWL_{tot} [mMSL]	2.0	2.2	2.3	2.5	2.5	2.6	2.9	3.2
HWL_{res} [mMSL]	1.8	2.1	2.2	2.4	2.5	2.5	2.8	3.1

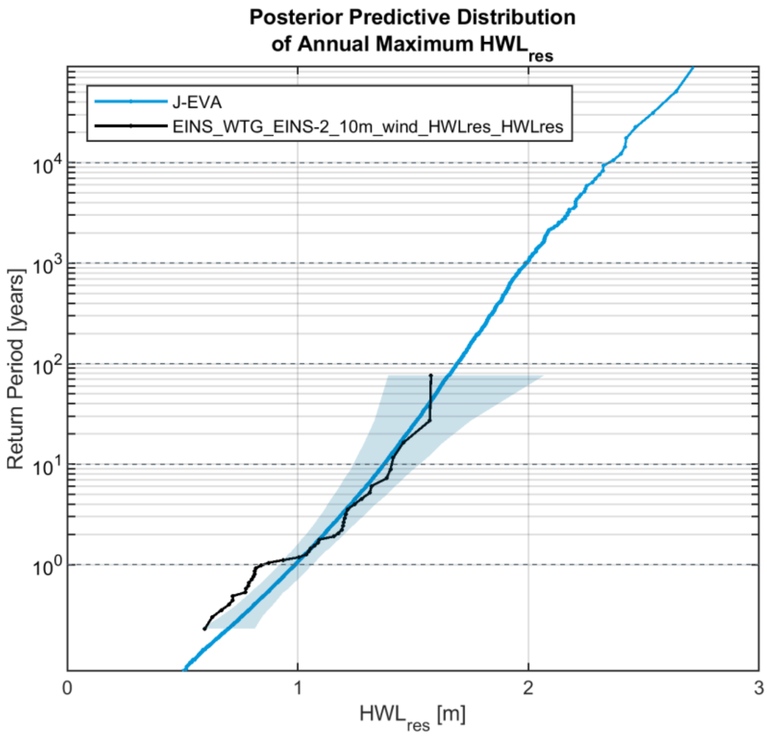

Figure 4.5 **Extreme Residual High Water Level (for year 2033) at EINS-2**
Hindcast data is shown in black. The blue line is the best estimate using the integrated posterior distribution parameters. The shaded area is the 2.5-97.5% credible interval of the estimate.

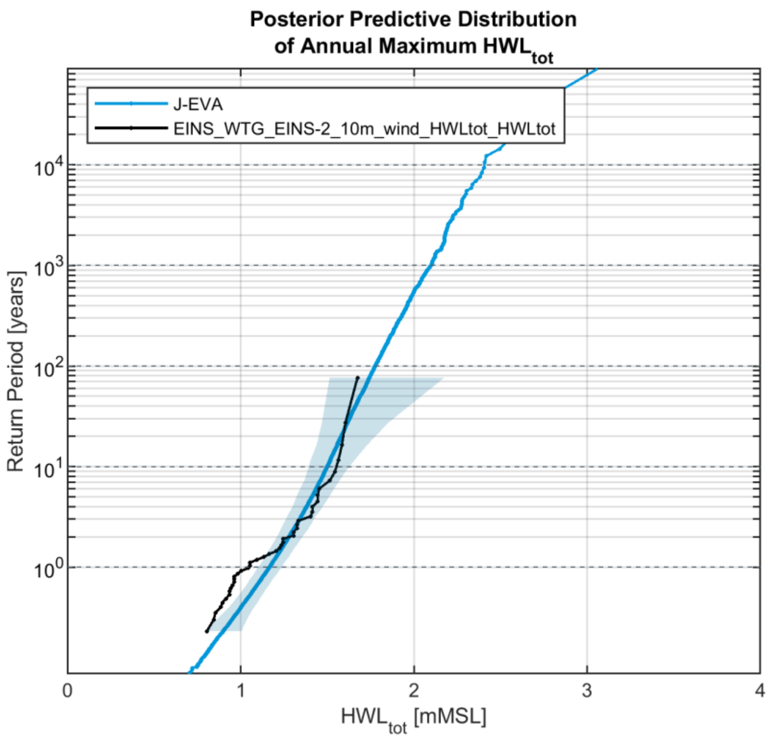

Figure 4.6 **Extreme Total High Water Level (for year 2033) at EINS-2**
Hindcast data is shown in black. The blue line is the best estimate using the integrated posterior distribution parameters. The shaded area is the 2.5-97.5% credible interval of the estimate.

4.2.2 Extreme low water levels

Figure 4.7 and Figure 4.8 show the best estimate of the residual and total low water level, respectively, from 80,000-year simulation, in the same manner as for high water levels above.

The model fits the data, which is indicated by the dashed black line, quite well for LWL_{res} but slightly overestimates (order of 0.1 m) for LWL_{tot}, but overall, the fit is quite good since the input hindcast data lies within the credible intervals of the spline model fit.

Extreme Low Water Levels for year 2033

Table 4.6 provides the extreme residual and total low water levels for the expected construction completion in year 2033.

Table 4.6 Extreme Low Water Levels for year 2033 at EINS-2

Variable	Return Period [years]							
	1	5	10	50	80	100	1000	10000
LWL_{tot} [mMSL]	-0.8	-1.0	-1.0	-1.1	-1.2	-1.2	-1.4	-1.6
LWL_{res} [mMSL]	-0.7	-0.9	-0.9	-1.1	-1.1	-1.1	-1.3	-1.6

Extreme Low Water Levels for year 2113

Table 4.7 provides the extreme residual and total low water levels for the expected lifetime of the island year 2113. Following Part A, [1], a sea level rise (SLR) of 0.8 m was added to the LWL relative to the vertical reference (MSL) of today.

Table 4.7 Extreme Low Water Levels for year 2113 at EINS-2
Levels are relative to the vertical reference (MSL) of today.

Variable	Return Period [years]							
	1	5	10	50	80	100	1000	10000
LWL_{tot} [mMSL]	0.0	-0.2	-0.2	-0.3	-0.4	-0.4	-0.6	-0.8
LWL_{res} [mMSL]	0.1	-0.1	-0.1	-0.3	-0.3	-0.3	-0.5	-0.8

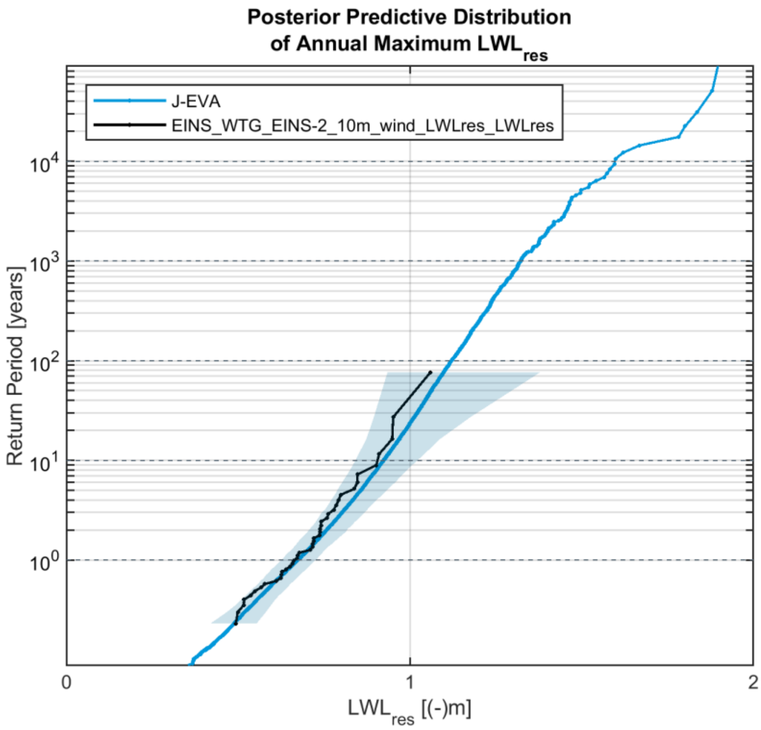

Figure 4.7 **Extreme Residual Low Water Level (for year 2033) at EINS-2.** Hindcast data is shown in black. The blue line is the best estimate using the integrated posterior distribution parameters. The shaded area is the 2.5-97.5% credible interval of the estimate.

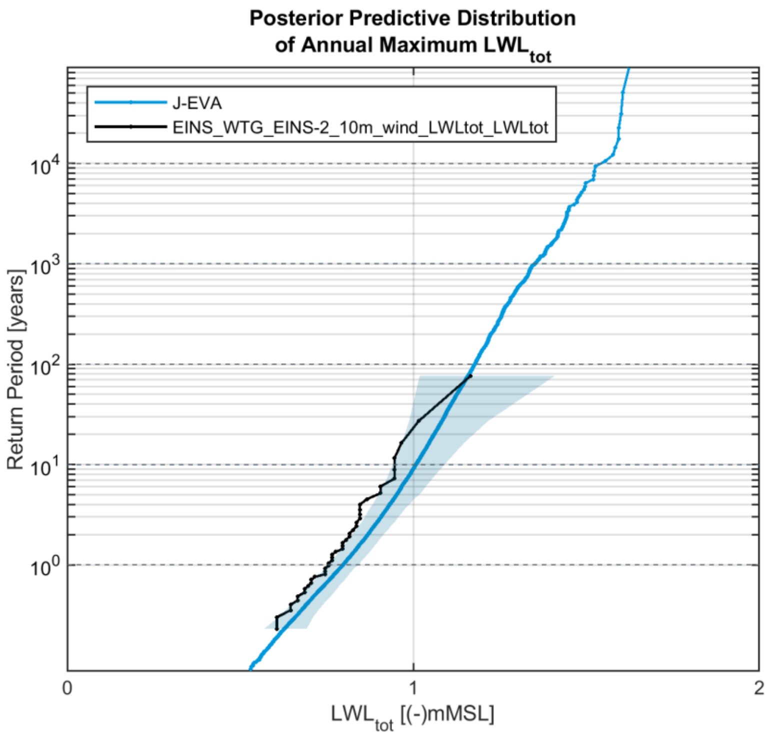

Figure 4.8 **Estimates of Total Low Water Level (for year 2033) at EINS-2.** Hindcast data is shown in black. The blue line is the best estimate using the integrated posterior distribution parameters. The shaded area is the 2.5-97.5% credible interval of the estimate.

5 Current

This section presents a summary of the current data basis established in [1], followed by a presentation of normal and extreme current conditions.

The current data is adopted from the hydrodynamic model forced by CFSR established for EINS (HD_{EINS}) [1]. The current consists of a tidal and a non-tidal (residual) component. The two components were separated by harmonic analysis (see Section 4.1.2). The current dataset is denoted EINS-HD-CFSR. Table 5.1 summarizes the metadata of the EINS-HD-CFSR dataset.

Table 5.1 Metadata of the EINS-HD-CFSR dataset.
Time series data is provided to Energinet (.csv, .mat, .nc, and .dfs0).

Name	Value
Dataset ID:	EINS-HD-CFSR
Start Date [UTC]:	1979-01-01 01:00:00
End Date [UTC]:	2022-09-30 23:30:00
Time Step [s]:	1800
Cell Size [m]:	~400 (Island area)

The current data is considered representative of 1-hour average values of depth-average and is given at 30-min interval.

The current analyses are presented in speed bins of 0.05 m/s and directional bins of 22.5°. Table 5.2 presents the variables of the EINS-HD-CFSR dataset, including the bin sizes applied in figures and tables throughout this report.

Table 5.2 Current variables of the EINS-HD-CFSR dataset.
The current direction is to where the current is flowing.

Variable name	Abbrev.	Unit	Bin size
Current speed - Depth-average - Total	$CS_{avg,tot}$	m/s	0.05
Current direction - Depth-average - Total	$CD_{avg,tot}$	°N-to	22.5

The current analyses cover the data period 1979-09-01 – 2022-08-31 (43 years), a round number of years, which is preferable for extreme value analyses. The normal conditions apply a 30-min interval (as the hindcast models), while the extreme conditions (J-EVA) apply a 1-hour interval (as native in CFSR).

The main body of this report presents results at EINS-2 (the location of max H_{m0}), while results at all analysis points are given in the data reports (listed in Table 11.1) which are attached to this report. The data reports contain all (scatter) tables and figures presented below.

5.1 Normal current conditions

The normal current conditions are presented in terms of:

- Normal current profile
- Time series
- Current roses
- Histogram
- Monthly statistics
- Directional statistics
- Maps of mean current speed

5.1.1 Normal current profile

Current profiles are assessed in Section 5 of Part A, [1].

For normal (mean) conditions, it is recommended to apply a power profile with α = 1/7, cf. Section 4.1.4.2 in DNV RP-C205 [3], with the surface (z = 0) current speed estimated as 8/7 (1.14) times the depth-averaged current speed.

However, it is noted that individual current profiles deviate substantially from the (mean) power profile, and the (mean) normal current profile can, therefore, not be applied to represent all single/individual current profiles.

5.1.2 Time series

Figure 5.1 shows a time series of current speed at EINS-2 during the 43-year hindcast period for total, tidal, and residual. The 'de-tiding' of current speed follows the method given in Section 4.1.2 for water level. The highest total and residual current speeds are almost the same, with values of 1.07 and 1.06 m/s, respectively (in 1990).

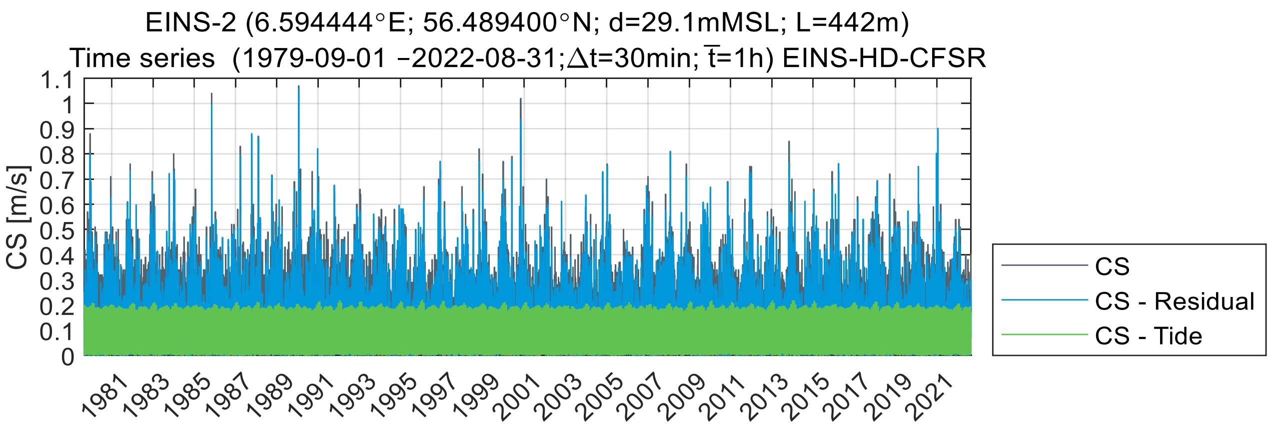

Figure 5.1 Time series of current speed at EINS-2

5.1.3 Current roses

Figure 5.2, Figure 5.3, and Figure 5.4 show current roses for total, tidal, and residual conditions at EINS-2. The total rose shows currents to most directions but with a predominance of current going towards northeast, which is due to the prevailing residual currents going towards the northeast. The northwest has the least occurrence of currents going to. The tidal currents are weak and travel mainly toward southeast, and secondarily towards north (the tide is < 0.1 m/s about 50% of the time).

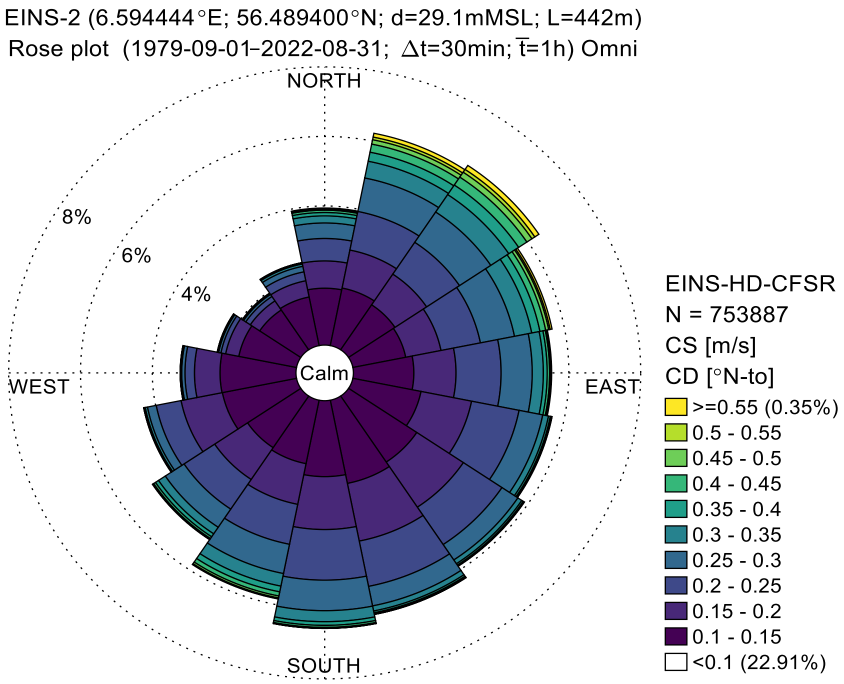

Figure 5.2 Total current rose at EINS-2

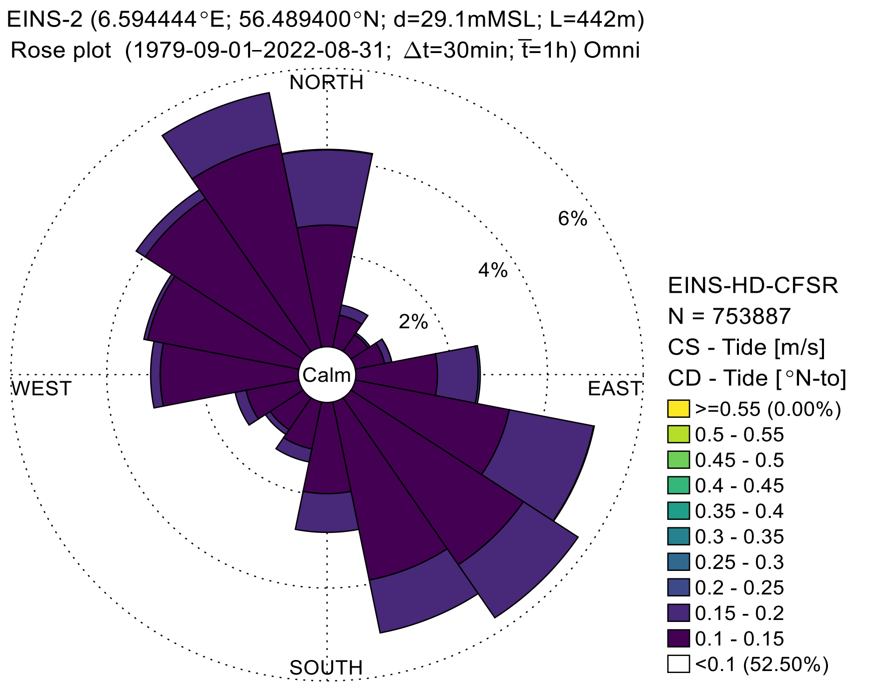

Figure 5.3 Tidal current rose at EINS-2

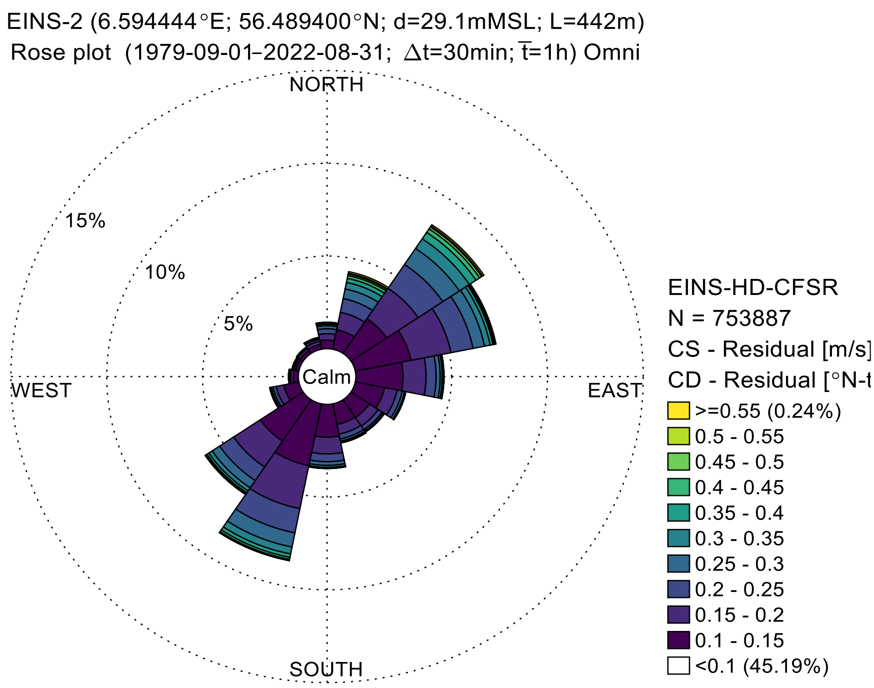

Figure 5.4 Residual current rose at EINS-2

5.1.4 Histogram

Figure 5.5 shows a histogram of current speed at EINS-2.

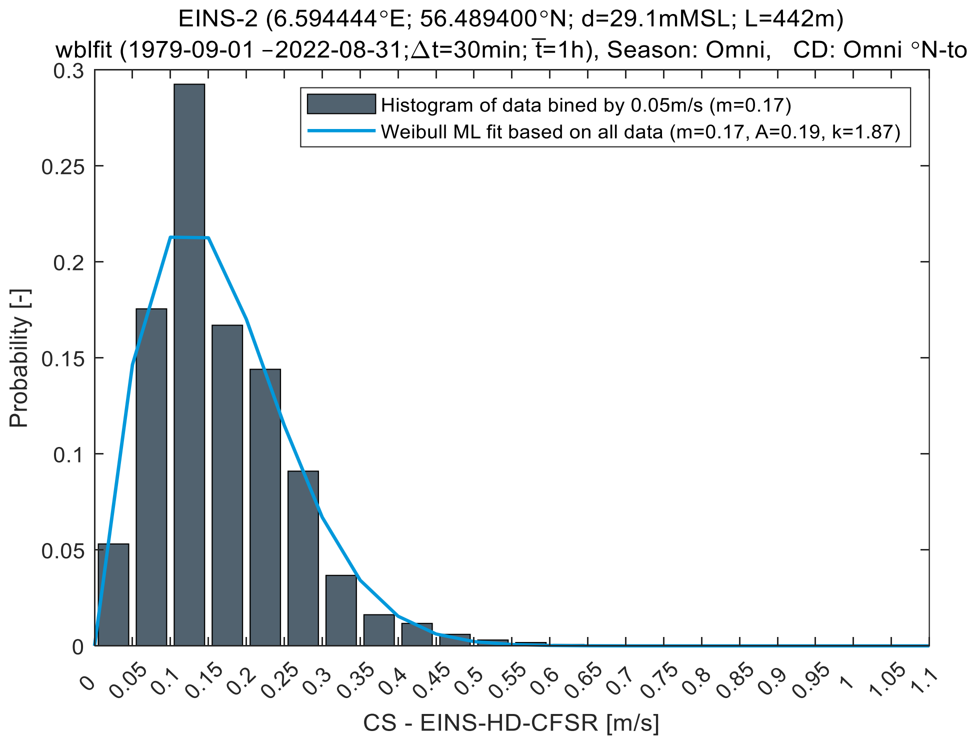

Figure 5.5 Histogram of current speed at EINS-2

5.1.5 Monthly statistics

Figure 5.6 shows monthly statistics of current speed at EINS-2. The monthly mean current speed varies within 0.15 - 0.2 m/s during the year, being weakest in summer and strongest in winter. The strongest current speeds (up to 1.07 m/s) occur during autumn to winter (Oct. – Jan.).

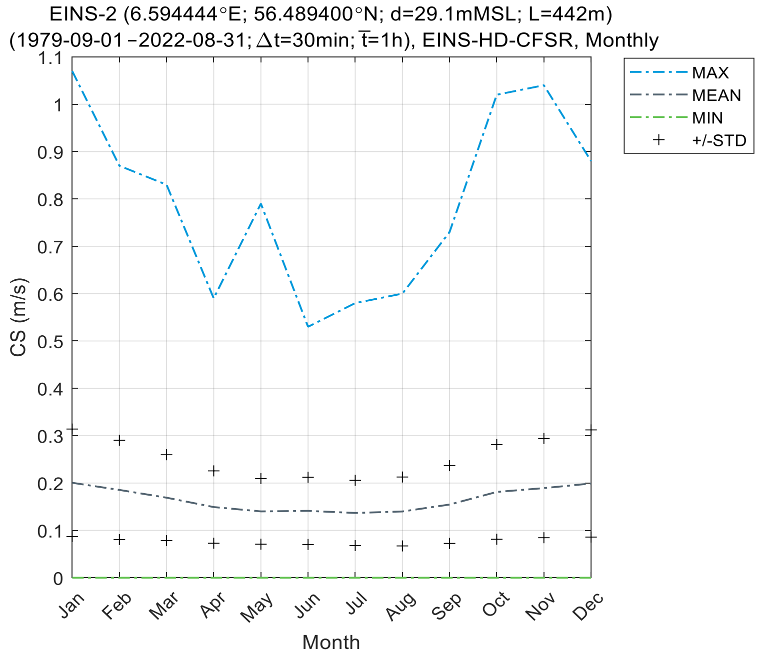

Figure 5.6 Monthly statistics of current speed at EINS-2

5.1.6 Directional statistics

Figure 5.7 shows directional statistics of current speed at EINS-2. The mean current speed is strongest towards the northeast (45°) of about 0.22 m/s, and weakest towards northwest (315°) of about 0.16 m/s. The strongest max current speeds occur towards the northeast and reach 1.06 m/s.

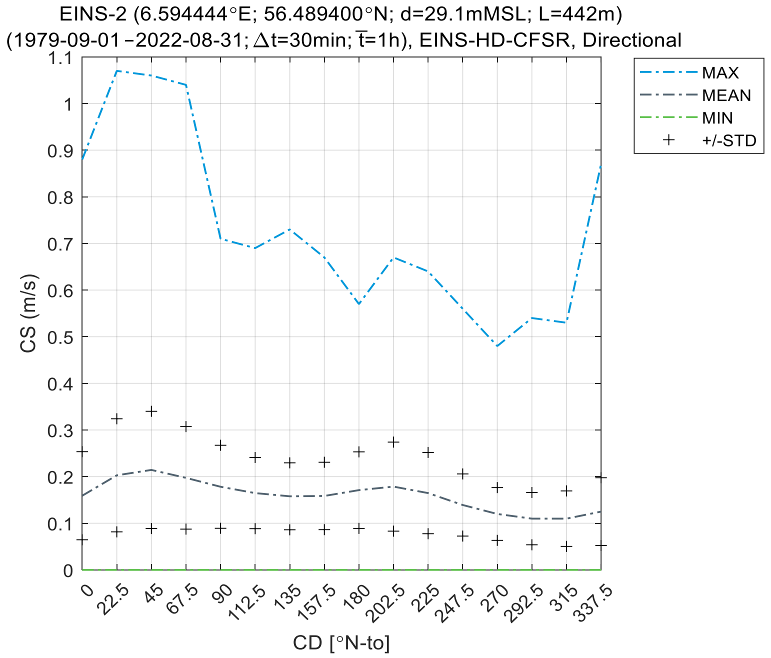

Figure 5.7 Directional statistics of current speed at EINS-2

5.1.7 Maps of normal current speed

Figure 5.8 presents the spatial variation across EINS of the mean total depth-averaged current speed. Mean values of CS_{tot} from the hindcast data at each mesh element are calculated and the variation is presented as contours. As seen, there is hardly any variation (0.17±0.03 m/s) across the EINS area.

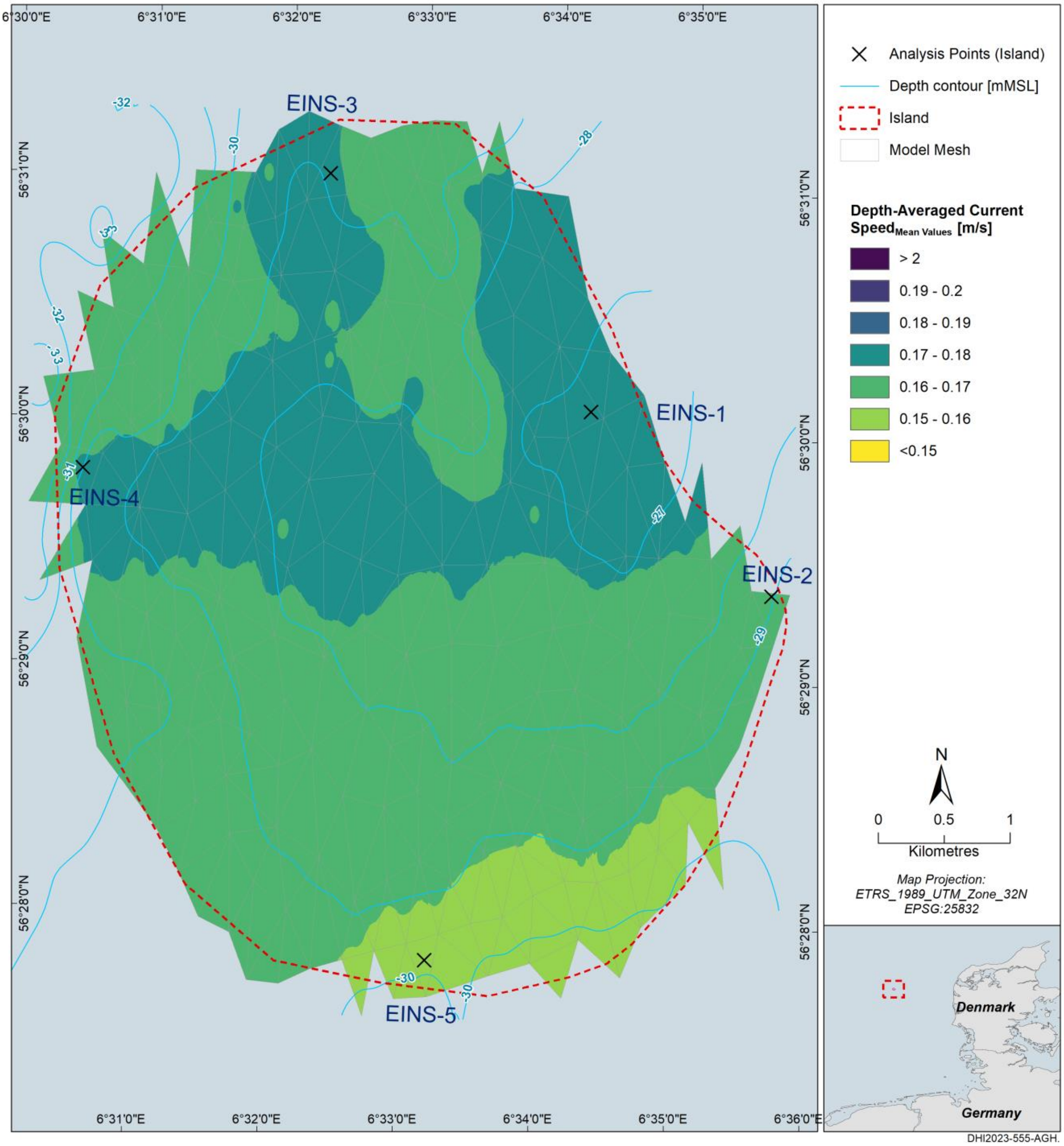

Figure 5.8 Spatial variation across EINS area of the mean total depth-averaged current speed
The colour map shows the current speed, and the contours show the water depth.

5.2 Extreme current conditions

The extreme current conditions are estimated following the steps outlined in Appendix D: J-EVA Summary. The input depth-average current time series was from the HD_{EINS} model. The total current speed is composed of two effects, namely tidal and residual. The residual current contribution can further be decomposed into contributions due to several effects, e.g., wind-driven, density-driven etc. At EINS, the extreme currents are dominated by the wind-induced residual. The storm events selected for the J-EVA analyses are based on the directional and seasonal variability (see Section 14.2.1), with filtering carried out using a criteria of regression quantile > 0.65 that is applied on the residual depth-average current speed storm events. The resulting 'retained' and 'removed' events are shown in Figure 5.9.

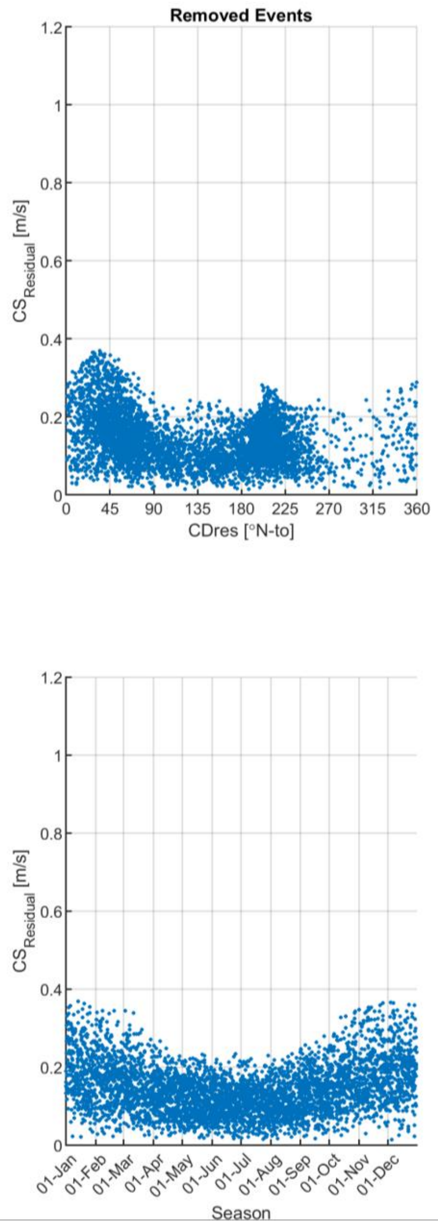

Figure 5.9 Selected events for residual depth-average current speed, CS_{res} at EINS-2.
Events above the 0.65 quantile are retained for the J-EVA analysis.

5.2.1 Extreme current profile

Current profiles are assessed in Section 5 in Part A, [1]. A generally applicable and feasible current profile for currents during extreme events does not exist.

For extreme surface (z = 0 m) currents, it is recommended to apply a factor of 1.3 to convert the depth-average current speed to surface (z = 0 m). This is based on detailed assessment of measured and modelled 3D current data.

For extreme near-seabed (1 m above) currents, it is recommended to apply the power profile with $\alpha = 1/7$, cf. Section 4.1.4.2 in DNV RP-C205 [3], and the surface (z = 0) current speed estimated as 8/7 (1.14) times the depth-averaged current speed. This corresponds to a factor ranging from 0.65 at 25 m depth to a factor of 0.72 at 50 m depth.

5.2.2 Extreme current speed

A J-EVA statistical model (see Section 14.3) has been set up for extreme residual depth-average current speed followed by simulation including the directional scaling (see Section 14.4) to estimate the extremes. The current direction (going-to) at the time of peak residual current speed and the season are used as covariates. It is to be noted that the total current speed is estimated by combining the residual current speed estimated using the J-EVA model and the random sampling of the tidal component from the input hindcast time series at the time of simulation. Furthermore, CD_{tot} may not be fully correlated with CD_{res}. Consequently, directional variation of CS_{tot} will not be correlated to that of CS_{res}.

Figure 5.10 shows the directional annual number of exceedances of the residual depth-average current speed estimated from an 80,000-year simulation in the same manner as for water level.

The model fits the omni-directional data quite well, as well as in the dominating northeast and southwest directions (see Figure 5.11). From a J-EVA point of view, it is also important that all data points representing storm events are within the light blue shaded area since this means that they have been resampled in the simulation.

Table 5.3 and Table 5.4 provides the values of the directional extreme depth-average residual and total current speeds. The directional extreme values are scaled according to DNV-RP-C205, [3].

For a few (weak) directional sectors there was no historical storm that corresponded to a 1-year return period. In those cases, the directional 1-year value was estimated by a log-linear extrapolation from the 5 and 10 year return period values.

The current profile in Section 5.2.1, is used to calculate the extreme surface and near-seabed current speeds. Table 5.5 and Table 5.6 provides the directional extreme surface residual and total current speeds, while Table 5.7 and Table 5.8 provides the directional extreme near-seabed residual and total current speeds.

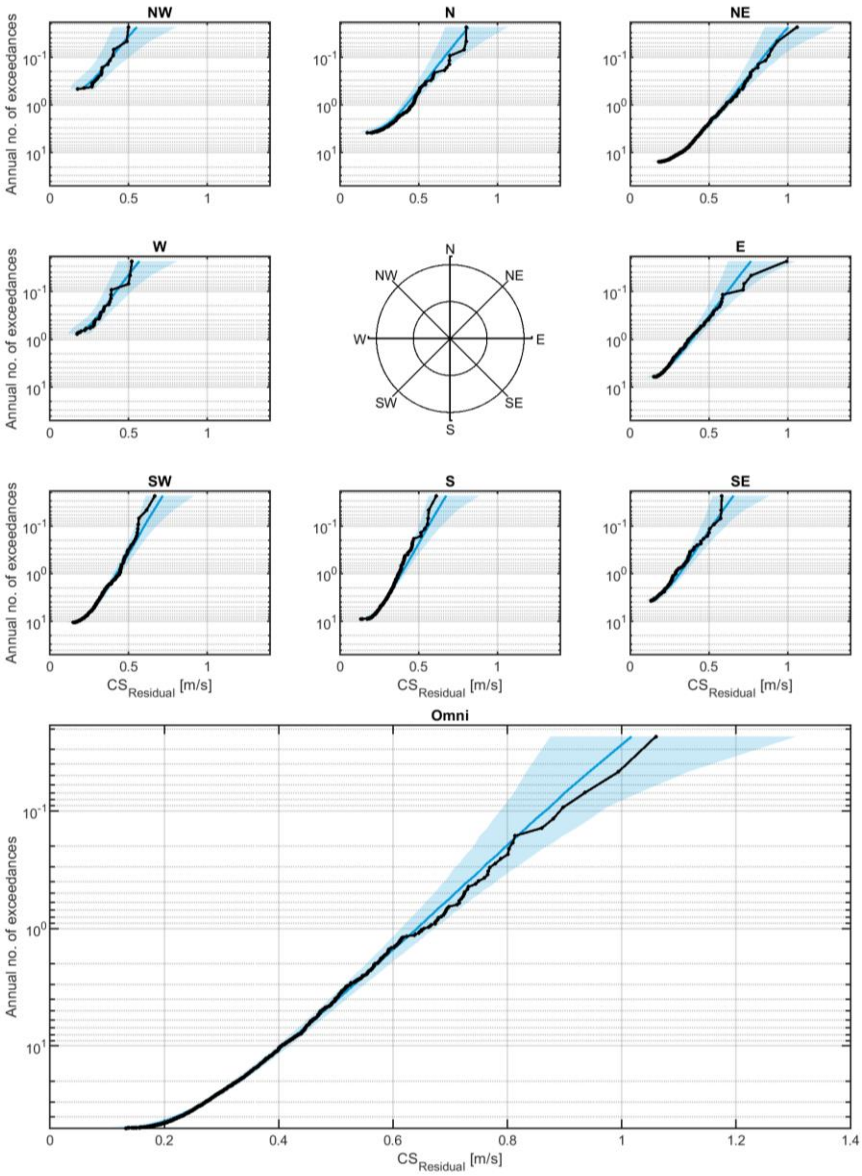

Figure 5.10 Directional exceedance probability of Residual Current Speed CS_{res} at EINS-2

Hindcast data is shown in black. The blue line is the best estimate using the integrated posterior distribution parameters. The shaded area is the 2.5-97.5% credible interval.

5.2.3 Extreme current rose

Figure 5.11 shows the extreme residual and total current rose using the storm events selected for the J-EVA analysis (see Section 5.2 and Figure 5.9). Extreme currents have a strong directionality, with northeast and southwest (going-to) being dominant.

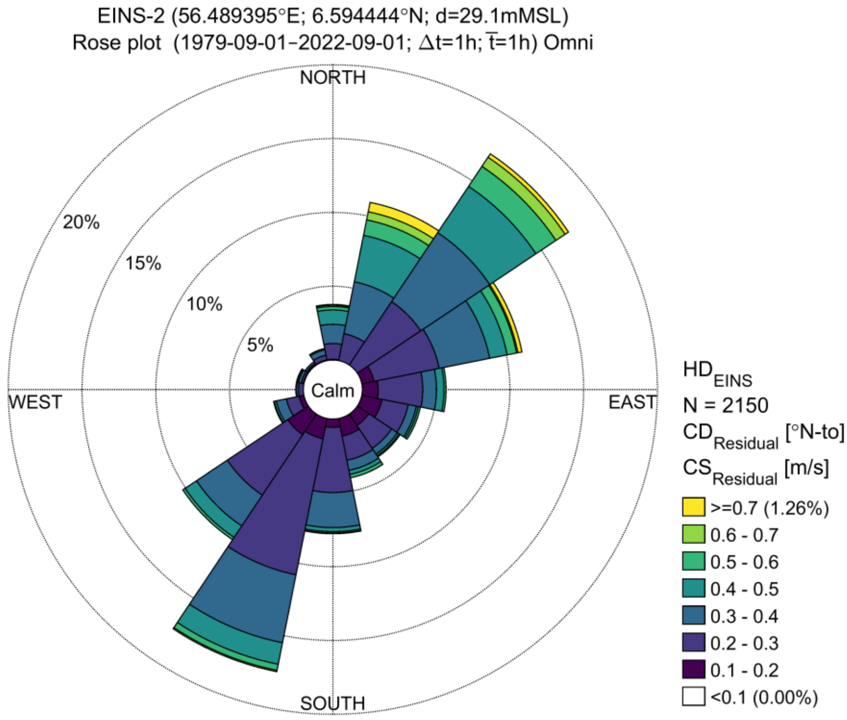

Figure 5.11 Extreme residual current rose using the storm events selected for J-EVA analysis.

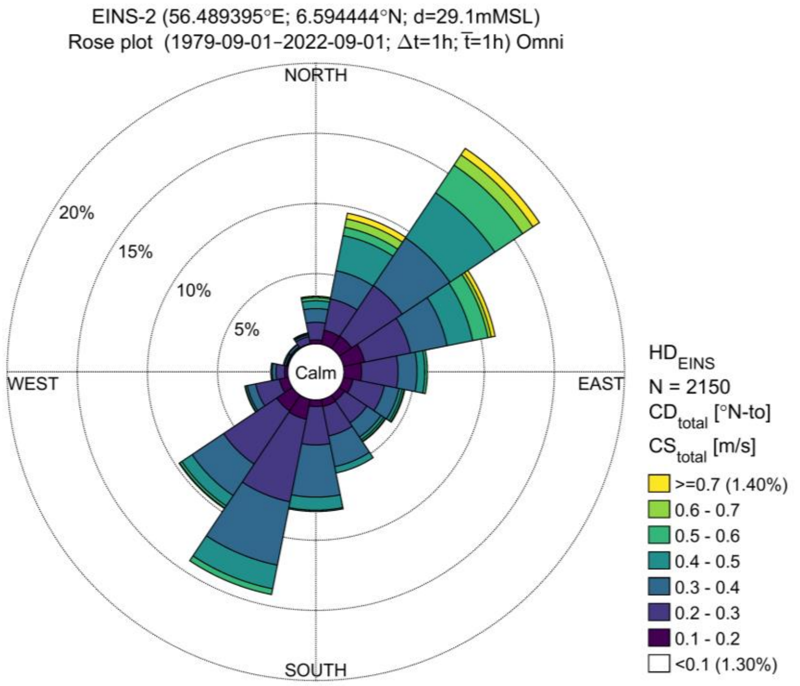

Figure 5.12 Extreme total current rose using the storm events selected for J-EVA analysis.

Table 5.3 Directional Extreme Depth-Average Residual Current Speed at EINS-2

22.5° Directional Extreme Depth-Average Residual Current Speed, CSres [m/s]								
Direction (CD [°N-to])	Return Period [years]							
	1	5	10	50	80	100	1000	10000
Omni	0.6	0.8	0.9	1.0	1.0	1.1	1.3	1.4
0	0.5	0.7	0.7	0.9	0.9	0.9	1.1	1.3
22.5	0.6	0.8	0.9	1.0	1.0	1.1	1.3	1.4
45	0.6	0.8	0.9	1.0	1.0	1.1	1.3	1.4
67.5	0.6	0.8	0.8	1.0	1.0	1.0	1.2	1.4
90	0.5	0.6	0.7	0.8	0.9	0.9	1.0	1.2
112.5	0.4	0.6	0.6	0.8	0.8	0.8	1.0	1.1
135	0.4	0.6	0.6	0.7	0.8	0.8	0.9	1.1
157.5	0.4	0.6	0.6	0.7	0.8	0.8	0.9	1.1
180	0.5	0.6	0.6	0.7	0.8	0.8	0.9	1.1
202.5	0.6	0.7	0.7	0.8	0.8	0.9	1.0	1.1
225	0.5	0.6	0.7	0.8	0.8	0.8	1.0	1.1
247.5	0.4	0.5	0.6	0.7	0.7	0.8	0.9	1.1
270	0.3	0.5	0.5	0.6	0.7	0.7	0.9	1.0
292.5	0.3	0.5	0.5	0.7	0.7	0.7	0.9	1.0
315	0.2	0.4	0.5	0.6	0.6	0.7	0.8	1.0
337.5	0.4	0.5	0.6	0.7	0.7	0.7	0.9	1.1

Table 5.4 Directional Extreme Depth-Average Total Current Speed at EINS-2

22.5° Directional Extreme Depth-Average Total Current Speed, CS [m/s]								
Direction (CD [°N-to])	Return Period [years]							
	1	5	10	50	80	100	1000	10000
Omni	0.7	0.8	0.9	1.0	1.1	1.1	1.3	1.5
0	0.6	0.7	0.8	0.9	1.0	1.0	1.2	1.3
22.5	0.7	0.8	0.9	1.0	1.1	1.1	1.3	1.5
45	0.7	0.8	0.9	1.0	1.1	1.1	1.3	1.5
67.5	0.7	0.8	0.9	1.0	1.1	1.1	1.3	1.5
90	0.6	0.7	0.8	0.9	0.9	0.9	1.1	1.3
112.5	0.5	0.6	0.7	0.8	0.9	0.9	1.0	1.2
135	0.5	0.6	0.7	0.8	0.8	0.8	1.0	1.2
157.5	0.5	0.6	0.6	0.8	0.8	0.8	1.0	1.1
180	0.5	0.6	0.7	0.8	0.8	0.8	0.9	1.1
202.5	0.6	0.7	0.7	0.8	0.8	0.8	1.0	1.1
225	0.5	0.6	0.7	0.8	0.8	0.8	1.0	1.1
247.5	0.4	0.6	0.6	0.7	0.7	0.8	0.9	1.1
270	0.4	0.5	0.5	0.7	0.7	0.7	0.9	1.0
292.5	0.3	0.5	0.5	0.7	0.7	0.7	0.9	1.0
315	0.3	0.5	0.5	0.7	0.7	0.7	0.9	1.1
337.5	0.4	0.6	0.6	0.8	0.8	0.8	1.0	1.1

Table 5.5 Directional Extreme Surface Residual Current Speed at EINS-2

22.5° Directional Extreme Surface Residual Current Speed, CS_{res}, surface [m/s]								
Direction (CD [°N-to])	Return Period [years]							
	1	5	10	50	80	100	1000	10000
Omni	0.8	1.0	1.1	1.3	1.4	1.4	1.6	1.9
0	0.7	0.9	1.0	1.1	1.2	1.2	1.4	1.7
22.5	0.8	1.0	1.1	1.3	1.4	1.4	1.6	1.9
45	0.8	1.0	1.1	1.3	1.4	1.4	1.6	1.9
67.5	0.8	1.0	1.1	1.3	1.3	1.4	1.6	1.9
90	0.6	0.8	0.9	1.1	1.1	1.1	1.4	1.7
112.5	0.6	0.8	0.8	1.0	1.0	1.0	1.3	1.5
135	0.6	0.7	0.8	1.0	1.0	1.0	1.2	1.5
157.5	0.6	0.7	0.8	1.0	1.0	1.0	1.2	1.5
180	0.6	0.8	0.8	1.0	1.0	1.0	1.2	1.4
202.5	0.7	0.9	0.9	1.1	1.1	1.1	1.3	1.5
225	0.7	0.8	0.9	1.0	1.1	1.1	1.3	1.5
247.5	0.5	0.7	0.8	0.9	1.0	1.0	1.2	1.5
270	0.4	0.6	0.7	0.8	0.9	0.9	1.1	1.4
292.5	0.4	0.6	0.7	0.9	0.9	0.9	1.1	1.4
315	0.2	0.5	0.6	0.8	0.8	0.9	1.1	1.4
337.5	0.5	0.7	0.7	0.9	0.9	1.0	1.2	1.5

Table 5.6 Directional Extreme Surface Total Current Speed at EINS-2

22.5° Directional Extreme Surface Total Current Speed, CS_{tot}, surface [m/s]								
Direction (CD [°N-to])	Return Period [years]							
	1	5	10	50	80	100	1000	10000
Omni	1.0	1.2	1.3	1.5	1.5	1.5	1.8	2.1
0	0.9	1.1	1.2	1.3	1.3	1.4	1.6	1.8
22.5	1.0	1.2	1.3	1.5	1.5	1.5	1.8	2.1
45	1.0	1.2	1.3	1.5	1.5	1.5	1.8	2.1
67.5	1.0	1.2	1.2	1.4	1.5	1.5	1.7	2.0
90	0.8	1.0	1.1	1.2	1.3	1.3	1.5	1.8
112.5	0.8	0.9	1.0	1.2	1.2	1.2	1.4	1.7
135	0.7	0.9	1.0	1.1	1.2	1.2	1.4	1.6
157.5	0.7	0.9	0.9	1.1	1.1	1.2	1.4	1.6
180	0.7	0.9	0.9	1.1	1.1	1.1	1.3	1.5
202.5	0.8	1.0	1.0	1.2	1.2	1.2	1.4	1.6
225	0.8	0.9	0.9	1.1	1.1	1.1	1.3	1.6
247.5	0.6	0.8	0.9	1.0	1.1	1.1	1.3	1.5
270	0.5	0.7	0.8	0.9	1.0	1.0	1.2	1.4
292.5	0.5	0.7	0.8	1.0	1.0	1.0	1.3	1.5
315	0.4	0.7	0.8	0.9	1.0	1.0	1.2	1.5
337.5	0.6	0.8	0.9	1.1	1.1	1.1	1.4	1.6

Table 5.7 Directional Extreme Near-Seabed Residual Current Speed at EINS-2

22.5° Directional Extreme Near-seabed Residual Current Speed, CS_{res}, near-seabed [m/s]								
Direction (CD [°N-to])	Return Period [years]							
	1	5	10	50	80	100	1000	10000
Omni	0.5	0.6	0.6	0.7	0.7	0.8	0.9	1.0
0	0.4	0.5	0.5	0.6	0.6	0.6	0.8	0.9
22.5	0.5	0.6	0.6	0.7	0.7	0.8	0.9	1.0
45	0.5	0.6	0.6	0.7	0.7	0.8	0.9	1.0
67.5	0.5	0.6	0.6	0.7	0.7	0.7	0.9	1.0
90	0.3	0.4	0.5	0.6	0.6	0.6	0.7	0.9
112.5	0.3	0.4	0.4	0.5	0.6	0.6	0.7	0.8
135	0.3	0.4	0.4	0.5	0.5	0.6	0.7	0.8
157.5	0.3	0.4	0.4	0.5	0.5	0.6	0.7	0.8
180	0.3	0.4	0.4	0.5	0.5	0.5	0.7	0.8
202.5	0.4	0.5	0.5	0.6	0.6	0.6	0.7	0.8
225	0.4	0.4	0.5	0.6	0.6	0.6	0.7	0.8
247.5	0.3	0.4	0.4	0.5	0.5	0.5	0.7	0.8
270	0.2	0.3	0.4	0.5	0.5	0.5	0.6	0.8
292.5	0.2	0.3	0.4	0.5	0.5	0.5	0.6	0.8
315	0.1	0.3	0.3	0.4	0.5	0.5	0.6	0.7
337.5	0.2	0.4	0.4	0.5	0.5	0.5	0.6	0.8

Table 5.8 Directional Extreme Near-Seabed Total Current Speed at EINS-2

22.5° Directional Extreme Near-seabed Total Current Speed, CS_{tot}, near-seabed [m/s]								
Direction (CD [°N-to])	Return Period [years]							
	1	5	10	50	80	100	1000	10000
Omni	0.5	0.7	0.7	0.8	0.8	0.8	1.0	1.1
0	0.5	0.6	0.6	0.7	0.7	0.8	0.9	1.0
22.5	0.5	0.7	0.7	0.8	0.8	0.8	1.0	1.1
45	0.5	0.7	0.7	0.8	0.8	0.8	1.0	1.1
67.5	0.5	0.7	0.7	0.8	0.8	0.8	1.0	1.1
90	0.5	0.6	0.6	0.7	0.7	0.7	0.8	1.0
112.5	0.4	0.5	0.6	0.6	0.7	0.7	0.8	0.9
135	0.4	0.5	0.5	0.6	0.6	0.7	0.8	0.9
157.5	0.4	0.5	0.5	0.6	0.6	0.6	0.7	0.9
180	0.4	0.5	0.5	0.6	0.6	0.6	0.7	0.8
202.5	0.5	0.5	0.6	0.6	0.6	0.7	0.7	0.9
225	0.4	0.5	0.5	0.6	0.6	0.6	0.7	0.9
247.5	0.4	0.4	0.5	0.6	0.6	0.6	0.7	0.8
270	0.3	0.4	0.4	0.5	0.5	0.6	0.7	0.8
292.5	0.3	0.4	0.5	0.5	0.6	0.6	0.7	0.8
315	0.2	0.4	0.4	0.5	0.6	0.6	0.7	0.8
337.5	0.4	0.5	0.5	0.6	0.6	0.6	0.8	0.9

5.2.4 Maps of extreme current speed

Figure 5.13 - Figure 5.15 present the spatial variation across EINS of total depth-averaged current speed for return periods of 1, 50 and 100 years. The extreme values of CS_{tot} from the hindcast data at each mesh element were calculated using traditional extreme value analysis, T-EVA (see Section 12). The J-EVA extremes of CS_{tot} at the five analysis locations were then used to scale the extremes in each mesh element using the inverse distance weighting method, see [14]. The maximum CS_{tot} varies within about 1.10±0.15 m/s for the 100-year return period.

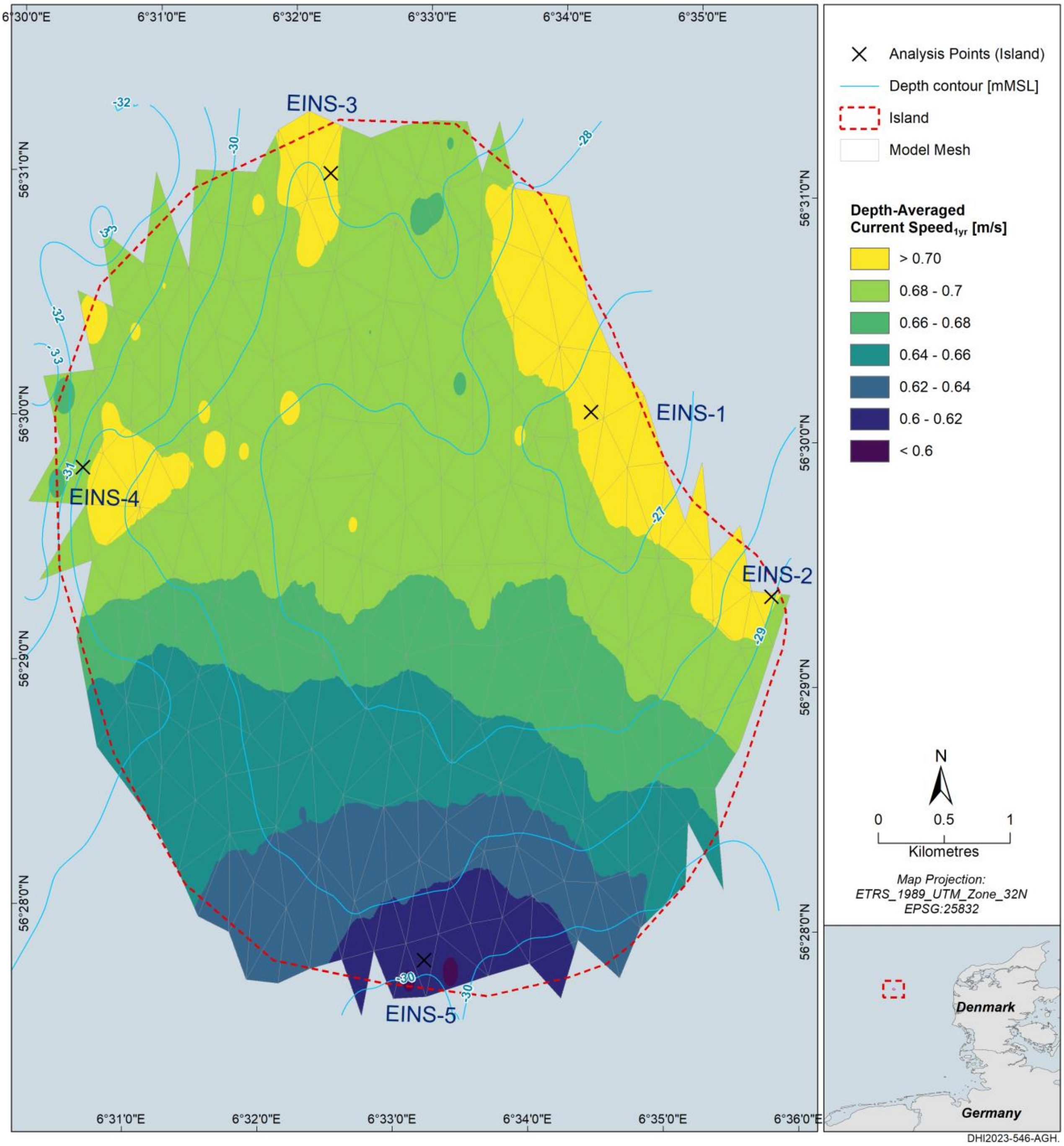

Figure 5.13 Spatial variation across EINS of total depth-averaged current speed for return period of 1 year

The colour map shows the current speed, and the contours show water depth.

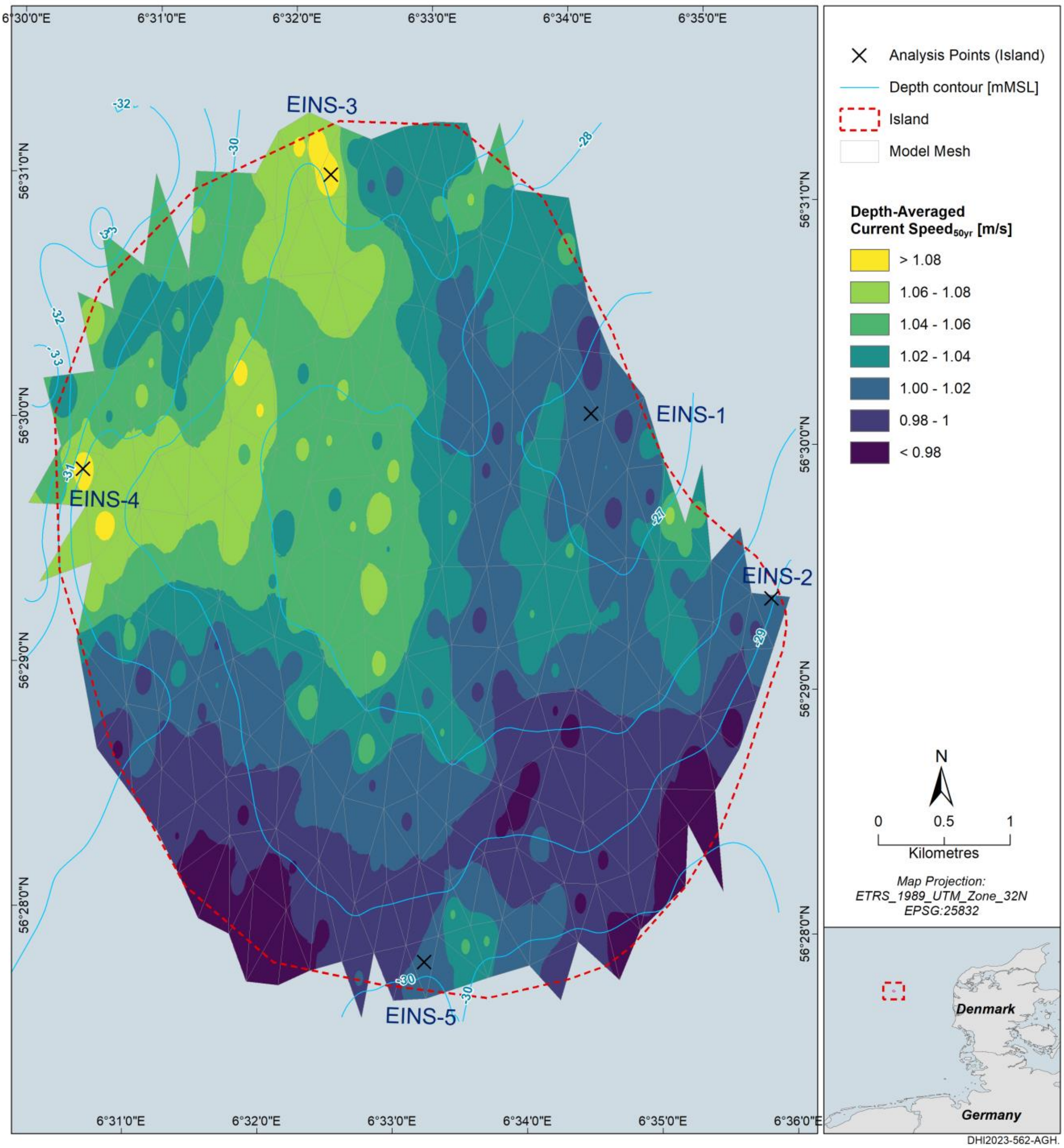

Figure 5.14 Spatial variation across EINS of total depth-averaged current speed for return period of 50 years

The colour map shows the current speed, and the contours shows water depth.

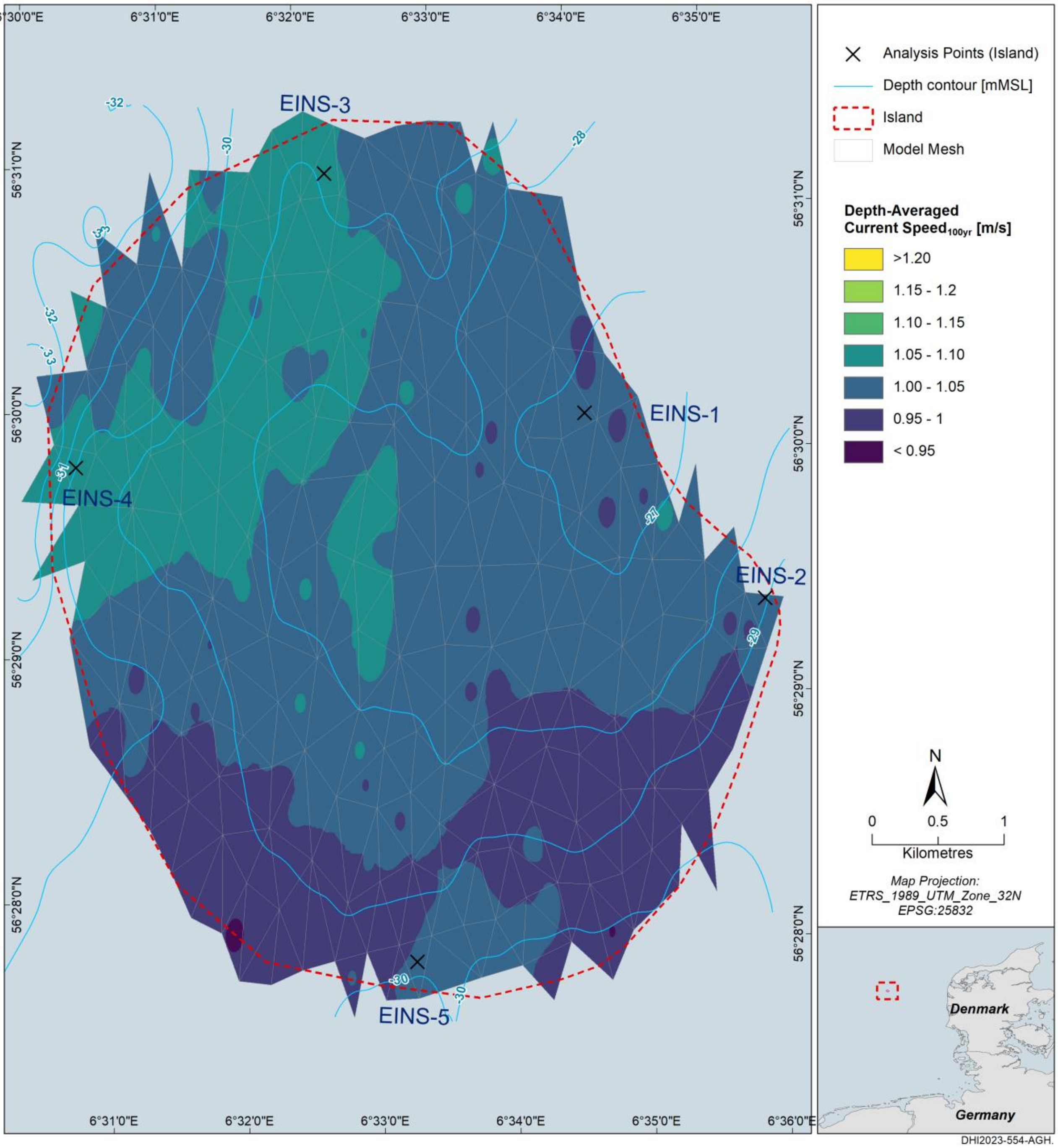

Figure 5.15 Spatial variation across EINS of total depth-averaged current speed for return period of 100 years

The colour map shows the current speed, and the contours show water depth.

6 Waves

This section presents a summary of the wave data basis established in [1], followed by a presentation of normal and extreme wave conditions.

The wave data is adopted from the spectra wave model forced by CFSR established for EINS (SW_{EINS}) in [2], containing total, wind-sea, and swell partition of the sea state (separated by the wave-age criterion as defined in Section 5.1 of [15]). The wave dataset is denoted EINS-SW-CFSR. Table 6.1 summarises the metadata of the EINS-SW-CFSR dataset.

Table 6.1 Metadata of the EINS-SW-CFSR dataset
Time series data is provided to Energinet (.csv, .mat, .nc, and .dfs0).

Name	Value
Dataset ID:	EINS-SW-CFSR
Start Date [UTC]:	1979-01-01 01:00:00
End Date [UTC]:	2022-09-30 23:30:00
Time Step [s]:	1800
Cell Size [m]:	~400 (Island area)

The wave data is considered representative of 3-hour average sea state and is given at 30-min interval.

The wave analyses are presented in height bins of 0. 5 m, period bins of 0.5 s, and directional bins of 22.5°. Table 6.2 presents the variables of the EINS-SW-CFSR dataset, incl. the bin sizes applied in analyses throughout this report.

Table 6.2 Wave variables of the EINS-SW-CFSR dataset
The wave direction is from where the wave is coming.

Variable name	Abbrev.	Unit	Bin size
Significant wave height	H_{m0}	m	0.5
Peak wave period	T_p	s	0.5
Mean wave period	T_{01}	s	0.5
Zero-crossing wave period	T_{02}	s	0.5
Peak wave direction	PWD	°N (clockwise from)	22.5
Mean wave direction	MWD	°N (clockwise from)	22.5
Direction standard deviation	DSD	°	5

The wave analyses cover the data period 1979-09-01 – 2022-08-31 (43 years), a round number of years, which is preferrable for extreme value analyses. The normal conditions apply a 30-min interval (as the hindcast models), while the extreme conditions (J-EVA) apply a 1-hour interval (as native in CFSR).

The main body of this report presents results at EINS-2 (the location of max H_{m0}), while results at all analysis points are given in the data reports (listed in Table 11.1) which are attached to this report. The data reports contain all (scatter) tables and figures presented below.

6.1 Normal wave conditions

The normal wave conditions are presented in terms of:

- Time series
- Wave rose
- Histogram
- Monthly statistics
- Directional statistics
- Scatter diagrams (H_{m0})
- Wind-wave misalignment
- Assessment of wave spectra, see Part A, [1].
- Maps of mean H_{m0}

6.1.1 Time series

Figure 6.1 show time series of the total, wind-sea, and swell partition of H_{m0}, T_p, and T_{02} at EINS-2 during the 43 years hindcast period. The mean is 1.94 m, and the maximum is 11.22 m (6th Nov. 1985).

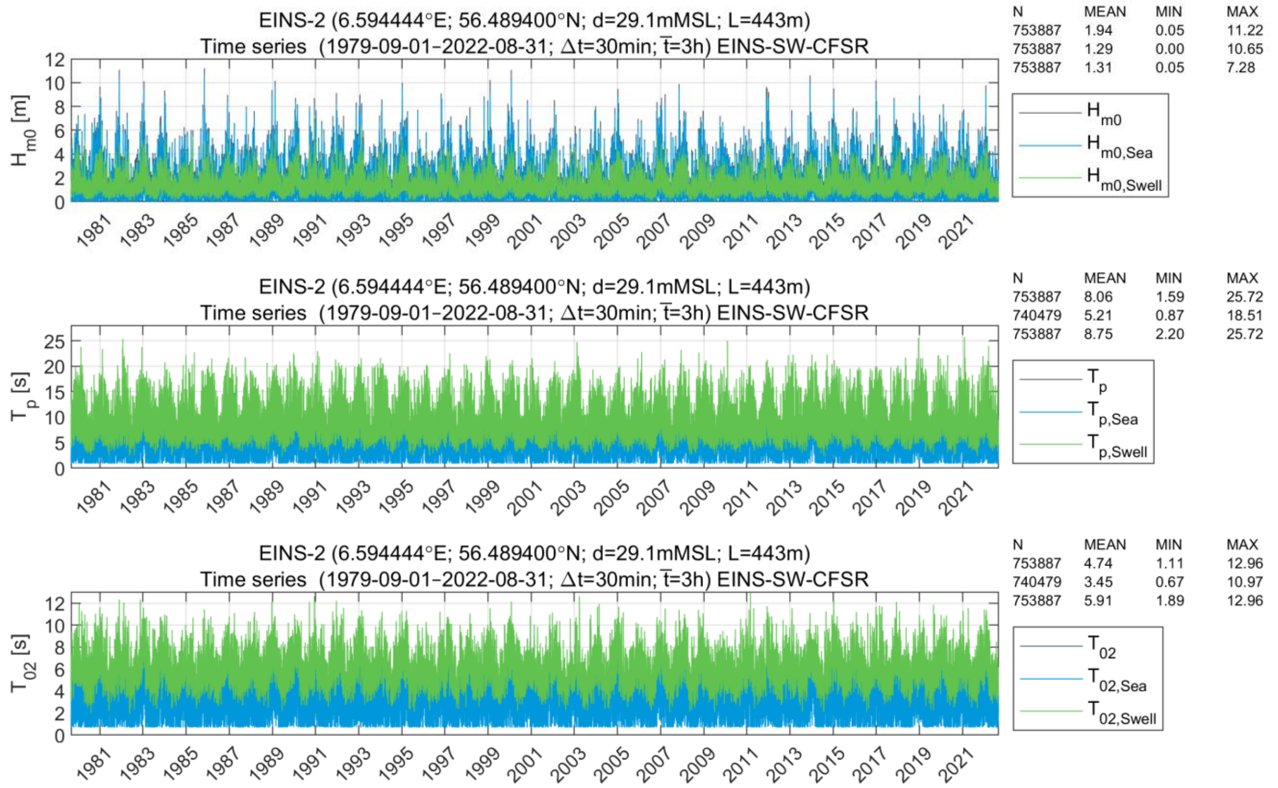

Figure 6.1 Time series of H_{m0}, T_p, and T_{02} at EINS-2

6.1.2 Wave roses

Figure 6.2 to Figure 6.4 show wave roses at EINS-2 based on H_{m0} and MWD for total, wind-sea and swell respectively. As typical for the North Sea, the waves arrive primarily from the northwest, reflecting the direction that is open to the North Atlantic, and allows swell to enter the North Sea. Waves from easterly directions occur less than about 20% of the time.

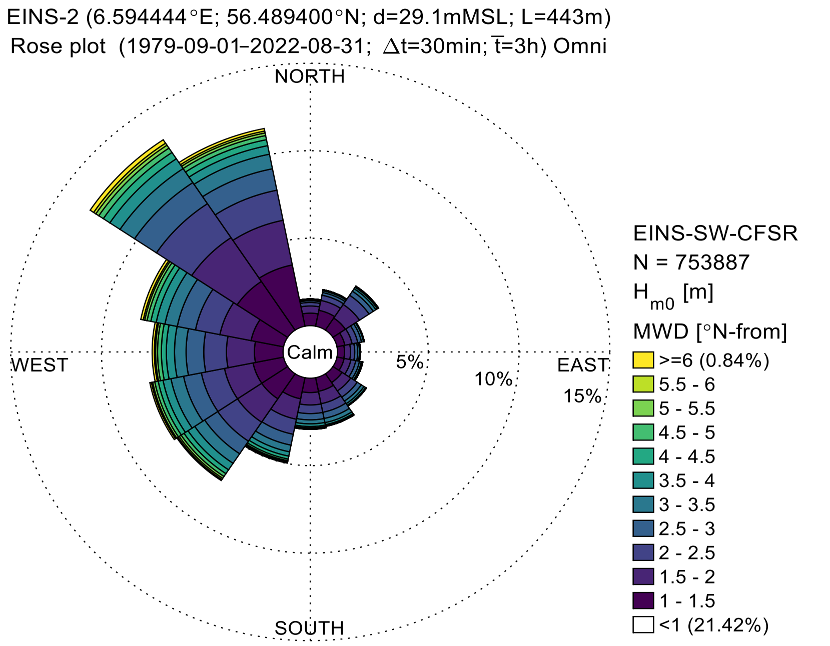

Figure 6.2 Wave rose at EINS-2; H_{m0} vs MWD – Total

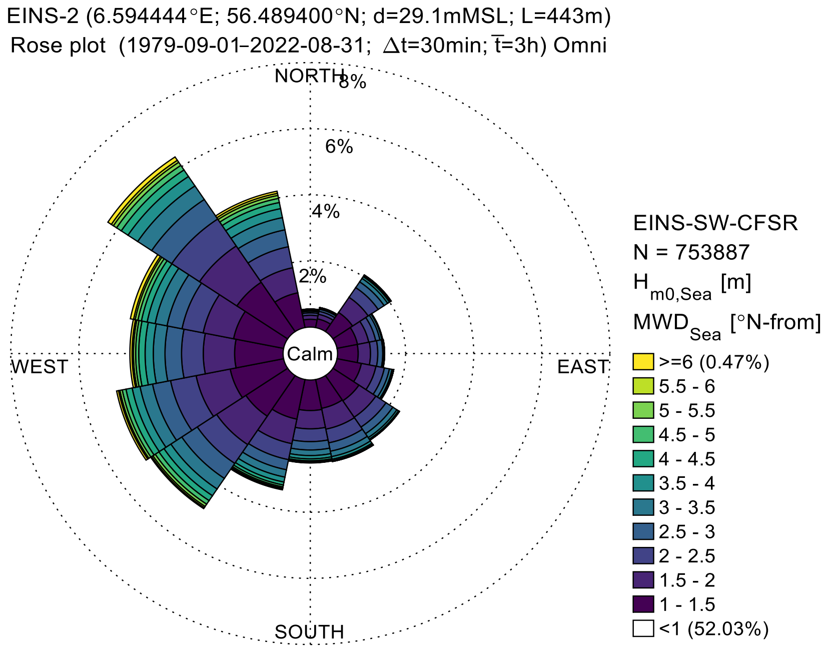

Figure 6.3 Wave rose at EINS-2; H_{m0} vs MWD – Wind-Sea

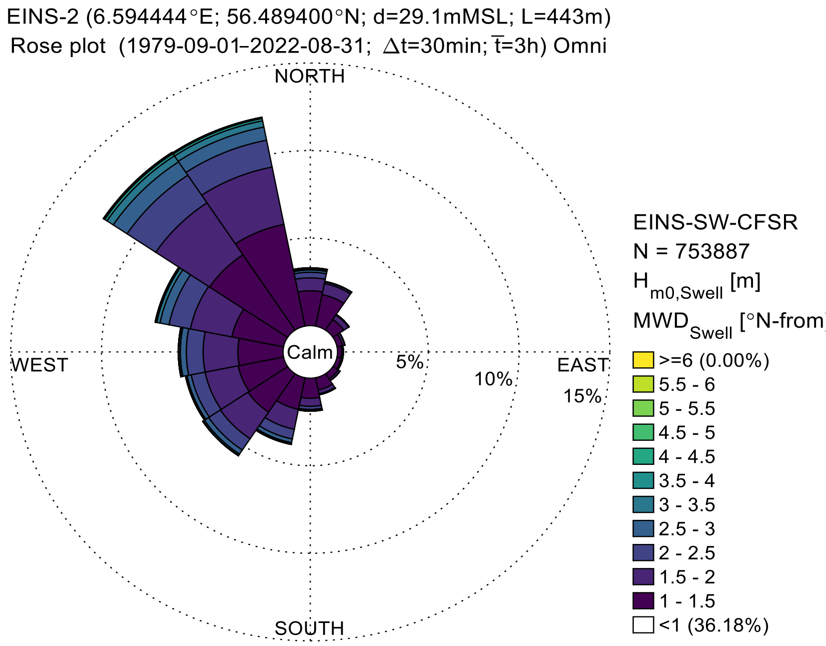

Figure 6.4 Wave rose at EINS-2; H_{m0} vs MWD – Swell

6.1.3 Histogram

Figure 6.5 shows a histogram of H_{m0} at EINS-2.

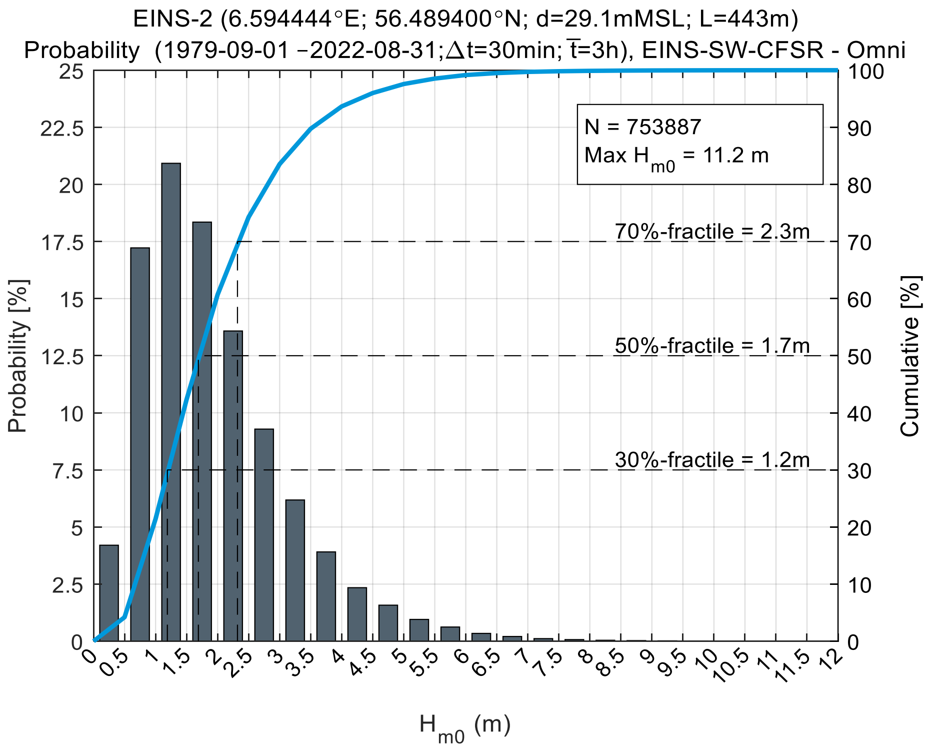

Figure 6.5 Histogram of H_{m0} at EINS-2

6.1.4 Monthly statistics

Figure 6.6 shows monthly statistics of significant wave height, H_{m0}, at EINS-2. The mean varies from 1.4 m during summer to 2.5 m during winter. The highest waves occurred during the months of Nov., Dec., and Jan.

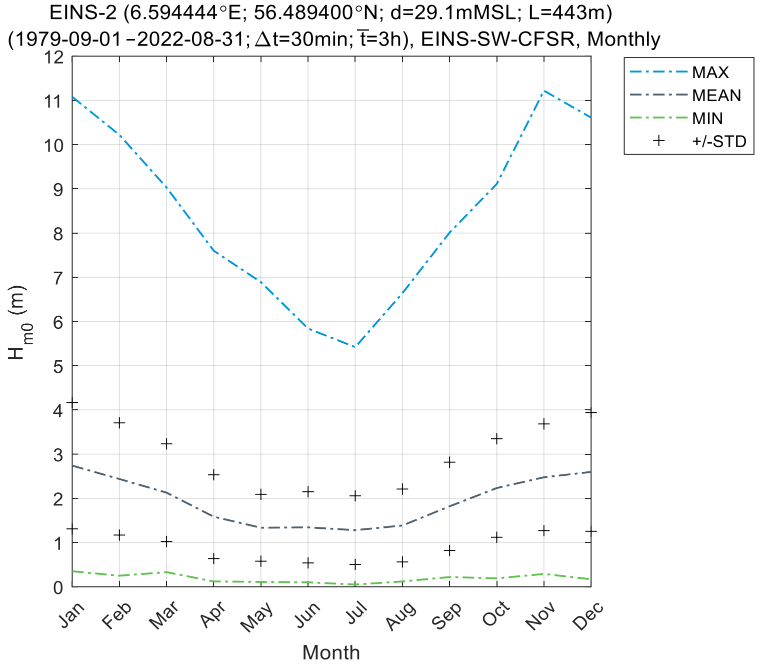

Figure 6.6 Monthly statistics of significant wave height at EINS-2

6.1.5 Directional statistics

Figure 6.7 shows directional statistics of significant wave height at EINS-2. The mean is highest from the northwest at about 2.1 m, and lowest from north at about 1.2 m. The highest waves occur from the north-western sector.

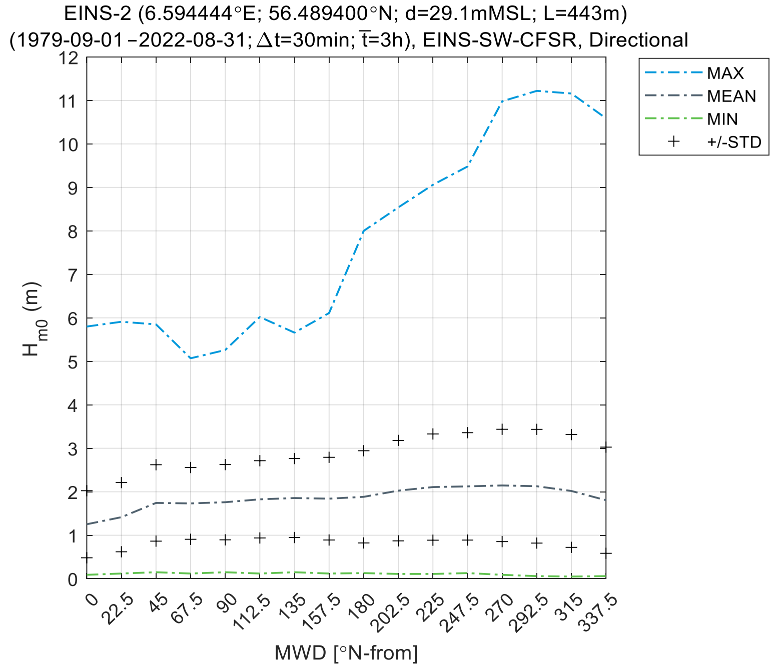

Figure 6.7 Directional statistics of significant wave height at EINS-2

6.1.6 Scatter diagrams (H_{m0})

This section presents scatter diagrams of H_{m0} against the following other metocean parameters at EINS-2:

- Figure 6.8 WS_{10} vs. H_{m0}
- Figure 6.9 H_{m0} vs. T_p
- Figure 6.10 H_{m0} vs. T_{02}
- Figure 6.11 H_{m0} vs. WL
- Figure 6.12 H_{m0} vs. CS

Each scatter diagram includes quantiles and functional fits to the 95%-tile highest data (except for WL and CS).

The scatter of WS_{10} vs H_{m0} shows a reasonable correlation, albeit with some scatter due to the (co-)occurrence of swell in the North Sea.

The wave periods (T_p and T_{02}) are very well correlated with $H_{m0,}$ especially for the high waves that are dominated by local wind.

There is a weak correlation between WL (total) and $H_{m0,}$ indicating a slight trend of positive high water during high waves.

The total current speed (CS) is almost entirely uncorrelated with H_{m0}, albeit there is a weak trend of stronger currents during high waves, but with significant scatter.

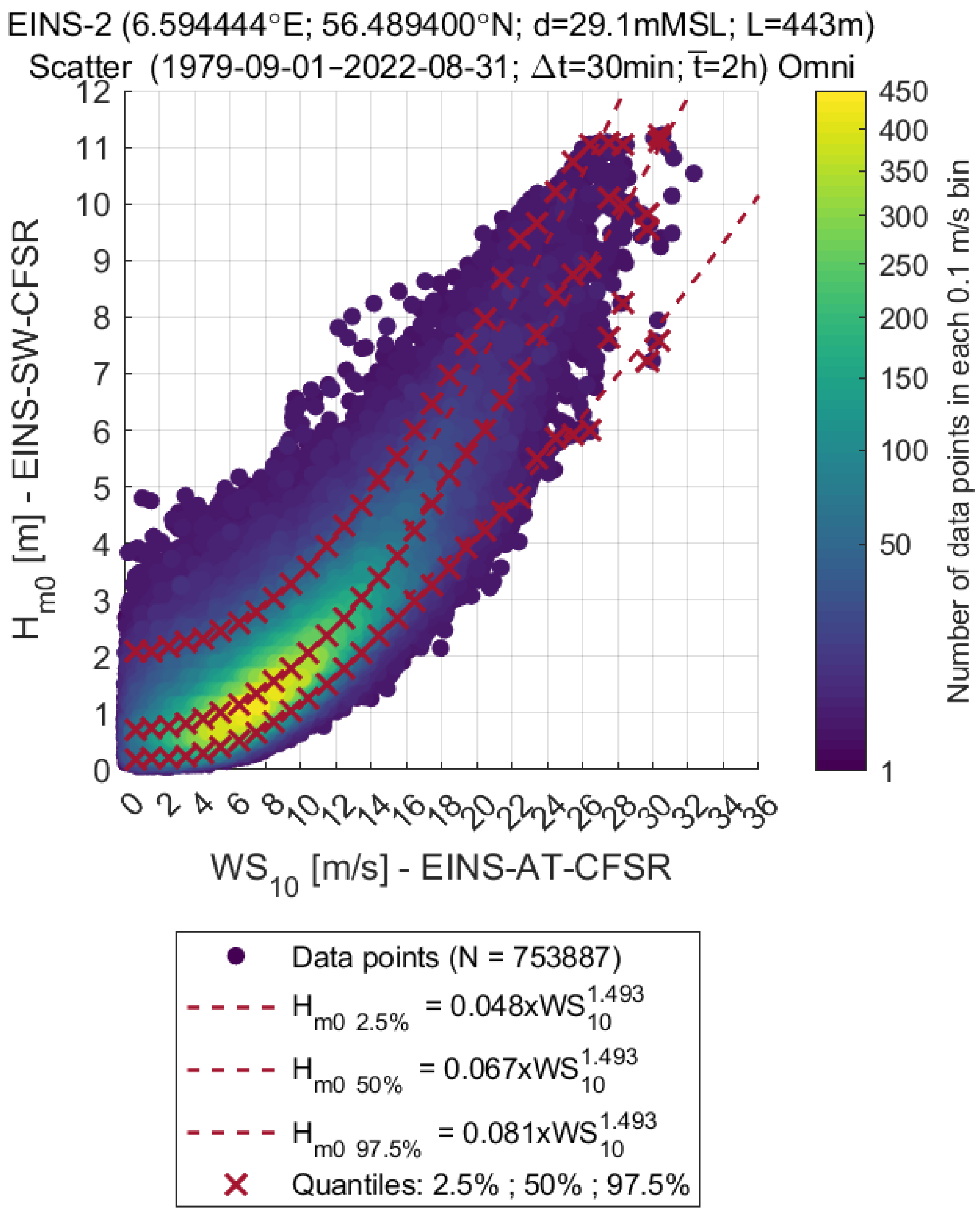

Figure 6.8 **Scatter diagram of WS_{10} vs H_{m0} at EINS-2**

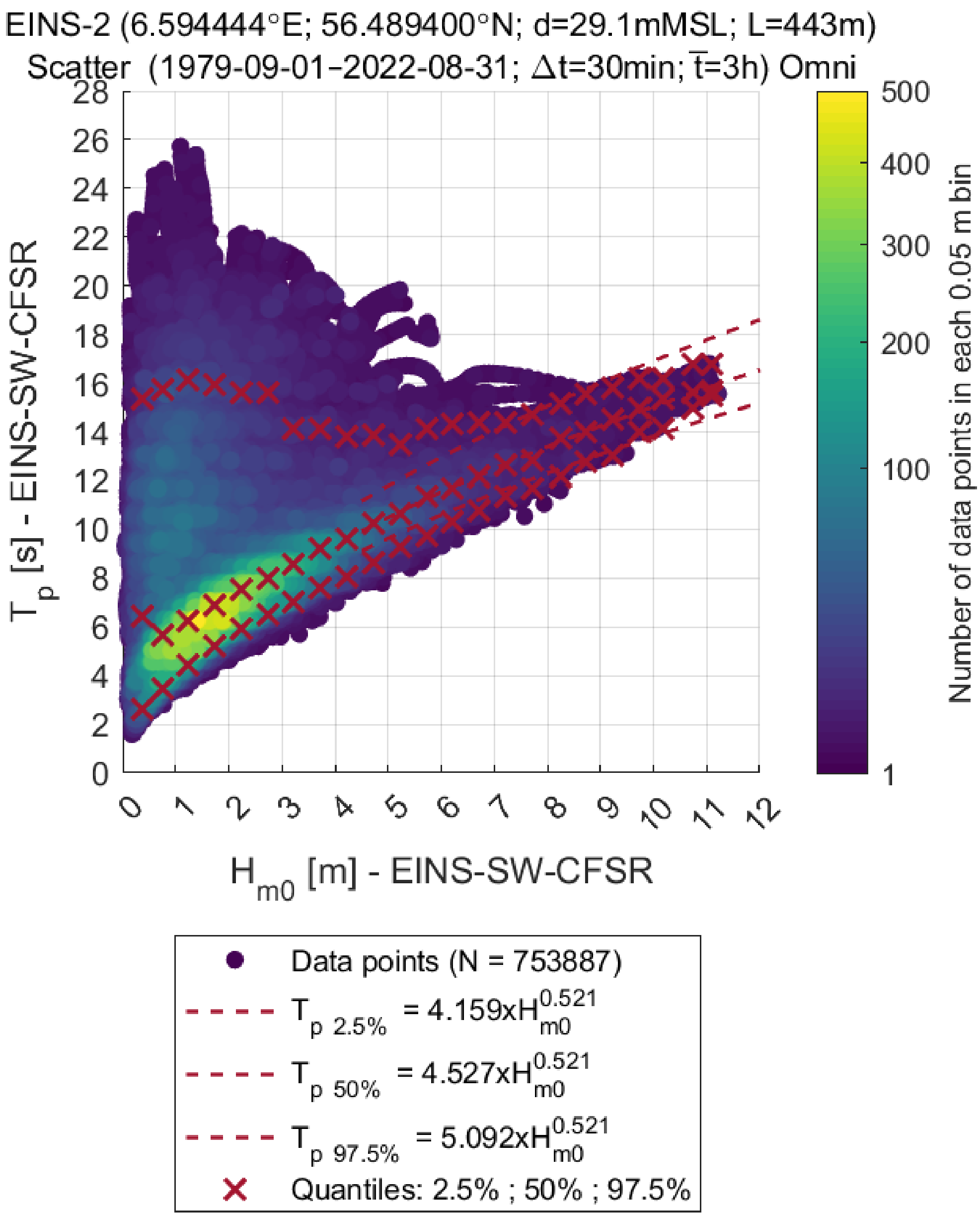

Figure 6.9 **Scatter diagram of H_{m0} vs T_p at EINS-2**

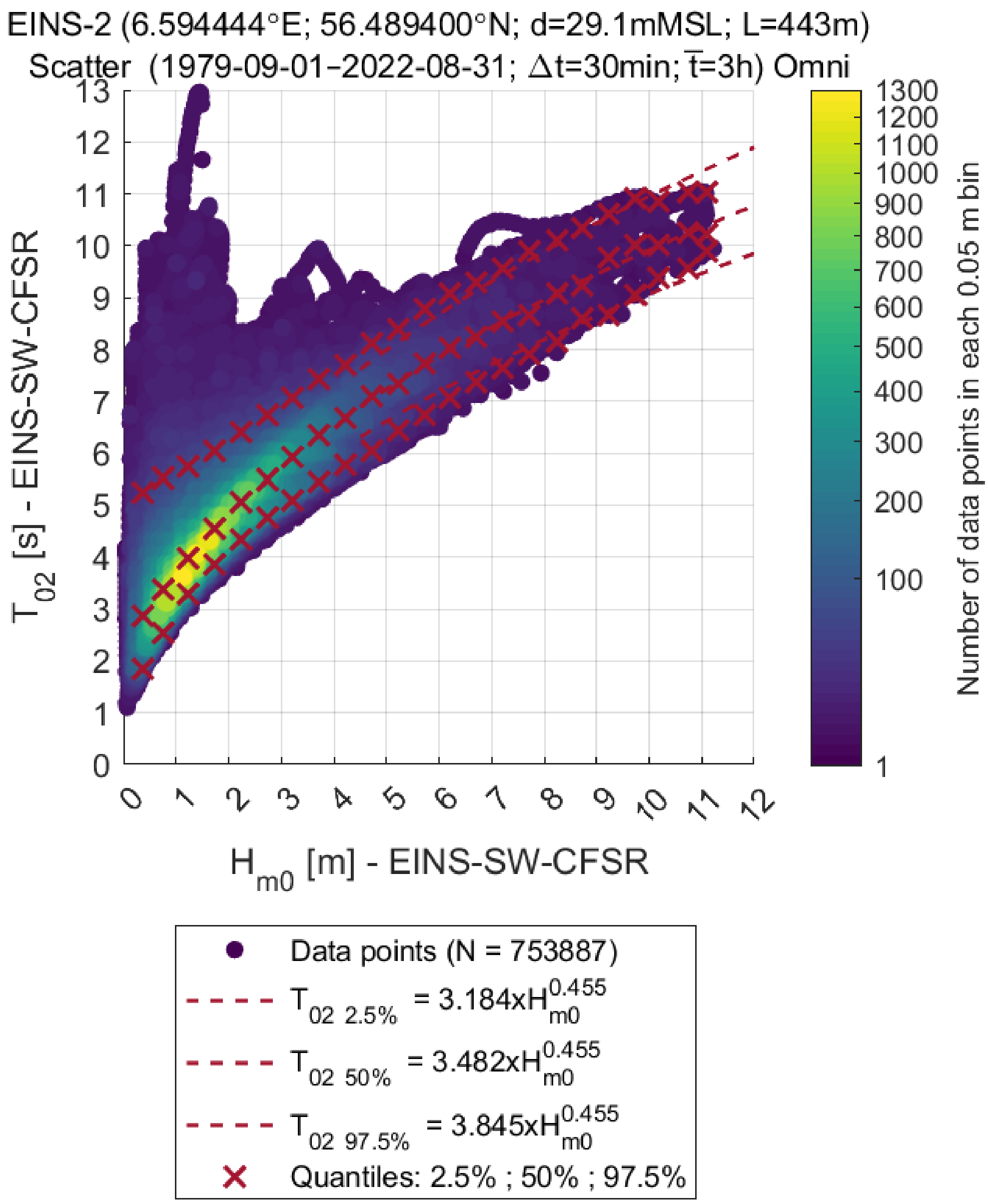

Figure 6.10 Scatter diagram of H_{m0} vs T_{02} at EINS-2

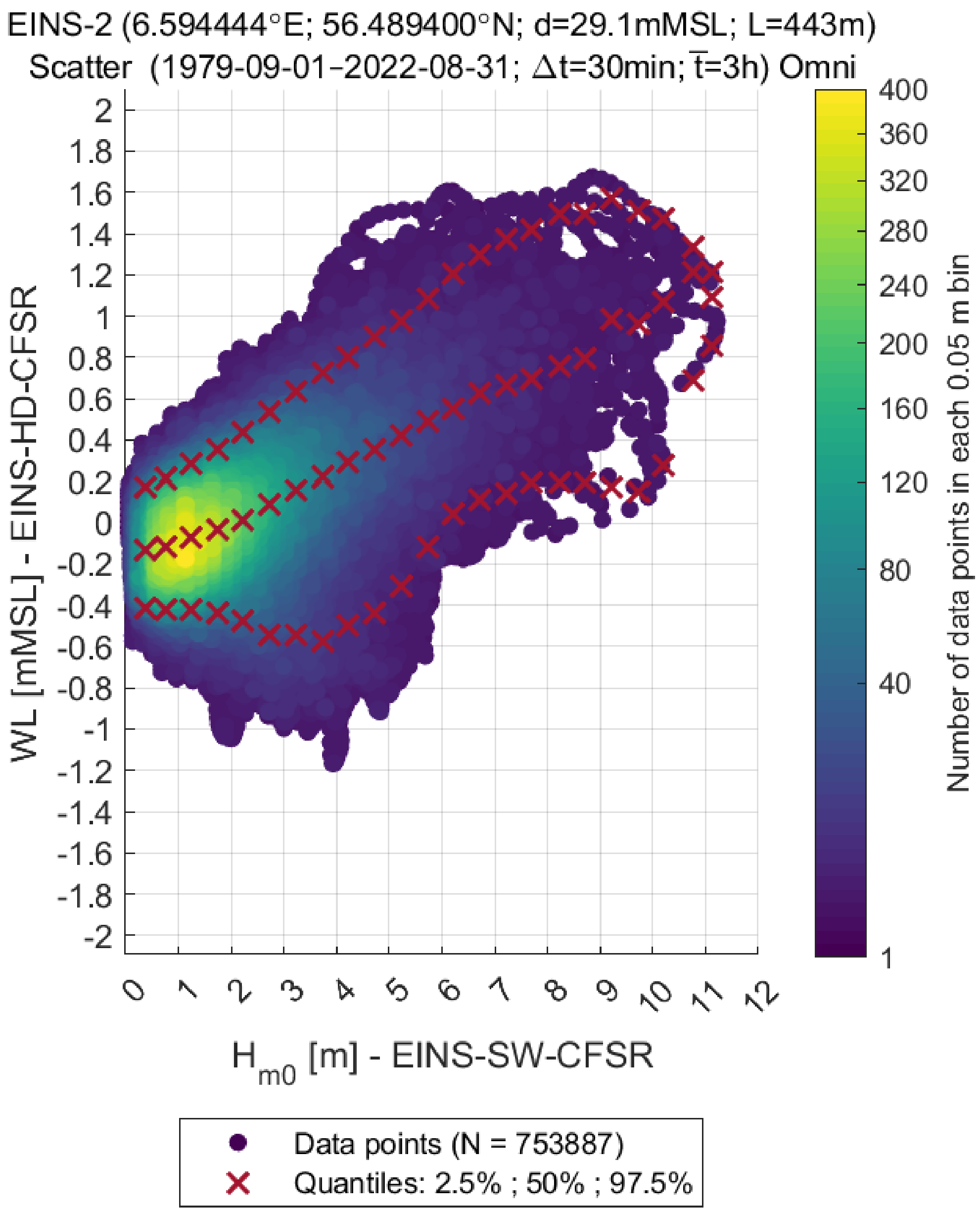

Figure 6.11 Scatter diagram of H_{m0} vs WL at EINS-2

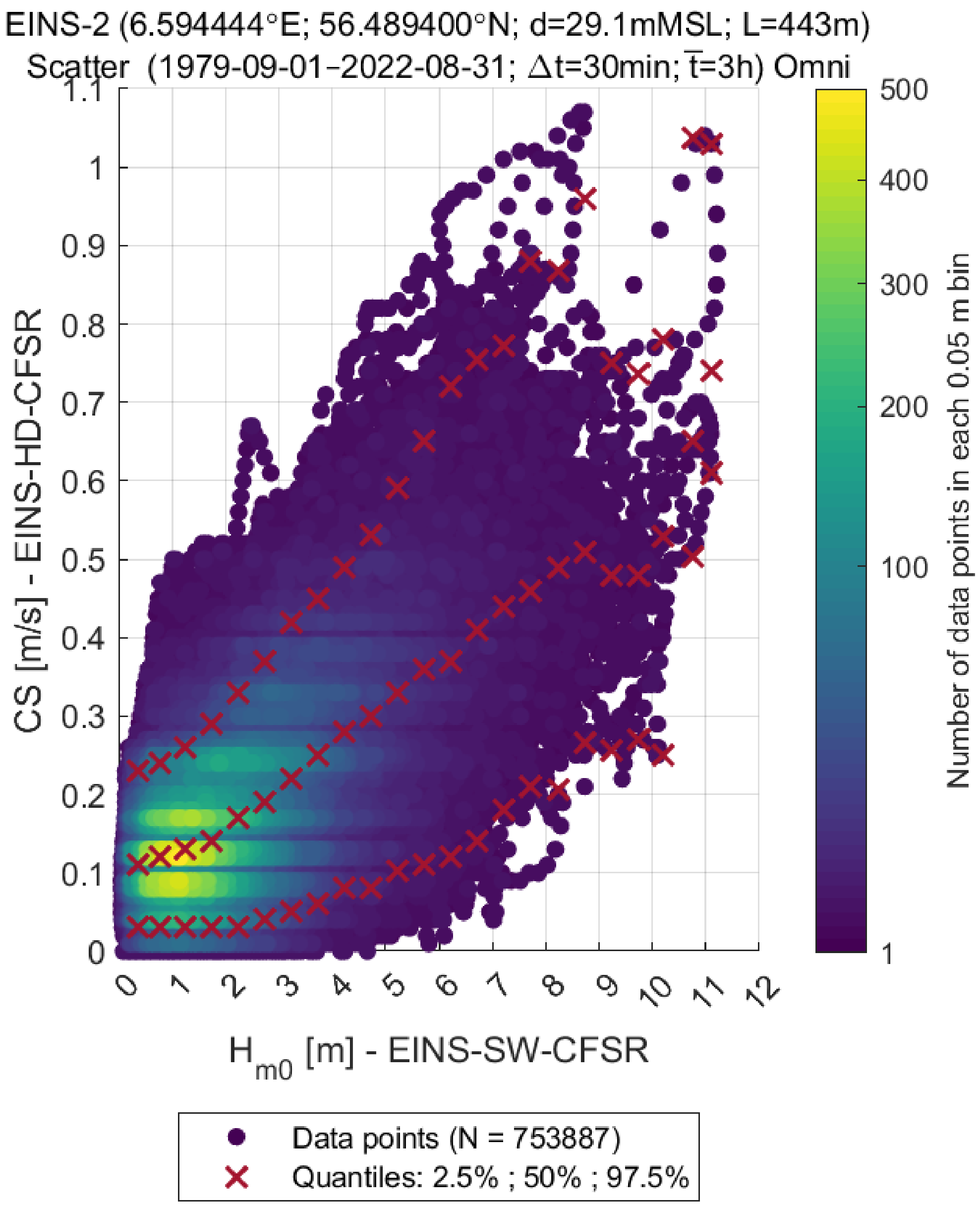

Figure 6.12 Scatter diagram of H_{m0} vs CS at EINS-2

6.1.7 Wind-wave misalignment

The wind-wave misalignment is calculated as WD_{10} minus the MWD. Figure 6.13 presents the misalignment vs. WS_{10} at EINS-2. The curves indicate the mean misalignment for each wind direction sector. The misalignment shows high scatter for wave height less than ~3 m, while the scatter (misalignment) is relatively low for higher waves when the wind starts to pick up because extreme waves in the North Sea are generally dominated by the local wind.

Figure 6.14 shows a trend of most frequent misalignment between 0 – 22.5°. For omni and almost all directions the main probability of misalignment is within ±45. Hence, the wind and wave directions are generally reasonably aligned.

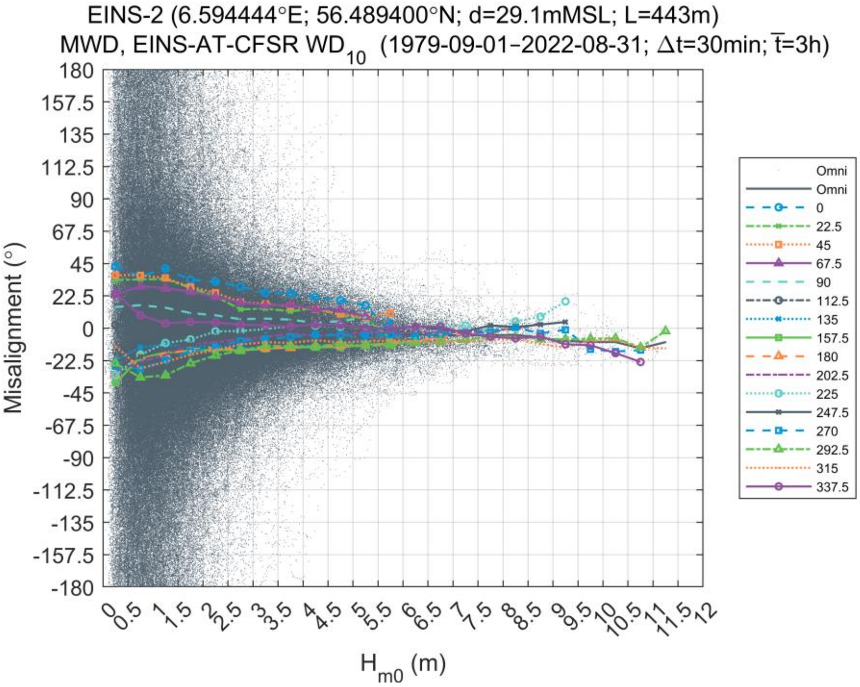

Figure 6.13 Wind-wave misalignment vs. H_{m0} at EINS-2

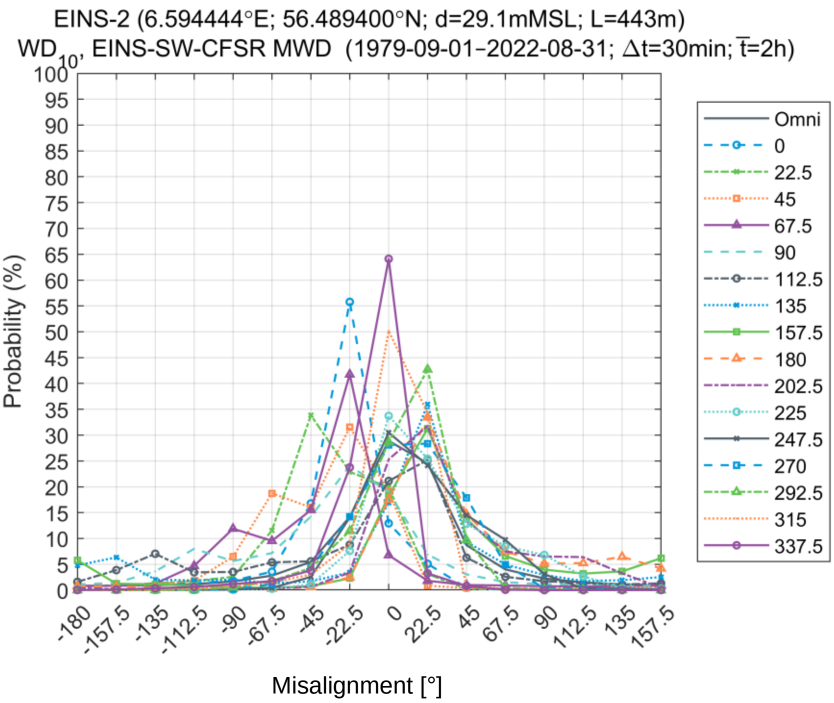

Figure 6.14 Probability of wind-wave misalignment per direction at EINS-2

6.1.8 Swell waves

This section presents a qualitative assessment of wind-sea and swell waves. Figure 6.1 presents time series of the total, wind-sea, and swell partition of H_{m0} at EINS-2, and Figure 6.15 presents a scatter plot of $H_{m0,Swell}$ vs H_{m0}. The figures show a predominance of wind-sea for the higher sea states.

Figure 6.16 presents the average ratio of wind-sea to total energy (blue) and swell to total energy (orange), (the energy being proportional to the square of H_{m0}). For the lower sea states (H_{m0} < 2.5 m, which occurs ~75% of the time), the swell partition is responsible for more than half (50-80%) of the total wave energy, while for moderate sea states (2.5 m < H_{m0} < 7.0 m, which occurs ~25% of the time) the wind-sea partition is responsible for the majority (50-90%) of the energy.

For the very highest sea states (H_{m0} > 7.0 m, which occurs <0.3% of the time), the swell partition constitutes less than 15% of the total energy. Such quantification obviously depends on the chosen separation criterion between wind-sea and swell (in this case the wave-age, see Section 5.1 of [15]), and it should be considered whether this criterion is suitable for the purpose in mind.

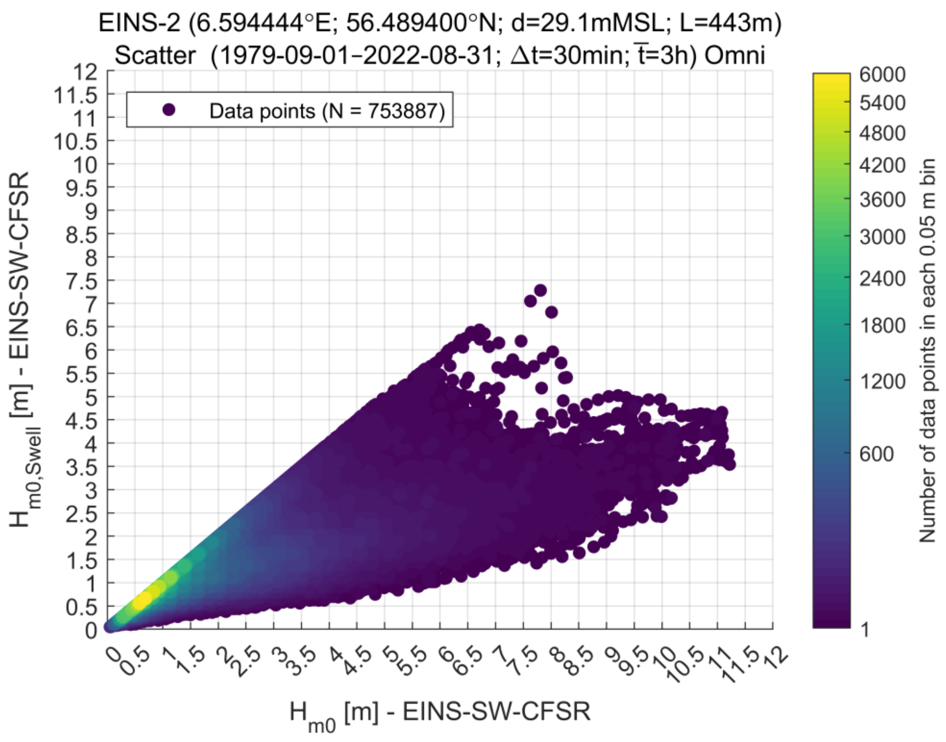

Figure 6.15 Scatter plot of $H_{m0,Swell}$ vs H_{m0} at EINS-2

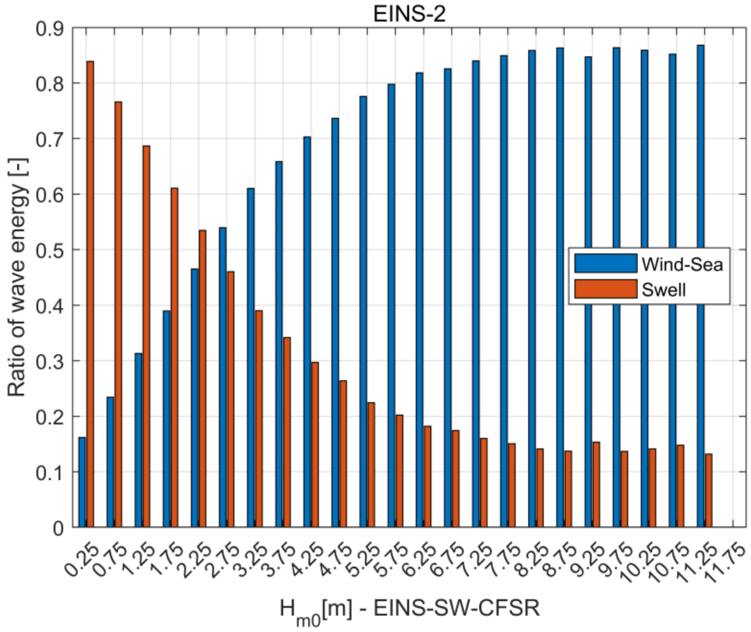

Figure 6.16 Average ratio of wind-sea to total energy (blue) and swell to total energy (orange) vs. H_{m0} (total) at EINS-2

6.1.9 Assessment of wave spectra

Assessment of wave spectra is addressed in Part A, [1]. For moderate and severe sea states, H_{m0} > 1.5 m, the spectrum is often single-peaked and can be well represented by a JONSWAP spectrum. For information on JONSWAP gamma values, it is recommended to apply the guidelines in Section 3.5.5 of RP-C205 [16], i.e. defining γ based on T_p and H_{m0}. For low sea states, H_{m0} < 1.5m, the spectra are often bi-modal, and should be represented by a JONSWAP spectrum for each of the wind-sea and swell partitions separately.

6.1.10 Maps of mean H_{m0}

Figure 6.17 and Figure 6.18 present maps across the EINS site of the weighted mean significant wave height, $\overline{H_{m0}}$, calculated as follows.

$$\overline{H_{m0}} = \left[\frac{1}{N}\sum_{i=1}^{N} {H_{m0}}_{i}^{\,m}\right]^{\frac{1}{m}} \tag{6.1}$$

where $m = (1{,}2)$ is the power coefficient, and N is the total number of hindcast data points (m = 1 is the mean H_{m0}, while m = 2 is the mean wave energy). There is little variation across the EINS site with $\overline{H_{m0,m=1}}$ of about 1.9 m.

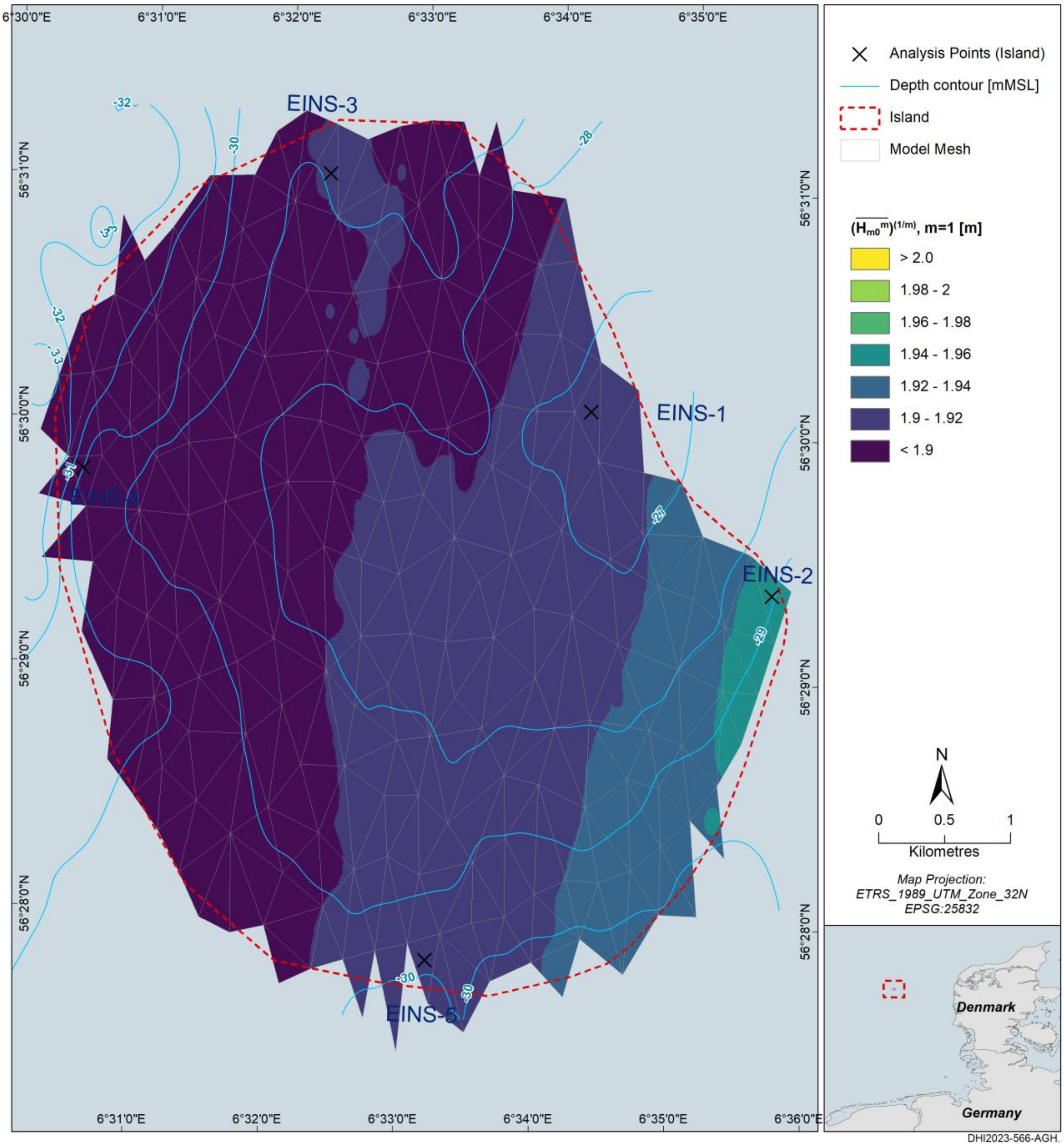

Figure 6.17 Spatial variation of $\overline{H_{m0}}$ across the EINS site for $m = 1$
The colour map shows the wave height, and the contours show water depth.

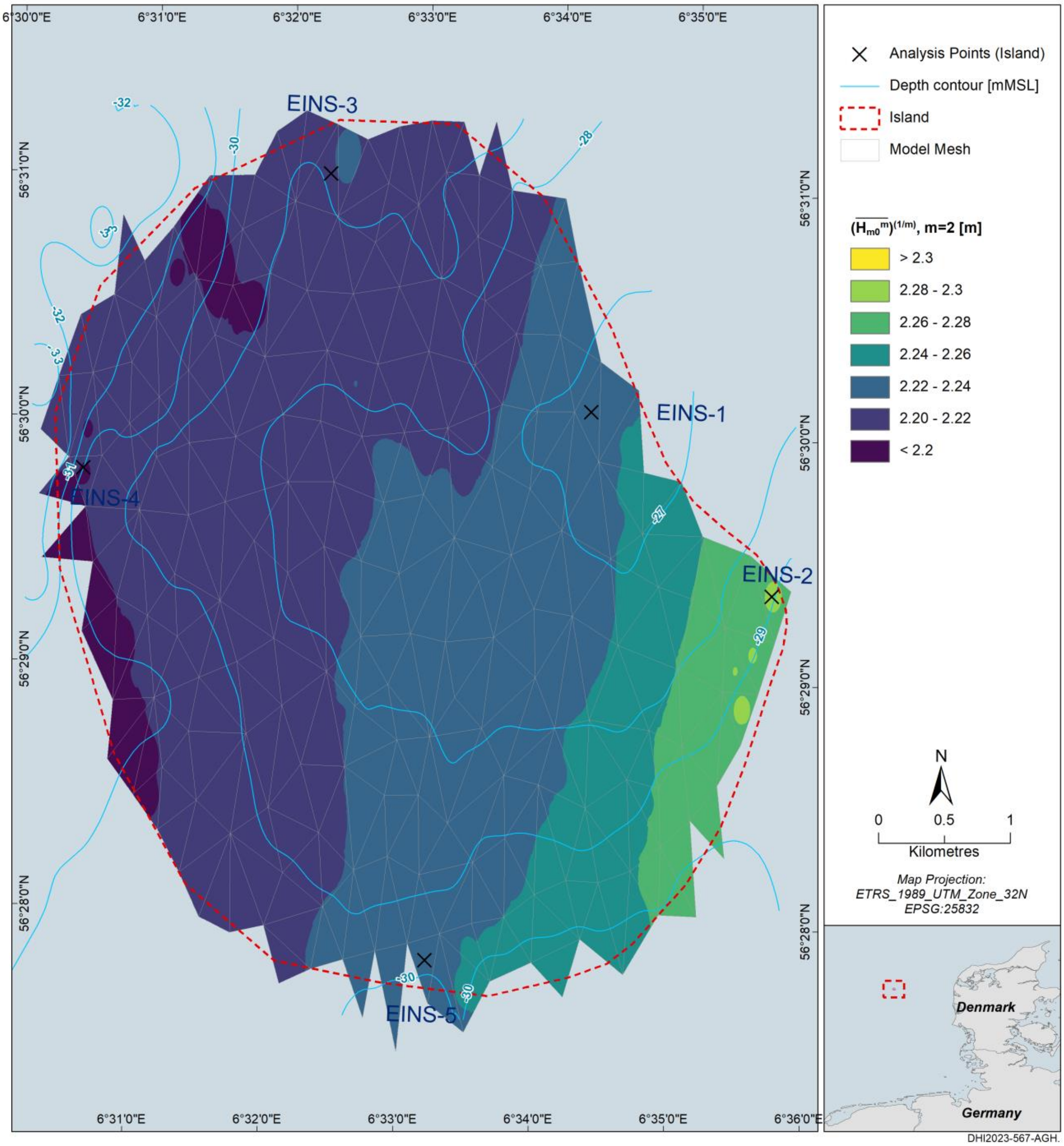

Figure 6.18 Spatial variation of $\overline{H_{m0}}$ across the EINS site for $m = 2$

The colour map shows the wave height, and the contours show water depth.

6.2 Extreme wave conditions

The extreme current conditions are estimated following the steps outlined in Appendix D: J-EVA Summary. The input time series is from the SW_{EINS} model. The storm events selected for the J-EVA analyses are based on the directional and seasonal variability (see Section 14.2.1) with filtering carried out using combined criteria of regression quantile and inverse wave age > 0.5 that is applied on the combined normalised storm events comprising of H_{m0}, CS_{res}, and WS. The combination of the time series is carried out to not miss out on peak events of associated variables (CS_{res} and WS) in case there is a small time shift in their peak events with respect to H_{m0}. The resulting ‘retained’ and ‘removed’ events are shown in Figure 6.19.

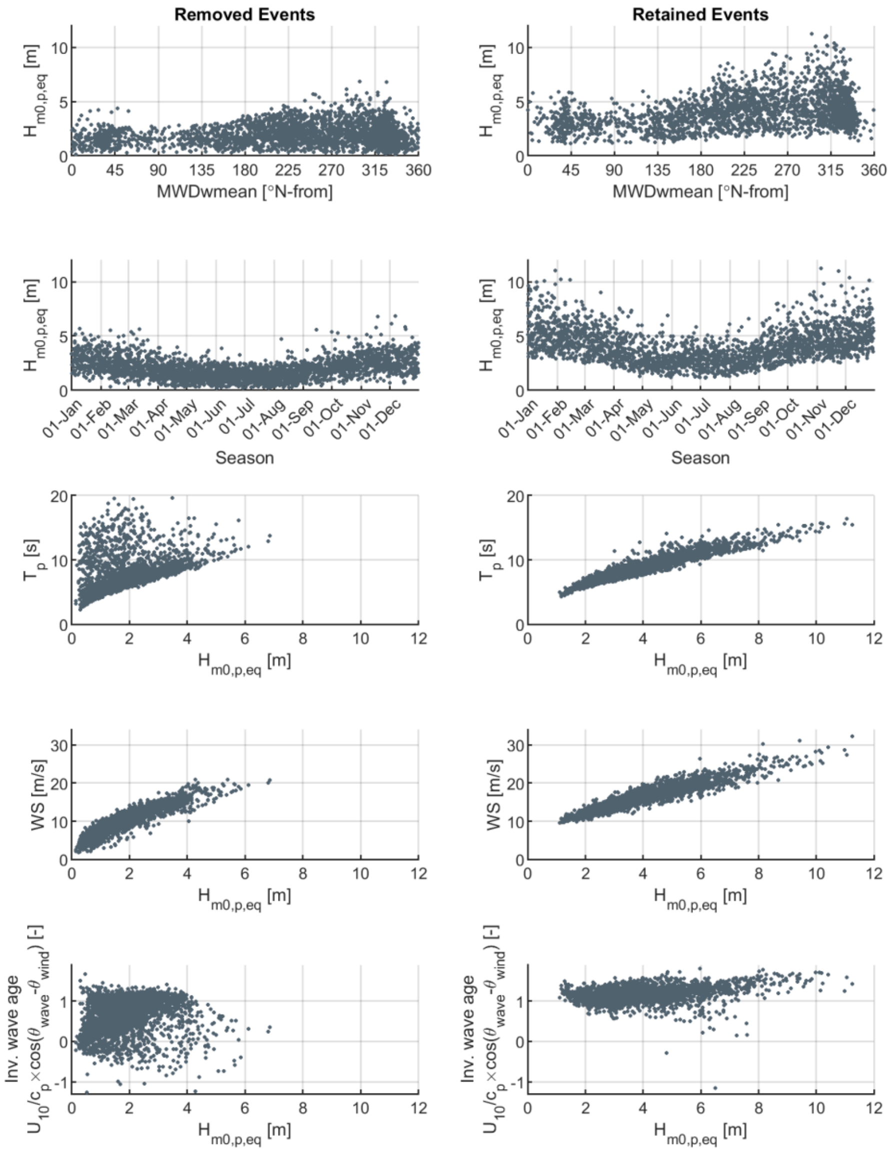

Figure 6.19 Selected events for the significant wave height H_{m0} and wind speed WS at EINS-2.
Events above the combined criteria of regression quantile and inverse wave age > 0.5 are retained for the J-EVA analysis.

6.2.1 Extreme significant wave height, H_{m0}

This section provides the directional extremes of the marginal wave parameters and conditioned variables.

A J-EVA statistical model (see Section 14.3) has been set up for extreme wave heights and conditioned (associated) variables, followed by simulation, including the directional scaling (see Section 14.4) to estimate the extremes. The storm model mean wave direction (MWD) and season have been used as co-variates and the model fitted to characteristic storm variable values ($H_{m0,p,eq}$, $\ln \sigma_{eq}$, T_p, etc.). Furthermore, for the long-term distribution, the $H_{m0,p,eq}$ (equivalent peak H_{m0} from the storm model) has been limited to 0.6 times the water depth (see Section 14.7).

Figure 6.20 shows the best estimate of H_{m0} using the integrated parameters of the posterior predictive distribution of H_{m0} from an 80,000-year simulation, which is used to calculate the best estimate for 1-, 5-, 10-, 50-, 80-, and 100-year return periods. Best estimates for larger return periods are calculated based on simulating up to 4 x 10^6 years of events, where the minimum number of exceedances N_e = 25 is chosen for the 80,000-year return period.

The extreme values are presented (Table 6.3 - Table 6.13) for a maximum return period of 10,000- year. The figure also shows joint distributions of conditioned variables to H_{m0}, such as wave periods (T_p, T_{02}), residual water level (WL_{res}) and residual current speed (CS_{res}). These subplots show hindcast data in black points with the simulated values from J-EVA in the coloured dots, where ‘cooler’ colours indicate a lower number of exceedances. Derived contours pertaining to return periods of 1, 5, 10, 50, 80 and 100 years are outlined in grey.

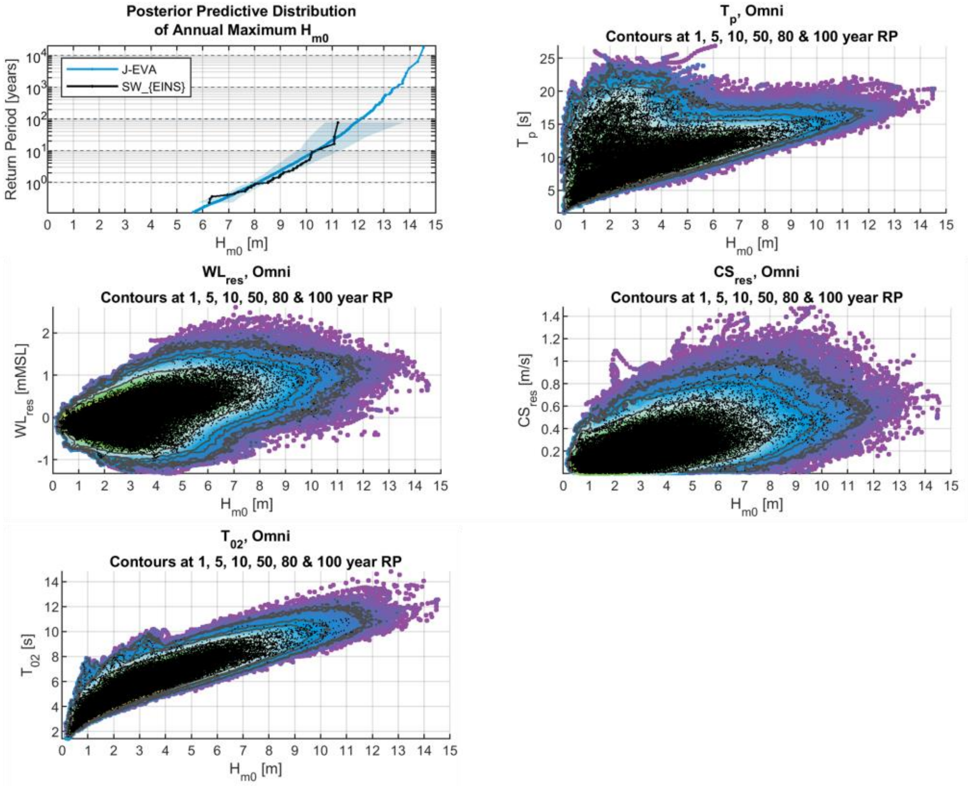

Figure 6.20 Estimates of marginal and conditioned variables from 10,000-year simulation at EINS-2.

Hindcast data is presented as black markers. The blue solid line (top-left) is the best estimate of H_{m0} using the distribution parameters that are integrated over the posterior distribution. The blue shaded area (top-left) is the 2.5-97.5 % credible interval. Contours of conditioned variables shown as coloured dots from the result of a simulation of 10,000 years using the distribution parameters from the posterior predictive distribution at different return periods are shown for T_p (top-right), T_{02} (third row left), WL_{res} (second row left), and CS_{res} (second row right) against H_{m0}. Black dots show original hindcast. Warmer colours indicate a higher density of points.

Figure 6.21 shows the directional annual number of exceedances of the significant wave height estimated from an 80,000-year simulation, which is used to calculate the best estimate for 1-, 5-, 10-, 50-, 80-, and 100-year return periods (The 45-degree bins presented here are for visual inspection of directional fits. The final directional values are based on 22.5-degree bins).

The best estimate predicts the significant wave height very well, as indicated by the good fit between the hindcast data (black line) and best estimate (blue line). The prediction in different directions is also good.

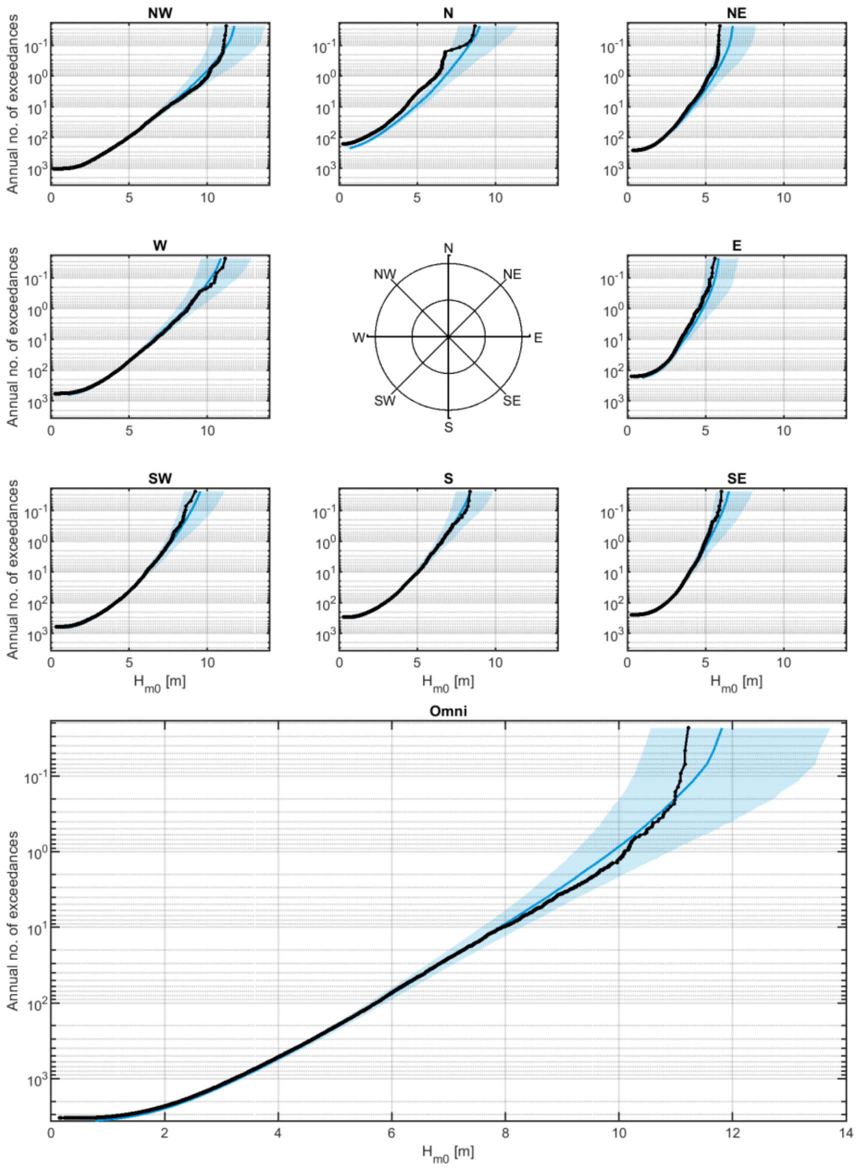

Figure 6.21 Directional exceedance probability of H_{m0}.
Hindcast data is shown in black. The blue line is the best estimate using the integrated posterior distribution parameters. The shaded area is the 2.5-97.5% credible interval.

Table 6.3 provides the values of the directional significant wave height. The directional extreme values are scaled according to DNV-RP-C205, [3].

Warmer colours (red) indicate larger values. Large values of H_{m0} are observed in the west and north-west directions, mainly due to large fetch as seen in Figure 1.1.

Table 6.3 Extreme significant wave height, H_{m0}, at EINS-2

Extreme significant wave height, H_{m0} [m]								
	Return Period, T_R [years]							
MWD [°N-from]	1	5	10	50	80	100	1,000	10,000
Omni	8.1	9.7	10.3	11.6	12.0	12.1	13.5	14.6
0	5.7	6.9	7.4	8.6	8.9	9.1	10.5	11.6
22.5	5.2	6.3	6.7	7.5	7.8	7.9	9.0	10.1
45	5.3	6.2	6.6	7.3	7.5	7.6	8.5	9.3
67.5	4.7	5.6	5.9	6.6	6.7	6.8	7.6	8.3
90	4.5	5.3	5.6	6.3	6.5	6.6	7.3	8.0
112.5	4.7	5.5	5.8	6.4	6.6	6.6	7.5	8.2
135	5.1	5.9	6.2	6.9	7.1	7.2	8.1	9.0
157.5	5.7	6.6	7.0	7.8	8.0	8.1	9.2	10.2
180	6.6	7.6	8.0	8.8	9.0	9.1	10.1	11.3
202.5	7.5	8.5	8.8	9.6	9.8	9.9	11.0	11.9
225	7.9	8.9	9.3	10.1	10.3	10.4	11.5	12.5
247.5	8.1	9.5	9.9	10.9	11.1	11.2	12.3	13.3
270	8.1	9.7	10.3	11.6	11.9	12.0	13.0	14.0
292.5	8.1	9.7	10.3	11.6	12.0	12.1	13.5	14.6
315	8.1	9.7	10.3	11.6	12.0	12.1	13.5	14.6
337.5	8.1	9.7	10.3	11.6	12.0	12.1	13.4	14.4

6.2.2 Maps of extreme H_{m0}

Figure 6.22 to Figure 6.24 present maps of extreme H_{m0} across the EINS island area for return periods of 1-, 50-, and 100 years. The extreme values of H_{m0} from the hindcast data at each mesh element are calculated using T-EVA. The J-EVA extremes of H_{m0} at the five analysis locations are then used to scale the extremes in each mesh element using the inverse distance weighting method, [14]. The maximum H_{m0} of 11.2 and 11.6 m varies within about ±1 m for the 50- and 100-year return period.

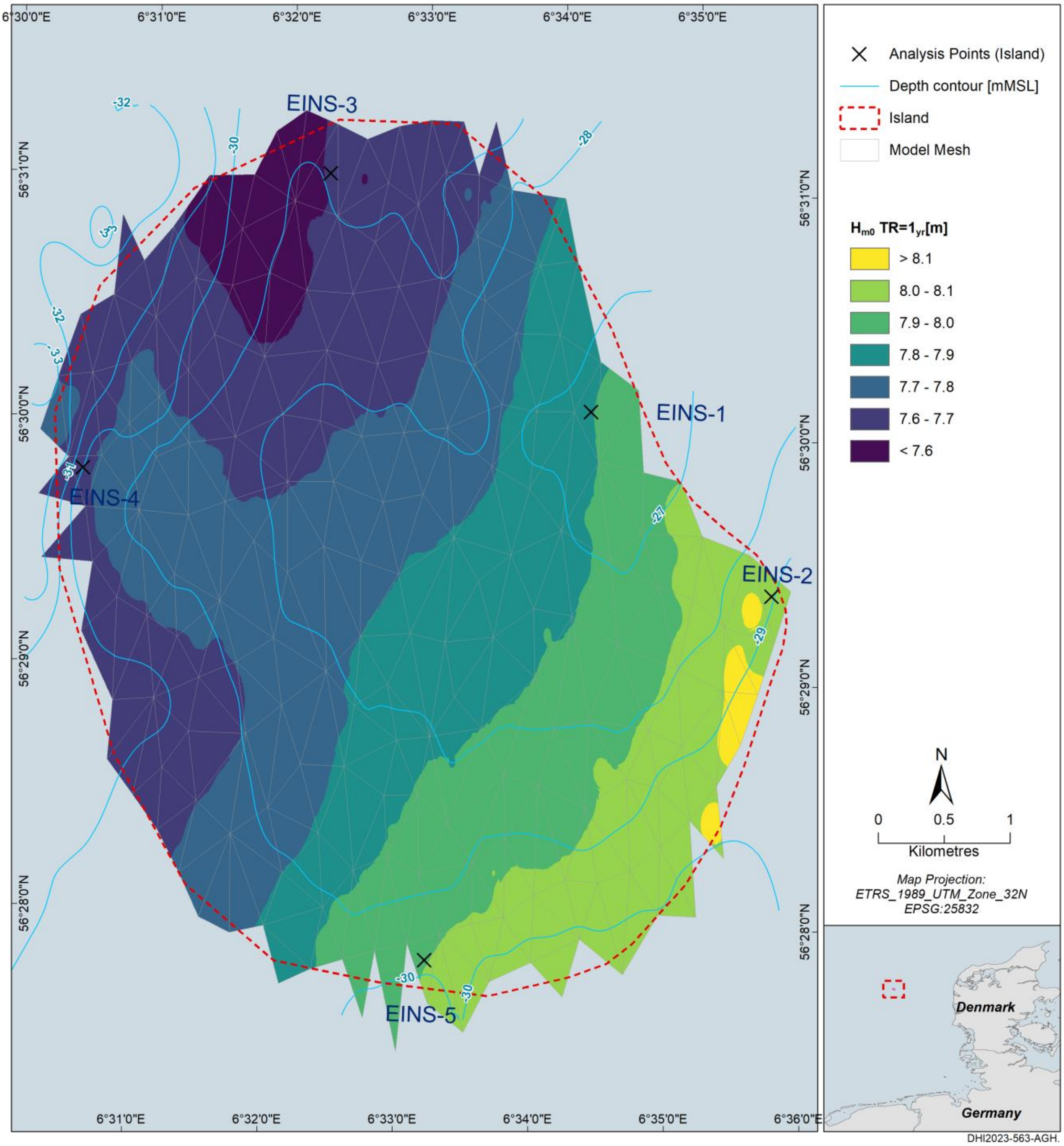

Figure 6.22 Spatial variation across EINS of H_{m0} for return period of 1 year
The colour map shows the wave height, and the contours show water depth.

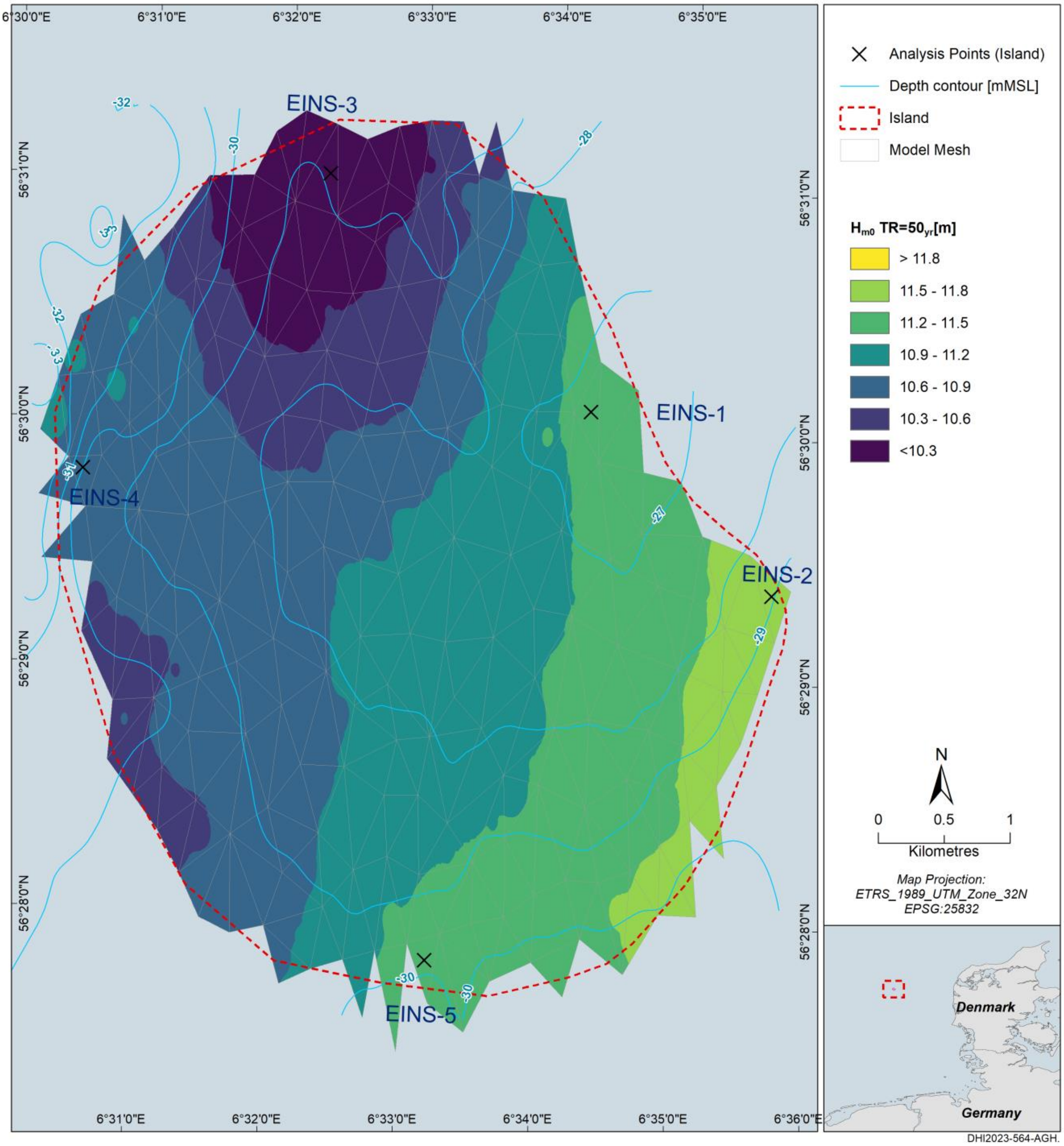

Figure 6.23 Spatial variation across EINS of H_{m0} for return period of 50 years
The colour map shows the wave height, and the contours show water depth.

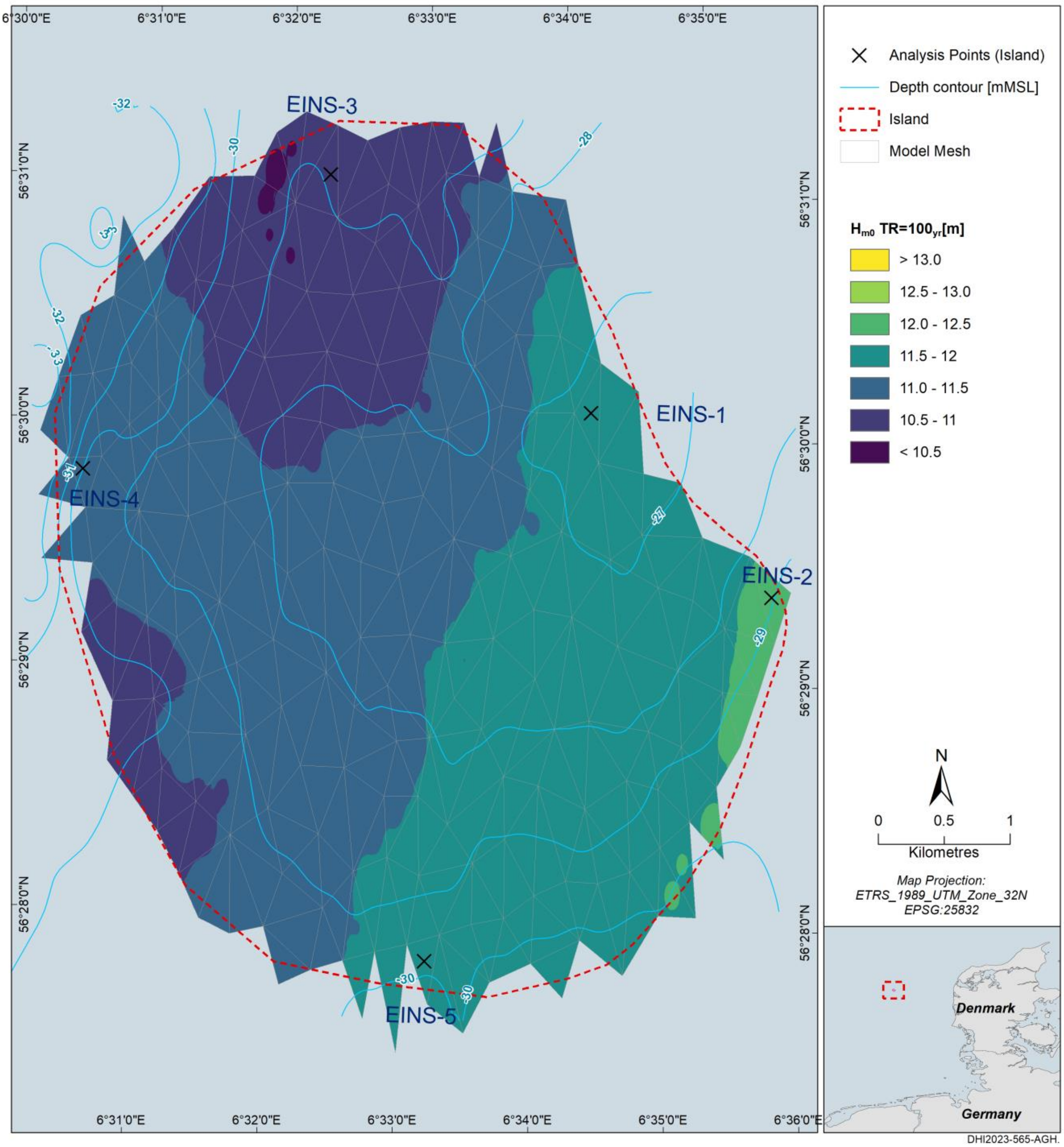

Figure 6.24 Spatial variation across EINS of H_{m0} for return period of 100 years
The colour map shows the wave height, and the contours show water depth.

6.2.3 Variables conditioned on H_{m0}

The correlation between H_{m0} and other variables is presented in Figure 6.20 for the 80,000-year simulated storms in J-EVA.

The conditioned variables are obtained by selecting the 250 simulated events that are closest to the annual maxima for each return period, and then finding the 2.5%, 50%, and 97.5% quantile of the conditioned variable in each event. From this method, the conditioned variables do not necessarily increase smoothly with increasing return period, and therefore a fit to the conditioned variables was applied to obtain a robust estimation.

Power or linear functional forms are applied to the range of return periods. Here, 'Y' denotes the variable conditional on H_{m0}, while 'a' and 'b' are fitted parameters.

Wave periods (T_p, T_{02}, TH_{max}), and current speed (CS):	$Y_{\|Hm0} = a \cdot H_{m0}^{b}$	**(6.2)**
WL_{tot}:	$Y_{\|Hm0} = a \cdot H_{m0} + b$	**(6.3)**

The following tables present the 50 %-tile values of the conditioned variables, while 2.5, 50 and 97.5 %-tile values at all analysis points are provided in the Excel Data Reports (listed in Table 11.1) attached to this report.

It is noted that for conditioned variables the directional values can sometimes exceed that of omni. This could fx be in case omni waves are dominated by wind-sea, while a certain sector is dominated by swell. In this case the swell-dominated directional sector will higher (conditional) T_p than omni.

T_p conditioned on H_{m0}

Figure 6.25 shows the extreme H_{m0} for each return period against T_p and fit based on (6.2), while Table 6.4 provides the 50 %-tiles of $T_{p|Hm0}$ at EINS-2.

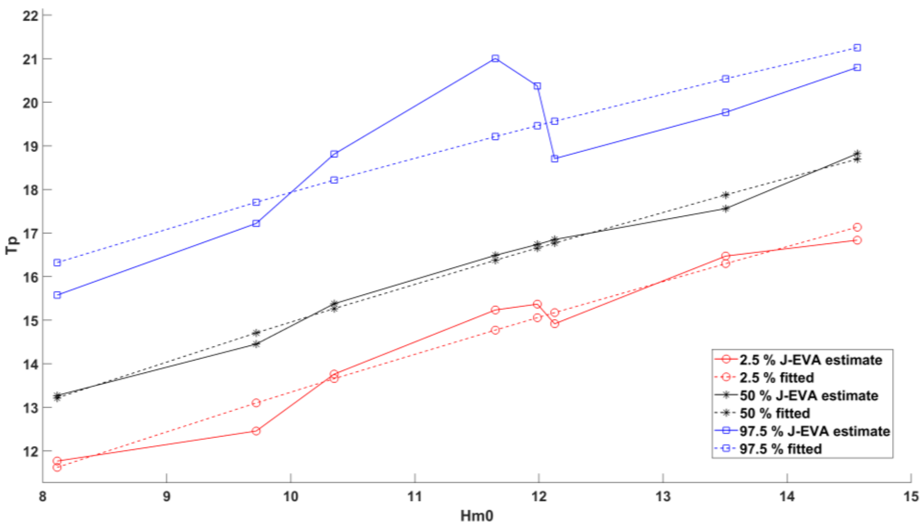

Figure 6.25 Omni T_p conditioned on H_{m0}, $T_{p|Hm0}$ at EINS-2

Table 6.4 T_p conditioned on H_{m0}, $T_{p|Hm0}$ 50% at EINS-2

Peak wave period conditioned on H_{m0}, $T_{p|Hm0}$ [s] 50%								
	Return Period, T_R [years]							
MWD [°N-from]	1	5	10	50	80	100	1,000	10,000
Omni	13.2	14.7	15.3	16.4	16.7	16.8	17.9	18.7
0	11.4	13.0	13.6	14.9	15.2	15.4	17.0	18.1
22.5	10.6	11.5	11.8	12.4	12.6	12.7	13.4	14.2
45	10.2	10.9	11.1	11.6	11.8	11.8	12.4	12.9
67.5	8.7	9.5	9.7	10.3	10.4	10.5	11.1	11.6
90	8.3	9.0	9.2	9.7	9.8	9.9	10.4	10.9
112.5	8.4	9.1	9.4	9.8	10.0	10.0	10.6	11.1
135	9.1	9.8	10.1	10.6	10.8	10.9	11.6	12.3
157.5	9.9	10.8	11.2	11.9	12.1	12.2	13.1	13.9
180	11.0	11.9	12.3	13.0	13.1	13.2	14.1	15.0
202.5	11.9	12.7	13.1	13.8	13.9	14.0	14.9	15.6
225	12.4	13.3	13.6	14.3	14.4	14.5	15.3	16.0
247.5	12.6	13.8	14.1	14.9	15.0	15.1	15.9	16.6
270	13.0	14.4	14.9	15.9	16.1	16.2	16.9	17.6
292.5	13.2	14.6	15.2	16.2	16.5	16.6	17.6	18.4
315	13.6	15.0	15.6	16.6	16.9	17.0	18.1	18.9
337.5	13.8	15.3	15.9	17.0	17.3	17.4	18.4	19.2

T_{02} conditioned on H_{m0}

Figure 6.26 shows the extreme H_{m0} for each return period against T_{02} and fit based on (6.2), while Table 6.5 provides the 50 %-tiles of $T_{02|Hm0}$ at EINS-2.

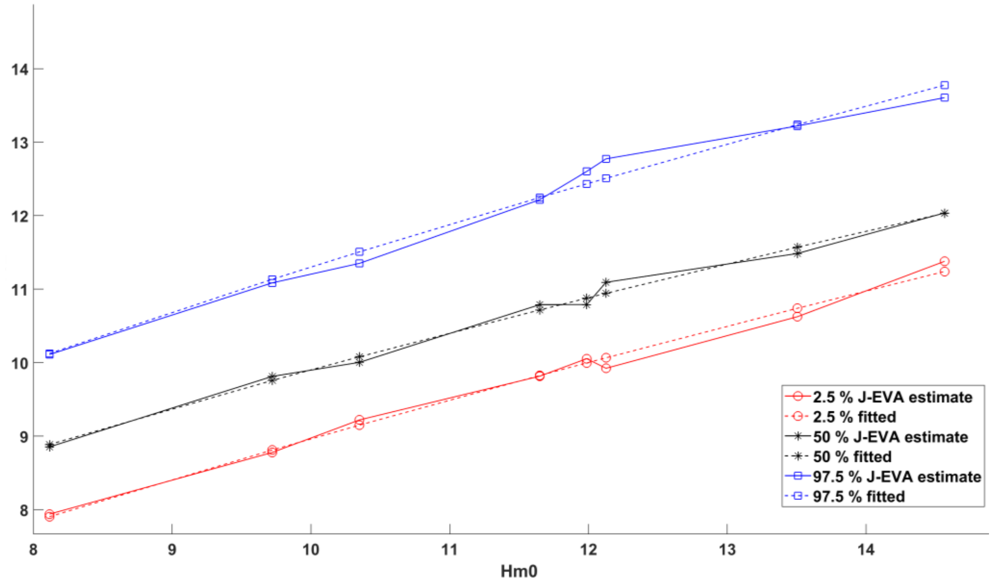

Figure 6.26 Omni T_{02} conditioned on H_{m0}, $T_{02|Hm0}$ at EINS-2

Table 6.5 T_{02} conditioned on H_{m0}, $T_{02|Hm0}$ 50% at EINS-2

T_{02} conditioned on H_{m0}, $T_{02\|Hm0}$ [s] 50%								
	Return Period, T_R [years]							
MWD [°N-from]	1	5	10	50	80	100	1,000	10,000
Omni	8.9	9.8	10.1	10.7	10.9	10.9	11.6	12.0
0	7.6	8.6	8.9	9.7	9.9	10.0	10.9	11.5
22.5	7.1	7.6	7.8	8.2	8.3	8.3	8.8	9.2
45	6.8	7.2	7.3	7.6	7.7	7.7	8.1	8.3
67.5	6.1	6.6	6.7	7.1	7.1	7.2	7.5	7.8
90	5.9	6.4	6.5	6.8	6.9	6.9	7.3	7.5
112.5	6.0	6.4	6.6	6.9	6.9	7.0	7.3	7.6
135	6.3	6.7	6.8	7.2	7.2	7.3	7.7	8.0
157.5	6.7	7.2	7.4	7.8	7.9	7.9	8.4	8.8
180	7.4	7.9	8.1	8.4	8.5	8.6	9.0	9.5
202.5	8.0	8.4	8.6	9.0	9.1	9.1	9.6	9.9
225	8.3	8.8	8.9	9.3	9.4	9.4	9.9	10.2
247.5	8.5	9.1	9.3	9.7	9.8	9.8	10.2	10.6
270	8.7	9.4	9.7	10.2	10.3	10.4	10.8	11.1
292.5	8.9	9.7	10.0	10.6	10.7	10.8	11.4	11.8
315	9.1	10.0	10.3	11.0	11.1	11.2	11.8	12.3
337.5	9.3	10.3	10.6	11.3	11.4	11.5	12.1	12.6

WL_{tot} conditioned on H_{m0}

Figure 6.27 shows the extreme H_{m0} for each return period against WL_{tot} and fit based on (6.3), while Table 6.6 provides all %-tiles of $WL_{tot|Hm0}$ at EINS-2. For the 2.5%-tile, a negative trend was observed, in which case a mean value is applied across all return periods.

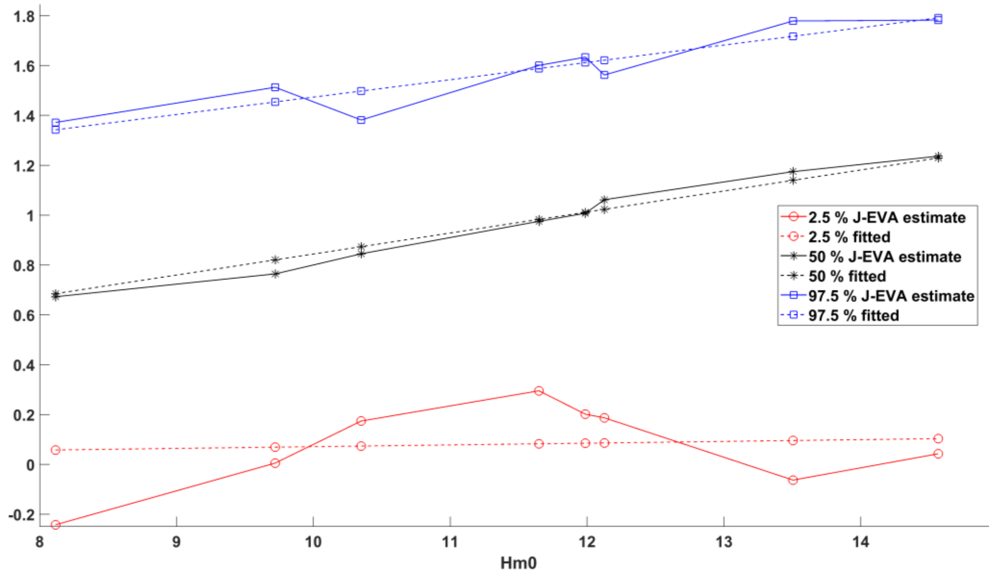

Figure 6.27 Total WL conditioned on H_{m0}, $WL_{tot|Hm0}$ at EINS-2

Table 6.6 Total WL conditioned on H_{m0}, $WL_{tot|Hm0}$ at EINS-2

WL_{tot} conditioned on H_{m0}, $WL_{tot\|Hm0}$ [m]			
Return Period, T_R [years]	2.5%-tile	50%-tile	97.5%-tile
1	0.1	0.7	1.3
5	0.1	0.8	1.5
10	0.1	0.9	1.5
50	0.1	1.0	1.6
80	0.1	1.0	1.6
100	0.1	1.0	1.6
1,000	0.1	1.1	1.7
10,000	0.1	1.2	1.8

CS_{res} conditioned on H_{m0}

Figure 6.28 shows the extreme H_{m0} for each return period against CS_{res} and fit based on (6.2), while Table 6.7 provides all %-tiles of $CS_{res|Hm0}$ at EINS-2.

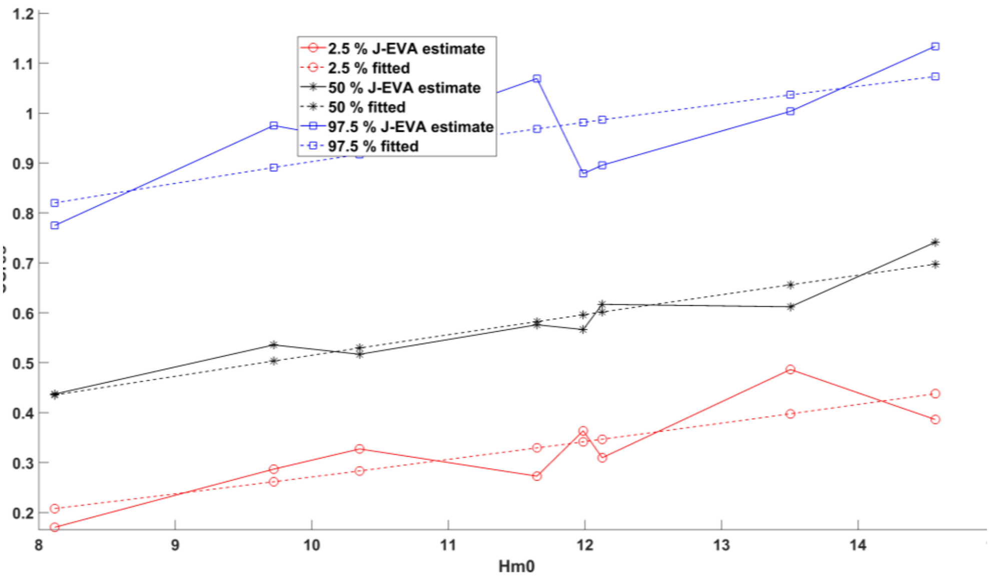

Figure 6.28 Residual CS conditioned on H_{m0}, $CS_{res|Hm0}$ at EINS-2

Table 6.7 Residual CS conditioned on H_{m0}, $CS_{res|Hm0}$ at EINS-2

CS_{res} conditioned on H_{m0}, $CS_{res\|Hm0}$ [m/s]			
Return Period, T_R [years]	2.5%-tile	50%-tile	97.5%-tile
1	0.2	0.4	0.8
5	0.3	0.5	0.9
10	0.3	0.5	0.9
50	0.3	0.6	1.0
80	0.3	0.6	1.0
100	0.3	0.6	1.0
1,000	0.4	0.7	1.0
10,000	0.4	0.7	1.1

CS_{tot} conditioned on H_{m0}

Figure 6.29 shows the extreme H_{m0} for each return period against CS_{tot} and fit based on (6.2), while Table 6.8 provides all %-tiles of $CS_{tot|Hm0}$ at EINS-2.

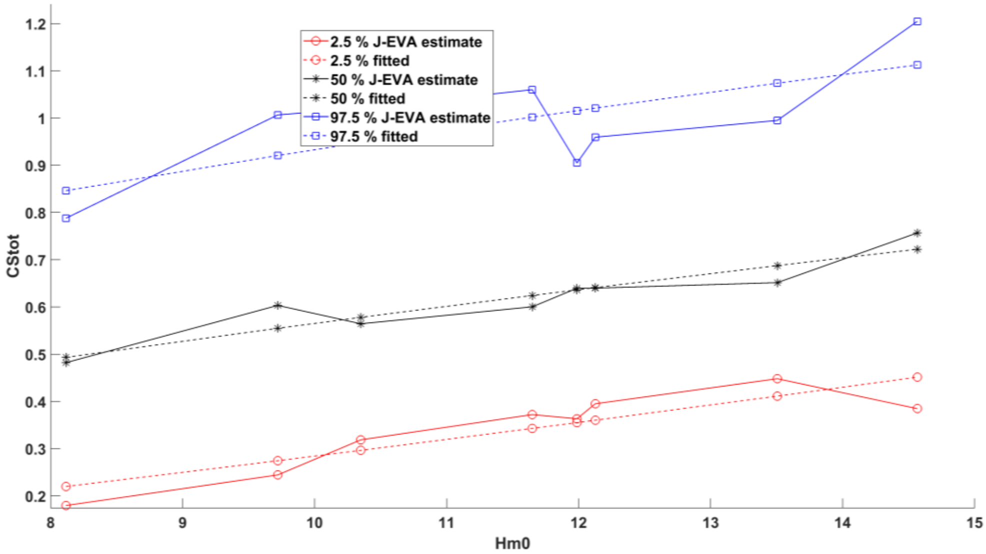

Figure 6.29 Total CS conditioned on H_{m0}, $CS_{tot|Hm0}$ at EINS-2.

Table 6.8 Total CS conditioned on H_{m0}, $CS_{tot|Hm0}$ at EINS-2.

CS_{tot} conditioned on H_{m0}, $CS_{tot\|Hm0}$ [m/s]			
Return Period, T_R [years]	2.5%-tile	50%-tile	97.5%-tile
1	0.2	0.5	0.8
5	0.3	0.6	0.9
10	0.3	0.6	0.9
50	0.3	0.6	1.0
80	0.4	0.6	1.0
100	0.4	0.6	1.0
1,000	0.4	0.7	1.1
10,000	0.5	0.7	1.1

6.2.4 Extreme maximum wave height, H_{max}

The extreme maximum wave heights, H_{max}, were derived based on the Glukhovskiy short-term wave heigh distribution (given in Section 1.3 in Appendix C: T-EVA – Traditional EVA) that considers the local water depth. The choice of the short term distribution is discussed and justified in Section 6.2.1 of [1].

Table 6.9 presents the directional extreme H_{max} values. The directional extreme values are scaled according to DNV-RP-C205, [3]. The values have been truncated to account for wave breaking and limitations in accordance with Section 6.2.6.

Table 6.9 Extreme maximum wave height, H_{max}, at EINS-2

Extreme maximum wave height, H_{max} [m]								
	Return Period, T_R [years]							
MWD [°N-from]	1	5	10	50	80	100	1,000	10,000
Omni	14.7	17.2	18.2	20.3	20.8	21.1	23.3	23.4
0	10.4	12.6	13.4	15.2	15.7	15.9	18.1	20.4
22.5	9.8	11.7	12.5	14.1	14.5	14.6	16.5	18.3
45	10.1	11.8	12.4	13.7	14.1	14.3	16.0	17.8
67.5	9.1	10.7	11.3	12.6	13.0	13.2	14.7	16.3
90	8.7	10.3	10.9	12.1	12.5	12.7	14.1	15.8
112.5	9.0	10.5	11.0	12.2	12.5	12.7	14.4	16.1
135	9.6	11.1	11.6	12.9	13.2	13.4	15.2	17.2
157.5	10.6	12.2	12.8	14.1	14.4	14.6	16.6	18.9
180	11.9	13.6	14.2	15.6	16.1	16.3	18.0	20.0
202.5	13.5	15.1	15.8	17.2	17.6	17.8	19.6	21.7
225	14.1	15.8	16.5	17.9	18.4	18.6	21.7	22.2
247.5	14.7	16.6	17.3	18.8	19.2	19.4	22.1	22.8
270	14.7	17.2	18.2	20.0	20.4	20.7	22.7	22.8
292.5	14.7	17.2	18.2	20.3	20.8	21.1	23.1	23.4
315	14.7	17.2	18.2	20.3	20.8	21.1	23.3	23.4
337.5	14.7	17.2	18.2	20.3	20.8	21.0	23.3	23.4

T_{Hmax} conditioned on H_{max}

Figure 6.30 shows the extreme T_{Hm0} for each return period against H_{max} and fit based on (6.2), while Table 6.10 provides 50 %-tiles of T_{Hmax} at EINS-2.

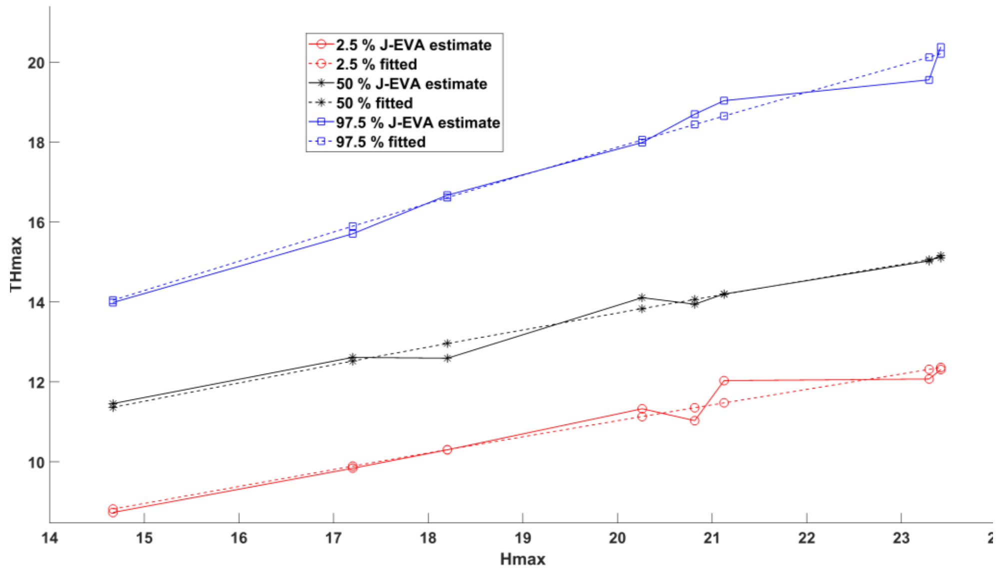

Figure 6.30 Omni T_{Hmax} conditioned on H_{max}, T_{Hmax} at EINS-2

Table 6.10 T_{Hmax} conditioned on H_{max}, T_{Hmax} at EINS-2

T_{Hmax} conditioned on Hmax, T_{Hmax} [s] 50%								
	Return Period, T_R [years]							
MWD [°N-from]	1	5	10	50	80	100	1,000	10,000
Omni	11.4	12.5	13.0	13.8	14.1	14.2	15.1	15.1
0	10.1	11.3	11.7	12.5	12.8	12.9	13.9	14.8
22.5	9.1	10.0	10.3	10.9	11.1	11.1	11.9	12.5
45	8.8	9.4	9.7	10.1	10.3	10.3	10.9	11.4
67.5	7.9	8.5	8.7	9.1	9.3	9.3	9.8	10.2
90	7.5	8.1	8.3	8.7	8.8	8.9	9.3	9.8
112.5	7.6	8.1	8.3	8.7	8.8	8.8	9.3	9.7
135	8.0	8.6	8.8	9.3	9.4	9.5	10.0	10.7
157.5	8.7	9.4	9.6	10.1	10.3	10.3	11.0	11.8
180	9.7	10.3	10.5	11.0	11.1	11.2	11.7	12.3
202.5	10.4	11.0	11.2	11.7	11.8	11.9	12.5	13.1
225	10.8	11.4	11.6	12.0	12.1	12.2	12.9	13.1
247.5	11.1	11.8	12.0	12.5	12.6	12.7	13.5	13.7
270	11.5	12.4	12.7	13.2	13.4	13.4	14.0	14.0
292.5	11.9	12.8	13.1	13.8	14.0	14.1	14.7	14.8
315	12.0	13.1	13.5	14.2	14.5	14.6	15.3	15.4
337.5	12.2	13.3	13.7	14.4	14.6	14.7	15.5	15.6

6.2.5 Extreme maximum wave crest, C_{max}

The extreme maximum wave crests, C_{max}, were derived based on the Forristall short-term wave height distribution (given in Section 1.3 in Appendix C: T-EVA – Traditional EVA). The choice of the short-term distribution is discussed and justified in Section 6.2.1 of DHI [1].

The maximum wave crest is given relative to still water level, $C_{max,SWL}$, and relative to mean sea level, $C_{max,SWL}$. The latter, $C_{max,MSL}$, is derived by convoluting the short-term distribution with the simultaneous (residual) water level.

The values of $C_{max, MSL}$ are provided for the construction completion (2033), and for the design lifetime end (2113) respectively. Following Part A, [1], an estimated sea level rise (SLR) of 0.8 m was added to the estimate of 2033 relative to the vertical reference (MSL) of today.

Table 6.11 presents the directional extreme $C_{max,SWL}$, while Table 6.12 and Table 6.13 presents the directional extreme $C_{max,MSL}$ for 2033 (construction complete) and 2113 (end of lifetime). The directional extreme values are scaled according to DNV-RP-C205, [3].

The values have been truncated to account for wave breaking in accordance with Section 6.2.6.

Table 6.11 Extreme maximum wave crest relative to SWL, $C_{max,SWL}$ at EINS-2

Extreme maximum wave crest relative to SWL, $C_{max,SWL}$ [mSWL]								
	Return Period, T_R [years]							
MWD [°N-from]	1	5	10	50	80	100	1,000	10,000
Omni	9.7	12.1	13.1	15.3	16.0	16.3	19.2	19.9
0	6.3	8.0	8.7	10.1	10.6	10.8	13.0	15.4
22.5	6.0	7.4	7.9	9.2	9.6	9.7	11.4	13.2
45	6.2	7.4	7.9	9.0	9.3	9.4	10.9	12.5
67.5	5.5	6.7	7.2	8.2	8.5	8.6	9.9	11.3
90	5.3	6.4	6.9	7.8	8.1	8.2	9.4	10.9
112.5	5.5	6.6	7.0	7.9	8.1	8.3	9.7	11.1
135	5.9	7.0	7.4	8.4	8.6	8.8	10.3	12.0
157.5	6.6	7.8	8.2	9.3	9.6	9.8	11.5	13.6
180	7.5	8.9	9.4	10.5	11.0	11.1	12.8	14.8
202.5	8.7	10.1	10.7	12.0	12.4	12.6	14.4	16.7
225	9.2	10.7	11.3	12.7	13.2	13.4	15.4	18.0
247.5	9.7	11.4	12.1	13.7	14.0	14.2	18.8	19.4
270	9.7	12.1	13.0	14.9	15.4	15.7	19.2	19.4
292.5	9.7	12.1	13.1	15.3	16.0	16.3	19.2	19.9
315	9.7	12.1	13.1	15.3	16.0	16.3	19.2	19.9
337.5	9.7	12.1	13.1	15.3	16.0	16.3	19.2	19.9

Table 6.12 Extreme maximum wave crest relative to MSL – in 2033 (construction complete), at EINS-2

$C_{max,MSL}$ – 2033 [mMSL]	Return Period, T_R [years]							
MWD [°N-from]	1	5	10	50	80	100	1,000	10,000
Omni	10.3	12.9	13.9	16.3	17.0	17.3	20.3	20.4
0	6.5	8.4	9.2	10.8	11.4	11.6	14.1	16.3
22.5	5.9	7.3	7.9	9.2	9.6	9.7	11.4	13.3
45	6.0	7.2	7.7	8.8	9.1	9.2	10.7	12.4
67.5	5.2	6.3	6.8	7.8	8.1	8.2	9.5	10.8
90	5.0	6.1	6.5	7.4	7.8	7.9	9.0	10.5
112.5	5.2	6.2	6.7	7.6	7.8	8.0	9.3	10.7
135	5.7	6.8	7.3	8.2	8.5	8.6	10.1	12.0
157.5	6.6	7.8	8.4	9.5	9.8	10.0	11.7	14.0
180	7.8	9.2	9.8	11.0	11.4	11.6	13.2	15.2
202.5	9.1	10.6	11.2	12.6	13.0	13.2	15.0	17.3
225	9.8	11.3	11.9	13.3	13.9	14.1	16.0	18.7
247.5	10.3	12.1	12.8	14.4	14.7	15.0	19.2	19.8
270	10.3	12.9	13.9	15.8	16.3	16.5	19.8	19.9
292.5	10.3	12.9	13.9	16.3	17.0	17.3	20.1	20.4
315	10.3	12.9	13.9	16.3	17.0	17.3	20.3	20.4
337.5	10.3	12.9	13.9	16.3	17.0	17.3	20.3	20.4

Table 6.13 Extreme maximum wave crest relative to MSL – in 2113 (end of lifetime) at EINS-2.

$C_{max,MSL}$ – 2113 [mMSL]	Return Period, T_R [years]							
MWD [°N-from]	1	5	10	50	80	100	1,000	10,000
Omni	11.1	13.7	14.7	17.1	17.8	18.1	21.1	21.2
0	7.3	9.2	10.0	11.6	12.2	12.4	14.9	17.1
22.5	6.7	8.1	8.7	10.0	10.4	10.5	12.2	14.1
45	6.8	8.0	8.5	9.6	9.9	10.0	11.5	13.2
67.5	6.0	7.1	7.6	8.6	8.9	9.0	10.3	11.6
90	5.8	6.9	7.3	8.2	8.6	8.7	9.8	11.3
112.5	6.0	7.0	7.5	8.4	8.6	8.8	10.1	11.5
135	6.5	7.6	8.1	9.0	9.3	9.4	10.9	12.8
157.5	7.4	8.6	9.2	10.3	10.6	10.8	12.5	14.8
180	8.6	10.0	10.6	11.8	12.2	12.4	14.0	16.0
202.5	9.9	11.4	12.0	13.4	13.8	14.0	15.8	18.1
225	10.6	12.1	12.7	14.1	14.7	14.9	16.8	19.5
247.5	11.1	12.9	13.6	15.2	15.5	15.8	20.0	20.6
270	11.1	13.7	14.7	16.6	17.1	17.3	20.6	20.7
292.5	11.1	13.7	14.7	17.1	17.8	18.1	20.9	21.2
315	11.1	13.7	14.7	17.1	17.8	18.1	21.1	21.2
337.5	11.1	13.7	14.7	17.1	17.8	18.1	21.1	21.2

6.2.6 Wave breaking and limitations

The extreme H_{max} (Table 6.9) and C_{max} (Table 6.11) were derived following the Glukhovskiy and the Forristall short-term distributions respectively. The extreme distribution of H_{m0} (see Figure 6.20) did not indicate any upper limit. However, in practice, the highest waves are limited by the wave height to water depth ratio or wave steepness (height to length ratio). The water depth and wave periods of extreme sea states at EINS are such that shoaling is non-negligible. This means that the average wave steepness will increase and consequently that the probability of wave breaking will increase.

This section aims to address the occurrence/likelihood of wave breaking and to quantify the limiting individual wave height and wave crest conditions. This is sought by evaluating the magnitude and range of the individual wave period conditioned on H_{max}, T_{Hmax}, and by visiting the below common wave breaking criteria, followed by final recommendations on wave breaking and limitations.

- DNV RP-C205, [3] – Steepness-induced breaking (regular waves)
- DNV RP-C205, [3] – Depth-induced breaking (shallow water)
- Fenton, [17, 18] – Stream Function (monochromatic wave on a flat seabed)
- Paulsen, [19] – Steepness and non-linear crest height to water depth ratio

Individual wave period conditioned on H_{max}, T_{Hmax}

The individual wave period conditioned on H_{max}, T_{Hmax}, is fundamental for the steepness-induced breaking. The period will vary because of varying sea state characteristics (variability of T_p given H_{m0}) but also because of the randomness of the sea state itself. The variability of T_{Hmax} against H_{max} is assessed, using the following three approaches/datasets, and comparing to DNV RP-C205.

1. Figure 6.32: Scatter plot of measured T_{Hmax} vs. H_{max} at EINS-Island (Mini 1), and fit to values above $H_{max,95\%}$.
2. Figure 6.33: The most probable period, J-EVA (linear new wave, see Section 15.5.1) at EINS-3 (close to EINS Island measurements).
3. Figure 6.34: Linear simulations of the surface elevation based on modelled spectra and zero-crossing at EINS-3.

According to Section 3.7.4 in DNV RP-C205, [3], the most probable T_{Hmax} to be used in conjunction with long term extreme wave height H_{max}, may be taken as given by Eq. (6.4), or alternatively Eq. (6.5). T_{Hmax} used in conjunction with H_{100} should be varied in the range given by Eq. (6.6).

$$T_{Hmax} = 0.9 \cdot T_p \qquad \textbf{(6.4)}$$

$$T_{Hmax} = a \cdot H_{max}^{b} \qquad \textbf{(6.5)}$$

where a and b are empirical coefficients. For the southern part of the Norwegian Continental Shelf, a = 2.94, and b = 0.5 may be applied.

$$2.55 \cdot \sqrt{H_{100}} \leq T_{Hmax} \leq 3.32 \cdot \sqrt{H_{100}} \qquad \textbf{(6.6)}$$

Where H_{100} is the 100-year individual wave height, $H_{max,100yr}$

The highest measured individual wave was during storm Malik with H_{max} of 19 m and T_{Hmax} of 14.6 s, see Figure 6.31 (left). The second highest measured wave had H_{max} of 17 m and T_{Hmax} of 14.3 s on 2021-12-01, but it is likely an erroneous recording, and was removed from the analysis, see Figure 6.31 (right).

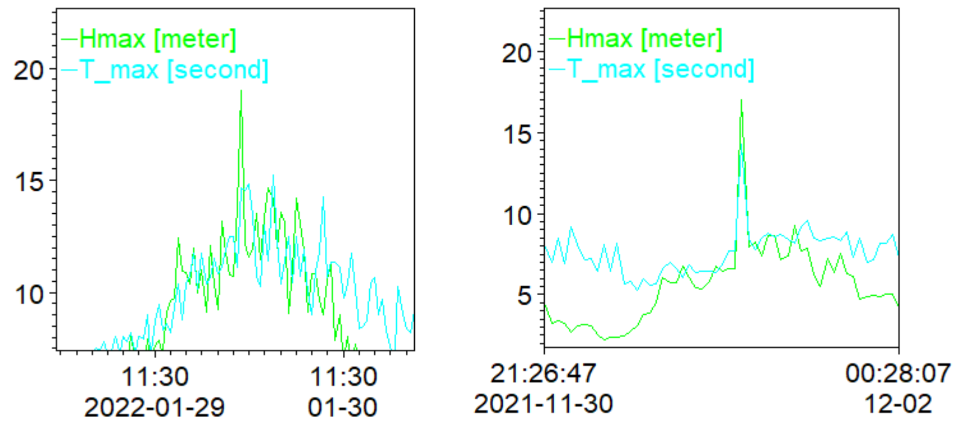

Figure 6.31 Time series of the two highest measured H_{max} (and T_{Hmax}). Left: Storm Malik. Right: is Likely an erroneous recording.

The above approaches were evaluated using the 50%-tile $T_{p|Hm0,100yr}$ = 15.7 s and $H_{max,100yr}$ = 18.8 m as estimated at EINS-3, the analysis point close to EINS Island (shown by orange lines in Figure 6.32 to Figure 6.34).

The results show a very good agreement between the measured and the most probable (J-EVA) $T_{Hmax,100yr}$. Eq. (6.4) (DNV by T_p) gives higher $T_{Hmax,100yr}$, while Eq. (6.5) (DNV by H_{max}) gives lower $T_{Hmax,100yr}$ for EINS-3:

- Eq. (6.4) (DNV by T_p): T_{Hmax} = 14.1 s
- Eq. (6.5) (DNV by H_{max}): T_{Hmax} = 12.7 s
- Eq. (6.6) (DNV range): T_{Hmax} = [11.1 – 14.4] s
- Figure 6.32 (**based on measured fit**): **T_{Hmax} = 13.7 s**
- Figure 6.33 (**most probable, J-EVA**): **T_{Hmax} = 13.3 s**
- Figure 6.34 (from modelled spectra): T_{Hmax} = 12.9 s

All the central estimates are within the DNV range given by Eq. (6.6), but the range of the 2.5 and 97.5%-tiles of the most probable (J-EVA) T_{Hmax} and the 2.5 and 97.5%-tiles of the measurements are both larger than the DNV range.

The DNV range is ±1.7 s (i.e. a factor 3.32/2.94 = 1.13), which agrees roughly with the corresponding ~87/13%-tiles of the measurements (Figure 6.32) and models (Figure 6.33). Such range (factor of 1.13) of the wave period could be an (upper bound) candidate as input to steepness-based breaking criteria.

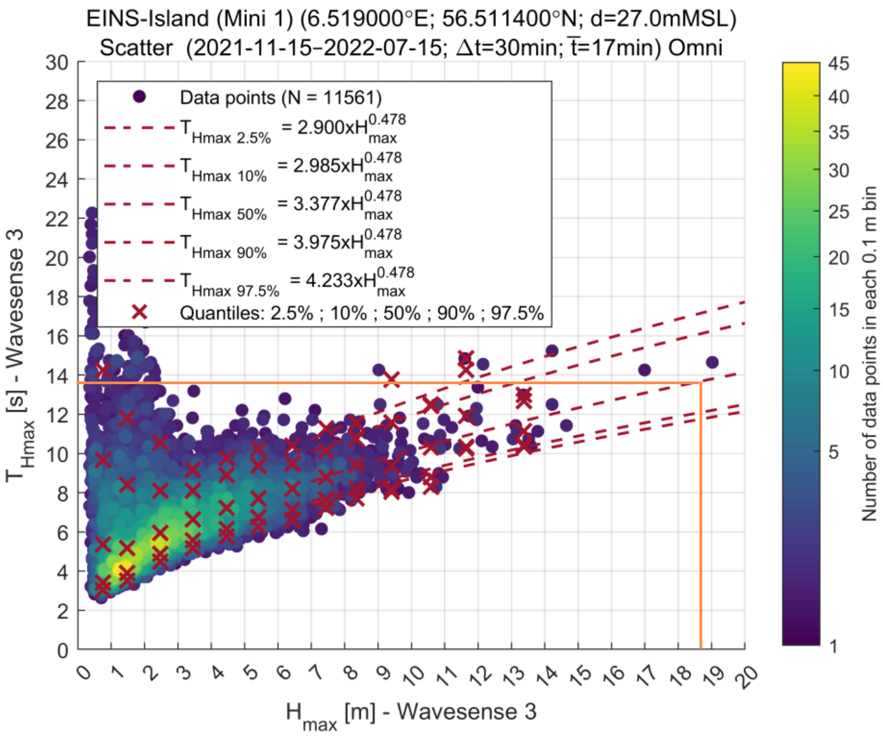

Figure 6.32 Scatter plot of measured T_{Hmax} vs. H_{max} at EINS-Island (Mini 1)
Orange line: $H_{max,100yr}$ = 18.8 m.

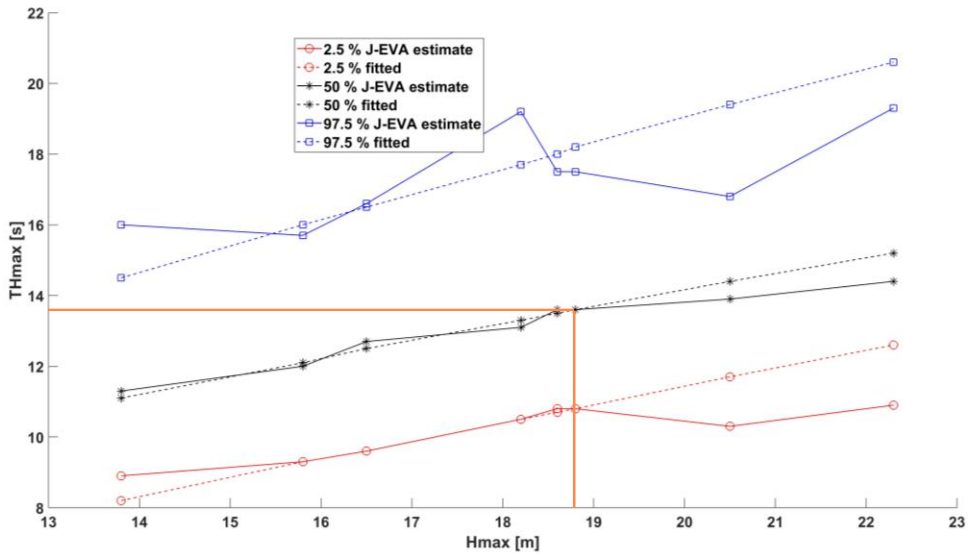

Figure 6.33 Omni T_{Hmax} conditioned on H_{max} at EINS-3 (from J-EVA)
Orange line: $H_{max,100yr}$ = 18.8 m.

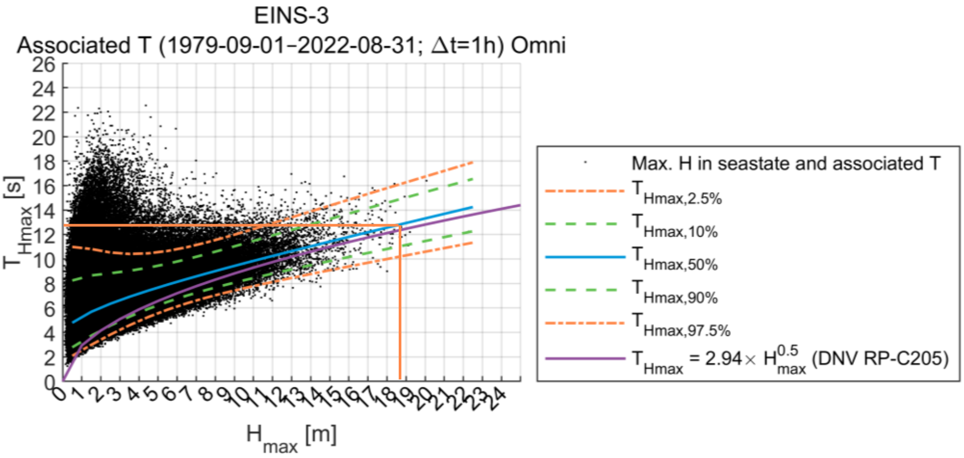

Figure 6.34 Scatter plot of modelled T_{Hmax} vs. H_{max} at EINS-3
Orange line: $H_{max,100yr}$ = 18.8 m.

DNV RP-C205, [3] – Steepness-induced breaking (regular waves)

A commonly adopted criterion for steepness-induced wave breaking limit is given in Section 3.4.6.1 of DNV RP-C205, [3], see Eq. (6.7) and Figure 6.35. This criterion is applicable to regular waves on a plane seabed.

However, the extreme waves at EINS are not regular, and it is well known that irregular and spread (short-crested) sea states can support higher waves; hence such a method should only be used with adequate mitigation measures.

$$\frac{H_b}{\lambda} = 0.142 \cdot \tanh\frac{2\pi d}{\lambda} \tag{6.7}$$

Where λ is the wavelength corresponding to water depth d. In deep water, the breaking wave limit corresponds to a maximum steepness of $S_{max} = H_b/\lambda = 1/7$.

DNV RP-C205, [3] – Depth-induced breaking (shallow water)

A common criterion for depth-induced wave breaking limit is given in Section 3.4.6.2 of DNV RP-C205, [3], and Section B4 in IEC-61400-3-1, [6], see Eq. (6.8) and Figure 6.35. This criterion is applicable in shallow water (d < 1/20 λ).

However, the water depths at EINS are not shallow according to the common definition of d < 1/20 λ, albeit the extreme waves will certainly 'feel' the seabed; hence such method should only be used for reference at EINS.

$$H_{max,lim} = 0.78 \cdot \mathrm{d} \tag{6.8}$$

A (potentially cautious) approach would be to use the 97.5%-tile of the conditioned water level to H_{m0}, $WL_{tot|Hm0,97.5\%}$, added to the water depth, d.

The wave crest in shallow water can be capped using the same criterion by anticipating a ratio of 0.85 between the wave crest and wave height (based on stream function, see Table 6.14).

Fenton, [17, 18] – Stream Function (monochromatic wave on a flat seabed)

In this section, Fenton's stream function theory was applied to quantify the limiting wave height (H_m), and wave crest (C_m), of a monochromatic wave given the total water depth (d) and the wavelength (λ) (or wave period), [17, 18], see Eq. (6.9). Using stream function theory means that C_m and H_m occur in the same individual wave, which is not necessarily the case in real sea states.

$$\frac{H_m}{d} = \frac{0.141063\,\frac{\lambda}{d} + 0.0095721\left(\frac{\lambda}{d}\right)^2 + 0.0077829\left(\frac{\lambda}{d}\right)^3}{1 + 0.0788340\,\frac{\lambda}{d} + 0.0317567\left(\frac{\lambda}{d}\right)^2 + 0.0093407\left(\frac{\lambda}{d}\right)^3} \tag{6.9}$$

Figure 6.35 shows common limiting wave heights of regular wave theory, along with that of stream function; the figure is adopted from IEC-61400-3-1, [6].

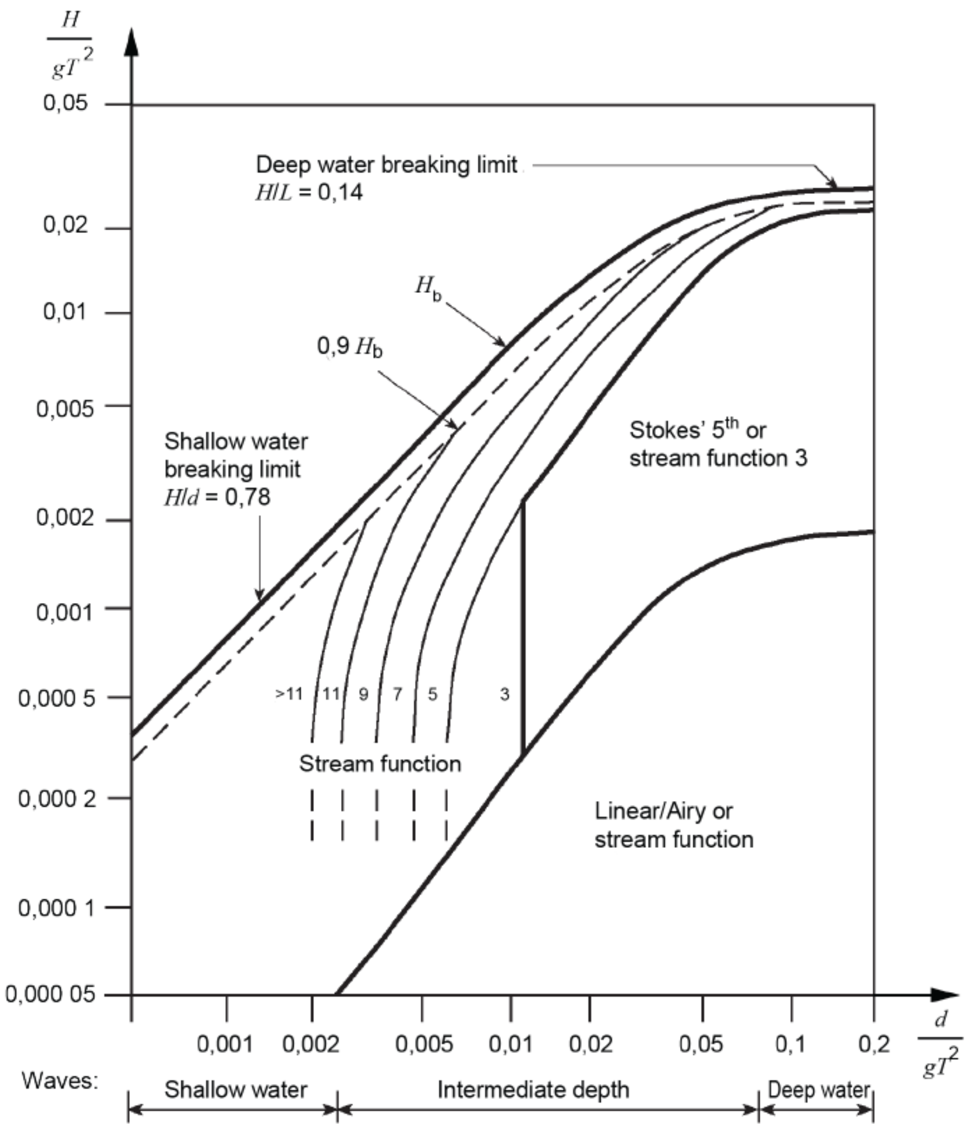

Figure 6.35 Limiting wave heights of regular wave theory; from [6]

The water depth is taken as the mean water depth plus the 97.5%-tile of the total water level conditional on H_{m0} ($WL_{tot|Hm0,97.5\%}$), and the wave period is taken as the 97.5%-tile wave period conditional on H_{max} ($T_{Hmax,97.5\%}$). These inputs are conservative in the sense that lower values (shallower water or shorter wave period) would lead to lower limiting wave height. Figure 6.36 shows the limiting (10.000-yr) stream function wave at EINS-2.

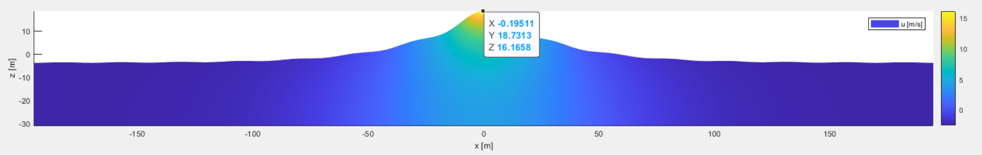

Figure 6.36 Limiting (10.000-yr) stream function wave at EINS-2 (analysis point with highest H_{max}).

Table 6.14 summarises the limiting (10.000-yr) wave height (H_m) and wave crest (C_m) according to stream function at EINS-2 using the upper bound $WL_{tot|Hm0,97.5\%r}$ and $T_{Hmax,97.5\%}$.

At EINS, the stream function suggests a limiting wave height and wave crest in between the estimated 100 and 1.000-yr H_{max} and C_{max} values. This means that according to stream function theory, the estimated 1,000-yr H_{max} and C_{max} cannot exist, and it can be argued that the H_{max} and C_{max} values for this and higher return periods may be reduced.

However, it is noted that while stream function can represent very non-linear (steep) waves, it does not account for directional spreading, opposing current or uneven wave shape (the wave front being steeper than the back of the wave). Directional spreading can lead to higher waves (compared to unidirectional waves), and thus a stream function wave cannot be considered an ultimate upper limit. Nevertheless, it is very rare that those values would be exceeded, considering the rather conservative input of the 97.5%-tile conditional water level and wave period,

In practical engineering applications, directional spreading is sometimes compensated for by the use of a ‘directional spreading factor’ (to compensate for not all energy of the wave spectrum travelling in the same direction).

Table 6.14 Limiting wave and crest of stream function conditioned on 97.5%-tile – 10,000-year

Name	d [mMSL]	$WL_{tot\|Hm0,97.5\%}$ [mMSL]	$T_{Hmax,97.5\%}$ [s]	$H_{max,Glukhoskiy}$ [m]	H_m [m]	$C_{max,Forristall}$ [mSWL]	C_m [mSWL]
EINS-1	26.6	1.9	20.5	22.2	**20.5**	17.8	**17.3**
EINS-2	29.1	1.8	21.0	24.1	**22.2**	19.3	**18.7**
EINS-3	28.9	1.8	18.2	22.9	**21.6**	18.2	**17.7**
EINS-4	30.1	1.9	18.9	24.4	**22.5**	20.0	**18.4**
EINS-5	29.8	2.1	20.3	24.9	**22.8**	19.9	**19.1**

Paulsen, [19] – Steepness and non-linear crest height to water depth ratio

An alternative method of estimating the breaking (probability) is given by Paulsen et.al., [19]. They quantify the probability that a random wave in a sea state is breaking via the sea state steepness and the non-linear crest height to water depth ratio.

The sea state steepness is calculated based on the linear dispersion relation, T_{01}, and H_{m0} as $R = k_{01}H_{m0}$, and the wave is breaking when the non-linear crest height exceeds a limit α given by Eq. (6.10).

$$\alpha = \min\left(\frac{\beta_0\left(1+\frac{1}{2}\beta_0\right)}{k_{01}}, \alpha_0 h\right)$$

$$\beta_0 \in [0.3; 0.5] \tag{6.10}$$

$$\alpha_0 = 0.4$$

h is the water depth, including tide and surge

Figure 6.37 compares this non-breaking wave crest criterion to the extreme wave crests at a location in the North Sea of similar water depth to EINS (~26 mMSL). The figure shows the Forristall crest to still water level, η, against the significant wave height, H_{m0} (grey line) for return periods of 1 to 10,000 years.

This is compared to the depth-limited crest ($0.4 \times h$), Eq. (6.10), at which all crests are assumed to break (blue line). The slight increase in increasing H_{m0} is caused by the increase in surge for the increasing return period. It is observed that waves with crests above ~11 m are breaking based on this criterion.

The green and orange lines show the limits of the steepness-based criterion. The wave crests lie in between these limits but approach the upper limit for an increasing return period. This is because the steepness of the sea state is increasing for an increasing return period. This assessment supports that breaking is to be expected at the EINS site.

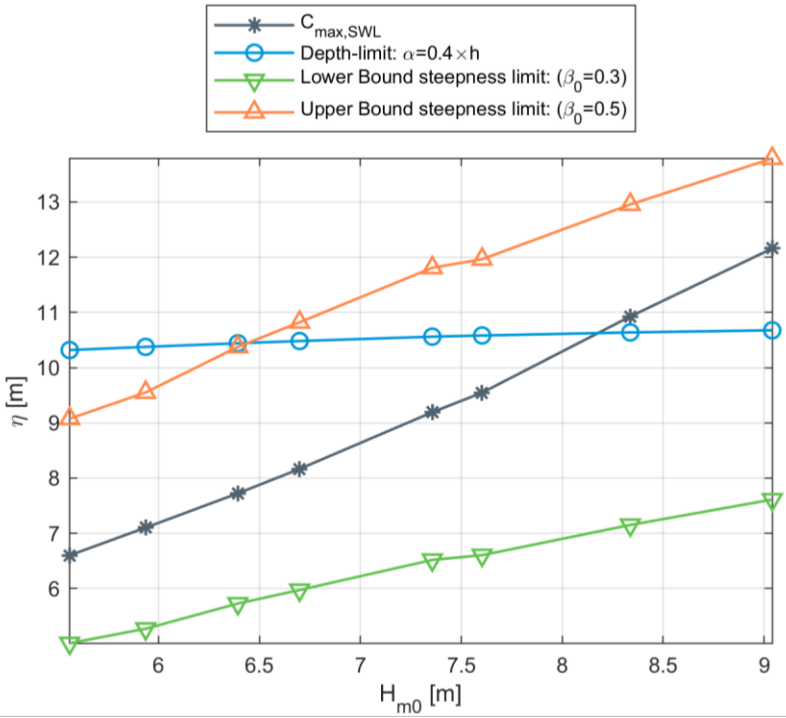

Figure 6.37 Maximum non-breaking crest height according to Paulsen et.al., [19], compared to the wave crests at a location in the North Sea

Recommendations on wave breaking

All the wave breaking, limitation and probability approaches described above are prone to some general simplifications and somewhat crude assumptions about individual waves in extreme sea states. However, there is consensus that the higher waves will break, and as such it is recommended that wave breaking, and related loads, are accounted for in the design of EINS.

Concerning breaker type, we do not recommend following the procedure outlined in e.g. IEC-61400-3-1 Annex B, [6]. This approach classifies wave breaking type as function of seabed slope and wave steepness. For most offshore sites in the North Sea, this will classify breaking waves as spilling, and no additional load to that of stream function theory would be accounted for.

Recommendations on wave limitations

The comparison of measured and modelled relations between H_{max} and T_{Hmax} demonstrated a very good agreement, and it showed that the estimated individual wave periods at EINS are in line with the local measurements.

Several of the wave limitation approaches suggest that the extreme sea states are prone to steepness- or depth-induced wave breaking. The former is dependent on which quantile of the wave period one considers. The DNV range for the 100-year return period, Eq. (6.6), corresponds to a factor of 1.13 times the central value of T_{Hmax}, which is thus a candidate for such range.

In conclusion, it is recommended to use the DNV steepness criteria, Eq. (6.7), with 1.13 times $T_{Hmax,50\%}$, and $WL_{Hm0,50\%}$ as input, to limit H_{max}. And to limit C_{max} accordingly using a ratio of 0.85 between the wave crest and the wave height.

Table 6.15 presents the recommended limits to H_{max} and C_{max} for 10.000 years. The limiting H_{max} is higher than those of the stream function, but slightly lower than those of the DNV shallow water criteria, Eq. (6.8) for 10,000-years. The limiting values are in between the 100- and 1,000-year return period values.

It is noted that neither regular wave theory nor stream function accounts for directional spreading etc., which can lead to higher waves. However, using the steepness criteria with an upper bound T_{Hmax} is considered an optimised and pragmatic, but still safe, approach for the individual extreme waves at EINS.

Table 6.15 Recommended limits to H_{max} and C_{max} based on DNV steepness criteria, Eq. (6.7), with upper bound (UB) as 1.13 times the 50%-tile T_{Hmax}, and the 50%-tile $WL_{|Hm0}$ – 10,000-year
Using a ratio of 0.85 between the C_{max} and H_{max} (based on stream function, see Table 6.14).

Name	d [mMSL]	$WL_{Hm0,50\%}$ [mMSL]	1.13 × $T_{Hmax,50\%}$ [s]	$H_{max,Glukhovskiy}$ [m]	$H_{b,Steepness,UB}$ [m]	$H_{b,Shallow,97.5\%}$ [m] (=0.78 x WL)	$C_{b,Steepness,UB}$ [m] (=0.85 x H_b)
EINS-1	26.6	1.2	17.9	22.2	**22.0**	22.2	**18.7**
EINS-2	29.1	1.2	17.5	24.1	**23.6**	24.1	**20.1**
EINS-3	28.9	1.1	16.4	22.9	**22.9**	23.9	**19.5**
EINS-4	30.1	1.2	17.2	24.4	**24.1**	24.9	**20.5**
EINS-5	29.8	1.2	17.9	24.9	**24.2**	24.9	**20.6**

7 Other Atmospheric Conditions

This section presents analyses of other atmospheric conditions than wind.

Other atmospheric conditions concern rainfall, air temperature, humidity, solar radiation, lightning, and visibility.

7.1 Rainfall

7.1.1 Data

Rainfall intensity-duration-frequency (IDF) curves were estimated based on the ERA5 1-hour resolution time series resampled over different durations (2, 3, 6, 12 and 24 hours) using a moving average procedure. The rainfall analysis was based on the six time series, referred to as 1h, 2h, 3h, 6h, 12h and 24h rainfall depths (measured in [mm]) and rainfall intensities (measured in [mm/h]), cf. Section 7.1 of Part A, [1].

7.1.2 Methodology

The rainfall time series data were analysed to provide estimates of rainfall intensities of 10 min duration for return periods of 1, 5, 10, 50, 80 and 100 years. In addition, Chicago design storms (CDS) were derived for return periods of 5 and 100 years.

The methodology applied includes the following steps:

1. Estimation of extreme rainfall depths for the six (6) durations based on the ERA5 rainfall time series data.
2. Area correction of the extreme rainfall statistics.
3. Estimation of IDF curves covering durations from 10 min to 24 hours.
4. Determination of CDS based on the estimated IDF curves.

For estimation of extreme rainfall statistics, a partial durations series approach was applied following the methodology used for estimation of the regional extreme rainfall model in Denmark [20, 21]. The extreme value series was defined by extracting the most extreme rainfall events of the 44-year record, corresponding to 3 events on average per year (i.e., the 132 largest events on record). A generalised Pareto distribution was fitted to the extreme value data series. The generalised Pareto distribution includes the exponential distribution as a special case, corresponding to a shape parameter equal to zero.

The extreme rainfall statistics estimated from the ERA5 data represent a spatial scale corresponding to the ERA5 grid cell size, i.e., approximately 900 km^2. Since rainfall is not uniform, especially for extreme events, the extreme rainfall statistics over a large area is smaller than the statistics over a small area. Areal reduction factors (ARF) have been introduced for scaling extreme rainfall statistics from a point to an area. The ARF is defined as:

$$ARF = \frac{Rainfall\ depth\ over\ an\ area}{Rainfall\ depth\ at\ a\ point} \tag{7.1}$$

The ARF depends on the rainfall duration with smaller ARFs for smaller durations. To estimate extreme rainfall statistics representative for the energy island the rainfall intensities were corrected by dividing the statistics from the ERA5 time series with ARFs.

ARFs have been estimated for Denmark but focus on design rainfall estimates for urban drainage systems with areas less than 50-100 km^2, [22, 23].[22, 23]. For correction of ERA5 based rainfall statistics, instead ARFs derived for the UK published in the Flood Studies Report [24] were applied. ARFs from the UK Flood Studies Report applied to the different durations are shown in Table 7.1.

Table 7.1 ARFs applied for correction of estimated extreme value statistics based on ERA5 rainfall data

Duration [h]	ARF
1	0.62
2	0.73
3	0.78
6	0.83
12	0.85
24	0.89

To extrapolate extreme rainfall statistics below 1 hour, an IDF curve was estimated using the same IDF model as applied in the Danish design rainfall guideline [25]:

$$i_T(d) = \alpha(d+\theta)^{-\nu} \quad (7.2)$$

where $i_T(d)$ is the rainfall intensity for duration *d* and return period *T*. The parameters α, θ and ν are estimated from the rainfall statistics for durations 1h-24h.

The CDS was originally proposed by Keifer and Chu (1957) [26]. Here the discrete version of the CDS as used in the Danish design rainfall guideline [25] was applied. The CDS is determined by defining a storm duration and an asymmetry coefficient that determines the shape of the storm. Two different shapes of the CDS were applied, respectively, a symmetric storm (corresponding to an asymmetry coefficient of 0.5) and a storm with an asymmetry coefficient that describes the most extreme rainfall events on record.

7.1.3 Results

The choice of extreme value distribution should balance model bias and sampling uncertainty of the estimated quantiles. Distributions with more parameters will, in general, decrease model error but at the expense of an increase in sampling uncertainty. Studies have shown that the 1-parameter exponential distribution is preferable for moderately long-tailed distributions where the slightly better fit of the 2-parameter generalised Pareto distribution cannot be justified due to its larger sampling uncertainty, cf. [27].

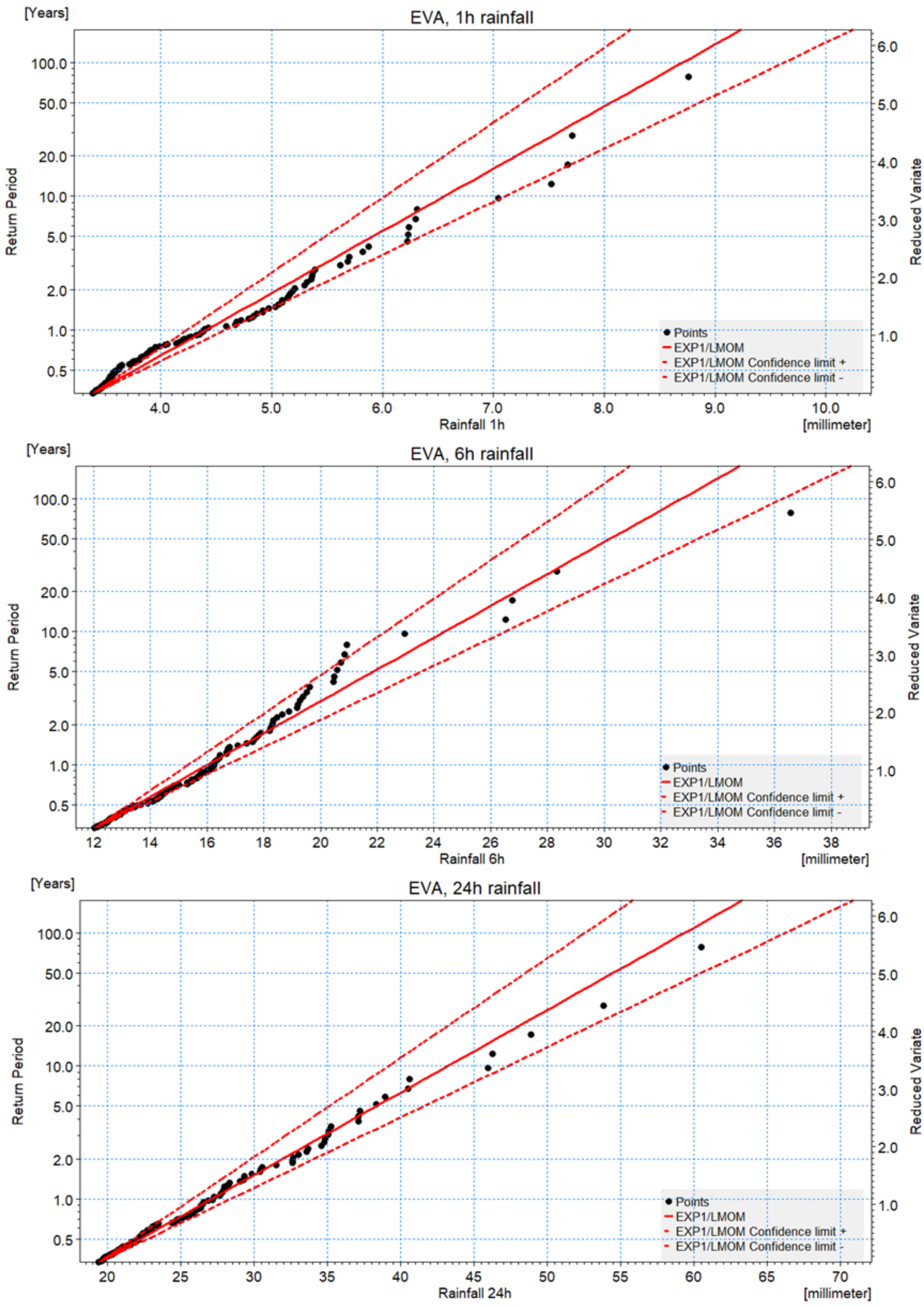

Figure 7.1 **Estimated extreme value distribution (full red line) and corresponding 95% confidence interval (dotted red line) compared to ERA5 rainfall depths (black dots) for 1h, 6h and 24h durations**

Analysis of the partial duration series of rainfall depths shows that for all 6 durations the exponential distribution is preferable compared to the generalised Pareto distribution considering the balance between model error and sampling uncertainty. In Figure 7.1 the estimated distributions are compared to the ERA5 extreme rainfall depths for the 1h, 6h and 24h durations. Estimated rainfall depths and associated sampling uncertainties in terms of standard deviation are shown in Table 7.2 for different return periods.

Table 7.2 Estimated rainfall depths and standard deviations for different durations and return periods

	Duration = 1h		Duration = 2h		Duration = 3h	
Return period [years]	Depth [mm]	St. dev. [mm]	Depth [mm]	St. dev. [mm]	Depth [mm]	St. dev. [mm]
1	4.41	0.09	7.81	0.15	10.59	0.21
5	5.91	0.22	10.45	0.38	14.15	0.51
10	6.56	0.27	11.59	0.48	15.68	0.64
50	8.06	0.40	14.23	0.70	19.25	0.95
80	8.50	0.44	15.00	0.77	20.29	1.04
100	8.71	0.46	15.37	0.80	20.78	1.08

	Duration = 6h		Duration = 12h		Duration = 24h	
Return period [years]	Depth [mm]	St. dev. [mm]	Depth [mm]	St. dev. [mm]	Depth [mm]	St. dev. [mm]
1	16.03	0.34	21.62	0.51	27.09	0.66
5	21.86	0.84	30.34	1.25	38.36	1.62
10	24.38	1.05	34.10	1.58	43.21	2.04
50	30.21	1.55	42.82	2.32	54.48	3.00
80	31.92	1.70	45.36	2.54	57.77	3.28
100	32.73	1.77	46.57	2.64	59.33	3.41

The IDF model Eq. **(7.2)** provides a good fit to the area-corrected rainfall intensities for the six return periods considered. In Figure 7.2 the ERA5 and area corrected estimates are shown together with the estimated IDF curve for return periods of 5 and 100 years. It should be noted that it is not possible to validate the extrapolation of the IDF curve to 10 min rainfall intensities. However, the applied IDF model has been shown to provide a good fit to extreme rainfall intensities in Denmark in the range 1 min – 48 hours duration [25]. Estimated parameters of the IDF curve are shown in Table 7.3. Estimated 10 min rainfall intensities for different return periods are shown in Table 7.4.

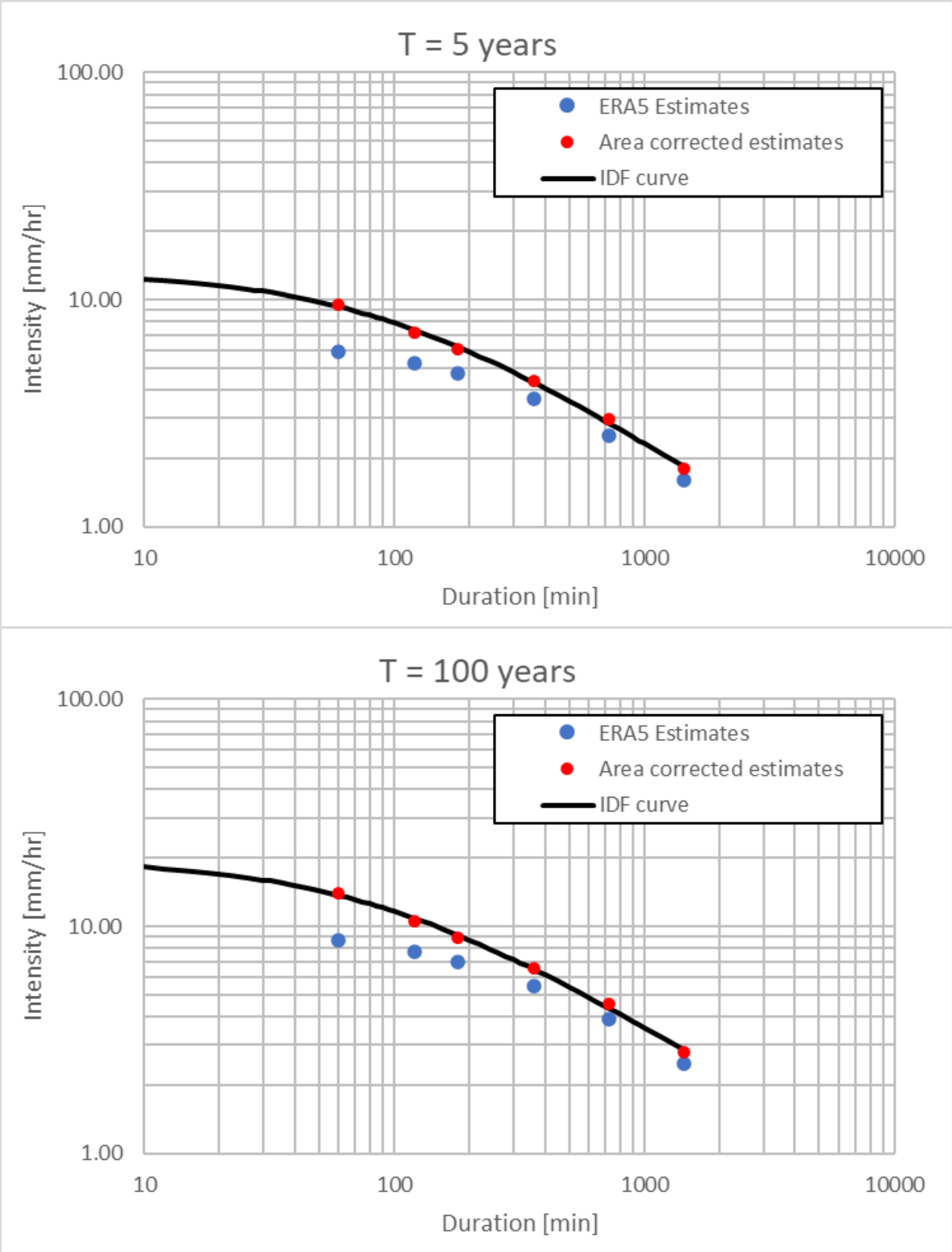

Figure 7.2 **ERA5 and area corrected estimates of rainfall intensities for 1h, 2h, 3h, 6h, 12h and 24h durations and estimated IDF curve for return periods of 5 and 100 years**

Table 7.3 Estimated IDF parameters for 5 and 100-year return periods

IDF parameter	T=5 years	T=100 years
α [mm/h]	313	362
θ [min]	91.0	82.2
υ [-]	0.701	0.661

Table 7.4 Estimated 10 min rainfall intensities for different return periods

Return period [years]	Intensity [mm/h]
1	9.20
5	12.3
10	13.7
50	16.7
80	17.8
100	18.2

The most extreme rainfall events on record were analysed to determine an asymmetry coefficient for the CDS that best describes the extreme rainfalls at the location. In Figure 7.3 are shown the 3 most extreme rainfall events from the ERA5 record normalised with respect to the maximum intensity and duration of the events. The most extreme events have shapes where the peak intensity occurs in the last 20-40% part of the event. The average asymmetry coefficient of the three events is 0.73.

For comparison, the most extreme observed event from EINS-North and EINS-South during the 6-month measurement campaign (see Part A) were analysed. The most extreme event occurred on 01-12-2021 with return periods of intensities ranging between 1 and 3 years at EINS-North and 0.33-2 years at EINS-South for durations between 1 and 12 hours. No other events above the 0.33 return period threshold were observed in the 6-month period.

The two observed events normalised with respect to the maximum intensity and duration of the events are shown in Figure 7.4. Note that the time series have a temporal resolution of 10 min as compared to the 1-hour resolution of ERA5. The event at EINS-North shows the same intensity characteristics as the ERA5 events and has an asymmetry coefficient of 0.75. The event at EINS-South does not have a well-defined single peak.

Based on the above results it is concluded that an asymmetry coefficient of 0.75 best represents the extreme rainfalls.

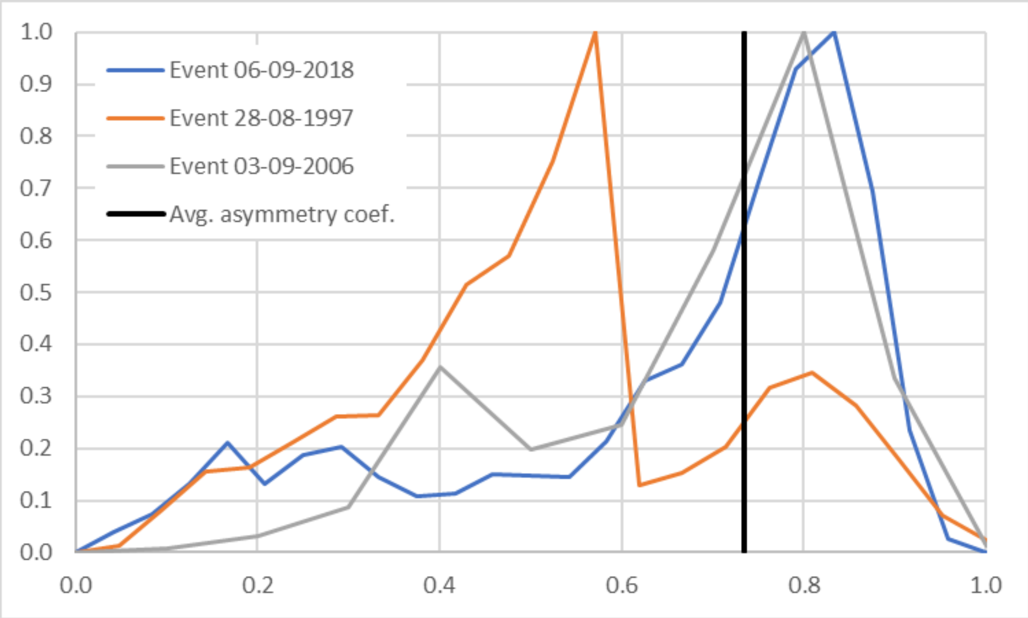

Figure 7.3 Selected extreme ERA5 rainfall events normalised with respect to maximum intensity and duration. The black line is the average asymmetry coefficient.

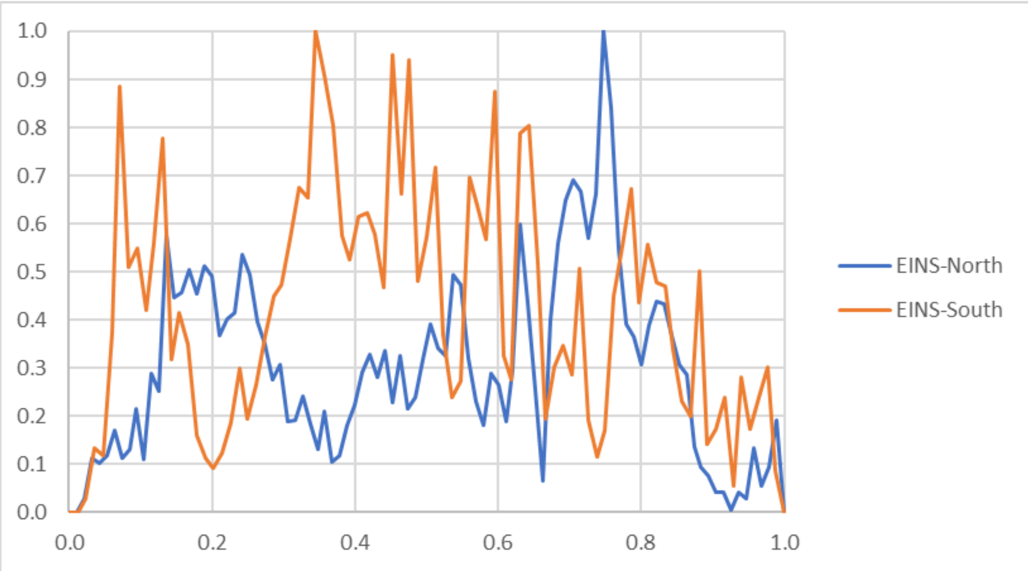

Figure 7.4 Most extreme events at EINS-North and EINS-South normalised with respect to maximum intensity and duration.

7.2 Air temperature, humidity, and solar radiation

Annual and monthly statistics of modelled air temperature at 2 m above sea level (asl), relative humidity and downward solar radiation, based on CFSR, cf. Section 7.2 of Part A, [1], at analysis point EINS-1 (shallowest) are illustrated in Figure 7.5. The results are summarised in Table 7.5 to Table 7.7.

There is a clear seasonal variation for all three variables. Air temperature, relative humidity and solar radiation are larger during the summer months and lower during the winter months. There is also a clear delay of around ~1 month between highest solar radiation and, air temperature and relative humidity.

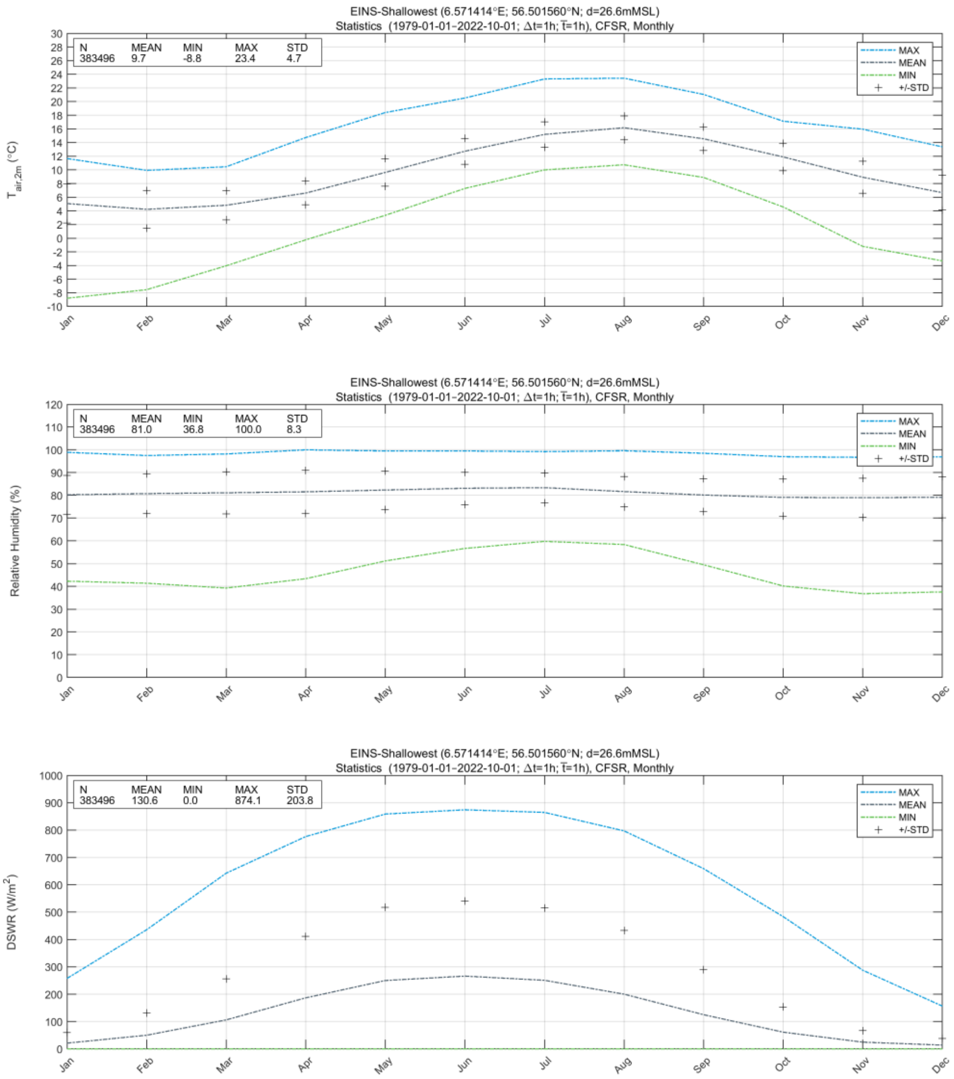

Figure 7.5 Monthly statistics of air temperature at 2 m asl (top), relative humidity (centre), and downward solar radiation (bottom) at EINS-1 (shallowest)

Table 7.5 Annual and monthly statistics for air temperature at 2 m asl at EINS-1 (shallowest) based on CFSR (1979-01-01 – 2022-10-01)

Air temperature at 2 m asl at EINS-1 (shallowest) [°C]						
Statistical		№ of data points	Mean	Min.	Max.	STD.
Annual		383,496	9.7	-8.8	23.4	4.7
Monthly	Jan.	32,735	5.1	-8.8	11.7	2.8
	Feb.	29,832	4.2	-7.5	9.9	2.7
	Mar.	32,736	4.8	-4.0	10.5	2.1
	Apr.	31,680	6.6	-0.2	14.7	1.8
	May	32,736	9.6	3.3	18.4	2.0
	Jun.	31,680	12.7	7.3	20.5	1.9
	Jul.	32,736	15.2	10.0	23.3	1.8
	Aug.	32,736	16.2	10.8	23.4	1.8
	Sep.	31,680	14.6	8.9	21.0	1.7
	Oct.	31,993	11.9	4.6	17.1	2.0
	Nov.	30,960	8.9	-1.2	16.0	2.4
	Dec.	31,992	6.7	-3.3	13.4	2.6

Table 7.6 Annual and monthly statistics for relative humidity at EINS-1 (shallowest) based on CFSR (1979-01-01 – 2022-10-01)

Relative humidity at EINS-1 (shallowest) [%]						
Statistical		№ of data points	Mean	Min.	Max.	STD.
Annual		383,496	81.0	36.8	100.0	8.3
Monthly	Jan.	32,735	80.3	42.3	98.9	8.6
	Feb.	29,832	80.8	41.4	97.5	8.7
	Mar.	32,736	81.1	39.3	98.2	9.3
	Apr.	31,680	81.6	43.4	100.0	9.5
	May	32,736	82.3	51.2	99.5	8.5
	Jun.	31,680	83.1	56.7	99.5	7.1
	Jul.	32,736	83.4	59.8	99.2	6.5
	Aug.	32,736	81.7	58.4	99.6	6.7
	Sep.	31,680	80.2	49.5	98.5	7.2
	Oct.	31,993	79.1	40.2	97.0	8.1
	Nov.	30,960	79.0	36.8	96.7	8.5
	Dec.	31,992	79.2	37.6	96.9	9.0

Table 7.7 **Annual and monthly statistics for downward solar radiation at EINS-1 (shallowest) based on CFSR (1979-01-01 – 2022-10-01)**

Downward solar radiation at EINS-1 (shallowest) [W/m²]						
Statistical		№ of data points	Mean	Min.	Max.	STD.
Annual		383,496	130.6	0.0	874.1	203.8
Monthly	Jan.	32,735	21.1	0.0	257.7	38.6
	Feb.	29,832	50.0	0.0	435.6	82.1
	Mar.	32,736	106.1	0.0	642.4	150.1
	Apr.	31,680	186.7	0.0	776.3	224.8
	May	32,736	250.1	0.0	858.6	267.9
	Jun.	31,680	266.1	0.0	874.1	274.5
	Jul.	32,736	250.8	0.0	864.5	265.2
	Aug.	32,736	200.1	0.0	797.0	232.1
	Sep.	31,680	125.0	0.0	658.8	165.4
	Oct.	31,993	61.1	0.0	483.4	93.0
	Nov.	30,960	24.7	0.0	287.4	43.2
	Dec.	31,992	13.9	0.0	156.4	24.9

7.3 Lightning

Lightning data was obtained from the LIS/OTD Gridded Climatology dataset [28] from NASA's Global Hydrology Resource Center (GHRC), cf. Section 7.4 of Part A, [1]. Table 7.8 summarises the statistics of the HRFC (High Resolution Full Climatology), HRMC (High Resolution Monthly Climatology) and LRMTS (Low Resolution Monthly Time Series) datasets for the whole EINS OWF. Figure 7.6 and Figure 7.7 show the monthly and yearly variation of flash rates, based on the HRMC and LRMTS datasets, respectively. It should be noted that both HRMC and LRMTS contain extensive smoothing (see [29] for further results).It should be noted that both HRMC and LRMTS contain extensive smoothing (see [29] for further results). Therefore, the values are different from the HRFC dataset (discussed in the paragraph above). The results from HRMC and LRMTS presented here are only shown to demonstrate the monthly and yearly variations, therefore, it is recommended to use the HRFC data set. Based on the HRFC data set the mean flash rate at the EINS OWF is 0.285 fl/(km^2 yr), i.e. 7.81e^{-4} fl/(km^2 day). As it can be seen from the figures, the flash rate in June and September is, on average, higher than in other months.

Table 7.8 **Statistics of flash rates at EINS**
HRFC dataset: Mean annual flash rate. HRMC: Mean flash rate in middle of each month, with monthly smoothing. LRMTS: Monthly time series of flash rate, with smoothing.

Data set	Units	Grid [°]	Max	Min	Mean
HRFC	fl/(km^2·year)	0.5	---	---	0.285
HRMC	fl/(km^2·day)	0.5	0.004	0.0	0.001
LRMTS	fl/(km^2·day)	2.5	0.005	0.0	0.002

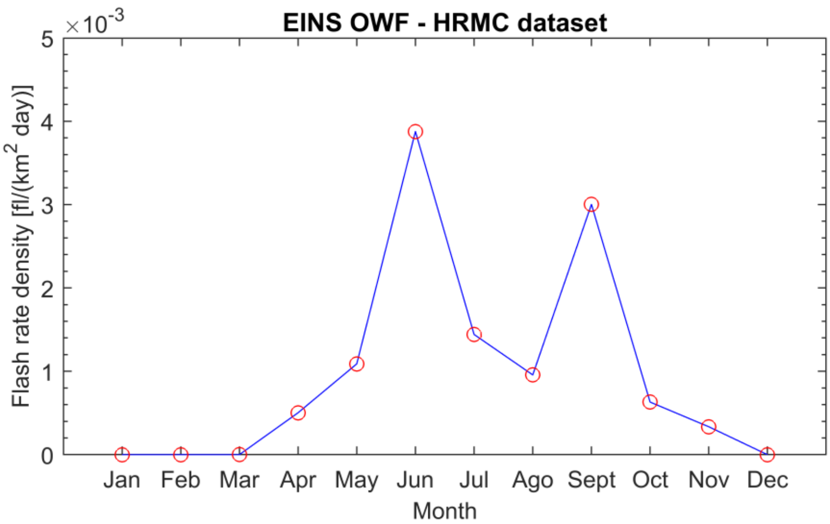

Figure 7.6 **Monthly variation of flash rate at EINS area based on HRMC data for the period July 1995 to February 2000**
Mean flash rate in middle of each month, with monthly smoothing

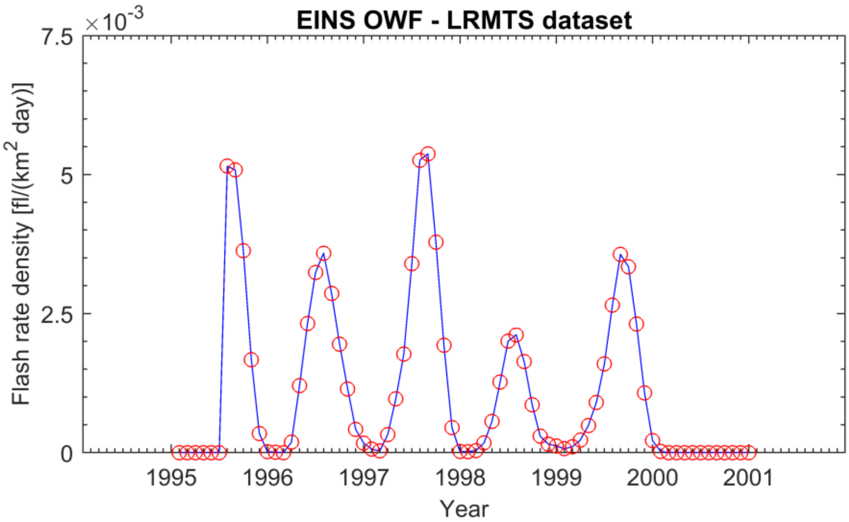

Figure 7.7 **Combined monthly time series of flash rates at EINS based on LRMTS data for the period July 1995 to February 2000**
Monthly time series of flash rate (weighted more toward LIS than other products)

7.4 Visibility

The visibility was derived from the air temperature at 2m height above sea surface, T_{2m}, and the relative humidity, RH, from CFSR, cf. Section 7.4 of Part A, [1], following the method described in [30], see (7.3). The dew point temperature, T_{dp}, was approximated using the Magnus formulae[3]. The visibility was capped at 50 km.

$$Visibility\ [\mathrm{km}] = 1.609 \times 6000 \times \frac{T_{2m} - T_{dp}}{RH^{1.75}} \tag{7.3}$$

Figure 7.8 shows time series of T_{2m}, RH and Visibility, and Figure 7.9 presents the probability of visibility at EINS-2. The visibility is most frequently between 4 and 20 km, with a 50%-tile of 12.8 km.

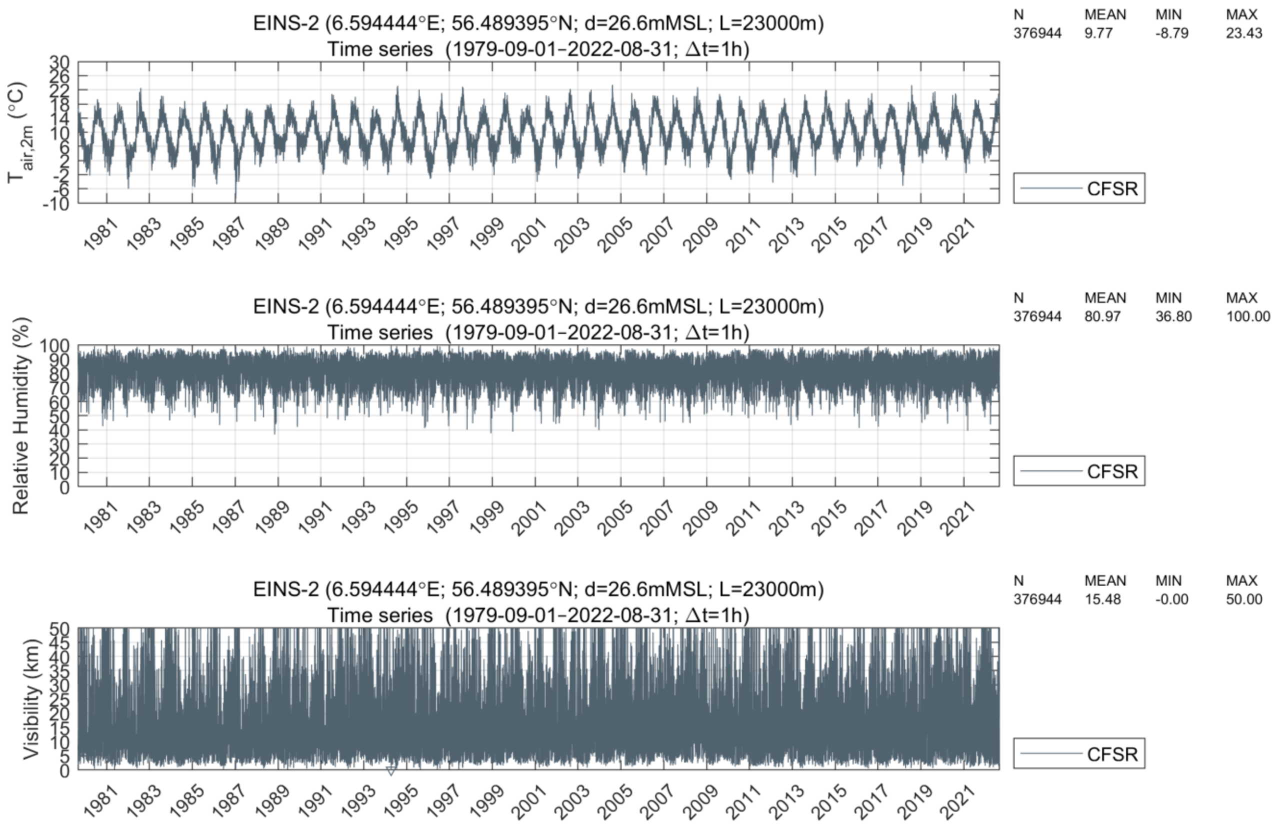

Figure 7.8 Time series of T_{2m}, RH and Visibility at EINS-2

[3] https://en.wikipedia.org/wiki/Dew_point

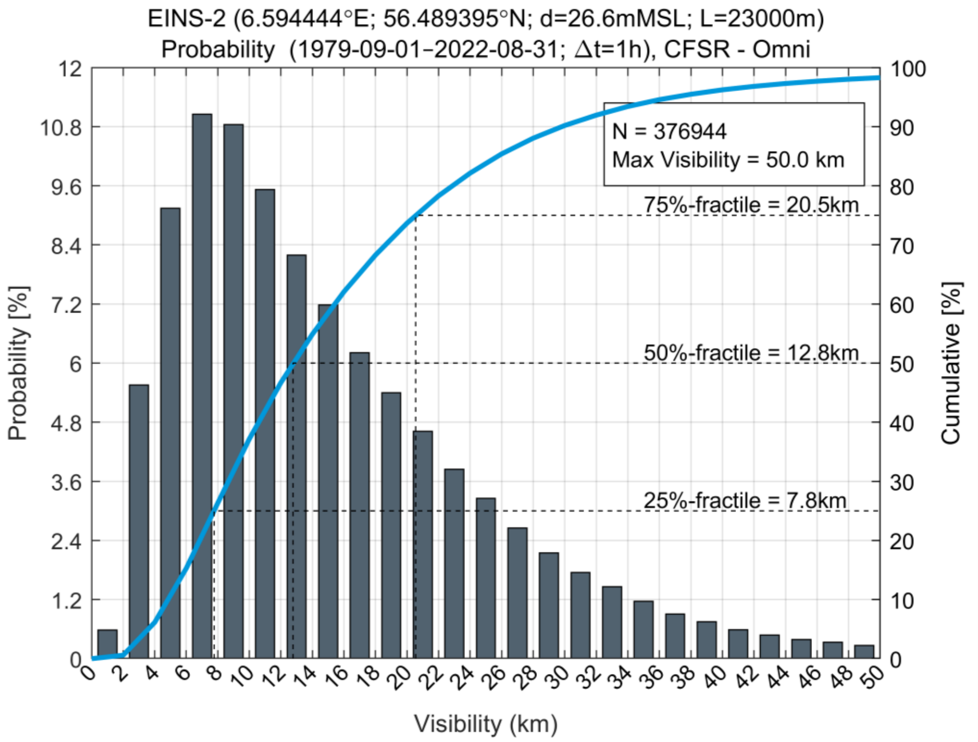

Figure 7.9 Probability of visibility at EINS-2

8 Other Oceanographic Conditions

This section presents analyses of other oceanographic conditions.

Other oceanographic conditions concern water temperature, salinity, and density, and marine growth.

8.1 Water temperature, salinity, and density

Information on the properties of seawater (temperature and salinity) was obtained from the HD_{UKNS3D} model described in Section 5.4 of Part A, [1]. Time series of seawater temperature and seawater salinity were extracted for the surface and near-seabed layer at four (4) locations: EINS-1 (shallowest), EINS-3 (max CS_{tot}), EINS-Island (Mini 2), and EINS-5 (South). The data cover a 10-year period (2013 to 2022) with a temporal resolution of 1-hour. Results of the analysis are presented only at the EINS-South location, where model outputs were validated. Results at the other stations are not produced since the variation in water temperature, salinity, and density across the site is limited.

Seawater temperature

Figure 8.1 presents the monthly statistics (mean, minimum, maximum, and standard deviation) of seawater temperature near the surface and near the seabed temperature at EINS-South. The statistics are summarised in for Table 8.1.

The seasonal variation in seawater temperature is clear at the surface with largest temperatures occurring in summer and early autumn (June to September) and the lowest temperatures during the winter and early spring (January to March). The monthly mean seawater temperatures at the surface are higher than those at the seabed for the entire year. The seasonal variation at the seabed is also clear but less pronounced. The highest temperatures occur during autumn and the lowest in spring, showing the delay in temperature changes over the depth.

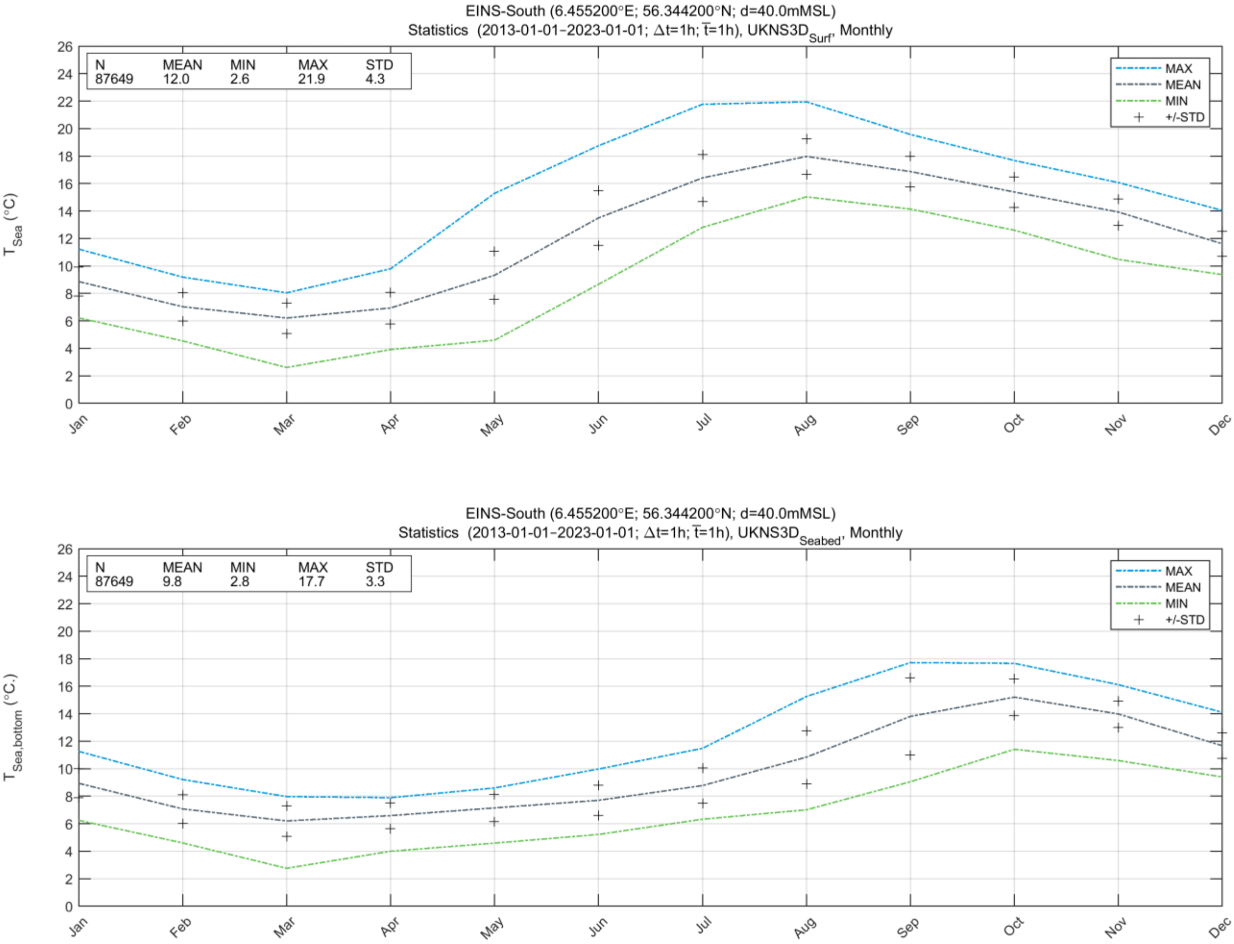

Figure 8.1 **Monthly statistics of surface (top panel) and bottom (bottom panel) seawater temperature at EINS-South**

Table 8.1 **Annual and monthly statistics for seawater temperature near the surface and near the seabed at EINS-South based on HD_{UKNS3D} (2013-01-01 to 2023-01-01)**
Near-surface and near-seabed data is extracted from top and bottom layers of HD_{UKNS3D}

Seawater temperature at EINS-South [°C] – Near-surface						
Statistical		№ of data points	Mean	Min.	Max.	STD.
Annual		87,649	12.0	2.6	21.9	4.3
Monthly	Jan.	7,441	8.9	6.2	11.2	1.0
	Feb.	6,768	7.0	4.5	9.2	1.0
	Mar.	7,440	6.2	2.6	8.0	1.1
	Apr.	7,200	6.9	3.9	9.8	1.1
	May	7,440	9.3	4.6	15.3	1.7
	Jun.	7,200	13.5	8.7	18.7	2.0
	Jul.	7,440	16.4	12.8	21.8	1.7
	Aug.	7,440	18.0	15.0	21.9	1.3
	Sep.	7,200	16.9	14.1	19.6	1.1
	Oct.	7,440	15.4	12.6	17.7	1.1
	Nov.	7,200	13.9	10.5	16.1	1.0
	Dec.	7,440	11.6	9.4	14.0	0.9
Seawater temperature at EINS-South [°C] - Near-seabed						
Statistical		№ of data points	Mean	Min.	Max.	STD.
Annual		87,649	10.3	2.7	17.7	3.4
Monthly	Jan.	7,441	8.9	6.2	11.3	1.0
	Feb.	6,768	7.1	4.6	9.2	1.0
	Mar.	7,440	6.2	2.7	8.0	1.1
	Apr.	7,200	6.6	4.0	7.9	0.9
	May	7,440	7.4	4.6	9.4	1.0
	Jun.	7,200	8.4	6.0	10.8	1.1
	Jul.	7,440	10.2	6.5	13.1	1.5
	Aug.	7,440	12.6	7.6	16.1	1.9
	Sep.	7,200	15.0	11.0	17.7	1.9
	Oct.	7,440	15.3	11.7	17.7	1.2
	Nov.	7,200	14.0	10.6	16.1	1.0
	Dec.	7,440	11.7	9.4	14.1	0.9

Seawater salinity

Figure 8.2 presents the monthly statistics (mean, minimum, maximum, and standard deviation) of seawater salinity near the surface and near the seabed salinity at EINS-South. The statistics are summarised in Table 8.2.

The seasonal variation in seawater salinity is clear at the surface. The highest and mean salinity values are almost constant during the whole year, while the lowest salinity values vary considerably during the spring and summer months. During the first month of spring, minimum salinity values at the surface drop to a minimum in May, where then minimum salinity values increase slowly until November. There is little seasonal variation near the seabed.

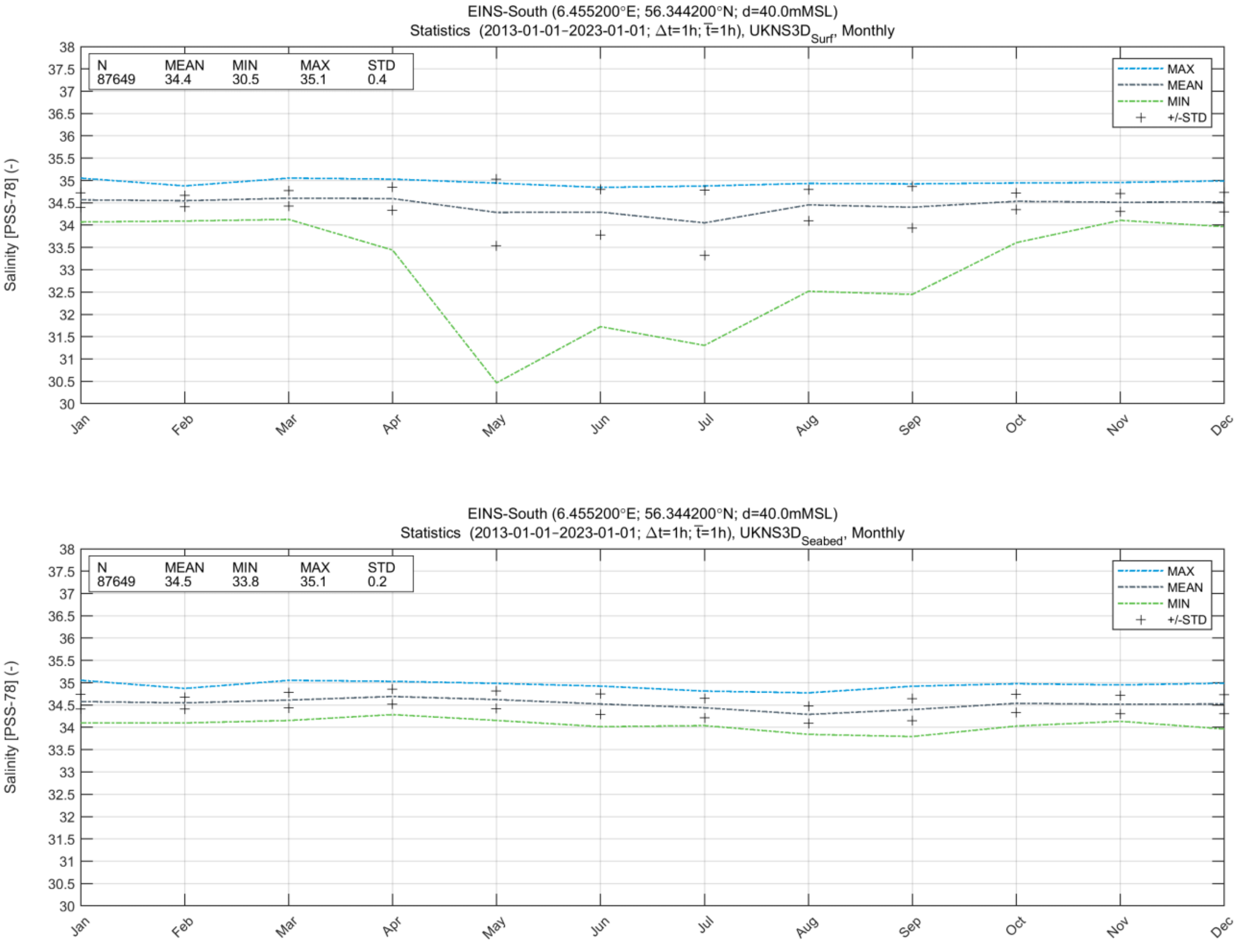

Figure 8.2 Monthly statistics of surface (top panel) and bottom (bottom panel) seawater salinity at EINS-South

Table 8.2 **Annual and monthly statistics for seawater salinity near the surface and near the seabed at EINS-South based on HD_{UKNS3D} (2013-01-01 to 2023-01-01)**
Near-surface and near-seabed data is extracted from top and bottom layers of HD_{UKNS3D}

Seawater salinity at EINS-South [PSS-78] - Near-surface						
Statistical		№ of data points	Mean	Min.	Max.	STD.
Annual		87,649	34.4	30.5	35.1	0.4
Monthly	Jan.	7,441	34.6	34.1	35.1	0.2
	Feb.	6,768	34.5	34.1	34.9	0.1
	Mar.	7,440	34.6	34.1	35.1	0.2
	Apr.	7,200	34.6	33.4	35.0	0.3
	May	7,440	34.3	30.5	34.9	0.8
	Jun.	7,200	34.3	31.7	34.8	0.5
	Jul.	7,440	34.1	31.3	34.9	0.7
	Aug.	7,440	34.5	32.5	34.9	0.3
	Sep.	7,200	34.4	32.4	34.9	0.5
	Oct.	7,440	34.5	33.6	34.9	0.2
	Nov.	7,200	34.5	34.1	35.0	0.2
	Dec.	7,440	34.5	34.0	35.0	0.2
Seawater salinity at EINS-South [PSS-78] - Near-seabed						
Statistical		№ of data points	Mean	Min.	Max.	STD.
Annual		87,649	34.5	33.8	35.1	0.2
Monthly	Jan.	7,441	34.6	34.1	35.1	0.2
	Feb.	6,768	34.5	34.1	34.9	0.1
	Mar.	7,440	34.6	34.2	35.1	0.2
	Apr.	7,200	34.7	34.3	35.0	0.2
	May	7,440	34.6	34.2	35.0	0.2
	Jun.	7,200	34.5	34.0	34.9	0.2
	Jul.	7,440	34.4	34.0	34.8	0.2
	Aug.	7,440	34.3	33.8	34.8	0.2
	Sep.	7,200	34.4	33.8	34.9	0.2
	Oct.	7,440	34.5	34.0	35.0	0.2
	Nov.	7,200	34.5	34.1	35.0	0.2
	Dec.	7,440	34.5	34.0	35.0	0.2

Seawater density

The density of seawater was calculated from the seawater temperature and salinity from the HD$_{UKNS3D}$ model using the international one-atmosphere equation of the state of seawater derived by Millero, F.J. & Poisson, A. [31]. [31].

Figure 8.3 presents the monthly statistics (mean, minimum, maximum, and standard deviation) of near sea surface and near-seabed water density at the EINS-South location. The statistics are summarised in Table 8.3.

The seasonal variation in seawater density is clear at the surface with the largest density occurring in winter (December to March) and the lowest density seen during spring and summer (April to September). There is little seasonal variation in seawater density at the seafloor, but the lowest density levels occur during September to November, showing the delay in density changes over the depth, i.e., the variations follow roughly the combined pattern of temperature and salinity.

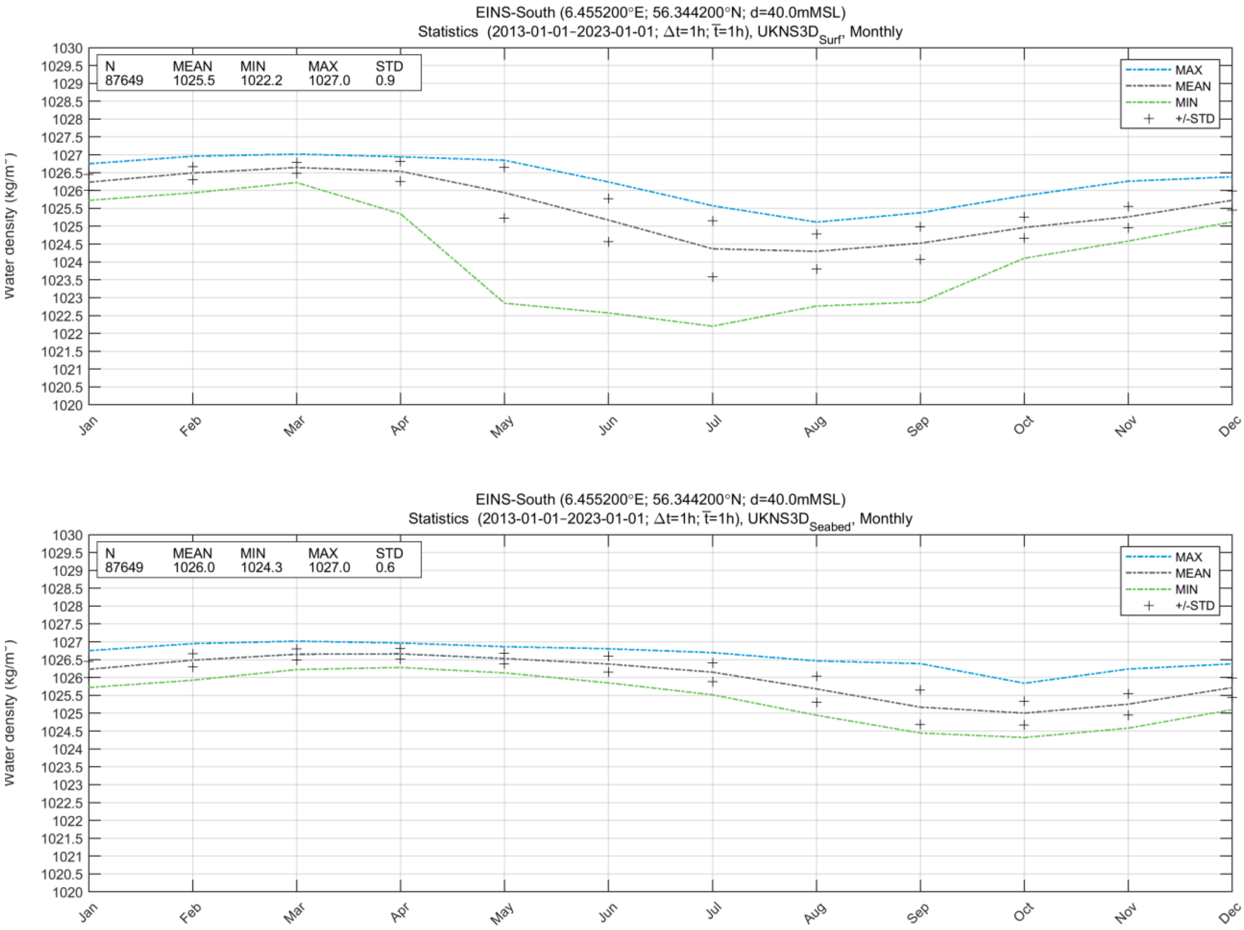

Figure 8.3 Monthly statistics of surface (top panel) and bottom (bottom panel) seawater density at EINS-South

Table 8.3 Annual and monthly statistics for seawater density at EINS-South based on HD_{UKNS3D} (2013-01-01 to 2023-01-01)
Near-surface and near-seabed data is extracted from top and bottom layers of HD_{UKNS3D}.

Seawater density at EINS-South [kg/m^3] - Near-surface						
Statistical		№ of data points	Mean	Min.	Max.	STD.
Annual		87,649	1025.5	1022.2	1027.0	0.9
Monthly	Jan.	7,441	1026.2	1025.7	1026.7	0.2
	Feb.	6,768	1026.5	1025.9	1027.0	0.2
	Mar.	7,440	1026.6	1026.2	1027.0	0.2
	Apr.	7,200	1026.5	1025.3	1026.9	0.3
	May	7,440	1025.9	1022.8	1026.8	0.7
	Jun.	7,200	1025.2	1022.6	1026.2	0.6
	Jul.	7,440	1024.4	1022.2	1025.6	0.8
	Aug.	7,440	1024.3	1022.8	1025.1	0.5
	Sep.	7,200	1024.5	1022.9	1025.4	0.5
	Oct.	7,440	1025.0	1024.1	1025.9	0.3
	Nov.	7,200	1025.3	1024.6	1026.3	0.3
	Dec.	7,440	1025.7	1025.1	1026.4	0.3
Seawater density at EINS-South [kg/m^3] - Near-seabed						
Statistical		№ of data points	Mean	Min.	Max.	STD.
Annual		87,649	1026.0	1024.3	1027.0	0.6
Monthly	Jan.	7,441	1026.2	1025.7	1026.8	0.2
	Feb.	6,768	1026.5	1025.9	1026.9	0.2
	Mar.	7,440	1026.7	1026.2	1027.0	0.2
	Apr.	7,200	1026.7	1026.3	1027.0	0.1
	May	7,440	1026.5	1026.1	1026.9	0.2
	Jun.	7,200	1026.4	1025.8	1026.8	0.2
	Jul.	7,440	1026.1	1025.5	1026.7	0.3
	Aug.	7,440	1025.7	1024.9	1026.5	0.4
	Sep.	7,200	1025.2	1024.4	1026.4	0.5
	Oct.	7,440	1025.0	1024.3	1025.8	0.3
	Nov.	7,200	1025.3	1024.6	1026.2	0.3
	Dec.	7,440	1025.7	1025.1	1026.4	0.3

9 Marine growth

Marine growth is defined as the unwanted settlement and growth of marine organisms on submerged surfaces of ship hulls, buoys, piers, offshore platforms, etc. It may also be referred to as “marine fouling” or “biofouling”. The composition and extent of marine growth vary with the biogeographical region being higher at tropical regions than at other latitudes.

The assessment of marine growth is based on scientific publications (see [32], [33], [34], [35]). From those publications there are not available marine growth time series, only values of observed marine growth weight at different water depths.

Numerous factors influence the amount and type of marine growth, including salinity, temperature, depth, current speed, and wave exposure, in addition to biological factors such as food availability, larval supply, presence of predators, and the general biology and physiology of the fouling species. Extensive knowledge on factors that affect the level of marine growth in the North Sea has been obtained through years of operation and maintenance of gas and oil platforms. Once a new hard substrate has been introduced into the environment, the organisms colonise quickly, and can grow within days. Typically, a succession in species composition will take place as the age of the deployed substrate increases. The succession is a result of organisms competing for space, and a quasi-steady state in fouling communities will be established within less than 4 to 6 years. Along with succession, individual organisms grow larger which creates an increasing thickness of marine growth. Predators such as starfish become an integral part of the fouling ecosystem finding empty spaces in the marine growth cover. In the southern North Sea (< 56° N), some studies have shown that marine growth on offshore installations (6900 records from 39 locations duing 1996-2017) may vary between 0 and 350 mm with an average of 52.76 mm (± 36.54 mm standard deviation) [32]. Of those installations located in regions with high concentrations of chlorophyll (0.84 mg/m^3) showed thicker layers of marine growth. DNV [16] states that values, up to 150 mm between sea level and LAT –10 m, may be seen in the Southern North Sea.

Studies carried out in two existing offshore wind farms, Egmond aan Zee (52.6° N, 4.41° E) and Princess Amalia (52.58° N, 4.02° E), located at a depth range of 17 – 22 m within the Dutch EEZ have demonstrated that marine growth below the splash zone (±1 m) is dominated by mussels, starfish (predating on mussels), various crustaceans (sessile and mobile), sea anemones and polychaetes (tube-building and mobile) [33], [34], [35]. Thickness of marine growth was measured/estimated on two monopiles in the Egmond aan Zee wind farm 1.7 years after monopile erection and probably too early to reflect a mature fouling community. Below the splash zone, marine growth ranged between 5 and 15 cm in the upper 6-7 m of a monopile. Below 6-7 m, the thickness of marine growth decreased to between 1 and 5 cm but with 100% cover. The marine growth will add to the weight of substructures (monopiles) ranging between 1 and 6.5 kg/m^2 depending on depth. Weight data from the two existing wind farms (Egmond aan Zee and Princess Amalia) differs with respect to depth-distribution as Egmond aan Zee showed increasing weight under water from 2 kg/m^2 at 2 m to 6.5 kg/m^2 at 10 m and decreasing to 1.5 kg/m^2 at 15 m. In contrast, marine growth in Princess Amalia wind farm, monitored after 4 and 6 years of installation, peaked at 2 m with weight under water at 4.3 kg/m^2 gradually decreasing to 1 kg/m^2 at 10 m, to increase again to

1.5 kg/m^2 at 17 m. Slightly smaller values are expected at higher latitudes of the North Sea.

In [36], density data were acquired from A12-CCP and the Q1 Haven platforms operated by Petrogas E&P Netherlands B.V. to model density across 39 platforms located in the southern North Sea. Weight varied from 2 to 113 kg/m^2 (average 47 kg/m^2), thickness from 5 to 120 mm (average 35 mm) with densities between 311 and 945 kg/m^3. The model predicted a reduction in weight with depth and a generalised density of 612 kg/m^3.

At Central and Northern North Sea (56°N to 59°N), DNV [16] suggest applying a thickness of marine growth of 10 cm (from sea surface to 40 m depth) to account for the added weight on the structural component. The density of the marine growth may be set equal to 1325 kg/m^3 (resulting in thickness of 1-5 mm considering a weight of 1-6.5 kg/m^2) unless more accurate data are available. We suggest following DNVs recommendation, which also will be in line with the observed/calculated depth distribution of ash free and wet weight of biomass.

10 References

[1] DHI, "Energy Island North Sea, Metocean Site Conditions Assessment, Part A: Data Basis – Measurements & Models, 2023-06-09 ", 2023.

[2] NORSOK, "Actions and action effects, N-003, Edition 3, April 2016," 2016.

[3] *Environmental Conditions and Environmental Loads*, DNV-RP-C205, DNV, 2021. [Online]. Available: http://rules.dnvgl.com/docs/pdf/DNV/codes/docs/2014-04/RP-C205.pdf

[4] Energinet, "Scope of Services – North Sea Energy Island Metocean Conditions Assessment, document number: 2/05192-6, 2022-06-22," 2022.

[5] Energinet, "Scope of Services – Site Metocean Conditions Assessment for Offshore Wind Farms, North Sea, Document number: 22/08564-1, 2022-11-08," 2022.

[6] *Wind energy generation systems – Part 3-1: Design Requirements for fixed offshore wind turbines. Ed. 1.0*, IEC-61400-3-1, 2019.

[7] DHI, "Energy Island North Sea, Metocean Site Conditions Assessment, Part B: Data Analyses – Energy Island, 2023-06-16," 2023.

[8] DHI, "Energy Island, North Sea, Metocean Site Conditions Assessment, Part C: Data Analyses – Wind Farm Area (FEED), due Apr. 2023," 2023.

[9] DHI, "Energy Island North Sea, Metocean Site Conditions Assessment, Part D: Data Basis – Hindcast revalidation note, due Jan. 2024," 2024.

[10] D. L. Codiga, "Unified Tidal Analysis and Prediction Using the UTide Matlab Functions. Technical Report 2011-01," Graduate School of Oceanography, University of Rhode Island, Narragansett, RI. 59pp, 2011.

[11] B. B. a. S. L. R. Pawlowicz, "Classical tidal harmonic analysis including error estimates in MATLAB using T-TIDE, Computers & Geosciences 28, pp. 929-937," 2002.

[12] K. E. L. a. D. A. Jay, "Enhancing tidal harmonic analysis: Robust (hybrid L-1/L-2) solutions, Cont. Shelf Res. 29, pp. 78-88. DOI: 10.1016/j.csr.2008.1004.1011," 2009.

[13] J. Y. C. a. V. A. B. M. G. G. Foreman, "Versatile Harmonic Tidal Analysis: Improvements and Applications," *J. Atmos. Oceanic Tech. 26, pp. 806-817. DOI: 810.1175/2008JTECHO1615.1171,* 2009.

[14] D. Shepard, "A two-dimensional interpolation function for irregularly-spaced data," in *ACM National Conference*, 1968: Association for Computing Machinery, in ACM '68, pp. 517–524.

[15] DHI, "MIKE 21 Spectral Waves FM: User Guide," 2022.

[16] *Loads and site conditions for wind turbines*, DNV-ST-0437, DNV, 2021.

[17] J. D. Fenton, "The numerical solution of steady water wave problems," *Computers & Geosciences,* vol. vol. 14, pp. pp. 357-368, 1988.

[18] J. D. Fenton, "Nonlinear Wave Theories," *Ocean Engineering Science,* vol. Vol.9, 1990.

[19] B. T. S. Paulsen, Ben de; van der Meulen, Michiel; Jacobsen, Niels Gjøl, "Probability of wave slamming and the magnitude of slamming loads on offshore wind turbine foundations," *Coastal Engineering,* pp. 76-95, 2019.

[20] H. Madsen, P. S. Mikkelsen, D. Rosbjerg, and P. Harremoës, "Regional estimation of rainfall intensity-duration-frequency curves using generalized least squares regression of partial duration series statistics," *Water Resources Research,* vol. 38, no. 11, pp. 21-1-21-11, 2002, doi: https://doi.org/10.1029/2001WR001125.

[21] H. Madsen, I. Gregersen, D. Rosbjerg, and K. Arnbjerg-Nielsen, "Regional frequency analysis of short duration rainfall extremes using gridded daily rainfall data as co-variate.," presented at the Water Sci Technol., 2017.

[22] D. Rosbjerg and H. Madsen, "Initial design of urban drainage systems for extreme rainfall events using intensity–duration–area (IDA) curves and Chicago design storms (CDS)," *Hydrological Sciences Journal,* vol. 64, no. 12, pp. 1397-1403, 2019/09/10 2019, doi: 10.1080/02626667.2019.1645958.

[23] S. Thorndahl, J. E. Nielsen, and M. R. Rasmussen, "Estimation of Storm-Centred Areal Reduction Factors from Radar Rainfall for Design in Urban Hydrology," *Water,* vol. 11, no. 6, p. 1120, 2019. [Online]. Available: https://www.mdpi.com/2073-4441/11/6/1120.

[24] NERC, "Flood Studies Report," National Environment Research Council, UK, 1975, vol. II.

[25] K. Arnbjerg-Nielsen, H. Madsen, and P. S. Mikkelsen, "Regional variation af ekstremregn i Danmark- ny bearbejdning (1979–2005)," Ingeniørforeningen i Danmark - IDA, 2006.

[26] C. J. Keifer and H. H. Chu, "Synthetic Storm Pattern for Drainage Design," *Journal of the Hydraulics Division,* vol. 83, no. 4, pp. 1332-1-1332-25, 1957, doi: doi:10.1061/JYCEAJ.0000104.

[27] D. Rosbjerg, Madsen, H., Rasmussen, P.F., "Prediction in partial duration series with generalized Pareto-distributed exceedances,," *Water Resources Research,,* vol. 28(11), 3001-3010., 1992.

[28] D. J. Cecil. *LIS/OTD Gridded Lightning Climatology Data Collection, Version 2.3.2015*, NASA EOSDIS Global Hydrology Resource Center Distributed Active Archive Center, Huntsville, Alabama, U.S.A., doi: http://dx.doi.org/10.5067/LIS/LIS-OTD/DATA311.

[29] D. J. B. Cecil, D. E.; Blackeslee, R. J., "Gridded lightning climatology from TRMM-LIS and OTD: Dataset description," *Atmospheric Research,* vol. 135-136, pp. 404-414, 2014.

[30] P. R. J. Doran, D. J. Beberwyk, G. R. Brooks, G. A. Gayno, R. T. Williams, J. M. Lewis and R. J. Lefevre, "The MM5 at the AF Weather Agency – new products to support military operations," in *8th Conference on Aviation, Range, and Aerospace Meteorology, American, Dallax, TX, USA.*, 1999.

[31] F. J. Millero and A. Poisson, "International one-atmosphere equation of state of seawater," *Deep Sea Research Part A. Oceanographic Research Papers,* vol. 28, no. 6, pp. 625-629, 1981/06/01/ 1981, doi: https://doi.org/10.1016/0198-0149(81)90122-9.

[32] L. P. Almeida and J. W. P. Coolen, "Modelling thickness variations of macrofouling communities on offshore platforms in the Dutch North Sea," *Journal of Sea Research,* vol. 156, p. 101836, 2020/01/01/ 2020, doi: https://doi.org/10.1016/j.seares.2019.101836.

[33] M. C. Bruijs, "Biological Fouling - Survey of marine fouling on turbine support structures of the Offshore Windfarm Egmond aan Zee.," in "KEMA Nederland B.V.," 50863511-TOS/PCW 10-4207, 2010.

[34] W. L. Bouma, S., "Benthic communities on hard substrates of the offshore wind farm Egmond aan Zee (OWEZ) - Including results of samples collected in scour holes," in "Bureau Waardenburg bv," OWEZ_R_266_T1_20120206_hard_substrate, 2012.

[35] T. V. d. M. Vanagt, L. and Faasse, M. , "Development of hard substrate fauna in the Princess Amalia Wind Farm. Monitoring 3.5 years after construction.," 2013.

[36] J. W. P. A. Coolen, L. P.; Olie, R., "Modelling marine growth biomass on North Sea offshore structures," presented at the Structures in the Marine Environment (SIME2019), Glasgow, UK, 2019.

[37] J. E. Heffernan and J. A. Tawn, "A conditional approach for multivariate extreme values," *Journal of the Royal Statistical Society. Series B,* vol. 66, no. 3, pp. 497-546, 2004.

[38] H. F. Hansen, D. Randell, A. R. Zeeberg, and P. Jonathan, "Directional–seasonal extreme value analysis of North Sea storm conditions," *Ocean Engineering,* vol. 195, 2020, doi: 10.1016/j.oceaneng.2019.106665.

[39] P. S. Tromans and L. Vanderschuren, "Response Based Design Conditions in the North Sea: Application of a New Method," presented at the Offshore Technology Conference, Houston, Texas, 1995. [Online]. Available: dx.doi.org/10.4043/7683-MS.

[40] G. Z. Forristall, "On the Use of Directional Wave Criteria," *Journal of Waterway, Port, Coastal, and Ocean Engineering,* vol. 130, no. 5, pp. 272-275, 2004, doi: 10.1061/(asce)0733-950x(2004)130:5(272).

[41] *Environmental Conditions and Environmental Loads*, DNV-RP-C205, DNV, 2014. [Online]. Available: http://rules.dnvgl.com/docs/pdf/DNV/codes/docs/2014-04/RP-C205.pdf

[42] G. Z. Forristall, "Wave Crest Distributions: Observations and Second-Order Theory," *Journal of Physical Oceanography,* vol. 30, no. 8, pp. 1931-1943, 2000, doi: dx.doi.org/10.1175/1520-0485(2000)030<1931:wcdoas>2.0.co;2.

[43] A. J. Battjes and W. H. Groenendijk, "Wave height distributions on shallow foreshore," *Coastal Enginnering,* vol. 40, no. 3, pp. 161-182, 2000.

[44] P. S. Tromans and L. Vanderschuren, "Response Based Design Conditions in the North Sea: Application of a New Method," *OTC-7683,* pp. 387-397, 1995.

[45] P. S. Tromans, A. R. Anaturk, and P. Hagemeijer, "A new model for the kinematics of large ocean waves-Application as a design wave.," *International Society of Offshore and Polar Engineers,* 1991.

[46] P. Thompson, Y. Cai, R. Moyeeda, D. Reeve, and J. Stander, "Bayesian nonparametric quantile regression using splines," *Computational Statistics and Data Analysis,* vol. 54, pp. 1138-1150, 2010.

[47] P. Jonathan, D. Randell, Y. Wu, and K. Ewans, "Return level estimation from non-stationary spatial data exhibing multidimensional covaiate effects," *Ocean Engineering,* no. 88, pp. 520-532, 2014.

[48] P. Eilers and B. Marx, "Multivariate calibration with temperature interaction using two-dimensional penalized signal regression," *Chemometrics and Intelligent Laboratory Systems,* vol. 66, no. 2, pp. 159-174, 2003.

[49] I. D. Currie, M. Durban, and P. H. C. Eilers, "Generalized linear array models with applications to multidimensional smoothing," *Journal of the Royal Statistical Society: Series B (Statistical Methodology),* vol. 68, no. 2, 2006.

[50] P. H. C. Eilers, I. D. Currie, and M. Durban, "Fast and compact smoothing on large multidemsional grids," *Computational Statistics & Data Analysis,* vol. 50, no. 1, pp. 61-76, January 2006.

[51] P. J. Green and B. W. Silverman, "Nonparametric Regression and Generalized Linear Models," *Chapman & Hall,* 1994.

[52] S. Lang and A. Brezger, "A Bayesian P-Splines," *Journal of Computational and Graphical Statistics,* no. 13, pp. 183-212, 2004.

[53] G. O. Roberts and J. S. Rosenthal, "Examples of Adaptive MCMC," *Journal of Computational and Graphical Statistics,* vol. 18, pp. 349-367, 2009.

[54] H. Rue, "Fast Sampling of Gaussian Markov Random Fields with Applications," *Journal of the Royal Statistical Society,* vol. Series B, 2001.

11 Appendix A: List of Data Reports

This appendix presents a list of data reports attached to this report.

Table 11.1 List of data reports (.xlsx) attached to this report.
Metocean (including T-EVA), and extreme conditions (J-EVA).

Filename
Normal conditions (including T-EVA)
EINS-1_Metocean-Data-Report_2023-06-30.xlsx
EINS-2_Metocean-Data-Report_2023-06-30.xlsx
EINS-3_Metocean-Data-Report_2023-06-30.xlsx
EINS-4_Metocean-Data-Report_2023-06-30.xlsx
EINS-5_Metocean-Data-Report_2023-06-30.xlsx
Extreme conditions (based on J-EVA)
EINS-1_J-EVA_Data_Report_2023-06-30.xlsx
EINS-2_J-EVA_Data_Report_2023-06-30.xlsx
EINS-3_J-EVA_Data_Report_2023-06-30.xlsx
EINS-4_J-EVA_Data_Report_2023-06-30.xlsx
EINS-5_J-EVA_Data_Report_2023-06-30.xlsx

12 Appendix B: Comparison of J-EVA and T-EVA

This section presents a comparison between the traditional extreme value analysis (T-EVA) and the joint extreme value analysis (J-EVA).

Introduction

It is significant to understand the fundamental differences between J-EVA and T-EVA, and the reason for preferring J-EVA over T-EVA. The differences arise mainly from the considerations summarised in Table 12.1.

Table 12.1 Differences between T-EVA and J-EVA

T-EVA	J-EVA
Characterises nature less accurately	Characterises nature more accurately
Less consistent estimates of joint parameters	Consistent joint probabilities of conditioned (associated) parameters
Storms are characterised only by the conditioning parameter	Storms are characterised by ALL variables (wave, current, water level and wind)
Fitting of directional extremes decoupled with monthly extremes	Consistent directional and seasonal extreme values
Fitting of monthly extremes decoupled with directional extremes	
Evolution of a storm remains in a particular direction/month	Storms can build up in one sector, peak in another and finally decay in a third sector
Parameters of distribution remain fixed – Frequentist approach	Parameters of the distribution are allowed to vary – Bayesian approach
Uncertainty of an estimate is larger, particularly for larger return periods	Uncertainty is accounted for in the estimate leading to lower uncertainty for high return values
Large “subjectivity” in EVA distributions	Less “subjectivity” in EVA distributions

Comparison at EINS-2

Figure 12.1 - Figure 12.3 shows the extreme value distributions of H_{m0}, H_{max}, and $C_{max,MSL}$ at EINS-2 using T-EVA (results for all wind, water level, current, and waves variables of T-EVA are given in the data reports). These plots depict the final distributions chosen from a sensitivity analysis using multiple thresholds, distributions (see section on sensitivity below), and fitting methods to assess the goodness of fit (visually), the magnitude (inter-compared), depth considerations (waves), and general guidelines and practices for conducting EVA.

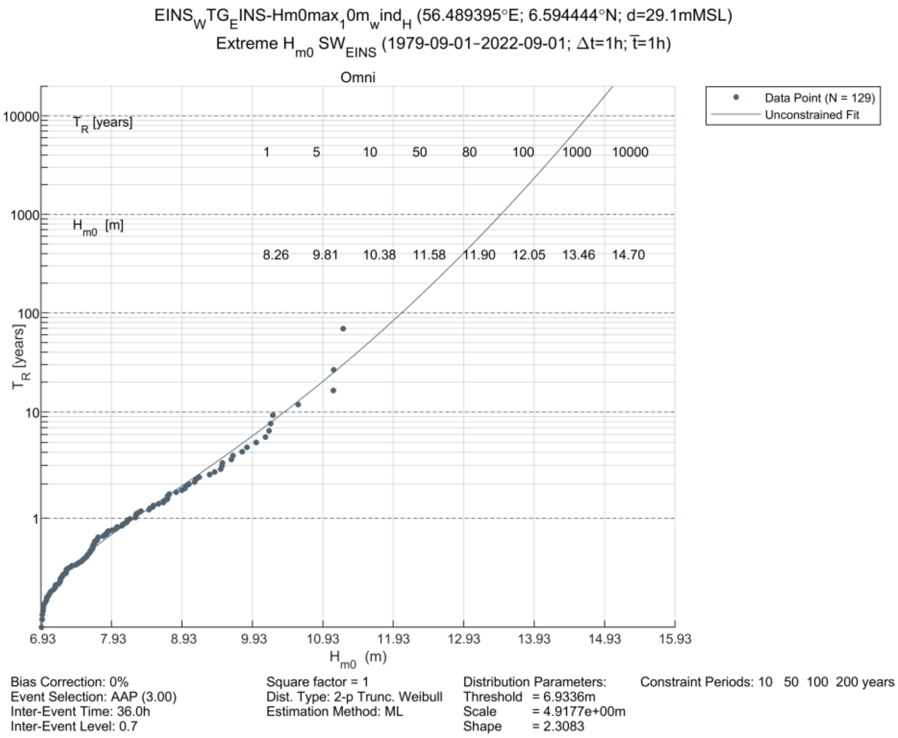

Figure 12.1 Extreme value distribution of H_{m0} at EINS-2

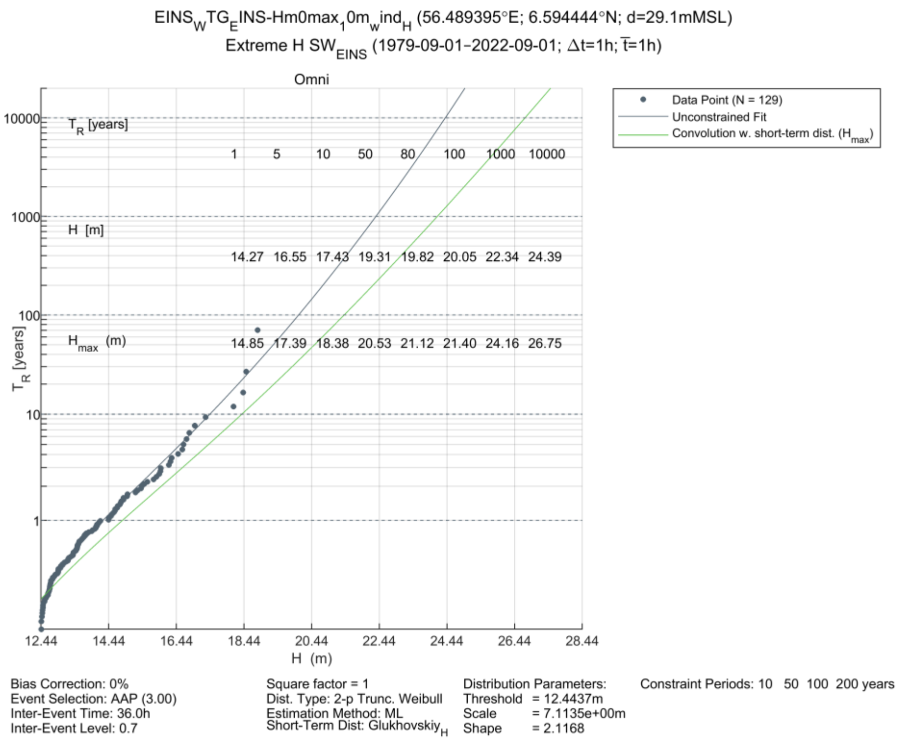

Figure 12.2 Extreme value distribution of H_{max} at EINS-2

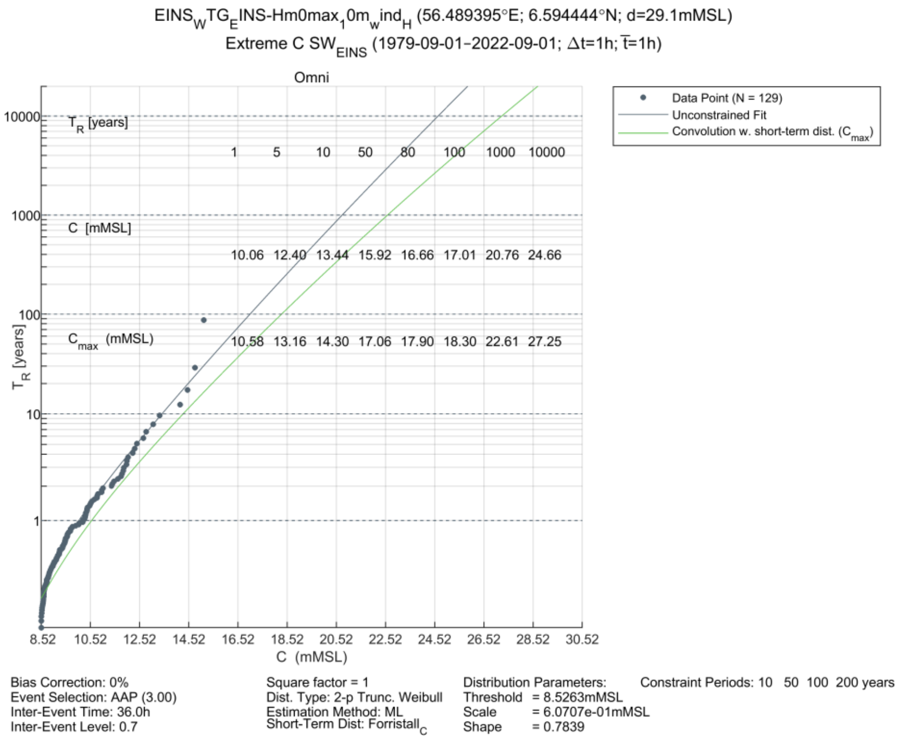

Figure 12.3 Extreme value distribution of $C_{max, MSL}$ at EINS-2

Figure 12.5 - Figure 12.5 and Table 14 shows the differences between the estimated extreme values using T-EVA and J-EVA for the following parameters:

- H_{m0}, H_{max}, $C_{max, SWL}$, $C_{max, MSL}$, WS, CS, HWL_{tot}, LWL_{tot}, HWL_{res}, LWL_{res}.

Note that the truncation to water depth, see Section 6.2.6, to H_{max} and $C_{max,SWL}$ results in identical values for T-EVA and J-EVA for high return periods.

The numbers show that the estimates using T-EVA are generally slightly larger although the magnitude of differences depends on the parameter. The largest difference of 1 m is observed for H_{max} and $C_{max,MSL}$ respectively for 1.000- and 100-year return periods.

The reason for such differences is that T-EVA and J-EVA are fundamentally different approaches and cannot be directly compared. Cf. Table 12.1, J-EVA uses a Bayesian approach, multi-variate fitting for directions and seasons, embedding of statistical uncertainty, etc. In T-EVA, the estimated extremes are rather sensitive to choices of distribution and fitting, which according to common practise is based on sensitivity tests, inspection of the quality of fits, and assessment of how stable the estimated fits/values are.

Table 12.2 Differences between the estimated extremes of T- and J-EVA

Differences, T-EVA – J-EVA										
T_R [yr]	H_{m0}	H_{max}	$C_{max,SWL}$	$C_{max,MSL}$	WS	CS	HWL_{tot}	LWL_{tot}	HWL_{res}	LWL_{res}
1	0.2	0.1	0.2	0.3	-0.3	0.1	-0.1	0.0	0.0	0.0
5	0.1	0.1	0.2	0.3	-0.3	0.0	0.0	-0.1	0.0	0.0
10	0.0	0.1	0.2	0.3	-0.2	0.1	0.0	0.0	0.1	0.0
50	-0.1	0.1	0.2	0.7	0.3	0.1	0.0	-0.1	0.1	-0.1
80	0.0	0.2	0.2	0.9	0.3	0.1	0.0	-0.1	0.1	0.0
100	-0.1	0.3	0.3	1.0	0.2	0.1	0.0	-0.1	0.1	-0.1
1000	0.0	1.0	0.4	0.4	0.4	0.1	0.2	-0.2	0.2	-0.1
10000	0.2	0.0	0.0	-0.1	0.0	0.1	0.3	-0.3	0.3	-0.2

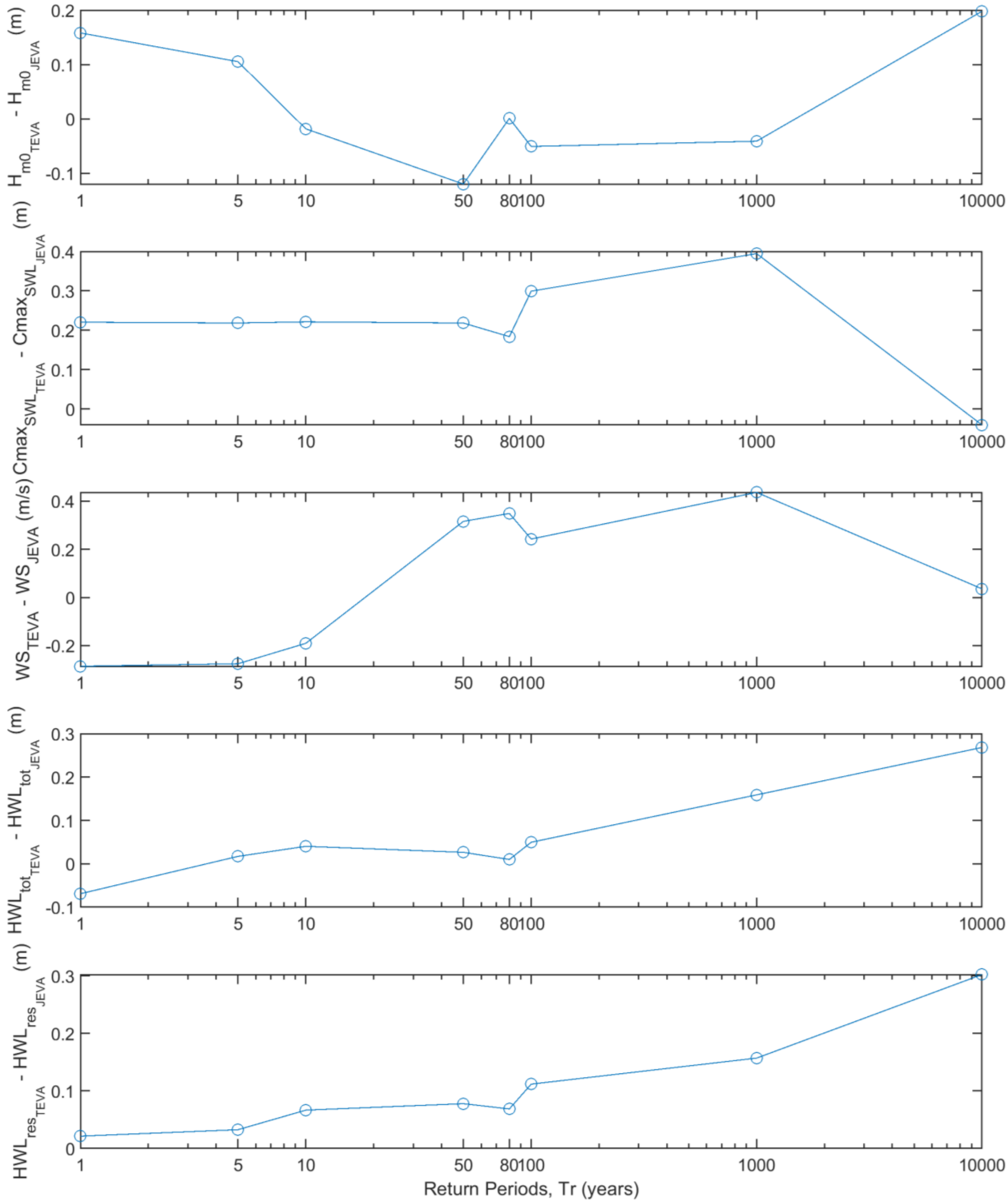

Figure 12.4 Differences between the estimated extremes of T- and J-EVA
Top to bottom: H_{m0}, $C_{max,SWL}$, WS, HWL_{tot}, and HWL_{res}.

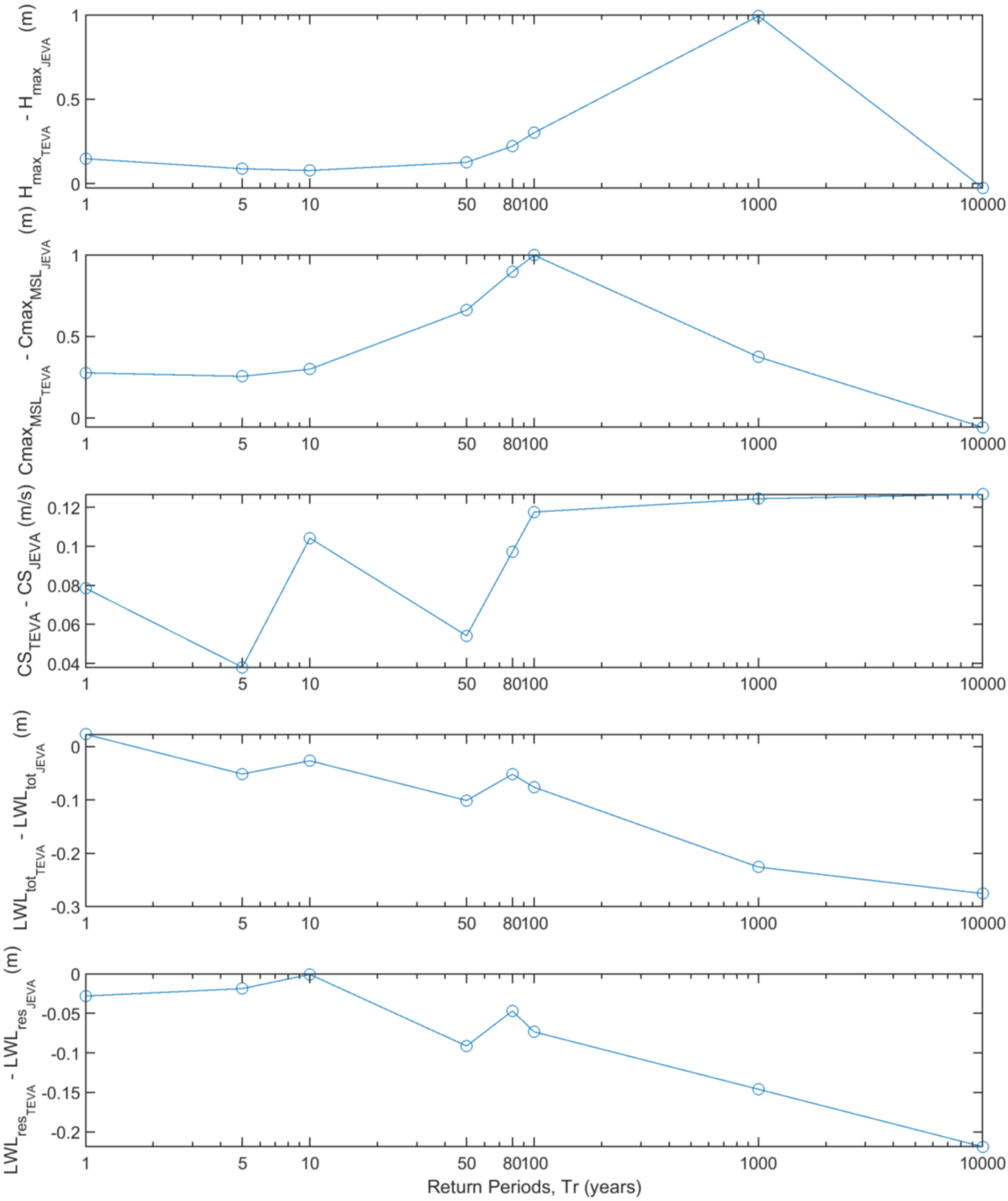

Figure 12.5 Differences between the estimated extremes of T- and J-EVA
Top to bottom: H_{max}, $C_{max,MSL}$, CS, LWL_{tot}, and LWL_{res}.

Sensitivity of T-EVA to distribution, threshold, and fitting

Figure 12.6 - Figure 12.9 presents sensitivity of T-EVA to distribution, threshold, and fitting for all considered variables (WS, H_{m0}, WL, and CS). The plots depict the 100-year value vs. number of events year. These plots were used to assess the variability of the estimate according to various distributions and fittings (ML = Maximum Likelihood, LS = Least-squares), and together with visual inspection of the actual distribution plots this governed the choice of settings for T-EVA of each variable.

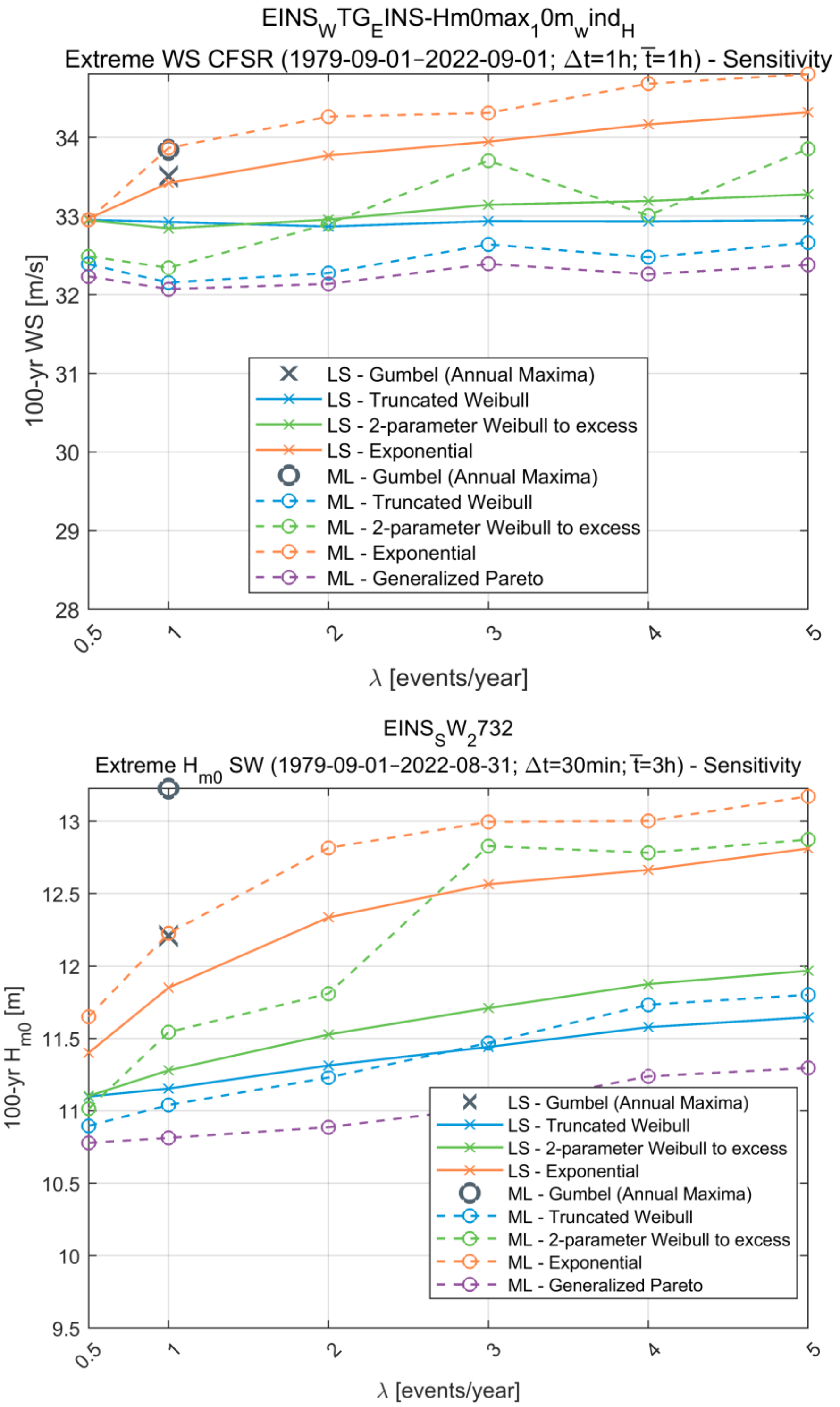

Figure 12.6 Sensitivity of T-EVA to distribution, threshold, and fitting – WS (top) and H_{m0} (bottom)

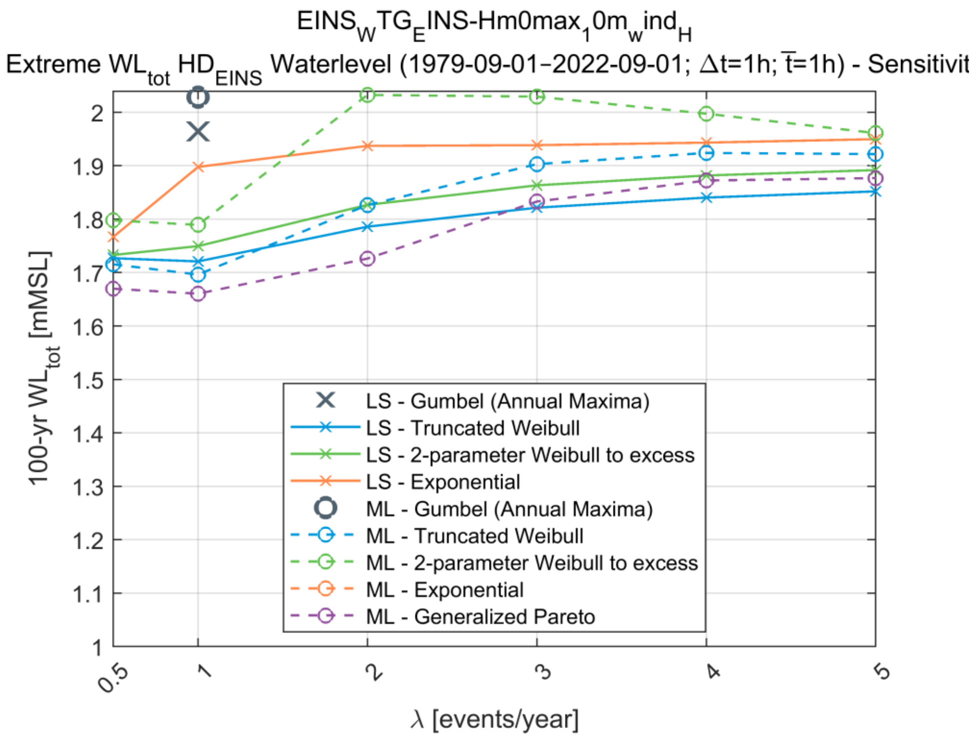

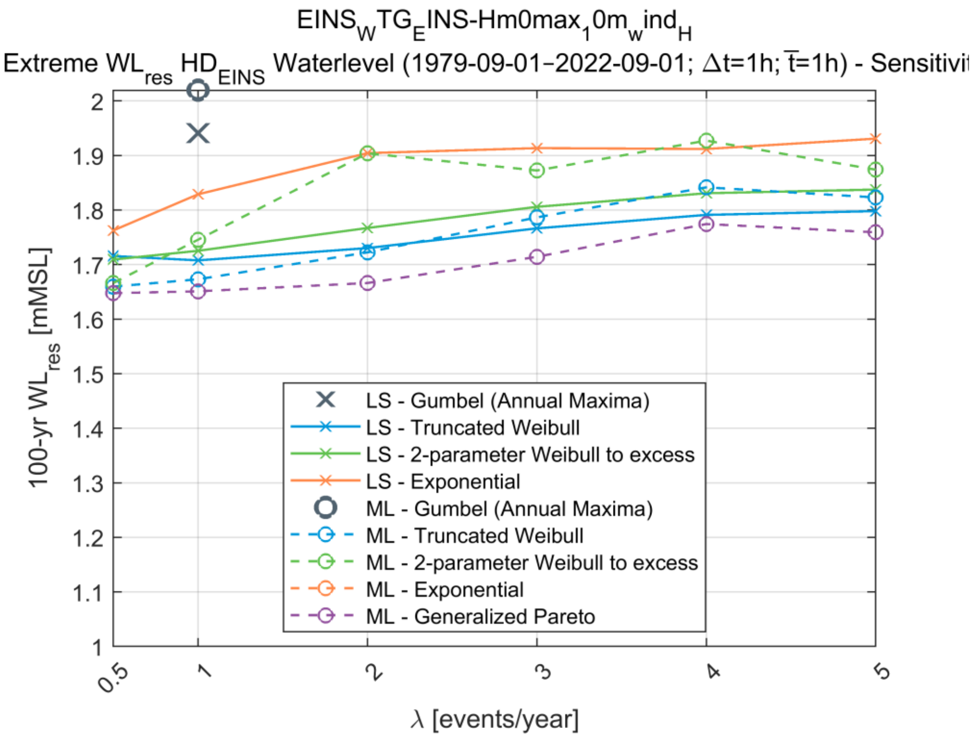

Figure 12.7 Sensitivity of T-EVA to distribution, threshold, and fitting – WL_{tot} (top) and WL_{res} (bottom)

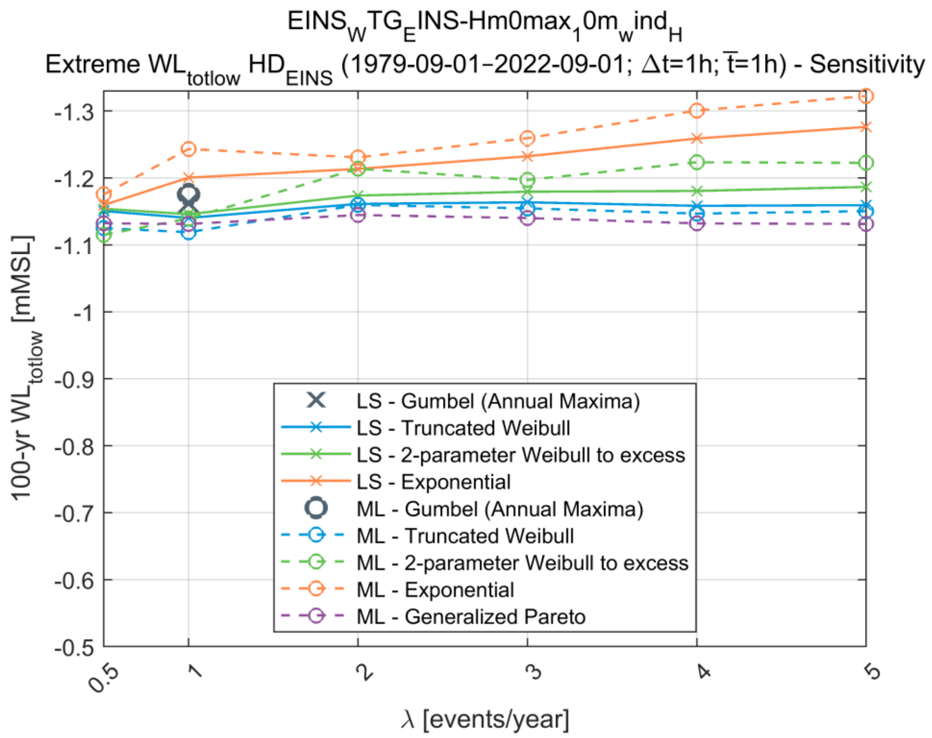

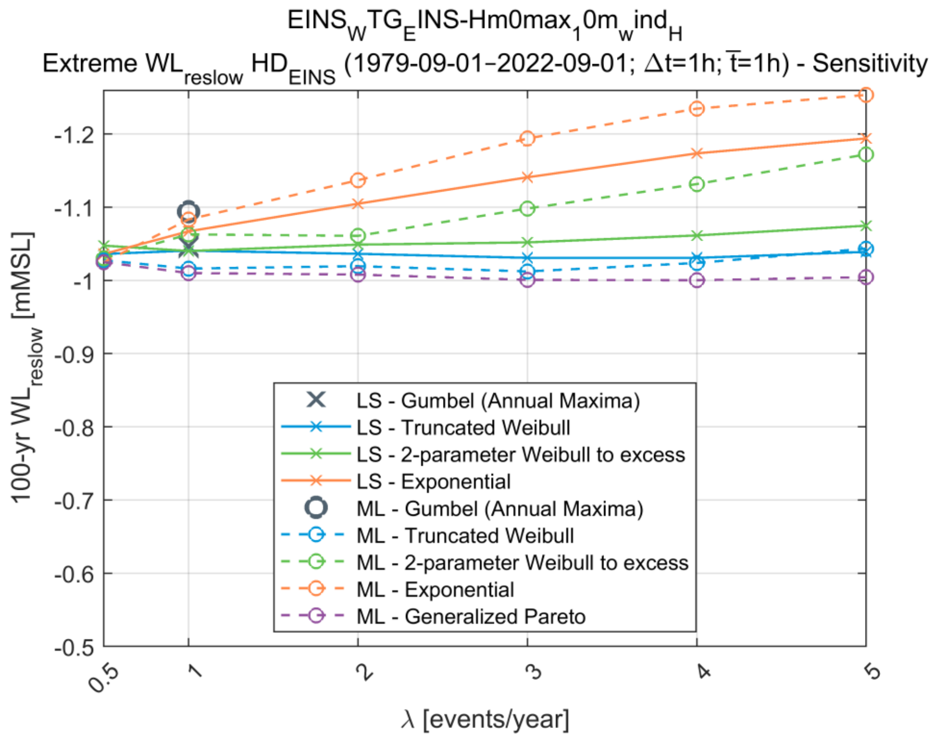

Figure 12.8 Sensitivity of T-EVA to distribution, threshold, and fitting – WL$_{tot,low}$ (top) and WL$_{res,low}$ (bottom)

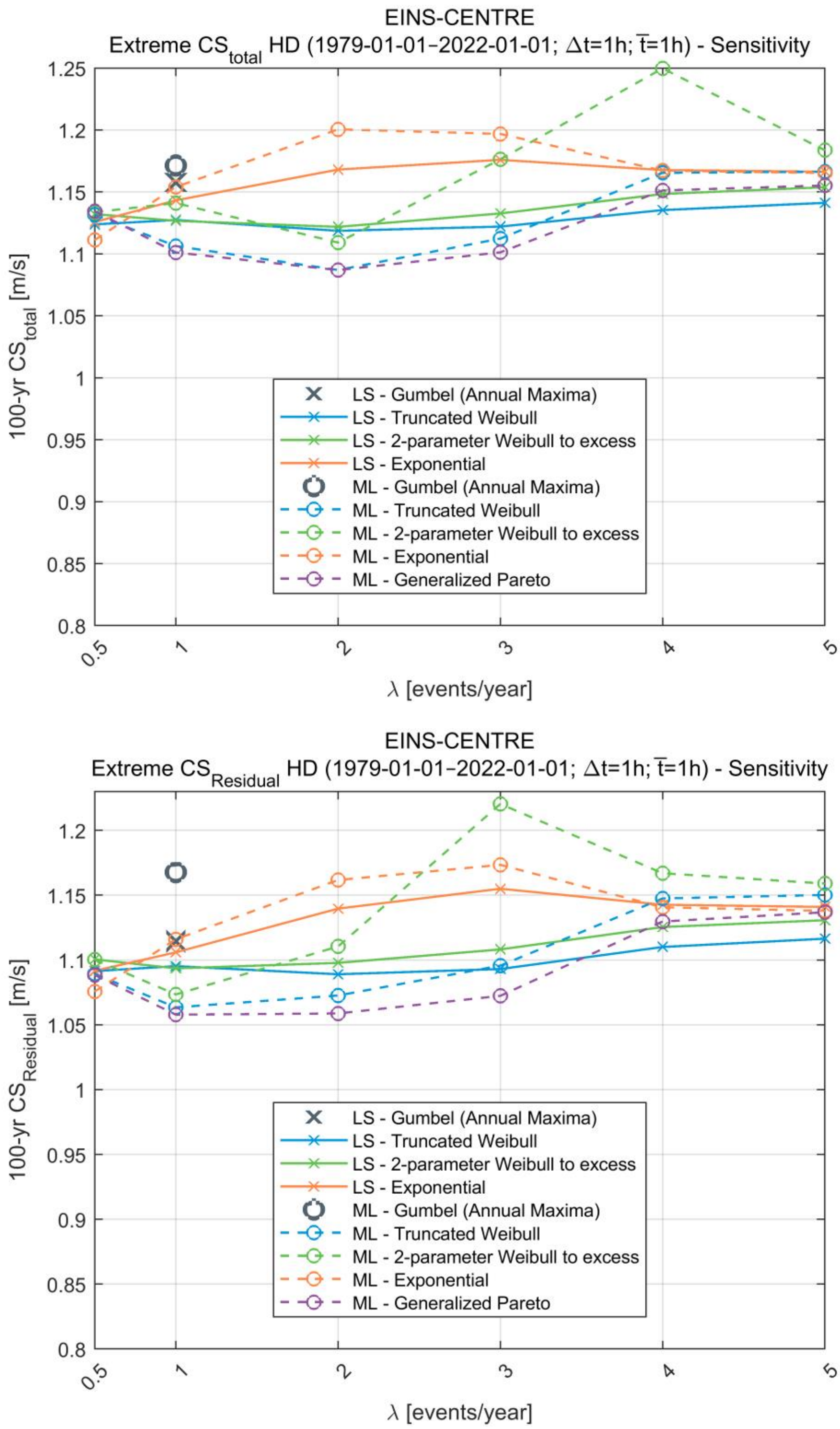

Figure 12.9 Sensitivity of T-EVA to distribution, threshold, and fitting – CS_{tot} (top) and CS_{res} (bottom)

13 Appendix C: T-EVA – Traditional EVA

This document describes the DHI extreme value analysis (EVA).

13.1 Summary of approach

Extreme values with conditioned long return periods are estimated by fitting a probability distribution to historical data. Several distributions, data selection and fitting techniques are available for estimation of extremes, and the estimated extremes are often rather sensitive to the choice of method. However, it is not possible to choose a preferred method only on its superior theoretical support or widespread acceptance within the industry. Hence, it is common practice to test several approaches and make the final decision based on goodness of fit.

The typical extreme value analyses involved the following steps:

1. Extraction of independent identically-distributed events by requiring that events are separated by at least 36 hours (or similar), and that the value between events had dropped to below 70% (or similar) of the minor of two consecutive events. The extraction is conducted individually for omni and directional/seasonal subsets respectively.
2. Fitting of extreme value distribution to the extracted events, individually for omni and directional/seasonal subsets. Distribution parameters are estimated either by maximum likelihood or least-square methods. The following analysis approaches are used (see Section 13.2 for details):
   - Fitting the Gumbel distribution to annual maxima.
   - Fitting a distribution to all events above a certain threshold (the Peak-Over-Threshold method). The distribution type can be exponential, truncated Weibull or 2-parameter Weibull to excess.
3. Constraining of subseries to ensure consistency with the omni/all-year distribution; see Section 13.4 for details.
4. Bootstrapping to estimate the uncertainty due to sampling error; see Section 13.6 for details.
5. Values of other parameters conditioned on extremes of one variable are estimated using the methodology proposed in [37] (Heffernan & Tawn).

Figure 13.1 shows an example of EVA based on 38 years of hindcast data and a Gumbel distribution fitted to the annual maxima using max. likelihood.

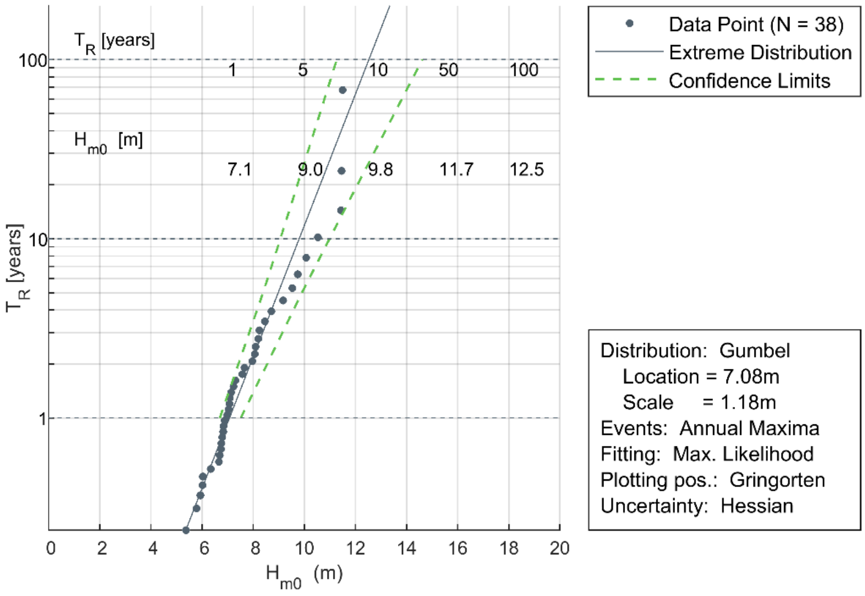

Figure 13.1 Example of traditional extreme value analysis of H_{m0}.
A Gumbel distribution fitted to the annual maxima using maximum likelihood.

13.2 Long-term distributions

The following probability distributions are often used in connection with extreme value estimation:

- 2-parameter Weibull distribution
- Truncated Weibull distribution
- Exponential distribution
- Gumbel distribution

The 2-parameter Weibull distribution is given by:

$$P(X < x) = 1 - \exp\left(-\left(\frac{x}{\beta}\right)^{\alpha}\right) \tag{13.1}$$

with distribution parameters α (shape) and β (scale). The 2-parameter Weibull distribution used in connection with Peak-Over-Threshold (POT) analysis is fitted to the excess of data above the threshold, i.e., the threshold value is subtracted from data prior to fitting.

The 2-parameter *truncated* Weibull distribution is given by:

$$P(X < x) = 1 - \frac{1}{P_0}\exp\left(-\left(\frac{x}{\beta}\right)^{\alpha}\right) \tag{13.2}$$

with distribution parameters α (shape) and β (scale) and the exceedance probability, P_0, at the threshold level, γ, given by:

$$P_0 = \exp\left(-\left(\frac{\gamma}{\beta}\right)^{\alpha}\right) \tag{13.3}$$

The 2-parameter truncated Weibull distribution is used in connection with Peak-Over-Threshold analysis, and as opposed to the non-truncated 2-p Weibull, it is fitted directly to data, i.e., the threshold value is **not** subtracted from data prior to fitting.

The exponential distribution is given by:

$$P(X < x) = 1 - \exp\left(-\left(\frac{x-\mu}{\beta}\right)\right), \quad x \geq \mu \tag{13.4}$$

with distribution parameters β (scale) and μ (location). Finally, the Gumbel distribution is given by:

$$P(X < x) = \exp\left(-\exp\left(\frac{\mu - x}{\beta}\right)\right) \tag{13.5}$$

with distribution parameters β (scale) and μ (location).

13.3 Individual wave and crest height

Short-term distributions

The short-term distributions of individual wave heights and crests conditional on H_{m0} are assumed to follow the distributions proposed by Forristall, (Forristall G. Z., 1978) and (Forristall G. Z., 2000). The Forristall wave height distribution is based on Gulf of Mexico measurements, but experience from the North Sea has shown that these distributions may have a more general applicability. The Forristall wave and crest height distributions are given by:

$$P(X > x \mid H_{m0}) = \exp\left(-\left(\frac{x}{\alpha H_{m0}}\right)^{\beta}\right) \tag{13.6}$$

where the distribution parameters, α and β, are as follows:

Forristall wave height: $\alpha = 0.681$ $\beta = 2.126$

Forristall crest height (3D): $\alpha = 0.3536 + 0.2568 \cdot S_1 + 0.0800 \cdot Ur$

$\beta = 2 - 1.7912 \cdot S_1 - 0.5302 \cdot Ur + 0.284 \cdot Ur^2$

$S_1 = \dfrac{2\pi}{g}\dfrac{H_{m0}}{T_{01}^2}$ and $U_r = \dfrac{H \cdot L^2}{d^3}$

For this type of distribution, the distribution of the extremes of a given number of events, N, (waves or crests) converges towards the Gumbel distribution conditional on the most probable value of the extreme event, H_{mp} (or C_{mp} for crests):

$$P(h_{\max} \mid H_{mp}) = \exp\left(-\exp\left(-\ln N\left(\left(\frac{h_{\max}}{H_{mp}}\right)^{\beta} - 1\right)\right)\right) \tag{13.7}$$

13.3.1 Individual waves (modes)

The extreme individual wave and crest heights are derived using the storm mode approach, (Tromans, P.S. and Vanderschuren, L., 1995). The storm modes, or most probable values of the maximum wave or crest in the storm (H_{mp} or C_{mp}), are obtained by integrating the short-term distribution of wave heights conditional on H_{m0} over the entire number of sea states making up the storm. In practice, this is done by following these steps:

1. Storms are identified by peak extraction from the time series of significant wave height. Individual storms are taken as portions of the time series with H_{m0} above 0.7 times the storm peak, H_{m0}.
2. The wave (or crest) height distribution is calculated for each sea state above the threshold in each individual storm. The short-term distribution of H (or C) conditional on H_{m0}, $P(h|H_{m0})$, is assumed to follow the empirical distributions by Forristall (see Section 13.3). The wave height probability distribution is then given by the following product over the n sea states making up the storm:

$$P(H_{\max} < h) = \prod_{j=1}^{n_{seastates}} P\left(h \mid H_{m0,j}\right)^{N_{waves,j}} \tag{13.8}$$

with the number of waves in each sea state, N_{waves}, being estimated by deriving the mean zero-crossing period of the sea state. The most probable maximum wave height (or mode), H_{mp}, of the storm is given by:

$$P(H_{\max} < h) = \frac{1}{e} \tag{13.9}$$

This produces a database of historical storms each characterised by its most probable maximum individual wave height which is used for further extreme value analysis.

13.3.2 Convolution of short-term variability with long-term storm density

The long-term distribution of individual waves and crests is found by convolution of the long-term distribution of the modes (subscript $_{mp}$ for most probable value) with the distribution of the maximum conditional on the mode given by:

$$\begin{aligned} P(H_{\max}) &= \int_0^\infty P\left(h_{\max} \mid H_{mp}\right) \cdot p\left(H_{mp}\right) dH_{mp} \\ &= \int_0^\infty \exp\left(-\exp\left(-\ln N\left(\left(\frac{h}{H_{mp}}\right)^\beta - 1\right)\right)\right) \cdot p\left(H_{mp}\right) dH_{mp} \end{aligned} \tag{13.10}$$

The value of N, which goes into this equation, is determined by defining equivalent storm properties for each individual storm. The equivalent storms have constant H_{m0} and a duration such that their probability density function of H_{max} or C_{max} matches that of the actual storm. The density functions of the maximum wave in the equivalent storms are given by:

$$p\left(H_{\max} \mid H_{m0,eq}, N_{eq}\right) = \frac{d}{dH}\left[1 - \exp\left(-\left(\frac{H_{\max}}{\alpha \cdot H_{m0,eq}}\right)^\beta\right)\right]^{N_{eq}} \tag{13.11}$$

The β parameter in eq. (13.10) comes from the short-term distribution of individual crests, eq. ((13.6), and is a function of wave height and wave period.

Based on previous studies, it has been assessed that the maximum crest heights are not sensitive to β_C for a constant value of 1.88 and hence, it is decided to apply $\beta_C = 1.88$. The number of waves in a storm, N, was conservatively calculated from a linear fit to the modes minus one standard deviation.

13.4 Subset extremes

Estimates of subset (e.g., directional, and monthly) extremes are required for several parameters. To establish these extremes, it is common practice to fit extreme value distributions to data sampled from the population (i.e., the model database) that fulfils the specific requirement e.g., to direction, i.e., the extremes from each direction are extracted and distributions fitted to each set of directional data in turn. By sampling an often relatively small number of values from the data set, each of these directional distributions is subject to uncertainty due to sampling error. This will often lead to the directional distributions being inconsistent with the omnidirectional distribution fitted to the maxima of the entire (omnidirectional) data set. Consistency between directional and omnidirectional distributions is ensured by requiring that the product of the n directional annual non-exceedance probabilities equals the omnidirectional, i.e.:

$$\prod_{i=1}^{n} F_i\left(x, \hat{\theta}_i\right)^{N_i} = F_{omni}\left(x, \hat{\theta}_{omni}\right)^{N_{omni}} \qquad (13.12)$$

where N_i is the number of sea states or events for the i'th direction and $\hat{\theta}_i$, the estimated distribution parameter. This is ensured by estimating the distribution parameters for the individual distributions and then minimising the deviation:

$$\delta = \sum_{x_j} \left[-\ln\left(-N_{omni} \ln F_{omni}\left(x, \hat{\theta}_{omni}\right)\right) + \ln\left(-\sum_{i=1}^{n} N_i \ln F_i\left(x_j, \hat{\theta}_i\right)\right)\right]^2 \qquad (13.13)$$

Here x_j are extreme values of the parameter for which the optimisation is carried out, i.e., the product of the directional non-exceedance probabilities is forced to match the omnidirectional for these values of the parameter in question.

The directional extremes presented in this report are given without scaling, that is, a T_{yr} event from direction i will be exceeded once every T years on the average. The same applies for monthly extremes. A T_{yr} monthly event corresponds to the event that is exceeded once (in that month) every T years, which is the same as saying that it is exceeded once every *T*/12 years (on average) of the climate for that month.

13.4.1 Optimised directional extremes

The directional extremes are derived from fits to each subseries data set meaning that a T_R year event from each direction will be exceeded once every T_R years on average. Having e.g., 12 directions, this means that **one** of the directions will be exceeded once every T_R/12 years on average. A 100-year event would thus be exceeded once every 100/12 = 8⅓ years (on average) from **one** of the directions.

For design application, it is often required that the summed (overall) return period (probability) is T_R years. A simple way of fulfilling this would be to take the return value corresponding to the return period T_R times the number of directions, i.e., in this case the 12x100 = 1200-year event for each direction. However, this is often not optimal since it may lead to very high estimates for the strong sectors, while the weak sectors may still be insignificant.

Alternatively, an optimised set of directional extreme values may be produced for design purpose in addition to the individual values of directional extremes described above. The optimised values are derived by increasing (scaling) the individual T_R values of the directions to obtain a summed (overall) probability of T_R years while ensuring that the extreme values of the strong sector(s) become as close to the overall extreme value as possible. In practice, this is done by increasing the T_R of the weak directions more than that of the strong sectors but ensuring that the sum of the inverse directional T_R's equals the inverse of the targeted return period, i.e.:

$$\sum_{i=1}^{n} \frac{1}{T_{R,i}} = \frac{1}{T_{R,\mathrm{omni}}} \tag{13.14}$$

where n is the number of directional sectors and $T_{R,omni}$ is the targeted overall return period.

13.5 Uncertainty assessment

The extreme values are estimated quantities and therefore all associated with uncertainty. The uncertainty arises from several sources:

Measurement/model uncertainty

The contents of the database for the extreme value analysis are associated with uncertainty. This type of uncertainty is preferably mitigated at the source – e.g., by correction of biased model data and removal of obvious outliers in data series. The model uncertainty can be quantified if simultaneous good quality measurements are available for a reasonably long overlapping period.

True extreme value distribution is unknown

The distribution of extremes is theoretically unknown for levels above the levels contained in the extreme value database. There is no justification for the assumption that a parametric extreme value distribution fitted to observed/modelled data can be extrapolated beyond the observed levels. However, it is common practice to do so, and this obviously is a source of uncertainty in the derived extreme value estimates. This uncertainty, increasing with decreasing occurrence probability of the event in question, is not quantifiable but the metocean expert may minimise it by using experience and knowledge when deciding on an appropriate extreme value analysis approach. Proper inclusion of other information than direct measurements and model results may also help to minimise this type of uncertainty.

Uncertainty due to sampling error

The number of observed/modelled extreme events is limited. This gives rise to sampling error which can be quantified by statistical methods such as Monte Carlo simulations or bootstrap resampling. The results of such an analysis are termed the confidence limits. The confidence limits (see Section 13.6) should **not** be mistaken for the total uncertainty in the extreme value estimate.

Settings of the analysis (judgement)

Any EVA involves the need to define the various settings of the analysis (threshold, distribution, and fitting method), which introduces subjectivity to the analysis. The sensitivity of these settings can be assessed by comparing the resulting extreme values, and the goodness of fit can, to some extent, be objectively assessed by statistical measures. However, standard practice typically includes manual inspection of the fitted distributions. Hence, the final settings, and thus results, relies on the experience and preference of the metocean expert conducting the analysis ('engineering judgement'). The tail of the distributions (the values of long the return periods) can be particularly sensitive to the settings of the analysis.

13.6 Confidence limits

The confidence limits of extreme estimates are established from a bootstrap analysis or a Monte Carlo simulation.

The bootstrap analysis estimates the uncertainty due to sampling error. The bootstrap consists of the following steps:

1. Construct a new set of extreme events by sampling randomly with replacement from the original data set of extremes
2. Carry out an extreme value analysis on the new set to estimate T-year events

An empirical distribution of the T-year event is obtained by looping steps 1 and 2 many times. The percentiles are read from the resulting distribution.

In the Monte Carlo simulation, the uncertainty is estimated by randomly generating many samples that have the same statistical distribution as the observed sample.

The Monte Carlo simulation can be summarised in the following steps:

1. Randomly generating a sample consisting of N data points, using the estimated parameters of the original distribution. If the event selection is based on a fixed number of events, N is set equal to the size of original data set of extremes. If the event selection is based on a fixed threshold, the sample size N is assumed to be Poisson-distributed.
2. From the generated sample, the parameters of the distribution are estimated, and the T-year return estimates are established.

Steps 1 and 2 are looped numerous times, whereby an empirical distribution of the T-year event is obtained. The quartiles are read from the resulting distribution.

13.7 Joint probability analyses (JPA)

Values of other parameters conditioned on extremes of one variable are estimated using the methodology proposed in [37] (Heffernan & Tawn). This method consists in modelling the marginal distribution of each variable separately. The variables are transformed from physical space, X, to standard Gumbel space by the relationship:

$$Y = \mathrm{LN}\left(-\mathrm{LN}\left(F\left(X, \hat{\theta}\right)\right)\right) \quad (13.15)$$

where $\mathrm{F}(\mathrm{X}, \hat{\theta})$ denotes the distribution function of the variable, X, with estimated parameters, $\hat{\theta}$. No restriction is given on the marginal model of the variables. A combination of the empirical distribution for the bulk of events and a parametric extreme value distribution function fitted to the extreme tail of data was adopted here. For parameters which may have both a positive and a negative extreme such as the water level conditioned on wave height, both the positive and the negative extreme tail are modelled parametrically.

The dependence structure of the two variables is modelled in standard Gumbel distribution space, conditioning one variable by the other. The model takes the form:

$$(Y_2 | Y_1 = y_1) = a y_1 + y_1^b Z \quad (13.16)$$

with Y_1 being the conditioning variable and Y_2 the conditioned. The residual, Z, is assumed to converge to a normal distribution, G, with increasing y_1. The parameters, $\hat{a}$ and $\hat{b}$, are found from regression and the parameters, $\hat{\mu}$ and $\hat{\sigma}$, of the normal distribution, G, estimated from the residuals, Z:

$$Z = \frac{y_2 - a \cdot y_1}{y_1^b} \quad (13.17)$$

Figure 13.2 shows an example of the modelled dependence structure for H_{m0} and water level in standard Gumbel space. Figure 13.3 shows the same in physical space. The model is clearly capable of describing the positive association between wave heights and water level for this condition and appears also to capture the relatively large spreading.

The applied joint probability model is event-based. This means that independent events of the conditioning parameter are extracted from the model data. The combined inter-event time and inter-event level criterion described in Section 13.1 is applied to isolate independent events of the conditioning parameter. The conditioned parameter is extracted from the model time series at the point in time of the peak of the conditioning parameter. Time averaging of the conditioned parameter is often carried out prior to data extraction to reduce the influence of phases in the analysis (the fact that the water level may not peak at the same time as the peak wave height for instance).

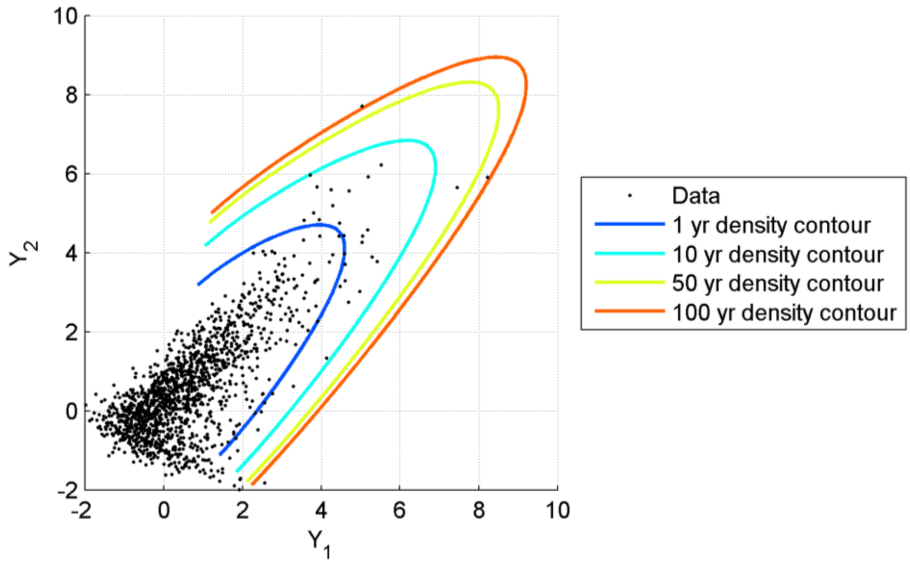

Figure 13.2 Dependence structure of H_{m0} and water level transformed into standard Gumbel space.

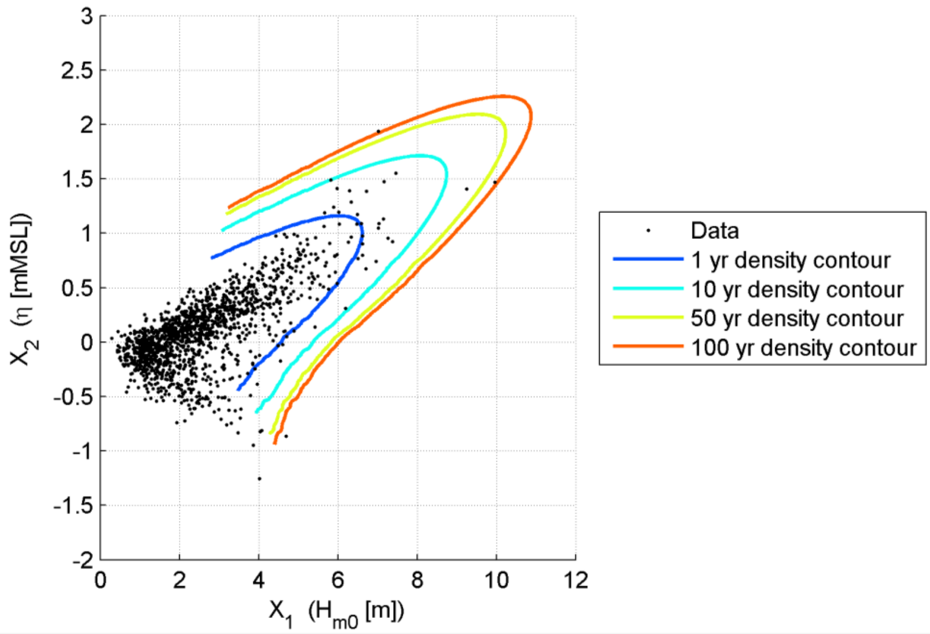

Figure 13.3 Dependence structure of H_{m0} and water level in physical space

14 Appendix D: J-EVA Summary

This section gives a generic overview of the Joint-Extreme Value Analysis (J-EVA) methodology applied to provide extreme estimates of metocean variables (e.g., H_{m0} and C_{max}). Aspects specific to EINS are also discussed.

14.1 Joint Extreme Values Analysis (J-EVA)

J-EVA (Joint-Extreme Value Analysis) is DHI's implementation of a consistent directional-seasonal extreme value analysis method incorporating a Markov Chain Monte Carlo (MCMC) Bayesian inference approach to include uncertainties. It is based on the work in [38].

J-EVA comprises of two models, 1) a storm model (see Appendix E: J-EVA – Storm Model), and 2) a statistical model (see Appendix F: J-EVA – Statistical Model). Both models are outlined in the following subsections which highlight the most relevant components of each. A concise step-by-step overview of the J-EVA methodology is as follows:

1. Extreme events (storms) are identified from either modelled hindcast according to criteria ensuring independent events. At EINS, the local peaks are identified from the corresponding time series of the variables for which extreme values are estimated, requiring at least 36 hours between peaks and a required drop in the time series value of 0.7 times the value of the lowest of the surrounding peaks. The start and end cut-off of the selected storm is set to 0.5 × maximum value of the time series.
2. Characteristic storm variables are computed as explained in Section 14.2.
3. The identified storms that are selected by their peak magnitude and duration are further filtered using regression quantile and (only for wave parameters) inverse wave age criteria.
4. From the J-EVA statistical model a spline model is constructed and fitted (both marginal distributions and conditional distributions between the storm parameters) to the storms with covariates for direction (e.g., wave or current direction) and season (e.g., months) when appropriate. The spline model varies smoothly across the covariates.
5. Posterior distributions of model parameters are found using a Markov Chain Monte Carlo (MCMC) approach. The posterior predictive distributions implicitly include uncertainties through the propagated errors in the prediction.
6. Many events (typically 1,000,000 years) are sampled from the posterior distributions and then real storm trajectories (displaying intra-storm variation and hence resolving the individual sea states) are simulated from matching the simulated storms with the historical storm time series using the J-EVA storm model. The EINS specific inputs are mentioned in Section 14.4 - 14.4.2.
7. Extreme values with return period T_r-years are then given by the $(N/T_r)^{th}$ largest value in N years of simulations.

While presenting the results of the J-EVA analysis, a credible interval is always presented as a shaded area. A credible interval is a concept used in Bayesian statistics, which is the central theme of the J-EVA analysis. The concept of credible interval is very different from the concept of the confidence interval used in Frequentist statistics approach. A credible interval is simply the central portion of the posterior distribution that contains a chosen percentage of the values. At EINS, a range of 2.5% - 97.5% interval is chosen that is equal to 95% credible interval. In other words, given the observed (simulated) data characterised by the likelihood function, the effect that is characterized by the posterior distribution has a 95 % probability of falling within this range.

14.2 J-EVA storm model

The J-EVA storm model makes use of the evolution in time (also termed intra-storm evolution) of historical storm events to make predictions of the evolution in time of possible events with extremely low exceedance probability.

A detailed description of the J-EVA storm model is given in Appendix E: J-EVA – Storm Model and in Section 2 of Hansen, et al. [38]. Outlined here is a concise description of the storm model.

Storm events evolve in time with a build-up phase, a storm peak, and a decay as the storm moves away and/or a low-pressure system decay. It is important to accurately model this time evolution and not just the storm peak itself, as the time evolution has a direct impact on the short-term response, e.g., C_{max}. Directionality is also important in this context as wind and wave direction typically shift during a storm passage. The J-EVA storm model is used to capture this evolution of relevant metocean variables (H_{m0}, T_p, WS_{10} etc.) in storm events.

The individual waves and crests are stochastic processes with distributions conditional on the underlying sea state properties. This also means that not only storm peak H_{m0}, but also storm duration become important. These are estimated in the J-EVA storm model.

A storm that lasts for many hours is more likely to produce an abnormal wave crest compared to a storm that decays rapidly. This was already treated by Tromans and Vanderschuren in their most probable maximum response model [39]. The application of the Tromans and Vanderschuren model has been adapted to characterise the storm magnitude, not by the most probable maximum response, but rather by the storm peak significant wave height $H_{m0,peq}$ of an ‘‘equivalent storm’’ exhibiting a Gaussian bell-shaped profile in time. Storm duration is then quantified using the standard deviation σ_{eq} of the Gaussian bell, expressed in multiples of the spectral zero-crossing period. The latter is like Tromans and Vanderschuren' N parameter. Read further in Section 15.2 of Appendix E: J-EVA – Storm Model and Section 2.1 of Hansen, et al. [38].

14.2.1 Directional and seasonal variability

J-EVA treats directional and seasonal variations in the statistical distribution of metocean variables (e.g., H_{m0}) using non-stationary extreme value distributions. This means that the distributions can vary with season and direction, according to the information in the historical extreme events. The non-stationarity is implemented using penalised B-splines that allow for smooth variations of distribution parameters in multiple dimensions. This is done to capture the significant directional and seasonal variations in the wind, wave, and current conditions at EINS. Read further on the penalised B-splines in Section 2.2 of Hansen, et al. [38].

For datasets with directionally or seasonally distinct distributions, it is possible to use only one covariate. For example, the marginal distribution of water level is direction-less and only fitted with a seasonal covariate at EINS.

14.3 J-EVA statistical model

The J-EVA statistical model is used to estimate the statistical distribution of the characteristic storm values of the metocean variables returned by the J-EVA storm model.

A detailed description of the J-EVA statistical model is given in Appendix F: J-EVA – Statistical Model and Section 2.2 of Hansen, et al. [38].What follows is an outline of the basis of the statistical model.

This model has a three-step process; 1) the independent estimate of non-stationary marginal models for each model parameter; 2) the estimation of the non-stationary conditional extreme models; and 3) the estimation of the rate of occurrence of storm events by a Poisson process. All parameters in 1) to 3) are inferred by Markov Chain Monte Carlo (MCMC) Bayesian inference.

MCMC is a statistical method to approximate a posterior distribution by randomly sampling in a probabilistic space, hence it utilises the known data. This technique has the advantage that the model parameters of interest are represented by statistical posterior distributions rather than fixed values and hence also provides an estimate of the uncertainty.

The marginal distributions are estimated using the assumption that the marginal probability distribution of each variable can be expressed as the sum of three parts. The first part describes the bulk of the data by a truncated gamma distribution using Bayesian inference with sample log-likelihood. While the second and third parts consisting of the upper and lower tails (if relevant) are then assumed to follow Generalised Pareto (GP) distributions. The tails are defined as exceedances of upper and lower quantile thresholds of the marginal distribution given covariates with specified non-exceedance probabilities.

14.3.1 Estimation of the model parameters

The estimation of the model parameters is carried out using Bayesian MCMC techniques. Model parameters, in this case, refer to the distribution parameters for the truncated gamma and GP distributions. Rather than using a single value for the model parameters, this method utilises a distribution of the model parameters which are then sampled from. A prior, or best-guess, based on the hindcast data is used to initiate the MCMC method.

J-EVA integrates over uncertainty when providing extreme value estimates. This type of extreme value estimate is called posterior predictive. This is particularly important when J-EVA returns extreme value estimates for return periods far beyond the duration of the historical time series (from measurement or hindcast) used for estimation, as the uncertainty in the estimates increases for increasing return periods. By integrating over the uncertainty, one accounts for the increased uncertainty and the provided extreme value estimates become more robust.

Posterior predictive distributions of metocean variables (e.g, H_{m0}, CS) are obtained by simulating many years, i.e., integrating across the posterior distributions of the model parameters. In practice this is done by integrating over a random set of iterations in the MCMC chains. Extreme values for various return periods are given by quantiles of the posterior predictive distributions (see Eq. 14.1) Using this approach, the extreme values provided by J-EVA implicitly include statistical uncertainty in contrast to T-EVA used by DHI where bootstrapping is often performed providing confidence intervals.

The extremes calculated from shorter hindcast time series are not necessarily higher than extremes obtained from longer time series (even though the statistical uncertainty is higher), as the estimated extremes depend on the data itself. However, when everything else is equal, increased uncertainty will result in increased extreme value estimates, when posterior predictive estimation is used.

Results in the form of posterior predictive extreme values (of e.g., H_{m0}, C_{max}) are obtained from quantiles (q_r) in the distribution of the annual maximum. The relationship between quantile and return period is given by:

$$q_r = \exp\left(-\frac{1}{T_r}\right) \quad \textbf{Eq. 14.1}$$

For the evolution of each storm event needed for determining the long term distributions of the short-term responses (H_{max} and C_{max}) the J-EVA storm model is applied again to scale the simulated events with the physical correct historical events. A cross validation scheme is applied to evaluate the predictive power of the spline model.

14.3.2 Conditional extreme model

A conditional extremes model, adopted from Heffernan and Tawn, [37], is used to model the joint probabilities. This type of joint probability model models the distributions of variables conditioned on one of the variables being extreme and is therefore useful for modelling the distribution of e.g., wave period or water level conditioned on extreme significant wave height. Figure 14.1 shows an example of a joint distribution of T_p and H_{m0} from 50,000 years simulated data compared to hindcast data. Likewise, parameters relevant for C_{max} (i.e., T_{01} and T_{02} and WL) are conditioned on extreme H_{m0}.

The conditional extreme model is further described in Section 1.4 and Section 5.3 of Hansen, et al. [38].

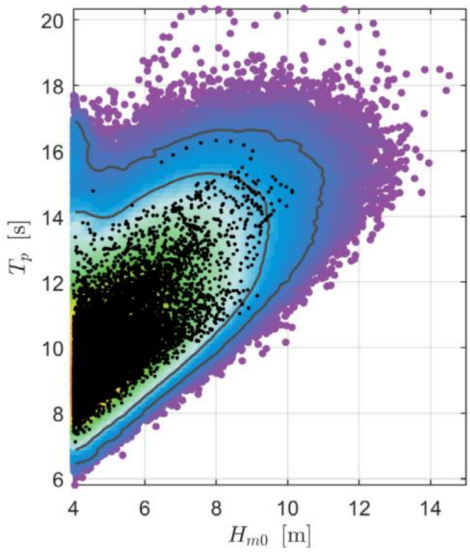

Figure 14.1 Example of joint distribution of T_p and H_{m0} [38].
T_p on H_{m0} for each sea-state in the simulated storms. Scatter plots of 50,000 years of simulated data (coloured round markers) compared to hindcast data (black dots); ''warmer'' colours indicate a higher rate of occurrence of simulated events. Solid lines represent directional density contours for the 10- and 100-year marginal extreme values.

14.4 J-EVA simulation

The concept of simulation is used to obtain the extreme value estimates based on the fitted statistical model parameters as explained in Section 14.3.1 and 14.3.2. The number of exceedances N_e of an extreme value is used as input, which is then applied on the largest chosen return period T_r. At EINS, the largest T_r = 10,000 years, so, if N_e is chosen as 50, then the number of simulations carried out for estimating the 10,000-year extreme are $5x10^5$. Extremes estimated for T_r<10,000 years will then have more exceedances contributing to the robustness of the estimate.

14.4.1 Directional Scaling

The concept and the need of directional scaling is explained in Forristall [40]. The concept itself is independent of the method used for estimating the extreme values. The directional scaling is applied to the estimated directional extremes following the recommendations in DNV [41].

In J-EVA, the implementation is carried out while simulating the extremes. In summary, a two-step scaling procedure is implemented for the marginal extremes.

1. The directional extremes are simulated for return periods corresponding to half the number of directional sectors. At EINS, this corresponds to simulating the directional extremes for return periods T_r = [1, 5, 10, 50, 80, 100, 1000, 10000] x 16/2 = [8, 40, 80, 400, 640, 800, 8000, 80000] years.
2. The estimated directional extremes are capped with the omnidirectional extreme corresponding to the original return periods. For example, if in step 1, the estimated H_{m0} = 14.9 m corresponding to a direction of 315° mean wave direction for T_r = 80000 years, then it is capped with H_{m0} = 14.6 m that corresponds to an omnidirectional H_{m0} for T_r = 10000 years.

The estimated fit parameters based on the unscaled extremes are used to evaluate the conditioned variables of the scaled extremes.

14.4.2 Simulation Optimization

The simulations used to obtain the extreme value estimates are optimised depending on the requested return periods, such that the very long simulations required to estimate extreme values with long return periods only include the relevant events above a high threshold. Shorter simulations with no threshold are then made for the short return period extremes. At EINS, because the directional scaling is applied, the largest T_r = 80,000 years. The optimization is carried out such that up to $T_r \leq 100$ years, the estimates are based on simulations of 80,000 years, while for $100 < T_r < 80{,}000$, the estimates are based on simulations of $N_e \times 80{,}000$ years.

14.5 Convolution of short-term distributions

The predicted events from the J-EVA storm model are numerically folded with the wave height and crest level distributions (e.g., Forristall [42] or Glukhovskiy [43]) to estimate the long-term distribution of the individual wave heights and crest levels. For further information, the reader is referred to Section 4 of Hansen, et al. [38].

The residual water level is modelled conditionally on the extreme significant wave height. A residual water level therefore becomes available for every storm and for every sea state in the storm such that it can be used in the short-term distribution.

14.6 Sampling of tidal signal

Tide is a deterministic process and thus not eligible for extreme value assessments assuming a random population, hence, to comply with statistical requirements, tidal variations are introduced separately to the extreme value estimation.

Water levels concurrent with waves are introduced via a model for the distribution of residual water level conditional on extreme H_{m0}, followed by the addition of a sampled tidal signal. By using this method, it has been assumed that the tide has no influence on H_{m0} nor on the residual water level. This assumption is often valid in intermediate to deep waters but may not be valid in shallow areas with the significant tide.

Tidal water level signals are sampled for every storm event from a hindcast tidal data series from within a period with similar seasonality to account for seasonal bias. The total water level, i.e., the distance from a fixed datum (MSL or LAT) to the still water level (SWL), is the sum of the residual and tidal water levels. It is, therefore, straightforward to include the effect of tide and surge on the extreme crest elevations in a statistically consistent manner.

Similarly, tidal current flow is sampled and combined with the residual current flow conditioned on the extreme waves.

14.7 Limitations on wave height

Wave breaking is implicitly accounted for via a depth-dependent reduction in the hindcast modelled H_{m0} (due to increased energy dissipation in the white-capping, bottom-friction, and wave breaking source terms).

Furthermore, for the long-term distribution of $H_{m0,peq}$ (equivalent peak H_{m0} from the storm model) has been limited to 0.6 times the water depth in the statistical model. This is considered a conservative estimate of the maximum depth-limited significant wave height.

Actual evidence of depth limits to significant wave height in field data sets is very rare. However, based on previous experience including literature studies, there is no knowledge of values higher than 0.6 being reported anywhere.

In exposed and shallow areas, this will significantly limit the tail of the H_{m0} distribution, see Figure 14.2 for a graphical example. The extrapolation of the extreme distribution extends past the expected physical limit of 0.6 times the water depth (in this example case, the water depth is approximately 17m).

Wave breaking is however not accounted for in the Forristall short-term distribution of C_{max} and only indirectly for some short-term distributions of H_{max}. (i.e., the Glukhovskiy distribution).

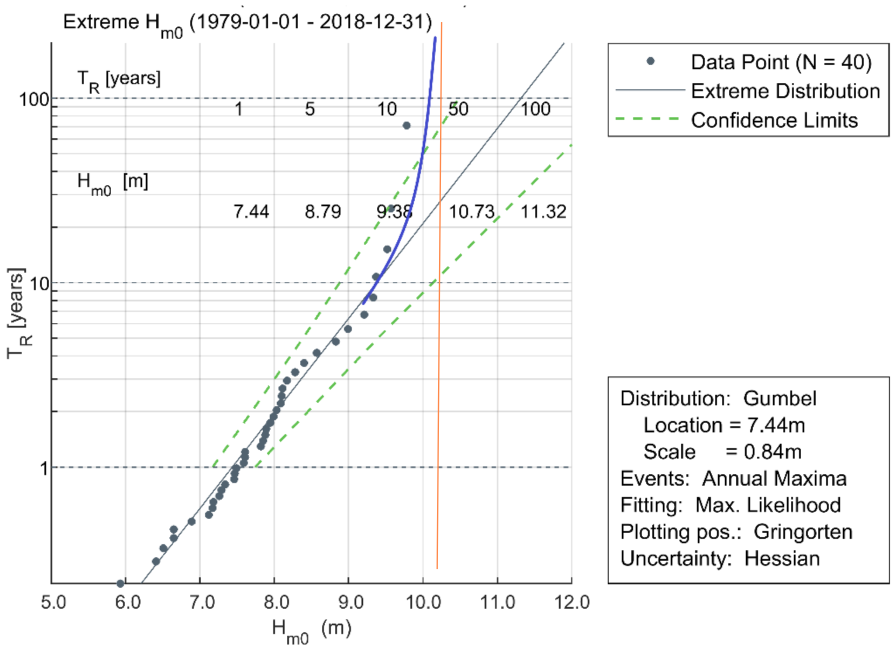

Figure 14.2 Example of extreme value distribution of H_{m0} at a water depth of 17 m with a Gumbel distribution fitted to the annual maxima using maximum likelihood (grey line). No limiting wave breaking is inferred. Upper limit of H_{m0} assumed as 0.6 x 17 = 10.2m shown by the orange line.

In such cases the limit of H_{m0} due to water depth in the J-EVA storm model would effectively reduce the extreme H_{m0} at the tail, also below the actual limit, i.e., towards the blue line.

15 Appendix E: J-EVA – Storm Model

The theory and methodology behind the DHI J-EVA storm model are described here. The methodology is based on the work presented in Hansen et al. (2020)[44].

The J-EVA (Joint-Extreme Values Analysis) storm model is a model for the description of wave characteristics of storm events. The model is used in conjunction with the J-EVA statistical model to describe the long-term distribution of individual wave and crest heights and possibly also wave-induced structural loading.

The model defines characteristic storm variables from the historical hindcast or measured record of slowly time-varying variables such as (but not limited to) significant wave height, peak period, mean or peak wave direction, storm surge and wind speed. These characteristic values are suitable for statistical modelling using the J-EVA statistical model. The statistical modelling of characteristic storm variables will allow for generation of long series of simulated storm parameters. The J-EVA storm model can then be applied in reverse to generate intra-storm time series of the slowly varying variables.

Numerical folding with any short-term distribution model of wave or crest height or a structural load or load response may be carried out on the intra-storm time series to generate the long-term distribution of the response.

15.1 Characterisation of Historical Storms

The J-EVA storm model is applied on a time series of slowly varying environmental variables. This time series must include the significant wave height and a measure of the mean wave period but can include any other environmental variable of interest. The time series must be on an equidistant time axis with sufficiently small-time step size that the time-evolution of the storm events of interest are adequately resolved.

The steps followed to convert this continuous time series into individual storm events and then to characterise each event are described in this section.

15.2 Wave Height and Storm Duration

Storm events are identified by their significant wave height. Standard metocean techniques for separating the continuous time series of significant wave heights into individual (storm) events consist in defining a minimum time separation between consecutive storm peaks and moreover often an additional requirement that the level must have dropped below a fraction of the minor of consecutive peaks in order for those to be defined as two separate events. This additional requirement ensures that storms with long durations are not unintentionally split into separate events.

The time series of H_{m0} is de-clustered into independent events by requiring that there is a pre-specified minimum interevent time between events. The minimum interevent time is dependent on the meteorological events generating the storms but is typically in the order of 18-36 hours for extra-tropical cyclones. Moreover, events are only separated if the significant wave height has passed below 75% of the minor of two adjacent events.

The distribution of the maximum short-term response in each historical storm is then calculated. The empirical short-term distribution of individual wave height H conditional on H_{m0} by Forristall (1978) is typically applied, though the actual choice of short-term distribution model is not important, as long as the distribution is continuous. The Forristall (1978) short-term distribution of H conditional on H_{m0}, $P(H < h|H_{m0})$, is given by:

$$P(H < h|H_{m0}) = 1 - \exp\left(-\left(\frac{h}{0.681H_{m0}}\right)^{2.126}\right) \tag{15.1}$$

The distribution of the maximum wave in storm i, $H_{max,i}$ is given by the following product over the n_i sea states making up storm i:

$$P(H_{max,i} < h) = \prod_{j=1}^{n_i} P(H < h|H_{m0,j})^{N_j} \tag{15.2}$$

The number of waves in sea state j, N_j, is estimated by dividing the duration of the sea state (time step size in the input time series) by the mean zero-crossing period[4] over the sea state. The most probable storm maximum wave height, $H_{mp,i}$, is found by solving the following equation for h:

$$P(H_{max,i} < h) = \frac{1}{\exp(1)} \approx 0.37 \tag{15.3}$$

It is shown in the original work by Tromans and Vanderschuren (1995), that when $P(H|H_{m0})$ is of a Weibull type distribution, Eq. (15.2) converges to a generalised Gumbel distribution:

$$P(H_{max,i} < h) \sim \exp\left(-\exp\left(-\ln N_i\left(\left(\frac{h}{H_{mp,i}}\right)^{\alpha} - 1\right)\right)\right) \tag{15.4}$$

where α is the shape factor of the wave height distribution (=2.126 in the Forristall 1978 distribution) and N_i is the equivalent number of waves in the storm.

The duration of the storm and thereby the value of N is related to the narrowness of the distribution of the storm maximum wave. Storms with long durations and thereby many sea states of similar magnitude will have a narrower distribution of the storm maximum wave, compared to those storms in which the maximum wave will come within a relatively short period in time (i.e. within very few sea states).

This property is used in the J-EVA storm model to characterise storms by peak magnitude and a duration. A Gauss-bell shaped curve is chosen to represent the variation in time of H_{m0}. The variation in time of H_{m0} is defined by equivalent storm peak, H_{m0}, hereafter termed $H_{m0,p,eq}$, and equivalent storm duration given by the Gauss-bell standard deviation, σ_{eq}, as:

$$H_{m0}(t^*) = H_{m0,p,eq} \times \exp\left(-\frac{(t^*)^2}{2\sigma_{eq}^2}\right) \tag{15.5}$$

t^* is a pseudo-time measured in *number of wave cycles* and can be converted to true time by use of the slowly varying mean wave period. Thus, $t^* = 0$ at the storm peak ($H_{m0} = H_{m0,p,eq}$) and any $t^* < 0$ defines the number of wave cycles

---

[4] The second moment period T_{02} is used as a proxy for the zero-crossing period when spectral wave model hindcast data is used as input

that will pass before the storm peak is reached, whereas any $t^* > 0$ defines the number of wave cycles that have passed since the storm peak.

Best-fit values of the peak ($H_{m0,p,eq}$) and standard deviation (σ_{eq}) of the Gauss-bell shaped storm are found by mean-square error minimisation of the differences between the actual storm maximum wave height probability density and that of the Gauss-bell shaped storm. The minimisation is carried out as follows:

Sea states with $H_{m0} < 0.75 \times H_{m0,p,eq}$ are found to have insignificant impact on the distribution of storm maximum wave height and can be neglected[5]. From Eq. (15.5), we have that the Gauss-bell shaped storm will cross under 75% of $H_{m0,p,eq}$ at a distance from the peak of $0.759\sigma_{eq}$ waves. Hence, we create an evenly spaced vector, $\boldsymbol{t}_m^*$ of m points, $\boldsymbol{t}_m^* \in [-0.759\sigma_{eq}; 0.759\sigma_{eq}]$ and evaluate H_{m0} along this vector for storm i:

$$H_{m0}(\boldsymbol{t}_m^*) = H_{m0,p,eq,i} \times \exp\left(-\frac{(\boldsymbol{t}_m^*)^2}{2\sigma_{eq,i}^2}\right) \tag{15.6}$$

Each point along this vector represents a sea state of $1.52\sigma_{eq,i}/m$ waves. The distribution of the maximum wave in the storm is now given by Eq. (15.2), i.e.:

$$P(H_{max,i} < h) = \prod_{j=1}^{m} P\left(H < h | H_{m0}(t_{m,j}^*)\right)^{1.52\sigma_{eq,i}/m} \tag{15.7}$$

The probability density is obtained by numerical differentiation of Eq.(15.7) and the squared difference of this probability density function and that of the actual storm is computed. Minimisation of the squared difference is carried out by changing the values of $H_{m0,p,eq,i}$ and $\sigma_{eq,i}$, whereby best-fit values of these parameters are obtained for storm i.

Two examples of storm characterisation are shown in Figure 15.1. The first storm (top panel) is an example of a persistent storm lasting for many hours, while the second storm (bottom panel) is more intense in its peak but lasting only a few hours. These differences are reflected in the relative values of $H_{m0,p,eq}$ and σ_{eq}.

15.3 Associated Environmental Variables

Characteristic storm values of all associated environmental variables to be included in the subsequent joint-probability analysis are required. Examples associated variables are:

- Peak wave direction, PWD
- Peak period, T_p
- Second moment period, T_{02}
- Directional spreading, σ_θ
- Residual water level, WL_{rsdl}
- Residual current speed, CS_{resi} and direction CD_{rsdl}
- Wind speed, WS and wind direction WD

---

[5] Though sea states with less than 75% of the peak significant wave height have negligible influence on the most probable maximum wave in the storm, sea states down to 65% of peak significant wave height have been included in the build-up of the storm, as these typically contain some of the steepest sea states, and the maximum wind speed may also fall early in the storm trajectory.

These variables vary during the storm and weighted average values are calculated to provide a characteristic value of the variable for each storm. The weight factor, w_j, for sea states $j, j = 1{:}\,n_i$ where n_i is the number of sea states in storm i, are computed from the contribution of the individual sea states to the total storm most probable maximum wave, H_{mp}:

$$w_j = \alpha\left(H_{mp,1:n} - H_{mp,1:n,\sim j}\right) \qquad (15.8)$$

where $H_{mp,1:n}$ is the most probable maximum wave height of the storm considering all sea states in the storm and $H_{mp,1:n,\sim j}$ is the most probable maximum wave height when sea state j is omitted and α is

a normalisation factor. An overbar (e.g. $\overline{T_p}$) is used to denote a characteristic (weighted average) value of an environmental variable.

The characteristic storm second moment period $\overline{T_{02}}$ is shown in Figure 15.1 for the two examples storms. $\overline{T_{02}}$ takes values close to the values at the storm peak.

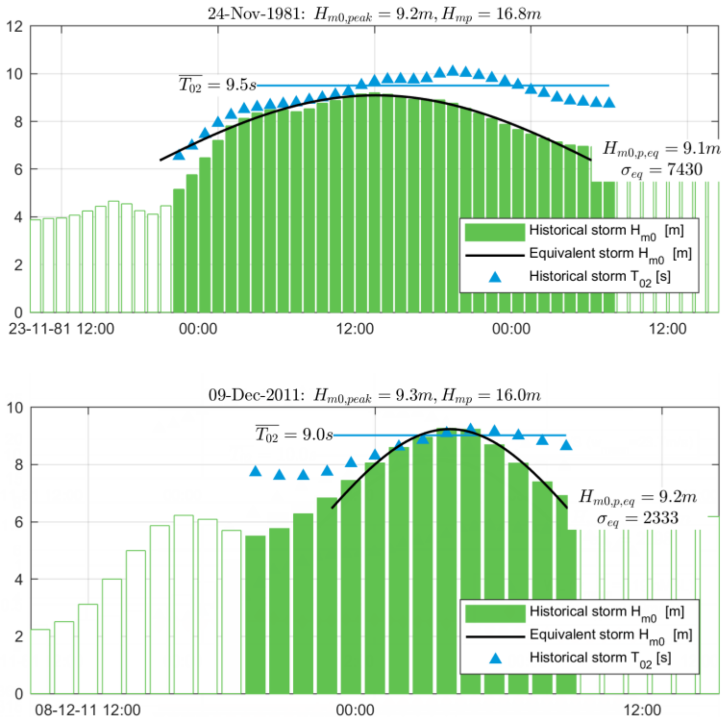

Figure 15.1 Two examples of hindcast historical storms and storm model parameterisation.
Vertical green bars[6]: Hourly values of H_{m0}. Blue triangles: Hourly values of T_{02}. Characteristic storm variables $H_{m0,p,eq}, \sigma_{eq}$ and $\overline{T_{02}}$ values printed on figure.

[6] The filled bars mark the sea states which are retained from each storm for subsequent intra-storm simulation, see section 15.4.

15.4 Simulation of Intra-Storm Variation

The J-EVA storm model is also used to simulate intra-storm variation of the environmental variables model. The intra-storm variation refers to the hourly variation of the variables during a storm event exemplified by for instance the build-up and subsequent decay of wind speed and significant wave height, the rotation of the mean wave direction and the increase in wave age from steep young wind waves during build-up to swell waves during storm decay.

The simulation of intra-storm variation consists in matching up simulated storms with similar historical storms followed by a scaling of the similar historical storm time series.

15.4.1 Similarity and Storm Resampling

A methodology developed to identify the historical storms most similar to the simulated storm is described in this section. The method builds on a flexible concept of storm dissimilarity. The smaller the dissimilarity, the more representative the historical storm is assumed to be of the simulated storm.

The dissimilarity criteria are established in order to select a historical storm to represent the storm modelled through the J-EVA statistical model. The dissimilarity criteria are inspired by Feld et.al (2015).

In the following, Ω is used to denote any characteristic storm variable (e.g. $H_{m0,p,eq}$ or $\overline{T_p}$) and ω to denote the corresponding intra-storm variable (H_{m0} or T_p).

Dissimilarity is first calculated for each variable listed below as follows for historical storm, i, and simulated storm, k:

$$d_{\Omega,\mathrm{i,k}} = \left|\Omega_{HIST,i} - \Omega_{SIM,k}\right| / \sigma_\Omega \tag{15.9}$$

with σ_Ω[7] being the standard deviation of this variable through all included historical storms. This weight factor is found to provide a reasonable balance between the various variables, but it is possible to apply weight factors in addition to this, in order to better match for instance significant wave height between historical and simulated storms.

Dissimilarities are calculated for the relevant variable which may be considered important in terms of describing the storm evolution.

Overall storm dissimilarity for simulated storm k, d_k, is calculated by summing up the square of the individual dissimilarities, for each historical storm, i.e.:

$$d_k^2 = \sum_{i=1}^{n} \sum_{\Omega=1}^{v} d_{\Omega,\mathrm{i,k}}^2 \tag{15.10}$$

where $\Omega = 1{:}\,v$ represent the v different environmental variables included in the dissimilarity criterion. After having ranked the historical storms in terms of (dis)similarity, one of the most similar historical storms is picked randomly amongst the least dissimilar ones. The randomly selected storm is then used to represent the intra-storm variability of the modelled storm, after appropriate scaling (see next section) is conducted.

[7] σ_{MWD} and σ_{Season} correspond to half of the standard deviation of the corresponding parameters, to account for their periodicity.

Typically, the representative storm is selected amongst the 20 most similar storms, but the end results are not very sensitive to this number because of the applied scaling.

15.4.2 Historical Storm Scaling

Having sampled a historical storm amongst the most similar ones, the intra-storm variation of the historical storm is scaled such that the characteristic storm variables of the scaled storm matches those of the simulated storm.

The proposed scaling methodology assumes that a constant scaling factor applies for the entire storm. As water levels vary around zero, a reference level of 10 meters below the sea surface is used in order to avoid division by zero.

Scaling of the selected historical storm variables to generate the time series of simulated storms is conducted as follows:

1. Establish a scaling or correction factor based on the characteristic storm variables of the simulated (subscript SIM) and selected historical storm (subscript $HIST$) using the generic formulation:

$$\alpha_{\Omega} = \Omega_{SIM} / \Omega_{HIST} \quad (15.11)$$

2. Correct the historical storm time series of parameter ω_{HIST} to obtain the intra-storm variability of the simulated storm, $\omega_{SIM.j}$, as follows (for time step j)):

$$\omega_{SIM,j} = \alpha_{\Omega} \cdot \omega_{HIST,j} \quad (15.12)$$

Specifically, for directional variables (wind, wave and current directions, here generalised by the notation θ), a rotation rather than scaling is applied:

$$\alpha_{\theta} = \overline{\theta_{SIM}} - \overline{\theta_{HIST}} \quad (15.13)$$

The intra-storm variability of the directional variable is then obtained as (at time step j):

$$\theta_k = \alpha_{\theta} + \theta_{HIST,j} \quad (15.14)$$

Typically, peak (or mean) wave direction is used as a co-variate (distributions vary with wave direction) and wind and current directions are not simulated in the J-EVA statistical model. In this case, the wave direction rotation factor, $\alpha_{\mathrm{PWD},}$ is also used to rotate the current and wind direction time series such that wind-wave and current-wave misalignment from the historical storm is maintained in the simulated storm.

For residual water levels, that can also take negative values, the scaling is done relative to a minimum level, WL_{ref}, that is never surpassed:

$$WL_j = \left(WL_{HIST,j} + WL_{Ref}\right)\frac{\overline{WL_{SIM}} + WL_{ref}}{\overline{WL_{HIST}} + WL_{Ref}} - WL_{Ref} \quad (15.15)$$

The reference water level could be taken as the water depth at the site, which in practice would mean that the water level in the simulated storm would be the water level in the historical storm shifted by the difference $\overline{WL_{SIM}} - \overline{WL_{HIST}}$. Typically, we use $WL_{Ref} = 10\ m$, which implies a moderate scaling of the water levels beyond the scaling that is coming from the simulated value from the long-term model, $\overline{WL_{SIM}}$.

In addition to the adjustment of the time series values, the time is also scaled in order to maintain the number of waves in the storm, and therefore keep H_{max} and C_{max} estimates the same. The time scaling is performed as follows:

$$Time_{SIM} = Time_{HIST} \cdot \alpha_{T_{02}} \cdot \alpha_{\sigma_{eq}} \tag{15.16}$$

with $\alpha_{T_{02}}$ and $\alpha_{\sigma_{eq}}$ being the scaling factors applicable for T_{02} and storm duration σ_{eq}, respectively.

It follows from this scaling method that an exact recovery of the historical storm is obtained in the case of an exact match between the simulated and historical characteristic storm variables.

Storms are defined to begin at the last up-crossing of 60% of peak H_{m0} prior to the peak and end at the first down-crossing of 75% of peak H_{m0} after the storm peak. Sea states with H_{m0} > 75% of peak H_{m0} are contributing to the distribution of the maximum wave within a storm. The extension down to 60% of peak H_{m0} at the storm build-up is introduced to ensure that the peak wind speed is included in the storm. The sea states thus included are marked as filled bars in Figure 15.1. Storm peaks must as a minimum be separated by the specified inter-event time, typically between 18 and 36 hours for extra-tropical cyclones, to be treated as separate events.

15.5 Heights and Periods of Individual Waves

The methods described in the previous sections define a way of developing time series of the slowly varying parameters (H_{m0}, T_p etc.) in each simulated storm, whereby we obtain the long-term distribution of the slowly varying parameters. From these time series we can easily derive the long-term distribution of individual wave and crest heights.

The individual wave and crest heights are stochastic variables conditional on the properties of the underlying sea state, and their distributions are typically termed the short-term distributions. We use Monte Carlo simulation to fold these short-term distribution with the long-term distribution of the underlying slowly varying sea state parameters. This Monte Carlo simulation involves sampling a maximum short-term response for every sea state in every simulated storm.

The Forristall crest height distribution is used here as an example of how to sample the hourly maximum of a short-term response. The inverse cumulative distribution function of the hourly maximum Forristall crest height is given by:

$$F^{-1}(\eta_{max}) = H_{m0}\alpha\left(-\ln\left(1 - P^{\frac{1}{N}}\right)\right)^{\frac{1}{\beta}} \tag{15.17}$$

where:

P	Non-exceedance probability	
N	Number of waves in sea state	($\approx 3600s/T_{02}$ for a one-hour sea state)

α	Distribution shape	$\sqrt{2}/4 + 0.2568S_1 + 0.0800Ur$ (Forristall Crest)
β	Distribution shape	$2 - 1.7912S_1 - 0.5302Ur + 0.2824Ur^2$ (Forristall Crest) $S_1 = \frac{2\pi}{g}\frac{H_{m0}}{T_{01}^2}$ $Ur = \frac{H_{m0}}{k_1^2 d^3}$
k_1	Wave number for frequency	$1/T_{01}$
d	Water depth	

The Monte Carlo analysis simply consists in sampling the non-exceedance probability P randomly and independently for every sea state and calculate the corresponding η_{max}. Note that the short-term distribution varies from sea state to sea state as the parameters H_{m0}, T_{01}, T_{02} and the water depth may vary (the latter due to effects of tide and surge). The long-term distribution of annual maximum crest height and corresponding extreme value estimates are derived by considering only annual maximum crest height, as explained in Eq. (15.5).

Crest height relative to a fixed datum are obtained by adding tide and surge values for each sea state prior to extraction of annual maxima.

15.5.1 Associated Wave Periods

The period of individual maximum waves (T_{Hmax}) will vary because of varying sea state characteristics (variability of T_p given H_{m0}) but also because of the randomness of the sea state itself. The most probable period, given a sea state (wave spectrum), is well approximated by the so-called linear new wave, [45], but there is obviously some random variability around this most probable value. This latter variability has been combined (convolved) with the random variability of the sea state characteristics by simulating linear random wave trains from a frequency spectrum for the sea states giving rise to the annual maximum waves and extracting the period of the highest wave from each simulation. Any frequency spectrum can be used for this, but the JONSWAP spectrum is typically adopted.

To obtain stable empirical conditional distributions of the wave periods many simulated sea states are required.

16 Appendix F: J-EVA – Statistical Model

This document describes the theory and methodology of the DHI J-EVA statistical model. The methodology is based on the work presented in Hansen et al. (2020)[46].

The J-EVA (Joint-Extreme Values Analysis) statistical model is a tool for making extreme value analysis of a set of parameters with a-priori unknown joint dependence properties. Application of J-EVA requires as input a set of independent ‘events’ with concurrent values of the parameters being modelled. A typical example is storm peak significant wave heights, associated wave period, storm surge, wind speed, but the tool is generic and can model any kind of stochastic non-discrete parameters, as long as they fulfil the requirements of independence and identical distribution (iid). The input data may come from measurements or numerical hindcast models or a combination hereof, and the usual requirements to data consistency and quality also apply here.

Covariates may be defined if a-priori knowledge about variations in extremal properties is suspected. Typical examples of covariates are direction and/or season. Non-parametric smooth variations with covariate(s) are implemented using a B-spline technique (see Section 16.3 for details) and periodicity (as is the case for both direction and season) is possible. The use of covariates also implies that the requirement of identical distribution only applies for random variables sharing the same covariates (as for instance waves from the same direction occurring during the same time of year). It is not recommended to apply the model across discontinuous (abrupt) covariate variations. Extreme value models incorporating covariates are called non-stationary extreme value model in the statistical literature.

The statistical uncertainty due to the typically limited sample size of historical extremes is estimated by the tool and may be propagated through to the end results. A Bayesian Markov Chain Monte Carlo (MCMC) technique is adopted (see Section 16.4 for details).

16.1 Model components

The J-EVA statistical model contains the following model components.

- Marginal models describing the marginal distribution of each parameter (i.e., the distribution of the parameter without considering the values of the remaining parameters)
- Rate of occurrence describing how often a parameter (event) occurs
- Conditional extremes model describing the distribution of other parameters conditional on a selected parameter being extreme

Each of the components is detailed below.

16.2 Marginal models

Marginal (univariate) distributions are fitted to each stochastic variable in turn. A combination of a gamma (Γ) distribution, modelling the bulk of the data, and Generalized Pareto (GP) tails modelling the distribution tails above a threshold is used for the marginal distributions. Whenever relevant, both the upper and lower tails are modelled with a GP distribution, the lower tail basically being a GP tail fitted to the reversed data below the low threshold.

$$P(x) = \begin{cases} P_\Gamma(u_1|\alpha,\mu)\left\{\left(1+\xi_1\dfrac{u_1-x}{\zeta_1}\right)^{-\frac{1}{\xi_1}}\right\} & ,x<u_1 \\ P_\Gamma(x|\alpha,\mu) & ,u_1 \le x \le u_2 \\ 1-\left(1-P_\Gamma(u_2|\alpha,\mu)\right)\left\{\left(1+\xi_2\dfrac{x-u_2}{\zeta_2}\right)^{-\frac{1}{\xi_2}}\right\} & ,x>u_2 \end{cases} \tag{16.1}$$

The gamma distribution is given by:

$$P_\Gamma(x|\alpha,\mu) = \frac{1}{\Gamma(\alpha)}\gamma\left(\alpha,\frac{\alpha}{\mu}x\right) \tag{16.2}$$

where $\Gamma(\alpha)$ is the complete gamma function and $\gamma\left(\alpha,\frac{\alpha}{\mu}x\right)$ is the lower incomplete gamma function.

The model parameters defining the marginal distributions are:

a	gamma distribution shape parameter
μ	gamma distribution mean parameter (gamma shape multiplied with gamma scale parameter)[8]
ξ_1	GP shape parameter for lower tail
ζ_1	GP scale parameter for lower tail[9]
ξ_2	GP shape parameter for upper tail
ζ_2	GP scale parameter for upper tail

The thresholds, at which the GP tails take over, are set as quantiles in the gamma distribution of the bulk data, i.e.

$$u_1 = P_\Gamma^{-1}(\kappa_1) \tag{16.3}$$

$$u_2 = P_\Gamma^{-1}(\kappa_2)$$

where κ is a constant (covariate-free) non-exceedance probability. Threshold uncertainty is included ensemble averaging results over a range of values for κ_1 and κ_2. These are sampled from a uniform distribution over a pre-set quantile interval.

The model parameters are estimated in a sequential way; first the gamma distribution is fitted to all data, then the threshold is calculated from the fitted gamma distribution and sampled threshold non-exceedance probability and

[8] The distribution parameters are practically uncorrelated with this formulation of the gamma distribution. This improves mixing of the MCMC chain
[9] As for the gamma distribution, an orthogonal parameterization has been used, where adjusted scale parameter, $\nu = \zeta(1+\xi)$, is sampled. For the ease of interpretation, the results are, however, presented for the scale parameter ζ.

finally the GP lower and upper tails fitted independently to the data sample below u_1/above u_2 respectively. The log-likelihood functions are:

$$\ell_{\Gamma,j}(\boldsymbol{z}|\boldsymbol{b}) = -\sum_{i=1}^{n}\left\{(\alpha-1)\ln z_{ij} - \frac{\alpha}{\mu}z_{ij} - \ln\Gamma(\alpha) - a(\ln\mu - \ln\alpha)\right\},$$

$$\ell_{GP_{LT},j}(\boldsymbol{z}|\boldsymbol{b}) = -\sum_{i:\, z_{ij}<u_1}\left\{\ln\zeta_1 + \left(1+\frac{1}{\xi_1}\right)\ln\left(1+\frac{\xi_1}{\zeta_1}(u_1 - z_{ij})\right)\right\} \tag{16.4}$$

$$\ell_{GP_{UT},j}(\boldsymbol{z}|\boldsymbol{b}) = -\sum_{i:\, z_{ij}>u_2}\left\{\ln\zeta_2 + \left(1+\frac{1}{\xi_2}\right)\ln\left(1+\frac{\xi_2}{\zeta_2}(z_{ij} - u_2)\right)\right\}$$

16.3 Rate of occurrence

The occurrence of events is considered a Poisson process and the Poisson annual rate of occurrence ρ is required for estimation of annual non-exceedance probabilities. In the covariate-free case, ρ is simply estimated by the total number of historical events divided by the length of the historical data series in years. In the case of covariates, the covariate domain is divided into m bins of constant area, Δ, and the rate the log-likelihood function of ρ approximated by [47]

$$\ell_{\rho,j}(\boldsymbol{z}|\boldsymbol{b}) = \sum_{k=1}^{m} c_k \ln\big(\rho(k\Delta)\big) - \Delta\sum_{k=1}^{m}\rho(k\Delta) \tag{16.5}$$

where c_k is the number of threshold exceedances in bin k.

16.4 Conditional extremes

The conditional extremes model by Heffernan & Tawn (2004), model distributions of parameters conditional on one parameter being extreme. This is useful for modelling for instance the distribution of spectral peak period or wind speeds when the significant wave height is extreme.

The original conditional extremes model proposed by Heffernan & Tawn makes use of probability integral transform to marginal distributions with standard Gumbel distributions. This introduces asymmetry in the marginal distributions and makes modelling of negatively dependent variables somewhat more complicated than positively dependent variables. Keef, Papastathopoulos, & Tawn (2013) propose a modification of the model replacing the Gumbel margins by Laplace margins whereby both positive and negative tails become exponential. This modification to the original model is applied in J-EVA.

The marginal distributions are defined over the entire range from the 'lower' end-point of the lower tail to the upper end-point of the upper tail by the combined Gamma-GP model (Eq. (16.1)).

Probability integral transformation to Laplace margins is given by:

$$Y_j = \begin{cases} \ln\big(2\mathrm{P}\,(X_j)\big), & \mathrm{P}\big(X_j\big) < 0.5 \\ -\ln\Big(2\big(1-\mathrm{P}(X_j)\big)\Big) & \mathrm{P}\big(X_j\big) \geq 0.5 \end{cases} \tag{16.6}$$

The Heffernan & Tawn (2004) conditional distribution for a set of variables with Laplace margins simplifies into one function for both positive and negative dependence (Keef, Papastathopoulos, & Tawn, 2013):

$$\left(Y_{j^c} | Y_j = y\right) = a_j y + y^{b_j} W_j \qquad (16.7)$$
$$j, j^c = 1,2, j^c \neq j$$

with the random variable, Y_{j^c}, being conditioned on the random variable, Y_j. We use notation Y to indicate that these variables have Laplace margins. W_j is a random variable from an unknown distribution. We introduce the additional parameters, m and s and assume that $Z_j = \left(W_j - m_j\right)/s_j$ follows a common distribution independent of covariates. Hence Eq. (16.7) may be written as:

$$\left(Y_{j^c} | Y_j = y\right) = ay + y^{b_j}\left(m_j + s_j Z_j\right), \qquad (16.8)$$
$$j, j^c = 1,2, j^c \neq j$$

The negative log-likelihood for pairs of the sample $\{y_{i1}, y_{i2}\}$ is given by:

$$\ell_{CE,j} = \sum_{i, x_{ij} > \psi_{ij}(\theta_i, \phi_i \lambda_j)} \left\{ \ln s_j y_{ij}^{\beta_j} + \frac{\left(y_{ij^c} - \left(a_j y_{ij} + m_j y_{ij}^{b_j}\right)\right)^2}{2\left(s_j y_{ij}^{\beta_j}\right)^2} \right\}, \qquad (16.9)$$
$$j, j^c = 1,2, j^c \neq j$$

$u_{CE,j}$ is the threshold with non-exceedance probability, λ_j, adopted for the conditional extremes model, meaning that the model is fitted to pairs of variables for which the non-exceedance probability of the conditioning variable exceeds λ_j. This threshold is set independently of the Generalized Pareto threshold u_2, and may be lower than that since the distribution below the GP threshold u_2 is defined by the gamma distribution.

Conditional extremes model threshold uncertainty is included by sampling λ_j from a uniform distribution over a pre-set quantile interval followed by ensemble averaging results over several different values of λ_j.

Residuals, r, are calculated from the estimated model parameters as:

$$r_{ij} = \frac{1}{\hat{s}_j}\left(\left(y_{ij^c} - \hat{a}_j y_{ij}\right) y_{ij}^{-\hat{b}_j} - \hat{m}_j\right) \qquad (16.10)$$

Multidimensional dependencies are modelled through the residuals. For each parameter, $j = 2, \ldots, n$, with n being the total number of variables modelled, the residual is calculated for each event i leading to a vector of residuals for each event $\boldsymbol{r}_i = [r_{i2}, \ldots, r_{in}]$. These n vectors of residuals are later used for simulating data in the model.

It then follows that the Laplace marginal value of parameter j conditioned on parameter 1 is given by

$$\left(Y_j | Y_1 = y\right) = a_j y + y^{b_j}\left(m_j + s_j r_j\right) \qquad (16.11)$$

The probability transform in Eq. (16.6) is inversed to get the non-exceedance probabilities of the associated parameters. The magnitude of each associated parameter is then calculated from its marginal distribution.

16.5 Covariates

Penalised B-splines are used to model the parameter variation with covariate. The basic idea of penalised B-splines, originally introduced by Eilers & Marx (1996), is to use B-splines with a moderately large number of evenly-spaced knots and control the parameter smoothness by a variance penalty factor, τ^2.

B-spline regression is started by dividing the domain over which to fit a curve into n' equal intervals by specifying the position of $n'+1$ knots. B(asis)-splines are then constructed as sequences of polynomial functions of degree, q, connected the knots. Each B-spline is positive in a range spanning $q+2$ knots, and zero elsewhere. Curve-fitting using B-splines consists in finding the coefficients, $\beta_{i=1:n'+q}$, with which to multiply the B-splines. The function value may be expressed as the linear combination of the spline basis, B, and the coefficients.

$$f(x) = \sum_{i=1}^{n'+q} \beta_i B_i(x) \tag{16.12}$$

Penalised B-splines (P-splines) are an extension of B-splines in which a penalty is put on the differences between adjacent β-coefficients. The degree of roughness is controlled by a variance parameter, τ^2, and the difference penalty matrix, $\mathbf{K}$. For first order differences, the difference matrix is given by:

$$\mathbf{K} = \begin{bmatrix} 1 & -1 & & & \\ -1 & 2 & -1 & & \\ & \ddots & \ddots & \ddots & \\ & & -1 & 2 & -1 \\ & & & -1 & 1 \end{bmatrix} \tag{16.13}$$

The basis of B-splines and the effect of roughness penalty, introduced through τ^2, is illustrated in Figure 16.1.

Both directional and seasonal variations are periodic. Periodic smoothing is introduced by 'wrapping' the spline at the ends. Specifically, the last q basis splines are merged with the first q splines and the total number of basis functions reduced by q. The difference penalty matrix is wrapped similarly, i.e., $\mathbf{K}$ is now:

$$\mathbf{K} = \begin{bmatrix} 2 & -1 & & & \dots & -1 \\ -1 & 2 & -1 & & & \\ & -1 & 2 & -1 & & \\ \vdots & & \ddots & \ddots & \ddots & \\ & & & -1 & 2 & -1 \\ -1 & & & & -1 & 2 \end{bmatrix} \tag{16.14}$$

B-splines are extendable to higher dimensions through tensor-product B-splines (see e.g.[48]). The multidimensional surface is now described by tensor-products of B-splines. The tensor-product B-splines in two dimensions are illustrated in Figure 16.2. The coloured shapes underlying the surface are the individual tensor-product B-splines scaled by the respective coefficients. The total number of β-coefficients to estimate is now $(n'_\theta + q) \times (n'_\phi + q)$. Different number of knots and different penalty factors may apply for each dimension. However, as Figure 16.2 also illustrates, large roughness penalty in one dimension may influence the smoothness in other dimensions. This indicates that roughness penalty should be determined for all dimensions simultaneously.

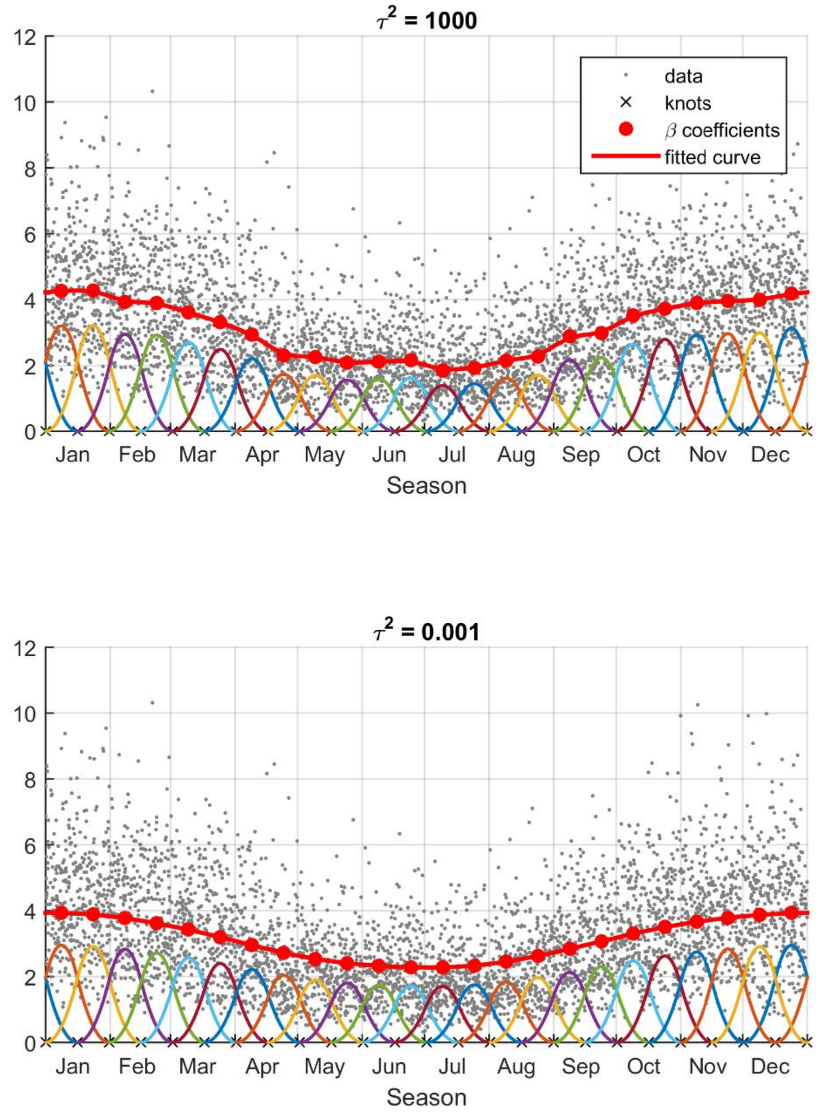

Figure 16.1 Quantile regression analysis for some fictive seasonally varying parameter, illustrating the components of P-splines
The coloured curves show the individual B-splines each multiplied by its respective b-coefficient. Quadratic B-splines (q=2) and first order penalty have been used.

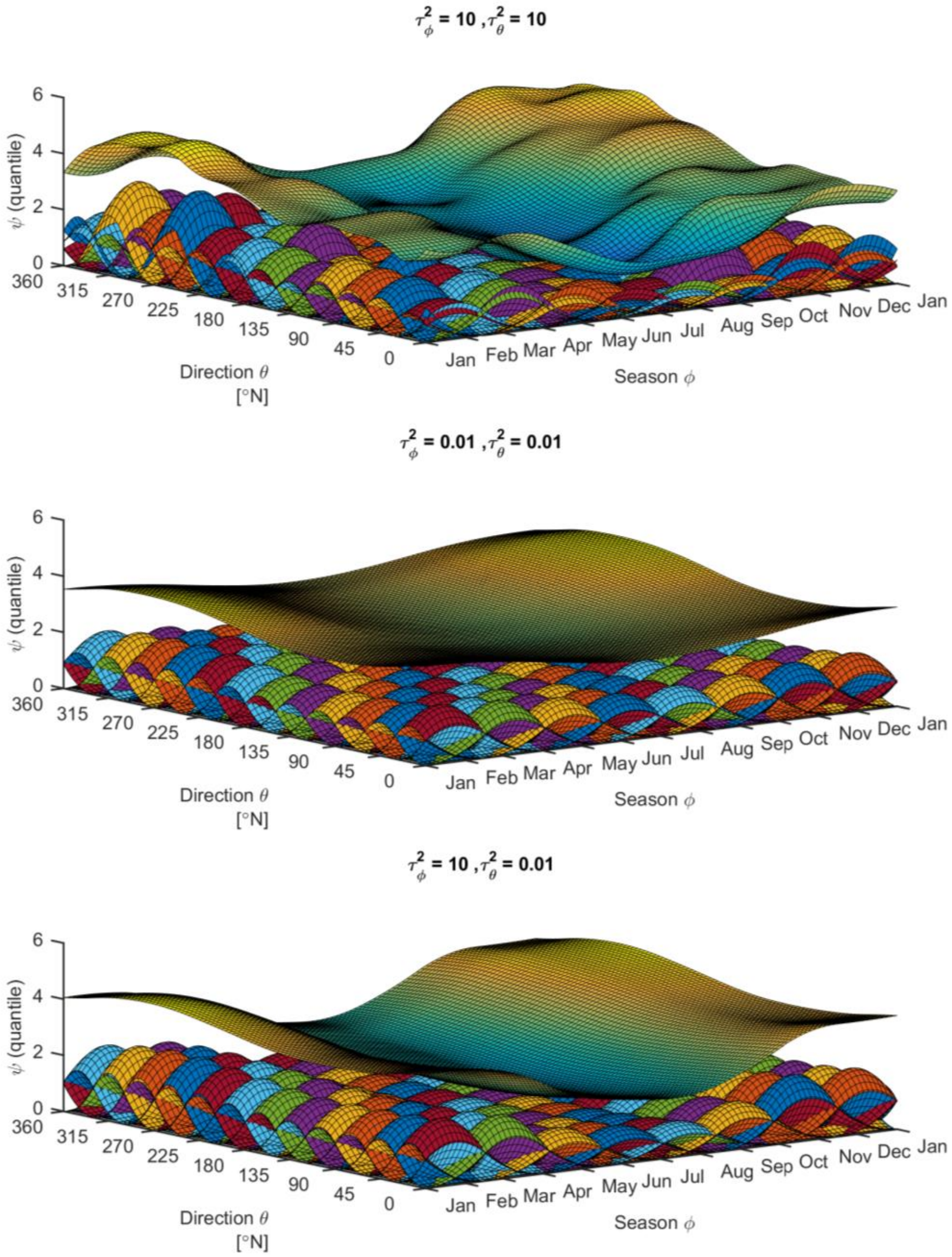

Figure 16.2 Quantile regression analysis, illustrating the components of tensor-product P-splines in two dimensions.
The coloured surfaces show the individual tensor-product B-splines each multiplied by its respective β -coefficient. Quadratic B-splines ($q = 2$) and first order penalty have been used.

Generalised linear array models

The penalised B-spline approach outlined above requires evaluation $\boldsymbol{x} = \boldsymbol{B\beta}$**,** where $\boldsymbol{B}$ is a (sparse) $m \times n$ matrix where m is the total number of data points irregularly spaced within the covariate domain, and n the total number of knots $n = n_1 \times n_2$. $\boldsymbol{\beta}$ is a $n \times 1$ vector of spline coefficients.

However, if we can organise our irregularly spaced data onto a regular $m_1 \times m_2$ grid, we may reduce the problem size substantially using Generalized Linear Array Models (GLAM) ([49],[50])These provide a computationally and memory-efficient framework for combining tensor product B-splines with array data and have been used in a very similar application in the past ([47])

In fact, the problem now reduces to evaluation of $\boldsymbol{B}_1\mathcal{M}(\boldsymbol{\beta})\boldsymbol{B}_2'$, where $\mathcal{M}(\boldsymbol{\beta})$ is a $n_1 \times n_2$ reordering of $\boldsymbol{\beta}$. $\boldsymbol{B}_1$ and $\boldsymbol{B}_2$ are size $m_1 \times n_1$ and $m_2 \times n_2$ respectively.

16.6 Parameter estimation

Distribution parameters for the model components described in Section 16.1 are defined by the $\boldsymbol{\beta}$ spline coefficients and parameter estimations thus consists in estimating the appropriate values of $\boldsymbol{\beta}$.

A Bayesian approach is applied to estimate the β-coefficients. The approach builds on work in[51], [52] and [53]

Priors

Spline Model

The prior for β up to a constant of proportionality is given by, [53]

$$(\boldsymbol{\beta}|\tau^2) \propto \frac{1}{(\tau^2)^{\frac{rk(\boldsymbol{K})}{2}}} \exp\left(-\frac{1}{2\tau^2}\boldsymbol{\beta}^T\boldsymbol{K}\boldsymbol{\beta}\right) \tag{16.15}$$

where $rk(\boldsymbol{K})$ is the rank of the penalty matrix, $\boldsymbol{K}$.

The variance parameter τ^2 is estimated through 10-fold cross-validation. Cross-validation is a robust and simple technique to optimise the predictive performance of a model, i.e., its capability of predicting the likelihood of a data sample that was not used to estimate the model. In this way the right complexity of the model is achieved – it is neither too simple nor is it over-fitting to the data. In this case, too simple a model would be too smooth and thereby ignore covariate effects that were truly present while a too complicated model would be exaggerating covariate effects by trying to adopt to the individual extreme events.

The 10-fold cross-validation consists in, for a given choice of τ^2, to fit the model to 90% of the data (training) and then calculate the likelihood of the remaining 10% of the data(validation). This is repeated 10 times such that all data points have been used one time for validation and the 10 likelihoods are then summed. This whole procedure is then repeated for a new choice of τ^2. Estimation of all values of τ^2 at once is not feasible as the model has as many values of τ^2 as the number of model parameters times the number of covariates. Instead, a sequential procedure has been adopted:

1. Values of τ^2 for the Γ-distribution are estimated by:
    - Estimate an appropriate global value by varying all τ^2 at the same time
    - Estimate a ratio between the shape α and mean μ by varying these separately (but using same value for season and direction)
    - Estimate the ratio between season ϕ and direction θ, using the relative ratio between α and μ as above
    - Repeat first sub-step but now using the relative ratios between α, μ, ϕ and θ.
2. The Γ-distribution is now fitted using the most appropriate combination of τ^2 estimated above and together with appropriate quantile thresholds κ_1, κ_2 this provides the non-stationary threshold above which the GP tail is assumed. For each GP tail, the steps a-d are followed though now with the ratio of GP shape ξ to scale ζ estimated under second sub-step above.

Figure 16.3 show an example of the results of a cross-validation, in this case for the upper tail of the $H_{m0,p,eq}$ variable. The rows in the plot show results of cross-validation steps *a* to *d*. Upper and lower subplots show the summed log-likelihood score on the 10 validation sets as against the prescribed value of τ^2. Row 2 and 3 show colour-scaled plots of the summed log-likelihood score for the tested combinations of τ_x^2 (along x-axis) and τ_y^2 (along y-axis). Yellow indicates higher cross-validation score (better predictive performance). The right-hand plots show the same results as the left-hand plots but smoothing the results across neighbouring τ^2 combinations. Results in left hand plots are normally used. The black dots show random combinations sampled from the probability distribution that can be constructed from the summed log-likelihood score. The black crosses indicate the optimum point.

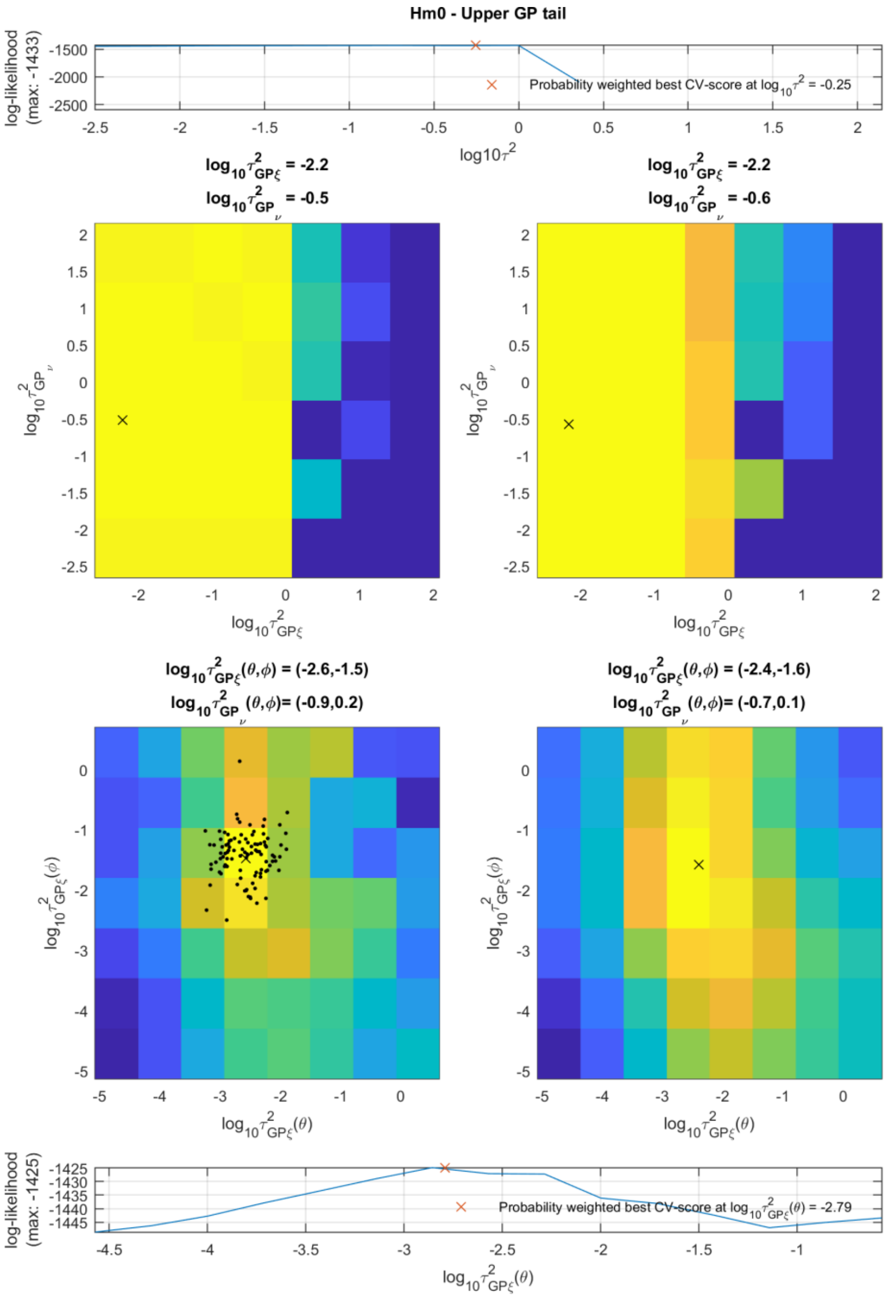

Figure 16.3 Example of cross-validation for the upper GP tail of the distribution of $H_{m0,p,eq}$.
See explanation in text for details

Marginal Distributions

In addition to the priors on the spline coefficients $\boldsymbol{\beta}$, we may also specify priors for the values of the actual distribution parameters or the support ranges. In the case of a negative GP shape parameter, the support range for the GP distribution has an upper end-point X_{max} given by (see Section 16.2 for definition of parameters)

$$X_{max} = -\frac{\zeta}{\xi} + u \tag{16.16}$$

The distribution tail will asymptotically approach this limit. If a physical absolute upper limit of a parameter is known, it may be introduced in the extreme value analysis by setting the upper end-point of the GP support range to be this limit.

Proposal generation

The posterior distributions are approximated using Markov Chain Monte Carlo methods with a Metropolis-Hastings (MH) sampling scheme. The MH scheme progresses as follows (for one model component):

1. Define start values[10], $\boldsymbol{\beta}^{(0)}$ Set iteration number $i = 1$.

2. For each model parameter; Propose candidate coefficients, $\boldsymbol{\beta}^*$ from a multivariate normal distribution $MVN\left(\boldsymbol{\beta}^{(i-1)}, \boldsymbol{S}\right)$. Two approaches are followed to estimate the covariance matrix $\boldsymbol{S}$
    - Following the approach of Rue ([54])also adopted by Lang and Brezger (/13/), proposals are drawn from a MVN with covariance matrix $\mathbf{S} = \left(\mathbf{B}^T\mathbf{B} + \frac{1}{\tau^2}\mathbf{K}\right)^{-1}$
    - Following Roberts and Rosenthal ([53])the empirical covariance matrix is estimated, and proposals drawn from a MVN with covariance matrix

    $$\mathbf{S} = (1-\epsilon)^2 2.38^2 \frac{\Sigma_n}{d} + \epsilon^2 \times 0.01 \frac{I_d}{d} \tag{16.17}$$

    where Σ_n is the empirical covariance matrix of size $d \times d$ estimated from the markov chain. The latter term $0.01 I_d/d$ is random noise and the small constant ϵ is used to control the degree of random noise in the proposal. Roberts and Rosenthal use $\epsilon = 0.05$ and we adopt the same value here.

    The latter approach requires an estimate of the covariance matrix, which can only be obtained from running the MCMC. Hence, approach a. is first run for a large number of iterations. As approach b. turns out to be computationally faster, the MCMC algorithm has been set to switch to this approach after a number of iterations. Multivariate normal random samples are generated from a Cholesky decomposition $\mathbf{L}$ of the covariance matrix $\mathbf{S}$. Hence

    $$\boldsymbol{\beta}^* = \boldsymbol{\beta}^{(i-1)} + \mathbf{L} \times \boldsymbol{u} \tag{16.18}$$

    where $\boldsymbol{u}$ is a vector of standard normal random (uncorrelated) samples.

3. Accept $\boldsymbol{\beta}^*$ with probability:

[10] Start values for spline coefficients are made by fitting constant models through (seasonally-directionally) binned data, followed by fitting a smoothing spline through the estimated parameter values

$$\mathcal{A}\left(\boldsymbol{\beta}^{(i-1)},\boldsymbol{\beta}^{*}\right) = \min\left\{1,\frac{\mathcal{L}(\boldsymbol{z}|\boldsymbol{\beta}^{*})\pi\left(\boldsymbol{\beta}^{*}|(\tau^{2})^{(i-1)}\right)\pi\left((\tau^{2})^{(i-1)}\right)}{\mathcal{L}(\boldsymbol{z}|\boldsymbol{\beta}^{(i-1)})\pi(\boldsymbol{\beta}^{(i-1)}|(\tau^{2})^{(i-1)})\pi((\tau^{2})^{(i-1)})}\right\} \quad (16.19)$$

4. Steps 2-3 are repeated for each model parameter after which the iteration counter i is incremented by one

Full model inference

The procedure detailed above is valid for one single model component (gamma distribution bulk, GP tail, Conditional extremes model). However, the full model requires estimation of all components in a hierarchical order as follows:

$$\left.\begin{array}{l}\text{Parameter 1: Gamma distribution bulk} \rightarrow \text{GP tails}\\ \text{Parameter 2: Gamma distribution bulk} \rightarrow \text{GP tails}\\ \dots\\ \text{Parameter n: Gamma distribution bulk} \rightarrow \text{GP tails}\end{array}\right\} \rightarrow \text{Conditional Extremes Model}$$

This is achieved as follows:

1. For each input variable (e.g., H_{m0}, T_p, ..., etc);
    - Fit the gamma distribution to all events and save several independent samples from the chain. Also fit the rate of occurrence model for the primary parameters of interest that are later used as conditioning parameters.
    - At each stored sample of the gamma distribution of bulk data, sample a threshold non-exceedance probability, compute the threshold, run a GP chain, and save an appropriate number of samples of this after burn-in. Both high and low tail are estimated independently in this way.

   This procedure results in n samples (*n = number of Gamma samples times number of GP samples*) of each marginal distribution.

2. Fit all conditional extremes models to the marginal distribution samples. The CE models are fitted simultaneously in order to achieve vectors of residuals emanating from the same historical events, whereby multidimensional dependencies can be carried over into storm simulations (see also Section 16.4). The conditional extremes model threshold ψ uncertainty is accounted for by updating the threshold non-exceedance probability λ for each update of the GP tail threshold in the marginal models. The iteration procedure for each λ update is as follows:
    - Sample a threshold non-exceedance probability and identify the events above this in the conditioning distribution.
    - Fit the CE model across all GP tail updates and to each variable in turn. The CE chain is run for several iterations for each GP tail update, but only the last iteration is stored. Also, the residuals are stored for the last iteration. By running this procedure over all variables in turn, a matrix of residuals is built for each stored CE iteration with size number of threshold exceeding events times number of variables.

The above procedure results in an equal number of samples of the marginal and conditional models, the latter with associated residuals. Several thresholds in both marginal tails and conditional extremes are incorporated in this sample, thus accounting for some of the threshold uncertainty. Equal weight is thereby given to all possible thresholds within the assumed plausible range. It is our experience with constant models that this is a reasonably good approximation for most data sets and superior to a constant threshold approach.

Proper implementation of the MCMC approach ensures that the final sample of model parameters thus obtained represents a sample from the posterior distribution of the model parameters. The uncertainty related to the extrapolation from a limited input data sample to events with a very low exceedance probability is reflected in this posterior distribution.

An overview of the different distribution parameters to be determined for each marginal and conditional extremes distribution is given in Table 16.1. The threshold quantiles are specified as constants and do therefore not vary with covariates. This means that a certain threshold for example for a GP tail model is taken as a constant (across covariate space) quantile in the underlying Gamma distribution. But as the Gamma distribution itself is non-stationary with respect to covariates, the actual threshold for the GP model will also vary with covariates. The quantiles are sampled uniformly from specified intervals.

Table 16.1 Overview of model parameters

Description	Symbol	Type[11]
Rate of occurrence	ρ	Tensor-Product B-spline
Γ distribution shape	α	Tensor-Product B-spline
Γ distribution mean	μ	Tensor-Product B-spline
GP low tail threshold quantile	κ_1	Constant
GP low tail shape parameter	ξ_1	Tensor-Product B-spline
GP low tail scale parameters	ζ_1	Tensor-Product B-spline
GP high tail threshold quantile	κ_2	Constant
GP high tail shape parameter	ξ_2	Tensor-Product B-spline
GP high tail scale parameters	ζ_2	Tensor-Product B-spline
CE threshold quantile	λ	Constant
CE a parameter	a	Tensor-Product B-spline
CE b parameter	b	Tensor-Product B-spline
CE mean parameter	m	Tensor-Product B-spline
CE standard deviation parameter	s	Tensor-Product B-spline

16.7 Simulation and return value estimation

Due to the complexity of the model and the need to ensemble average over the posterior distribution sample of the model parameters, return values are obtained by simulating events in the model. Popular speaking, such a simulation consists in sampling a very large number of events whereby the sought return value can be ‘read off’ as the i’th largest event in the simulated sample. The rank i depends on the simulation length (numbers of years simulated) and the return period in question.

Combined with an appropriate event (storm) model this procedure also allows for swift convolution of the long-term distribution of the slowly varying parameters with a short-term distribution of a certain type of response. The

[11] In the case of a constant (covariate-free) model, all parameters are constant.

classical example in this respect is the convolution of the long-term distribution of sea states with the short-term distribution of maximum wave crest heights to obtain the long-term distribution of the maximum crest elevation.

The simulation procedure followed to simulate one year of events is detailed below.

1. Sample a particular iteration from the MCMC chain
2. Sample the number of events from a Poisson distribution with arrival rate corresponding to the average annual number of events in the input data set
3. Sample non-exceedance probability for all events
4. For a non-stationary model, assign covariates to each event through the fitted non-stationary rate function for the conditioning variable
5. Calculate the magnitude of the conditioning variable for all events from its marginal non-stationary distribution
6. Resample events from the data set for all events with non-exceedance probability below the conditional extreme model quantile threshold \lambda as the conditional extremes model is only applicable for conditioning events with non-exceedance probability above λ. In practice, the resampling is done by searching for the nearest event in the data set in terms of all covariates and magnitude
7. Magnitudes of conditioned parameters $\eta_2, \ldots, \eta_n$ above the conditional extreme model quantile threshold λ are modelled through the conditional extremes model. A vector of residuals $\boldsymbol{r}_i = [r_{i2}, \ldots, r_{in}]$ emanating from the same event in the data set is sampled for each event from the stored residuals for the particular MCMC iteration. The Laplace marginal values for all conditioned parameters calculated from eq. (16.11) and the marginal distributions applied to convert the Laplace marginal values to the physical values.

Return values with long recurrence period requires many years to be simulated. Denoting the number of years n and the required return period T_r, reasonably converged estimates of return values are obtained when $n \geq 100T_r$. In other words, a 100-year return value requires simulation of around 10,000 years.

Return values are usually reported as quantiles in the distribution of the annual maximum. The annual maximum distribution is constructed from the simulation by only retaining the largest simulated value per year and the relationship between quantile and return period given by:

$$q_r = \exp\left(-\frac{1}{T_r}\right) \tag{16.20}$$

The return values hereby obtained reflect the uncertainty in the extreme value distributions and larger uncertainty will inflate the return values especially for return periods longer than the duration of the historical input data sample. This is achieved by integrating across the posterior distribution of the model parameters (effectively achieved by sampling amongst the MCMC iterations when simulating events in step 1). This type of distribution is also known as the posterior predictive annual maximum distribution.

Conditional distributions of associated parameters are readily obtained from the simulation of conditioned parameters.